

Development and Validation of a Computational Tool for Real-time Hybrid Simulation of Steel Frame Structures

Nestor E. Castaneda, Xiuyu Gao and Shirley J. Dyke

{necastaneda@sgh.com, Xiuyu.Gao@mcskenny.com, sdyke@purdue.edu}

Report IISL — 002, October 2012



Abstract

The use of traditional techniques such as the shake table or the pseudo-dynamic (PSD) test are often used to validate and disseminate new technologies associated with structural response attenuation. At full-scale, the ability to perform such tests on realistic structures is limited. Real-time hybrid simulation (RTHS) offers an economical and reliable methodology for testing integrated structural systems with rate dependent behaviors. Within a RTHS implementation, critical components of the structural system under evaluation are physically tested, while the more predictable ones are replaced with computational models. Real-time execution, or performing the test with a one-to-one time scale, ensures that the tests yield more realistic responses. As a result, RTHS implementations provide an alternate approach to evaluating structural / rate-dependent systems under actual dynamic and inertial conditions without need for full-scale structural testing. One significant challenge for successful RTHS is the availability of a robust and reliable simulation tool to accurately represent the physical complexities within the computational counterparts. Accurate computational models are required to ensure compatibility, stability and adequate synchronization between both computational and experimental substructures during testing. In this study, the RT-Frame2D tool is proposed. The development, implementation and validation of this open source real-time computational platform intended for the hybrid simulation of dynamically-excited steel frame structures, is presented. The computational platform is designed to recreate common sources of nonlinear behavior in steel frame structures, with adequate modeling and integration schemes to enable its flexible implementation within a typical RTHS platform. Through a series of numerical and experimental studies of typical RTHS scenarios, the capabilities of the tool are demonstrated, evaluated and validated. (RT-Frame2D and user manual are available at nees.org <http://nees.org/resources/realtimeframe2d>).

Acknowledgement: Financial support for this research has been provided by the National Science Foundation Grant NSF CNS-1028668 (MRI), NSF CMMI-1011534 (NEESR) and The Purdue University Cyber Center Special Incentive Research Grant (SIRG).

Data presented herein will be available for download in the NEEShub (nees.org).

TABLE OF CONTENTS

	Page
ABSTRACT.....	2
CHAPTER 1. INTRODUCTION	5
1.1. Motivation and objective	12
1.2. Overview of the study	14
CHAPTER 2. COMPUTATIONAL FRAMEWORK	17
2.1. Modeling of Mass	18
2.2. Modeling of Damping	20
2.3. Linear Beam-Column Elements.....	22
2.4. Beam-Column Element with Linear/Nonlinear Flexible Connections	29
2.5. Nonlinear Beam-Column Elements	35
2.6. Transformation from local to global coordinate systems.....	43
2.7. Structural joint modeling	45
2.8. Hysteretic rules	56
2.9. P- Δ effect modeling	58
2.10. Integration schemes for nonlinear dynamic analysis	61
2.10.1. Explicit Chen-Ricles (CR) integration scheme.....	62
2.10.2. Implicit-Newmark-beta integration scheme.....	68
2.11. RT-Frame 2D Implementation.....	70
CHAPTER 3. NUMERICAL EVALUATION.....	82
3.1. Evaluating real-time execution capabilities	82
3.2. RT-Frame2D numerical evaluation	93
CHAPTER 4. EXPERIMENTAL VALIDATION I: REAL-TIME HYBRID SIMULATION AT THE IISL	126
4.1. Experimental plan	127
4.2. RTHS platform at the Intelligent Infrastructure Systems Laboratory.....	129

	Page
4.3. Experimental set-up	133
4.3.1. 2D Steel frame specimen	133
4.3.2. Magneto-rheological (MR) damper device	138
4.3.3. Phenomenological Bouc-Wen model.....	140
4.3.4. MR Damper device characterization.....	141
4.3.5. Hydraulic actuator compensation scheme.....	144
4.4. Performance evaluation of RTHS	147
4.5. Implementation - I.....	150
4.6. Implementation - II	157
4.7. Implementation - III	171
4.8. Implementation - IV.....	181
CHAPTER 5. EXPERIMENTAL VALIDATION II: REAL-TIME HYBRID SIMULATION AT THE SSTL	207
5.1. Experimental plan	207
5.2. RTHS platform at the Smart Structures Technology Laboratory	208
5.3. Experimental set-up	210
5.3.1. Large-scale magneto-rheological damper device.....	210
5.3.2. Hyperbolic tangent model.....	212
5.3.3. MR Damper device characterization.....	214
5.3.4. Hydraulic actuator compensation scheme.....	215
5.4. MR Damper evaluation at the SSTL (UIUC)	216
CHAPTER 6. CONCLUSIONS	230
LIST OF REFERENCES.....	236

CHAPTER 1. INTRODUCTION

Despite the advances in the earthquake engineering field over the last years, earthquakes still remain as one of the major causes of disaster and threats to both human life and assets. While design methods are under continuous evaluation and improvement, new technologies associated with structural response attenuation (Soong and Spencer, 2002) have become a promising alternative for seismic mitigation in building structures. However, the use of traditional testing methodologies for full-scale validation of such systems to both develop appropriate design guidelines and standardize their use is limited. Two methodologies are commonly used for evaluating the performance of structural systems subjected to dynamic and earthquake loads: the shake table test (e.g. Yamaguchi and Minowa, 1998; Elwood, 2002; Kang, 2004) and the pseudo-dynamic test (PSD) (e.g. Mahin SA and Shing, 1985; Thewalt and Mahin, 1987; Mahin et al., 1989; Thewalt and Roman, 1994). In the shake table test, the structural specimen is placed on a platform and subjected to a ground motion excitation to induce realistic inertial and dynamic action on the specimen. However, reduced-scale structural models are typically tested due to the payload constraints of most shake tables. Alternatively, in PSD tests, the structural specimen is subjected to a set of displacement increments which are sequentially imposed using hydraulic actuators. Within each loading step, force signals measured from the test specimen are fed back into a numerical integration scheme to solve the equation of motion and calculate the next displacements to be imposed. However, testing under rate-dependent conditions is limited in PSD tests due to their expanded time scale execution, sometimes taking a thousand times longer than the shake table test. Moreover, despite the fact that large or full-scale structures may be considered with PSD tests, manufacturing costs and operational conditions may become prohibitive.

To enable researchers to perform larger earthquake engineering tests with accurate global behavior and reduced costs, continuous or real-time execution strategies are being combined with hybrid testing techniques to reduce the costs involved with the fabrication and full-scale testing of large-scale structures. When rate-dependency is involved, real-time execution is essential for accurate global response evaluation. In real-time hybrid simulation (RTHS), the system under evaluation is decomposed into experimental (physical) and computational (virtual) substructures (components). Critical components with unknown behavior can be evaluated experimentally, leading to a better understanding of these components, while the more predictable ones can be accounted for using computational models. The RTHS is then executed with a real-time constraint to enforce a one-to-one time scale between the experimental and computational substructures. As a result, a RTHS testing platform provides the ability to evaluate structural / rate-dependent systems under actual dynamic and inertial conditions without the need for testing the entire structure.

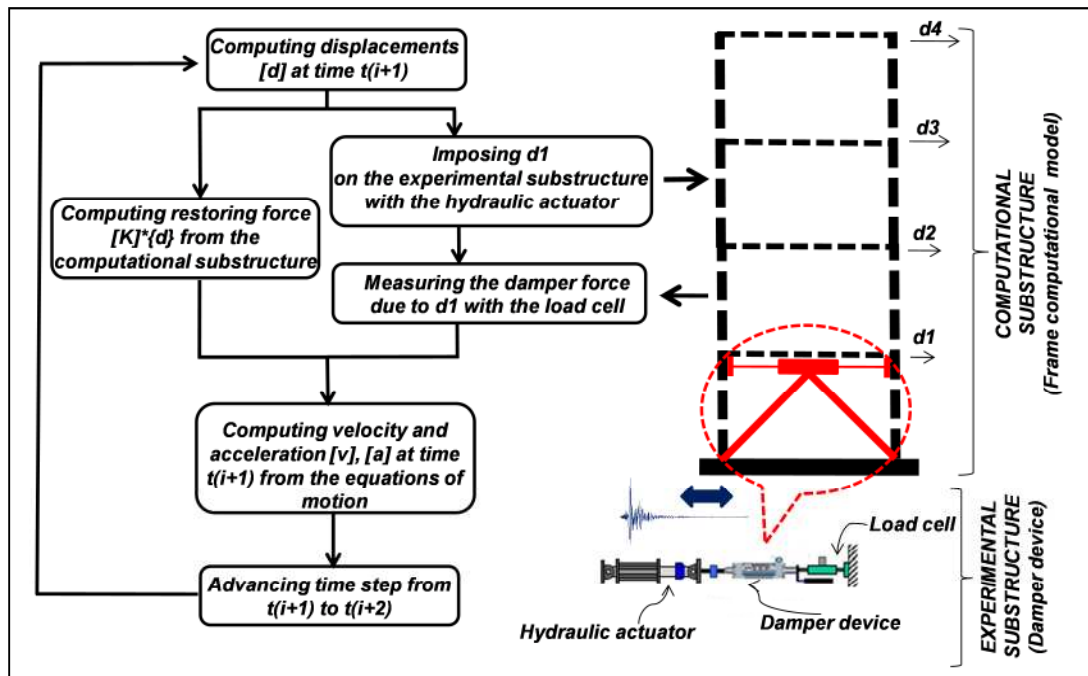


Figure 1.1: Diagram of tasks executed in one time step of a RTHS

Figure 1.1 provides a diagram showing the tasks executed during one time step of a RTHS in which a seismically-excited frame structure with a rate-dependent damping device is evaluated.

Note that here the damping device is assumed to be the focus of the test and thus is defined as the experimental substructure. The frame structure is considered computationally. Therefore, the experimental and computational substructures (components) are well-defined. These two substructures are connected at interface degrees of freedom (DOF), i.e. DOF that are shared by both substructures. At the starting point in the integration step, global displacements are provided from a computational platform used to solve the equation of motion with a numerical integration scheme. Displacements calculated at time $t(i+1)$, and belonging to interface DOF, are imposed on the experimental substructure, the damper, by hydraulic actuators. The resulting restoring forces exerted by the experimental substructure are then measured using load cells located at the hydraulic actuators. These measured restoring forces are then added to the computational restoring forces calculated within the computational platform at time $t(i+1)$. Note that the computed restoring forces may include complex nonlinear behavior. The integration scheme then is used to calculate the next set of global displacements at time $t(i+2)$ based on the current ground motion input as well as the experimental and computational restoring forces.

RTHS is of great interest in the earthquake engineering community for enabling the testing of larger and more complex specimens at a reduced cost from the traditional methods. Development of this technology has been pursued for only the last couple of decades (Bursi and Wagg, 2008). The first real-time hybrid simulation was implemented by testing a single degree of freedom (SDOF) system with a single actuator (Nakashima et al., 1992). Here, a modified central difference algorithm was used to calculate target displacements (displacements to be imposed by the hydraulic actuator on the test specimen) separately at the even and odd time steps (i.e., staggered integration). As a result, while the actuator was imposing the target displacement on the structure, the target

displacement for the next time step was being computed. Another implementation was performed in the United Kingdom (Darby et al., 1999) in which RTHS of several experimental substructures coupled at a single DOF was performed. A more complex implementation involving linear computational substructures with multiple DOF was later reported by Darby et al. (2000). Magonette (2001) also proposed testing techniques for real-time PSD evaluation of large-scale structural systems equipped with anti-seismic protection devices based on strain-rate sensitive materials. The first real-time hybrid testing using computational and experimental substructures with nonlinear behavior was reported in 2001 (Blakeborough et al., 2001). Here several testing procedures were evaluated through a variety of tests at small and large scale, with either linear or nonlinear substructures, to compare their performances. Mercan and Ricles (Mercan, 2003; Mercan and Ricles, 2004) proposed another real-time hybrid implementation using a Newmark explicit algorithm (Newmark, 1959) along with the previous staggered integration scheme proposed by Nakashima et al. (1992). An Alpha-Beta Tracker filter (Mahafza, 1998; Skolnik, 1990) was utilized to correct the calculated displacement in each time step and avoid high frequency content in the velocity response of rate-dependent systems. A combined RTHS implementation was proposed by Wu et al. (2007). Here, an equivalent force-feedback control loop was utilized to account for the solver iteration utilized by an implicit integration scheme to solve the equation of motion, while traditional displacement-based control (PID) was still adopted for motion control of hydraulic actuators during the test.

The advantages offered by the RTHS testing methodology has lead the attention of the research community towards the development and implementation of integrated and reusable platforms for RTHS testing. Some of these platforms can be found through the George E. Brown Network for Earthquake Engineering Simulation (NEES; <http://www.nees.org/>). For instance, the NEES facility at Lehigh University has been utilized for the NEESR research project *Performance-Based Design and Real-time, Large-scale Testing to Enable Implementation of Advanced Damping Systems*. The project focuses on the development and validation through RTHS procedures of

appropriate performance-based design guidelines for implementation of advanced damping systems in civil infrastructure (Friedman et al., 2010; Jiang et al., 2010; Jiang and Christenson, 2011; Chae, 2011; Phillips, 2012). Other NEES facilities with the capabilities to perform RTHS include NEES@berkeley and NEES@buffalo. Another and more recent RTHS platform is found in the Intelligent Infrastructure Systems Laboratory (IISL) at Purdue University. Here, a novel Cyber-physical Instrument for Real-time Structural hybrid Testing (CIRST) has been developed, implemented and validated (Gao, 2012; Gao et al., 2012; Castaneda et al., 2012). The instrument is mainly proposed for the evaluation and validation of small-scale frame structural configurations equipped with damper devices and re-configurable use. Other small-scale laboratories capable of performing RTHS include the Smart Structures Technology Laboratory (SSTL) at the University of Illinois, Urbana-Champaign (Phillips and Spencer (2011, 2012)), Western Michigan University (Shao et al., 2011; Shao and Enyart, 2012), and Johns Hopkins University (Nakata, 2011; Nakata and Stehman, 2012).

There are two main challenges in the implementation of RTHS: (i) phase lag introduced by the hydraulic actuator dynamics and (ii) computational time required for having available the target displacements (calculated from the computational substructures) to be imposed by the hydraulic actuator at the next time step.

The presence of phase lag introduced by the actuator dynamics causes the experimental displacements to lag behind the computed displacements. This lag leads to the measurement of incorrect restoring forces, and more importantly, potential instabilities. Instabilities within the RTHS system due to the presence of a phase lag have been investigated using single degree of freedom (SDOF) linear systems (Christenson et al., 2008; Gao et al., 2012). As presented by Gao et al. (2012), the equation of motion representing a RTHS implementation and defined in terms of the computational and experimental substructures is expressed as

$$(M_c + M_e)\ddot{y} + (C_c + C_e)\dot{y} + (K_c + K_e)y = -(M_c + M_e)\ddot{y}_g \quad (1.1)$$

where the indices “c” and “e” stand for the computational and experimental substructures. By introducing a time delay as a simple model for the phase lag due to the hydraulic actuator dynamics, the equation of motion is reformulated as

$$\begin{aligned} & (M_c + \Delta M_e - \Delta \delta t C_e) \ddot{y} + [C_c + \Delta C_e + \Delta \delta t (M_e \omega^2 - K_e)] \dot{y} + (K_c + \Delta K_e) y \\ & = -(M_c + M_e) \ddot{y}_g \end{aligned} \quad (1.2)$$

Here, Δ and δt express the amplitude and phase errors induced by the hydraulic actuator dynamics in the measured response, respectively. Because the hydraulic actuator system usually introduces a phase lag i.e. $\delta t > 0$, the resulting negative stiffness term K_e plays a critical role within the RTHS stability (see Equation (1.2)). It is clear that certain K_e test configurations could yield negative coefficients in the second term of the left side of Equation (1.2), leading to potential instabilities. This effect has been also studied in the past by Horiuchi et al. (1996, 1999). In these studies, the phase lag was interpreted as negative damping, which is consistent with the previous analysis.

Several schemes for compensating for the phase lag to the actuator dynamics have been presented in the literature. Most of these proposed approaches have considered the actuator dynamics to be modeled as a pure time delay. Typically, a digital control algorithm is applied to counteract the delay induced by the plant, i.e. the hydraulic actuator dynamics and the experimental substructure. Due to the highly nonlinear behavior present in the actuator, linearization of the plant is usually pursued for designing control algorithms with reliable performance within certain operational bandwidths of the system. For instance, an adaptive control law based on a first-order dynamic model of the plant was recently proposed by Chen and Ricles (2010). Control techniques based on model-based feed-forward or combined with feed-back arrangements have also been proposed (Shing et al., 2004; Reinhorn et al., 2004; Carrion and Spencer, 2007; Phillips and Spencer, 2011). In these approaches inverse of first-order or high-order models of the plant is used for compensation. A more recent approach, using a H_∞ control strategy

(Glover and McFarlane, 1989), was designed and implemented by Gao (2012). Experimental evaluation, performed using the RTHS platform at the IISL, demonstrated the effectiveness, robustness and potentiality of this control algorithm to accommodate large system uncertainties in the plant.

As mentioned previously, the second main challenge to broad implementation of RTHS for earthquake engineering experiments is the requirement for rapid calculations associated with the complex computational substructures. Target or computational displacements must be available “fast enough” so that they can be imposed to the experimental counterparts on time, i.e. within the integration time step. Prior researchers have developed several ways to circumvent these time constraints imposed by RTHS. A methodology based on a polynomial fit of previous displacements was proposed by Horiuchi (Horiuchi et al., 1996) to predict target displacements beyond the current time step. This methodology was later implemented and tested by Nakashima and Masaoka (Nakashima and Masaoka, 1999) when performing a real-time PSD test of a multiple degree of freedom (MDOF) system. In this implementation, the actuators were able to achieve a continuous behavior while the next time step calculations were completed. Once the new target displacement was available, an interpolation scheme was used to ensure that the calculated displacement was reached at the end of the next time step.

Clearly, a computational platform with real-time execution capabilities is a key component for ensuring a successful RTHS implementation. Moreover, the computational tool must have the capability to accurately recreate the physical complexities in the computational counterparts too and ensure adequate synchronization between both computational and experimental substructures. The focus of this study is on the development, implementation and validation of a computational platform that satisfies both of those requirements. Further considerations and objective for the development of such a RTHS computational platform is exclusively discussed in the subsequent section.

1.1 Motivation and objective

One main challenge to ensure a successful RTHS is the ability of the computational platform to recreate the physical behavior of the computational substructure with sufficient accuracy and under real-time execution constraints. For instance, during large seismic events, building members such as beams can yield in isolated locations, resulting in global nonlinear behavior that may significantly affect the structural response. If this effect is not properly considered in the modeling of the computational substructure, the results would not be comparable with those obtained using a full-scale testing equivalent.

Software environments to facilitate interfacing computational models with the experimental counterparts have been proposed within the research community. The first such tool was developed at the University of Illinois in Urbana-Champaign within the NEES System Integration project funded by NSF. The tool is called *UI-SIMCOR: The Multi-Site Substructure Pseudo-Dynamic Simulation Coordinator* (Spencer, 2003; Kwon et al., 2005). Additionally, a second tool called *OpenFresco: The Open-Source Framework for Experimental Setup and Control* (Schellenberg and Mahin, 2006; Schellenberg et al., 2006) was also developed at the University of California at Berkeley. This implementation makes use of the powerful object-oriented computational platform *OpenSEES: Open System for Earthquake Engineering Simulation* (Mckenna and Fenves, 2002; Mckenna et al., 2002). Both of these platforms were developed for hybrid simulation, but neither of these platforms were originally intended for real-time execution. Also, note that both of these platforms are available as open-source tools at nees.org.

Several advanced commercial and open-source simulation packages with a variety of numerical approaches are available for the analysis of frame structures. Among them, STAAD-III, GTSTRUDL, RISA-2D, SAP2000, ETABS, RAM FRAME, DRAIN-2D (Kannan and Powell, 1973), SARCF (Chung et al., 1988; Gomez et al., 1990), IDARC (Park et al., 1987; Kunnath et al., 1992), ANSR (Oughourlian and Powell, 1982) and

OpenSEES have become widely used by the industry and research community. Although these packages exhibit the state-of-the-art in structural analysis with a wide range of approaches for performing either first-order or second-order elastic-inelastic analyses, they share a common limitation for RTHS applications, *their inability to be executed in real-time*.

For many years, the earthquake engineering research community has relied on the use of the *MATLAB* (The Mathworks, 2011) environment for simulations involving structural dynamics and control. Many of the benchmark problems developed throughout the 90's were based in *MATLAB*. The availability of the *MATLAB/Real-time Workshop toolbox* and more recently *MATLAB/xPC* also facilitates the development of RTHS capabilities revolving around this environment. The choice of the *MATLAB* environment is ideal for easy integration of RTHS components such as the computational platform, predefined control algorithms or data exchange blocks between computational and experimental substructures.

A few research efforts based around developing computational frameworks within the *MATLAB* environment have been proposed. For instance, *HybridFEM: A program for nonlinear dynamic time history analysis and real-time hybrid simulation of large structural systems* (Karavasilis et al., 2009) has been developed in Lehigh University at the Engineering Research Center for Advanced Technology for Large Structural Systems (ATLSS). This tool relies on a library of nonlinear beam-column elements in conjunction with material models for steel and reinforced concrete and two integration schemes. However, this platform has been conceived and developed for in-house use and thus its use is restricted to RTHS applications performed at the ATLSS. Another, RTHS software has been developed at the University of Colorado-Boulder named *MERCURY: A Computational Finite-Element Program for Hybrid Simulation* (Saouma et al., 2010). The tool has been designed to run within either a *LabView* or *MATLAB/Simulink* environment and relies on several modeling features for nonlinear dynamic analysis with

a variety of elements and material models in addition to implicit and explicit integration schemes.

The need for an open-source computational environment with *reliable modeling and real-time execution capabilities* for RTHS applications has been justified. Moreover, a *flexible environment* for implementation of such platform, to enable its easy integration with the other RTHS components, has been also established. The primary focus of this study is the development, implementation and validation of an open-source real-time computational platform for RTHS of dynamically-excited steel frame structures. The tool is intended to satisfy the demands stated previously for the RTHS community, and has been given the name RT-Frame2D (RT-Frame2D and user manual are available at nees.org <http://nees.org/resources/realtimeframe2d>). This computational platform is designed to include models for the common sources of nonlinear behavior in steel frame structures and to ensure its efficient integration within a RTHS framework. Extensive numerical evaluations and challenging experimental implementations based around several RTHS scenarios are used to validate the proposed computational platform. Successful results are provided to demonstrate the accuracy, stability and real-time execution capabilities of the proposed computational platform.

1.2 Overview of the study

The focus of this study is the development, implementation and validation of RT-Frame2D, a computational platform appropriate for real-time hybrid simulation of dynamically-excited steel frame structures. This open-source tool is expected to provide researchers with access to RTHS capabilities, allowing for more versatile and cost-effective evaluation of earthquake engineering concepts. This study is organized as follows:

Chapter 2 presents relevant literature review and theoretical background regarding and used for development of the different modeling features offered by the proposed

computational platform. The chapter starts with an overview of the available modeling options in the proposed tool. Modeling of mass and damping is then introduced. A set of linear-elastic and nonlinear schemes for the modeling of beam-column elements in frame structures is then presented. A novel model for consideration of panel zone effect in frame structures is then presented. The importance of explicit procedures for solving the equations of motion within a RTHS application is emphasized and an unconditionally-stable integration scheme is presented as the primary integration scheme for the proposed computational platform. Accuracy and stability of the proposed integration scheme is discussed and evaluated. An additional integration scheme based on implicit format is also proposed and implemented in conjunction with a single-step scheme to avoid iterations associated to nonlinear solvers. Finally, relevant information associated to the implementation and execution of the computational platform within a *MATLAB/Simulink* environment is presented and discussed.

Numerical evaluation of the proposed computational platform is provided in Chapter 3. Two studies are performed for this evaluation. One study investigates the real-time execution capabilities of the computational platform for a set of given modeling considerations. The study is performed by quantifying the execution times required when subjecting the computational platform to the nonlinear dynamic analysis of six computational models with an increasing number of DOF, and using different modeling options. The second study performs a qualitative comparison of the modeling capabilities offered by the computational platform with those obtained using an open-source computational platform widely used in the earthquake engineering research community. The comparison is performed based on the displacement and absolute acceleration records for five different computational models.

The first portion of the experimental validation of the proposed computational platform is presented in Chapter 4. The computational platform is validated through implementation for real-time execution under various hybrid simulation scenarios. The RTHS are performed at the Intelligent Infrastructure Systems Laboratory (IISL) at Purdue

University using an experimental plan based on four experimental implementations. A small-scale damper and frame specimens are used as experimental substructures. Modeling and design considerations for the experimental substructures are extensively discussed in detail. Additionally, Chapter 4 presents relevant information about the development and implementation of a cyberphysical small-scale real-time hybrid simulation instrument (CIRST) used for completion of the proposed experimental plan. Experimental procedures and considerations for the computational platform in each experimental implementation are then presented. Corresponding results are also discussed.

Chapter 5 presents the second portion of the experimental validation of the proposed computational platform. Validation is performed in the Smart Structures Technology Laboratory (SSTL) at the University of Illinois in Urbana-Champaign. Here, an experimental implementation based on a RTHS of an experimental large-scale MR damper within a computational frame structure is proposed for validation. Main aspects considered in the experimental implementation followed by a description of the computational platform use are then presented. Experimental results are presented and discussed at the end of the Chapter.

Chapter 6 presents conclusions and proposes future directions that might enhance the current modeling and real-time execution capabilities offered by the computational platform.

CHAPTER 2. COMPUTATIONAL FRAMEWORK

One of the main challenges to ensure a successful implementation of real-time hybrid simulation (RTHS) is the ability to recreate the physical behavior of the simulated portion of the test with sufficient accuracy under fast execution so that compatibility can be guaranteed between the simulated and experimental components during testing. In this chapter, the main modeling features of a newly-developed computational platform (RT-Frame2D: User's Manual, 2012) for performing dynamic analysis of seismically-excited nonlinear steel frames with real-time execution capabilities are presented. RT-Frame 2D is proposed as a main component of the small-scale RTHS platform recently developed in the Intelligent Infrastructure Systems Laboratory (IISL) at Purdue University. It is developed and implemented within the context of a MATLAB /*Simulink* environment to enable its easy integration with the remaining RTHS components so that a unified platform can be generated, compiled and executed under a real-time kernel platform. The tool is coded with a MATLAB/*Embedded subset function* format (Mathworks, 2009). Several modeling features required to capture the behavior usually observed in steel frames under seismic ground excitations are available in RT-Frame2D. For instance, mass is modeled using a direct mass lumping scheme while the damping can be represented with either mass/stiffness proportional damping or Rayleigh damping modeling options. Second order effects (i.e., P- Δ effects) are included by considering the geometric stiffness matrix as a constant through the assumption of constant weight distribution on columns and small overall displacements during simulation. Several linear-elastic beam-column elements are available, depending on the desired boundary conditions at the element ends. Additionally, linear-elastic beam-column elements with flexible linear/nonlinear connections are also available.

Nonlinear beam-column elements can be represented with either a spread plasticity model (SPM) or a concentrated plasticity model (CPM). Two material models suitable for steel are also available: bilinear and tri-linear model with kinematic hardening, which can be used in conjunction with the previously mentioned beam-column elements. Two panel zone models are provided: a rigid-body version and a linear version with bidirectional tension/compression and shear distortion effect. Finally, and depending on the analysis type, the explicit unconditionally-stable Chen-Ricles (CR) and the implicit unconditionally-stable Newmark integration schemes are available for solving the equations of motion and evaluating the nonlinear response. Further descriptions of each of the proposed modeling features along with details about its implementation within a RTHS platform are discussed in the present chapter.

2.1 Modeling of Mass

The main details related to the modeling of inertial mass within the proposed RT-Frame2D computational framework are discussed in this section. A direct mass lumping (DML) approach to form a global mass matrix to represent the mass in the equation of motion is used. The global mass matrix is directly calculated by simply adding half of the mass contribution carried by each beam-column element at the corresponding global translational degrees of freedom (DOF). Moreover, adequate rotational mass values are placed on global rotational DOF to avoid condensation, resulting in a full-global diagonal mass matrix format. As later explained, these rotational mass values are defined in terms of the mass and length of the element.

Usually mass/inertial effects can be computed with either a direct mass lumping scheme or a variational mass lumping (VML) scheme. The mass matrix is computed in the VML scheme by the Hessian of a kinetic energy function which is approximated by velocity shape functions. If the velocity shape functions are the same as the displacement shape functions, then the resulting mass matrix is called a consistent mass matrix. Although a

consistent mass matrix is a more accurate representation of the inertial properties and leads to estimated natural frequencies that are always bounded by the exact ones, it also demands considerable execution time and storage/memory capacity when a large number of DOF are to be evaluated. For instance, when an explicit integration scheme is used to solve the global equations of motion, operations such as inverse and multiplication of the mass matrix are required to compute the global accelerations. Although the inverse operation can be calculated offline and inserted to the “real-time executable” portion of the code, the multiplication is still present at every integration step. Conversely, a diagonal-lumped mass matrix can be stored as a simple vector of reduced order (equal to the number of DOF) and the multiplication efforts can be significantly reduced because the diagonal terms are the only ones involved in such operation. Although some considerations need to be made when interpreting the results (it leads to estimated natural frequencies that may be higher or lower than the exact ones), the DML scheme entails considerable computational advantages because of the resulting diagonal matrix format.

$$\tilde{M}_e = (m/2) \begin{bmatrix} 1 & 0 & 0 & 0 & 0 & 0 \\ 0 & 1 & 0 & 0 & 0 & 0 \\ 0 & 0 & \alpha L^2 & 0 & 0 & 0 \\ 0 & 0 & 0 & 1 & 0 & 0 \\ 0 & 0 & 0 & 0 & 1 & 0 \\ 0 & 0 & 0 & 0 & 0 & \alpha L^2 \end{bmatrix} \quad (2.1)$$

Equation (2.1) shows the beam element stiffness matrix which is later assembled to form the global mass matrix in RT-Frame2D. Here m is the mass carried by the beam-column element, L is the length of the element and α is a nonnegative parameter for definition of rotational mass. Note that rotational mass associated with the rotational DOF is defined in terms of the three previous parameters. The value for the nonnegative parameter has been discussed extensively over the finite element literature but no consensus has been achieved. In the current RT-Frame2D release, the nonnegative parameter α can be selected by the user; although a default value of 1e-6 is proposed. Generally, the

nonnegative parameter α should be selected with a small value that guarantees numerical stability and does not overestimate the inertial effect.

2.2 Modeling of Damping

Damping is included using either mass/stiffness proportional damping or a Rayleigh damping modeling option (Chopra, 2001). Proportionality and further diagonalization of the damping matrix with respect to the mode shapes is guaranteed through the Rayleigh damping assumption because the global damping matrix is defined as a linear combination of the global mass and global stiffness matrices, as shown in Equation (2.2). Here $\tilde{M}, \tilde{C}, \tilde{K}$ are the global mass, damping and stiffness matrices, respectively, and λ_1, λ_2 are appropriate coefficients.

$$\tilde{C} = \lambda_1 \tilde{M} + \lambda_2 \tilde{K} \quad (2.2)$$

By diagonalization of the above equation with respect to the mode shapes, the following equation is obtained at each modal coordinate:

$$\zeta_n = \left(\frac{1}{2}\right)\left(\frac{\lambda_1}{\omega_n} + \lambda_2 \omega_n\right) \quad (2.3)$$

where ζ_n is the modal damping ratio and ω_n is the natural frequency at the “ n -th” mode. λ_1, λ_2 can be calculated from Equation (2.3) by assigning two modal damping ratio values at two different natural frequencies. A usual practice is to assign the same modal damping ratio value for two different modes, i.e. at two different natural frequencies. In the implementation herein, the first mode natural frequency is selected by default while

the second natural frequency at any other mode can be selected by the user. Therefore, the following equation is obtained for calculating the remaining damping ratios:

$$\zeta_n = \zeta_1 \left(\frac{\omega_1 \omega_c + \omega_n^2}{\omega_1 \omega_n + \omega_c \omega_n} \right) \quad (2.4)$$

where ζ_1 is the modal damping ratio of the first mode and ω_c is the natural frequency of the “*c-th*” mode, i.e the mode selected by the user. Equivalent expressions for the mass/stiffness proportional damping cases can be derived by following the previous procedure. However, λ_1 and λ_2 are calculated based on only the first mode. Equation (2.5) is obtained for the mass proportional case:

$$\zeta_n = \zeta_1 \left(\frac{\omega_1}{\omega_n} \right) \quad (2.5)$$

Additionally, the stiffness proportional case yields Equation (2.6). Clearly, stiffness proportional damping can yield large damping ratios which may be inappropriate for certain modes. Therefore, a threshold (or maximum) damping ratio can be selected by the user with this option.

$$\zeta_n = \zeta_1 \left(\frac{\omega_n}{\omega_1} \right) \quad (2.6)$$

2.3 Linear Beam-Column Elements

A choice of several linear-elastic beam-column elements is available in RT-Frame2D depending on the desired boundary conditions at the element ends, i.e. the presence of moment releases. Non-released (fixed-fixed) stiffness matrix coefficients are first calculated based on the principle of virtual forces, while stiffness matrices for the other cases are derived by means of equilibrium. Although displacement-based procedures using cubic-polynomial shape functions are commonly used for finding the stiffness matrix of beam-type elements, here a virtual-force approach is utilized. The advantage of using a virtual-force methodology will be more evident in later sections when a nonlinear beam-column element is introduced. The derivation starts by finding a 2x2 size flexibility matrix which relates rotations and moments of a simple supported beam element based on a virtual force approach. The corresponding stiffness matrix is then obtained as the inverse of the flexibility matrix. Figure 2.1 shows a simply supported beam-column element with corresponding properties and applied moments and rotations for reference throughout the formulation.

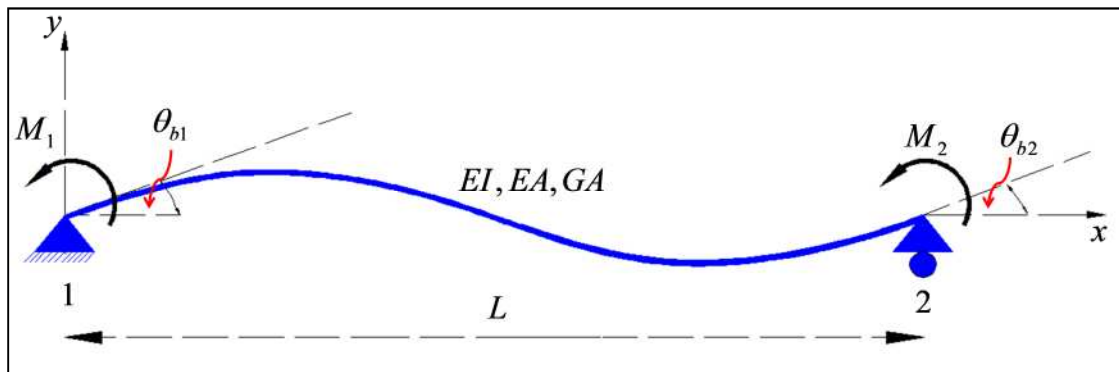


Figure 2.1: Simply supported beam-column element

Flexibility coefficients are calculated in terms of virtual flexural and shear strain energy, expressed as functions of moment and shear force distributions due to virtual unit moments applied at element ends

$$f_{ij} = \int_0^L \frac{m(x)_i m(x)_j}{EI} dx + \int_0^L \frac{v(x)_i v(x)_j}{GA} dx \quad (2.7)$$

Here f_{ij} is the flexibility coefficient at the “ i - j ” entry of the flexibility matrix; $m(x), v(x)$ are the moment and shear force distribution, respectively, due to the virtual unit moments applied at the element ends “ i - j ”; and, EI, GA are the flexural and shear stiffness, respectively. Integration of Equation (2.7) and substitution of the ratio ϕ yields

$$f_{11} = \frac{L}{12EI} (4 + \phi) \quad (2.8)$$

$$f_{12} = f_{21} = \frac{L}{12EI} (\phi - 2) \quad (2.9)$$

$$f_{22} = \frac{L}{12EI} (4 + \phi) \quad (2.10)$$

where the ratio ϕ is defined as: $\phi = \left(\frac{12EI}{GAL^2} \right)$. Therefore, the 2x2 stiffness matrix \tilde{K}_m for a simply supported beam can be calculated as the inverse of the flexibility matrix as

$$\tilde{K}_m = \begin{bmatrix} f_{11} & f_{12} \\ f_{21} & f_{22} \end{bmatrix}^{-1} = \frac{EI}{L} \begin{bmatrix} \left(\frac{4+\phi}{1+\phi} \right) & \left(\frac{2-\phi}{1+\phi} \right) \\ \left(\frac{2-\phi}{1+\phi} \right) & \left(\frac{4+\phi}{1+\phi} \right) \end{bmatrix} \quad (2.11)$$

where $\tilde{F}_{be} = \tilde{K}_m \tilde{u}_{be}$, and,

$$\tilde{F}_{be} = [M_1 \quad M_2]^T \quad (2.12)$$

$$\tilde{u}_{be} = [\theta_{b1} \quad \theta_{b2}]^T \quad (2.13)$$

Here θ_{b1}, θ_{b2} are the rotations at nodes 1 and 2 of the simply supported beam. The resulting \tilde{K}_m can be expanded to account for shear forces by applying the equilibrium relationship between shear forces and moments at the ends of the element as

$$\begin{bmatrix} V_1 \\ M_1 \\ V_2 \\ M_2 \end{bmatrix} = \tilde{R} \begin{bmatrix} M_1 \\ M_2 \end{bmatrix} = \begin{bmatrix} \left(\frac{1}{L}\right) & 1 & \left(-\frac{1}{L}\right) & 0 \\ \left(\frac{1}{L}\right) & 0 & \left(-\frac{1}{L}\right) & 1 \end{bmatrix}^T \begin{bmatrix} M_1 \\ M_2 \end{bmatrix} \quad (2.14)$$

Therefore, an expanded 4x4 \tilde{K}_{ms} matrix is calculated as

$$\tilde{K}_{ms} = \tilde{R} \tilde{K}_m \tilde{R}^T \quad (2.15)$$

Because axial effects are not coupled with the simply supported beam, they can be added separately to \tilde{K}_{ms} so that a final 6x6 element stiffness matrix \tilde{K}_e relating all forces and corresponding displacements can be obtained. DOF convention for \tilde{K}_e is shown in Figure 2.2.

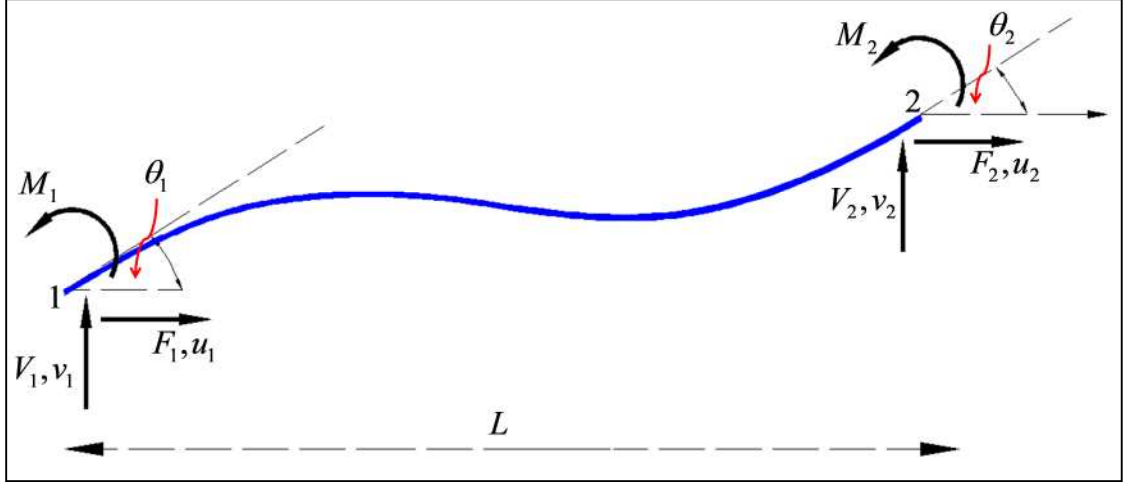


Figure 2.2: DOF convention for beam-column element

\tilde{K}_e is used to assemble the global stiffness matrix using standard assembling methods.

The resulting \tilde{K}_e stiffness matrix for a fixed-fixed configuration is defined as

$$\tilde{K}_e = \begin{bmatrix} \left(\frac{EA}{L}\right) & 0 & 0 & \left(-\frac{EA}{L}\right) & 0 & 0 \\ 0 & \left(\frac{12EI}{(1+\phi)L^3}\right) & \left(\frac{6EI}{(1+\phi)L^2}\right) & 0 & \left(-\frac{12EI}{(1+\phi)L^3}\right) & \left(\frac{6EI}{(1+\phi)L^2}\right) \\ 0 & \left(\frac{6EI}{(1+\phi)L^2}\right) & \left(\frac{(4+\phi)EI}{(1+\phi)L}\right) & 0 & \left(-\frac{6EI}{(1+\phi)L^2}\right) & \left(\frac{(2-\phi)EI}{(1+\phi)L}\right) \\ \left(-\frac{EA}{L}\right) & 0 & 0 & \left(\frac{EA}{L}\right) & 0 & 0 \\ 0 & \left(-\frac{12EI}{(1+\phi)L^3}\right) & \left(-\frac{6EI}{(1+\phi)L^2}\right) & 0 & \left(\frac{12EI}{(1+\phi)L^3}\right) & \left(-\frac{6EI}{(1+\phi)L^2}\right) \\ 0 & \left(\frac{6EI}{(1+\phi)L^2}\right) & \left(\frac{(2-\phi)EI}{(1+\phi)L}\right) & 0 & \left(-\frac{6EI}{(1+\phi)L^2}\right) & \left(\frac{(4+\phi)EI}{(1+\phi)L}\right) \end{bmatrix} \quad (2.16)$$

where $\tilde{F}_e = \tilde{K}_e \tilde{u}_e$, and

$$\tilde{F}_e = [F_1 \quad V_1 \quad M_1 \quad F_2 \quad V_2 \quad M_2]^T \quad (2.17)$$

$$\bar{u}_e = [u_1 \quad v_1 \quad \theta_1 \quad u_2 \quad v_2 \quad \theta_2]^T \quad (2.18)$$

Evaluation of the ratio ϕ is of particular interest since it defines the contribution of the shearing deformation, or the amount of strain energy. For members where the depth-to-span ratio is small, the influence of transverse shear deformation may be negligible and disregarded because $\phi \rightarrow 0$. For instance, the ratio ϕ for simply supported rectangular and circular section beams made with a homogenous isotropic material may be approximated using

$$\phi_r = \frac{E}{G} \left(\frac{h}{L} \right)^2 \approx 2.60 \left(\frac{h}{L} \right)^2 \quad (2.19)$$

and,

$$\phi_c = \frac{3E}{4G} \left(\frac{h}{L} \right)^2 \approx 1.95 \left(\frac{h}{L} \right)^2 \quad (2.20)$$

respectively, where “ h ” defines the depth for each of the sections. It is clear from Equation (2.19) and Equation (2.20) that a small depth-to-span value of approximately $h/L < 10\%$ produces ϕ values of 0.026 and 0.0195, respectively. These correspond to a change in the *Frobenius* norm of the stiffness matrices (when $\phi = 0$) of only 2.3% and 1.7%, respectively. This result can be interpreted to mean that a negligible portion of shear energy is present in the total strain energy. In fact, a value of $\phi = 0$ yields the classical stiffness matrix expression derived using only flexural strain energy.

$$\tilde{K}_e = \begin{bmatrix} \left(\frac{EA}{L}\right) & 0 & 0 & \left(-\frac{EA}{L}\right) & 0 & 0 \\ 0 & \left(\frac{12EI}{L^3}\right) & \left(\frac{6EI}{L^2}\right) & 0 & \left(-\frac{12EI}{L^3}\right) & \left(\frac{6EI}{L^2}\right) \\ 0 & \left(\frac{6EI}{L^2}\right) & \left(\frac{4EI}{L}\right) & 0 & \left(-\frac{6EI}{L^2}\right) & \left(\frac{2EI}{L}\right) \\ \left(-\frac{EA}{L}\right) & 0 & 0 & \left(\frac{EA}{L}\right) & 0 & 0 \\ 0 & \left(-\frac{12EI}{L^3}\right) & \left(-\frac{6EI}{L^2}\right) & 0 & \left(\frac{12EI}{L^3}\right) & \left(-\frac{6EI}{L^2}\right) \\ 0 & \left(\frac{6EI}{L^2}\right) & \left(\frac{2EI}{L}\right) & 0 & \left(-\frac{6EI}{L^2}\right) & \left(\frac{4EI}{L}\right) \end{bmatrix} \quad (2.21)$$

A beam-column element with moment releases are also available in RT-Frame2D. The stiffness matrix for these elements is derived based on the previous procedure by selecting specific flexibility coefficients of the simply supported beam, i.e. f_{ij} of Equation (2.7). For instance, in the fixed-pin beam-column element configuration, only the f_{11} coefficient (at end “i”) is utilized because no moment is assumed at end “j”. Therefore,

$$\tilde{K}_m = f_{11}^{-1} = \frac{12EI}{(4+\phi)L} \quad (2.22)$$

and \tilde{K}_m can be expanded to account for shear forces by considering the equilibrium relationship between the shear forces and the moment at the element end “i” as

$$\begin{bmatrix} V_1 \\ M_1 \\ V_2 \end{bmatrix} = \tilde{R}M_1 = \begin{bmatrix} \left(\frac{1}{L}\right) & 1 & \left(-\frac{1}{L}\right) \end{bmatrix}^T M_1 \quad (2.23)$$

Therefore, an expanded 3x3 \tilde{K}_{ms} matrix is calculated as

$$\tilde{K}_{ms} = \tilde{R} \tilde{K}_m \tilde{R}^T \quad (2.24)$$

As before, axial effects are not coupled and therefore can be added to \tilde{K}_{ms} so that a final 6x6 element stiffness matrix \tilde{K}_e , relating all forces and corresponding displacements, can be used to assemble the global stiffness matrix. \tilde{K}_e is still developed as a 6x6 matrix in order to be consistent in the global stiffness matrix assembly by standard methods. Therefore, entries in the 6th row and 6th column are padded with zeros. The resulting \tilde{K}_e stiffness matrix with a fixed-pin configuration is expressed as

$$\tilde{K}_e = \begin{bmatrix} \left(\frac{EA}{L}\right) & 0 & 0 & \left(-\frac{EA}{L}\right) & 0 & 0 \\ 0 & \left(\frac{12EI}{(4+\phi)L^3}\right) & \left(\frac{12EI}{(4+\phi)L^2}\right) & 0 & \left(-\frac{12EI}{(4+\phi)L^3}\right) & 0 \\ 0 & \left(\frac{12EI}{(4+\phi)L^2}\right) & \left(\frac{12EI}{(4+\phi)L}\right) & 0 & \left(-\frac{12EI}{(4+\phi)L^2}\right) & 0 \\ \left(-\frac{EA}{L}\right) & 0 & 0 & \left(\frac{EA}{L}\right) & 0 & 0 \\ 0 & \left(-\frac{12EI}{(4+\phi)L^3}\right) & \left(-\frac{12EI}{(4+\phi)L^2}\right) & 0 & \left(\frac{12EI}{(4+\phi)L^3}\right) & 0 \\ 0 & 0 & 0 & 0 & 0 & 0 \end{bmatrix} \quad (2.25)$$

By following this procedure, the stiffness matrix for a pin-fixed beam-column element can be computed by selecting only the f_{22} coefficient, yielding

$$\tilde{K}_e = \begin{bmatrix} \left(\frac{EA}{L}\right) & 0 & 0 & \left(-\frac{EA}{L}\right) & 0 & 0 \\ 0 & \left(\frac{12EI}{(4+\phi)L^3}\right) & 0 & 0 & \left(-\frac{12EI}{(4+\phi)L^3}\right) & \left(\frac{12EI}{(4+\phi)L^2}\right) \\ 0 & 0 & 0 & 0 & 0 & 0 \\ \left(-\frac{EA}{L}\right) & 0 & 0 & \left(\frac{EA}{L}\right) & 0 & 0 \\ 0 & \left(-\frac{12EI}{(4+\phi)L^3}\right) & 0 & 0 & \left(\frac{12EI}{(4+\phi)L^3}\right) & \left(-\frac{12EI}{(4+\phi)L^2}\right) \\ 0 & \left(\frac{12EI}{(4+\phi)L^2}\right) & 0 & 0 & \left(-\frac{12EI}{(4+\phi)L^2}\right) & \left(\frac{12EI}{(4+\phi)L}\right) \end{bmatrix} \quad (2.26)$$

Finally, the stiffness pin-pin beam-column element is readily obtained by padding all entries with zeros except those associated with the axial forces, yielding

$$\tilde{K}_e = \begin{bmatrix} \left(\frac{EA}{L}\right) & 0 & 0 & \left(-\frac{EA}{L}\right) & 0 & 0 \\ 0 & 0 & 0 & 0 & 0 & 0 \\ 0 & 0 & 0 & 0 & 0 & 0 \\ \left(-\frac{EA}{L}\right) & 0 & 0 & \left(\frac{EA}{L}\right) & 0 & 0 \\ 0 & 0 & 0 & 0 & 0 & 0 \\ 0 & 0 & 0 & 0 & 0 & 0 \end{bmatrix} \quad (2.27)$$

2.4 Beam-Column Element with Linear/Nonlinear Flexible Connections

A linear-elastic beam-column element with flexible linear/nonlinear connectors is also available in the RT-Frame2D computational platform. Connectors from beam-to-column elements or vice versa can be classified as ideally rigid, ideally pinned or flexible (semi-rigid). In fact a perfect rigid connection or perfect pinned connection does not exist, but this is ignored and most analytical models are developed based on these assumptions.

Flexible connections are modeled by including zero-length linear or rotational springs between two connected members to represent relative motions induced by the connection. The last procedure is prohibited when real-time execution needs to be achieved in the analysis because it would result in a substantial increment in the number of DOF. Rather, a “condensed” beam-column element model with flexible connections is proposed in RT-Frame2D. Computational models constructed with this element yield the same number of DOF as one with no flexible connections. Moreover, the resulting model saves considerable computational effort when updating the connector stiffness during real-time nonlinear analysis. The element is defined to account only for flexural flexibility in the connectors because this component is expected to have the most significant influence on the overall stiffness of a frame when subjected to lateral loads. Therefore, the connector flexibility is idealized by inserting zero-length rotational springs at the ends of a beam-column element. The stiffness values of these springs are defined as the ratio of transmitted moment to the rotation within the connection, i.e. the $M - \theta$, relationship. The process of identifying adequate spring stiffness values requires considerable judgment and knowledge of the connection under analysis. These stiffness values (and strengths) are usually calibrated to either experimental results or to results of a detailed finite element model of the connection (Kishi and Chen, 1986; Chen and Kishi, 1989).

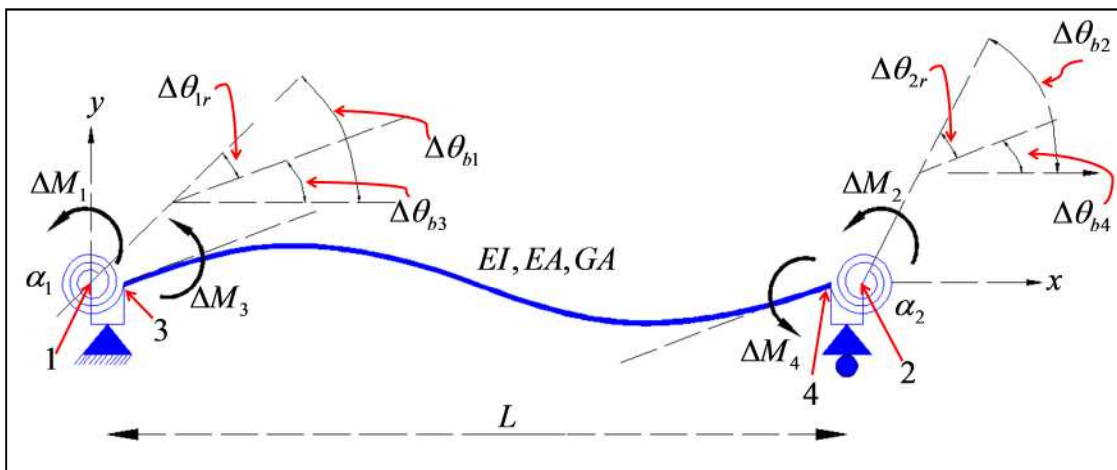


Figure 2.3: Simply supported beam with zero-length rotational springs at ends

For the purpose of derivation of the proposed element, linear or nonlinear functions defining the spring behavior are assumed to be already known and therefore are represented by single variables. Because $M - \theta_r$ can be defined with a nonlinear function, an incremental formulation is utilized. Figure 2.3 shows a simply supported beam with zero-length rotational springs at ends representing the flexible connections. Properties for each of the components, i.e. beam and springs along with node numbering including applied moments and rotations are added for reference throughout the formulation. Note that $\Delta\theta_{1r}$ and $\Delta\theta_{2r}$ define increment of relative rotations between rotations at nodes 1 - 3 and 4 - 2, respectively, i.e. rotations within the connections at element ends. Tangential moment-rotation relationships for each of the components are defined as

$$\begin{bmatrix} \Delta M_3 \\ \Delta M_4 \end{bmatrix} = \tilde{K}_l \begin{bmatrix} \Delta\theta_{b3} \\ \Delta\theta_{b4} \end{bmatrix} \quad (2.28)$$

$$\begin{bmatrix} \Delta M_1 \\ \Delta M_3 \end{bmatrix} = \tilde{K}_{\alpha_1} \begin{bmatrix} \Delta\theta_{b1} \\ \Delta\theta_{b3} \end{bmatrix} \quad (2.29)$$

$$\begin{bmatrix} \Delta M_4 \\ \Delta M_2 \end{bmatrix} = \tilde{K}_{\alpha_2} \begin{bmatrix} \Delta\theta_{b4} \\ \Delta\theta_{b2} \end{bmatrix} \quad (2.30)$$

where

$$\tilde{K}_l = \begin{bmatrix} k_{11} & k_{12} \\ k_{12} & k_{22} \end{bmatrix} = \frac{EI}{L} \begin{bmatrix} \left(\frac{4+\phi}{1+\phi}\right) & \left(\frac{2-\phi}{1+\phi}\right) \\ \left(\frac{2-\phi}{1+\phi}\right) & \left(\frac{4+\phi}{1+\phi}\right) \end{bmatrix} \quad (2.31)$$

$$\tilde{\mathbf{K}}_{\alpha_1} = \begin{bmatrix} \alpha_1 & -\alpha_1 \\ -\alpha_1 & \alpha_1 \end{bmatrix} \quad (2.32)$$

$$\tilde{\mathbf{K}}_{\alpha_2} = \begin{bmatrix} \alpha_2 & -\alpha_2 \\ -\alpha_2 & \alpha_2 \end{bmatrix} \quad (2.33)$$

Here α_1, α_2 are stiffness values for the zero-length rotational springs. α_1, α_2 can be defined with prescribed linear/nonlinear functions of the relative rotations as

$$\alpha_1 = \alpha_1(\theta_{1r}) \quad (2.34)$$

$$\alpha_2 = \alpha_2(\theta_{2r}) \quad (2.35)$$

where

$$\Delta\theta_{1r} = \Delta\theta_{b1} - \Delta\theta_{b3} \quad (2.36)$$

$$\Delta\theta_{2r} = \Delta\theta_{b2} - \Delta\theta_{b4} \quad (2.37)$$

Assembly of the previous component stiffness matrices yields

$$\tilde{\mathbf{K}}_{m\alpha} = \begin{bmatrix} \tilde{\mathbf{K}}_{m\alpha}^{11} & \tilde{\mathbf{K}}_{m\alpha}^{12} \\ \tilde{\mathbf{K}}_{m\alpha}^{12} & \tilde{\mathbf{K}}_{m\alpha}^{22} \end{bmatrix} = \begin{bmatrix} \alpha_1 & 0 & \vdots & -\alpha_1 & 0 \\ 0 & \alpha_2 & \vdots & 0 & -\alpha_2 \\ \cdots & \cdots & \cdots & \cdots & \cdots \\ -\alpha_1 & 0 & \vdots & (\alpha_1 + k_{11}) & k_{12} \\ 0 & -\alpha_2 & \vdots & k_{12} & (\alpha_2 + k_{22}) \end{bmatrix} \quad (2.38)$$

where $[\Delta M_1 \quad \Delta M_2 \quad \Delta M_3 \quad \Delta M_4]^T = \tilde{K}_{m\alpha} [\Delta\theta_{b1} \quad \Delta\theta_{b2} \quad \Delta\theta_{b3} \quad \Delta\theta_{b4}]^T$. Condensation of $\Delta\theta_{b3}, \Delta\theta_{b4}$, results in a 2x2 tangential stiffness matrix $\tilde{K}_m = \tilde{K}_{m\alpha}^{11} - \tilde{K}_{m\alpha}^{12} \tilde{K}_{m\alpha}^{22^{-1}} \tilde{K}_{m\alpha}^{12}$

$$\tilde{K}_m = \begin{bmatrix} \left(\alpha_1 - \frac{\alpha_1^2(\alpha_2 + k_{22})}{\Gamma} \right) & \frac{\alpha_1 \alpha_2 k_{12}}{\Gamma} \\ \frac{\alpha_1 \alpha_2 k_{12}}{\Gamma} & \left(\alpha_2 - \frac{\alpha_2^2(\alpha_1 + k_{11})}{\Gamma} \right) \end{bmatrix} \quad (2.39)$$

where

$$\Gamma = (\alpha_1 + k_{11})(\alpha_2 + k_{22}) - k_{12}^2 \quad (2.40)$$

and

$$\begin{bmatrix} \Delta M_1 \\ \Delta M_2 \end{bmatrix} = \tilde{K}_m \begin{bmatrix} \Delta\theta_{b1} \\ \Delta\theta_{b2} \end{bmatrix} \quad (2.41)$$

The resulting stiffness matrix \tilde{K}_m , relating increment of moments and rotations at ends 1 and 2, can be expanded to account for shear forces using the equilibrium relationship established in Equation (2.14). Moreover, axial effects can be separately added leading to a final 6x6 element tangential stiffness matrix \tilde{K}_e relating all force and displacement increments. \tilde{K}_e is used to assemble the global tangential stiffness matrix using standard assembling methods and based on the same DOF convention as shown in Figure 2.2. Equation (2.39) offers great potential because $\Delta\theta_{b3}, \Delta\theta_{b4}$ are not required to assemble the global tangential stiffness matrix and to calculate the corresponding moment increments

at the simply supported beam-column element ends. However, under nonlinear behavior of the connectors, the stiffness values α_1, α_2 need to be updated based on $\Delta\theta_{1r}, \Delta\theta_{2r}$ which in turn requires knowing $\Delta\theta_{b3}, \Delta\theta_{b4}$. This requirement can be avoided, if $\Delta\theta_{1r}, \Delta\theta_{2r}$ can be explicitly calculated from $\Delta\theta_{b1}, \Delta\theta_{b2}$ using

$$\Delta\theta_{1r} = \Delta\theta_{1r}(\Delta\theta_{b1}, \Delta\theta_{b2}) \quad (2.42)$$

$$\Delta\theta_{2r} = \Delta\theta_{2r}(\Delta\theta_{b1}, \Delta\theta_{b2}) \quad (2.43)$$

Use of Equations (2.28), (2.29) and (2.30) and enforcing equilibrium conditions at nodes 3 and 4, yields

$$\alpha_1 \Delta\theta_{1r} - k_{11}(\Delta\theta_{b1} - \Delta\theta_{1r}) - k_{12}(\Delta\theta_{b2} - \Delta\theta_{2r}) = 0 \quad (2.44)$$

$$\alpha_2 \Delta\theta_{2r} - k_{12}(\Delta\theta_{b1} - \Delta\theta_{1r}) - k_{22}(\Delta\theta_{b2} - \Delta\theta_{2r}) = 0 \quad (2.45)$$

from where

$$\begin{bmatrix} \Delta\theta_{1r} \\ \Delta\theta_{2r} \end{bmatrix} = \tilde{T}_{\theta\theta} \begin{bmatrix} \Delta\theta_{b1} \\ \Delta\theta_{b2} \end{bmatrix} = \begin{bmatrix} \frac{((\alpha_2 + k_{22})k_{11} - k_{12}^2)}{\Gamma} & \frac{((\alpha_2 + k_{22})k_{12} - k_{12}k_{22})}{\Gamma} \\ \frac{((\alpha_1 + k_{11})k_{12} - k_{12}k_{11})}{\Gamma} & \frac{((\alpha_1 + k_{11})k_{22} - k_{12}^2)}{\Gamma} \end{bmatrix} \begin{bmatrix} \Delta\theta_{b1} \\ \Delta\theta_{b2} \end{bmatrix} \quad (2.46)$$

$$\text{and } \Gamma = (\alpha_1 + k_{11})(\alpha_2 + k_{22}) - k_{12}^2$$

Note, that matrix $\tilde{T}_{\theta\theta}$ can be used to explicitly calculate incremental spring relative rotations based only on the rotation increments at element ends (nodes 1 and 2) without involving the rotation increments at nodes 3 and 4.

2.5 Nonlinear Beam-Column Elements

Several beam-column frame element models can be found in the literature for the analysis of nonlinear frame structures. These models can be mainly classified as *fiber section* or *resultant section* models which can be derived on *displacement-based* or *force-based/virtual-force* formulations with either *lumped/concentrated* or *distributed/spread* plasticity assumptions. The basis for the selection of one model over another depends on the particulars of the specific application, the extent of accuracy needed, and the computational allowance.

In the fiber section modeling approach, the section of the element under evaluation is subdivided into a number of “fibers”. Each fiber is predefined with material models that are usually represented with uniaxial or multiaxial stress-strain linear/nonlinear relationships. Resultant stresses and constitutive properties at each fiber can be integrated to calculate either moments or forces and tangent section stiffnesses acting on the overall section. The final state of the element can be calculated as the integral of the previous quantities at control sections over the length of the member. Very accurate solutions can be achieved when refined grid fiber section models are applied for the analysis of members with non-homogenous sections, such as in the case of typical reinforced concrete sections or composite sections (Kent and Park, 1971; Scott et al., 1982). However, the computational effort to perform the numerical integration could become expensive in addition to the large storage capacity to track the evolution of variables associated with each fiber. Therefore, fiber section models are computationally expensive

and may not be required when a system with a relatively large number of DOF is analyzed under real-time execution constraints.

Conversely, the resultant section models define the overall section response based on direct relations between stress resultants and generalized strains such as moment-curvature, axial load-axial strain, or other force-deformation linear/nonlinear relationships. Moreover, an appropriate selection of the force-deformation relationship can leverage the need for considering force interaction on the section and facilitate a reduced computational effort with the same level of accuracy. For instance, the force-deformation model proposed by Takeda et al. (Takeda et al., 1970) in which only a uniaxial nonlinear relationship between section moment and curvature is considered was found to be very satisfactory when compared to the measured response based on experimental static and dynamic tests. However, more advanced resultant models where force interaction is accounted for can also be achieved through use of the yield surface concept and classic plasticity theory. For instance, a bounding surface plasticity model defined in the stress-resultant space was implemented to account for the axial-bending interaction effect on beam-column elements (Hilmy and Abel, 1985; Hajjar and Gourley, 1997; El-Tawil and Deierlein, 2001a; El-Tawil and Deierlein, 2001b). The model was developed by defining two versions of the bounding surface: a finite surface that is more applicable for steel members, and a degenerate surface that is applicable for reinforced concrete and composite members.

Although a displacement-based implementation using cubic-polynomial shape functions (Hermite polynomial) is commonly used for calculating the stiffness matrix of a beam-column element based on standard finite element techniques, a force-based/virtual-force approach is more desirable because the exact force distribution is easily determined under certain conditions. The advantage of using a force-based/virtual force approach lies in the fact that non-uniform flexibility pattern arises due to the spread of plasticity through the length of the beam-column element, and therefore a cubic polynomial assumption for the displacement field is no longer accurate. This limitation can be overcome if several

elements are used for a single frame member. However, the consequent increment in the number of DOF will considerably reduce the opportunities for real-time execution in the analysis.

As introduced already, other classifications can be considered for the nonlinear beam-column element models based on concentrated or spread plasticity assumptions. Beam-column elements based on a concentrated plasticity assumption restrict the inelastic evolution to the element ends (Clough and Johnson, 1966; Giberson, 1967; Hajjar and Gourley, 1997). Although such assumption could be considered as a drawback, concentrated plasticity models are very accurate in instances where the plasticity is expected to be localized, for instance in the analysis of steel members. Additionally, they are conceptually simple and computationally inexpensive. Conversely, spread plasticity models recreate the actual behavior more accurately, where a gradual spread of plasticity into the member as a function of the loading history is observed (Lobo, 1994; Spacone et al. 1996a; Spacone et al. 1996b; El-Tawil and Deierlein 2001a; El-Tawil and Deierlein 2001b).

Here, a resultant section nonlinear beam-column element model formulated based on a virtual force concept and previously considered in IDARC2D (Valles et al., 1996) is implemented in the proposed RT-Frame2D computational platform. The model recreates yielding locations that are assumed to occur at the element ends or the moment resisting connections of a building. Yielding locations can be represented with either a spread plasticity model or a concentrated plasticity model. In this section, stiffness matrix coefficients for both plasticity models are presented. The spread plasticity model (Lobo, 1994; Valles et al., 1996) is introduced first. Following the same criteria of Section 2.3, a 2x2 flexibility matrix relating rotations and moments of a simply supported beam element and derived based on a virtual force approach is calculated. The corresponding stiffness matrix is then obtained as the inverse of the flexibility matrix generated. Figure 2.4 shows a simply supported beam-column element with corresponding properties and applied moments and rotations for formulation reference. Additionally, the moment distribution

only due to moment actions at the element ends and the variation of the flexural stiffness $EI(x)$ over the beam length is included for reference. In this formulation, $EI(x)$ is assumed to be linear whose variation pattern is governed by the spread of plasticity within the member length as explained later. GA is assumed to have a constant distribution over the member length.

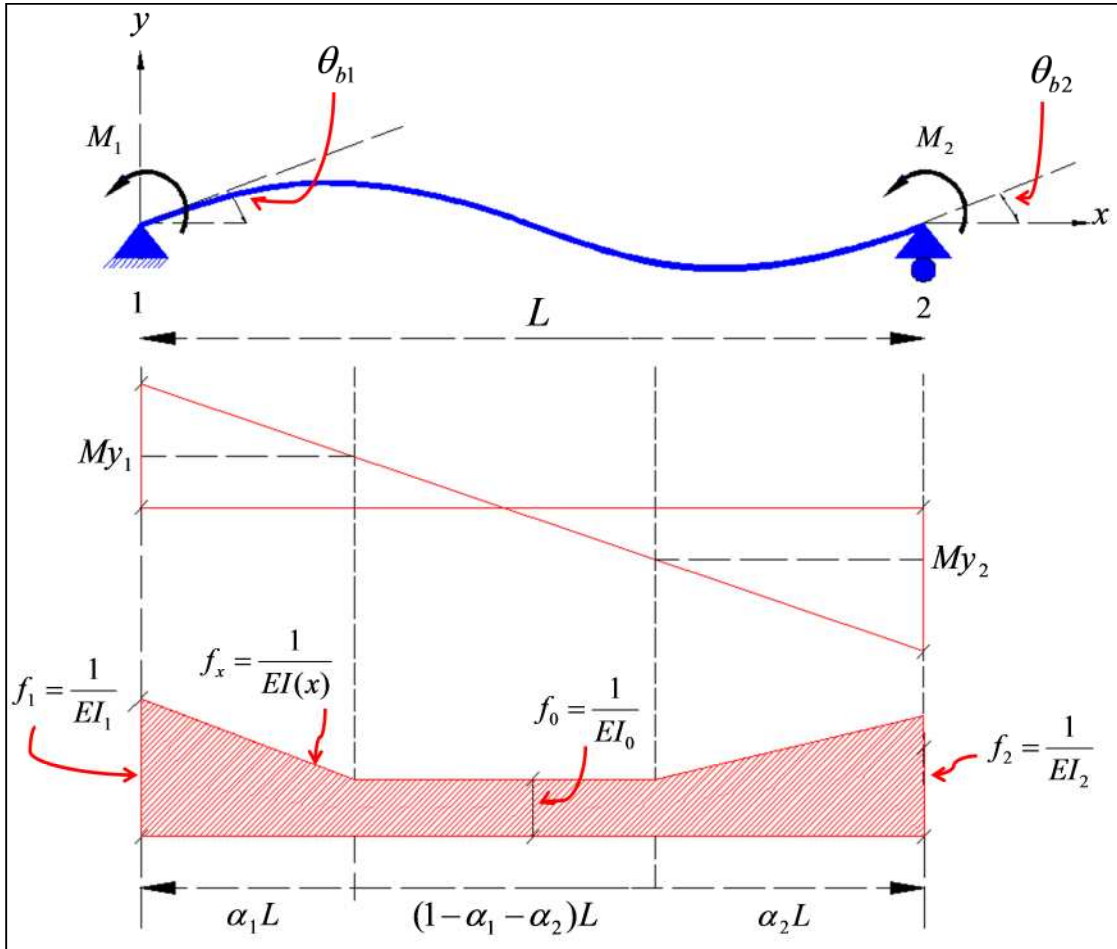


Figure 2.4: Nonlinear beam-column element

Flexibility coefficients are then calculated in terms of virtual flexural and shear strain energy expressed as functions of moment and shear force distributions due to virtual unit moments applied at element ends as

$$f_{ij} = \int_0^L \frac{m(x)_i m(x)_j}{EI(x)} dx + \int_0^L \frac{v(x)_i v(x)_j}{GA} dx \quad (2.47)$$

Here f_{ij} is the flexibility coefficient at the “ i - j ” entry of the flexibility matrix; $m(x), v(x)$ are the moment and shear force distribution due to virtual unit moments applied at element ends “ i - j ”. Integration of Equation (2.47) yields the flexibility coefficients

$$f_{11} = \frac{L}{12} \left[\frac{4}{EI_0} + \left(\frac{1}{EI_1} - \frac{1}{EI_0} \right) (6\alpha_1 - 4\alpha_1^2 + \alpha_1^3) + \left(\frac{1}{EI_2} - \frac{1}{EI_0} \right) \alpha_2^3 \right] + \frac{1}{GAL} \quad (2.48)$$

$$f_{12} = f_{21} = \frac{L}{12} \left[\frac{-2}{EI_0} - \left(\frac{1}{EI_1} - \frac{1}{EI_0} \right) (2\alpha_1^2 - \alpha_1^3) + \left(\frac{1}{EI_2} - \frac{1}{EI_0} \right) (2\alpha_2^2 - \alpha_2^3) \right] + \frac{1}{GAL} \quad (2.49)$$

$$f_{22} = \frac{L}{12} \left[\frac{4}{EI_0} - \left(\frac{1}{EI_2} - \frac{1}{EI_0} \right) (6\alpha_2 - 4\alpha_2^2 - \alpha_2^3) + \left(\frac{1}{EI_1} - \frac{1}{EI_0} \right) \alpha_1^3 \right] + \frac{1}{GAL} \quad (2.50)$$

Here EI_1, EI_2 are the instantaneous flexural stiffness at the two member section ends. EI_1, EI_2 evolution is calculated from a prescribed hysteresis model. α_1, α_2 and EI_0 are the yield penetration parameters and the flexural stiffness at the center of the member. The yield penetration parameters define the proportion of the element length where the acting bending moment is greater than the yielding or cracking moment M_y , as shown in Figure 2.4. Therefore, the yield penetration parameters are updated based on changes of the moment distribution over the element length. Two options for changes in the moment diagram are considered: a single curvature or a double curvature which are selected depending on the direction of loading. Rules for updating α_1, α_2 and EI_0 based on the previous considerations are found in Valles et al. (1996). The previous flexibility coefficients were rewritten so that no numerical instabilities are produced with the

stiffness matrix when structural states close to flexure or shear failure conditions are observed. The reformulated flexibility coefficients and currently used in IDARC2D (Valles et al., 1996) are

$$f_{11} = \frac{L}{12EI_0EI_1EI_2} f'_{11} + \frac{1}{GAL} \quad (2.51)$$

$$f_{21} = f_{12} = \frac{L}{12EI_0EI_1EI_2} f'_{12} + \frac{1}{GAL} \quad (2.52)$$

$$f_{22} = \frac{L}{12EI_0EI_1EI_2} f'_{22} + \frac{1}{GAL} \quad (2.53)$$

where

$$f'_{11} = 4EI_1EI_2 + (EI_0 - EI_1)EI_2(6\alpha_1 - 4\alpha_1^2 + \alpha_1^3) + (EI_0 - EI_2)EI_1\alpha_2^3 \quad (2.54)$$

$$f'_{12} = -2EI_1EI_2 - (EI_0 - EI_1)EI_2(2\alpha_1^2 - \alpha_1^3) - (EI_0 - EI_2)EI_1(2\alpha_2^2 - \alpha_2^3) \quad (2.55)$$

$$f'_{22} = 4EI_1EI_2 + (EI_0 - EI_1)EI_2\alpha_1^3 + (EI_0 - EI_2)EI_1(6\alpha_2 - 4\alpha_2^2 - \alpha_2^3) \quad (2.56)$$

Therefore, a 2x2 stiffness matrix \tilde{K}_m relating moments M_1, M_2 and corresponding rotations θ_{b1}, θ_{b2} for a simply supported beam based on a spread plasticity model are calculated as the inverse of the previous flexibility matrix as

$$\begin{bmatrix} M_1 \\ M_2 \end{bmatrix} = \tilde{K}_m \begin{bmatrix} \theta_{b1} \\ \theta_{b2} \end{bmatrix} = \begin{bmatrix} f_{11} & f_{12} \\ f_{21} & f_{22} \end{bmatrix}^{-1} \begin{bmatrix} \theta_{b1} \\ \theta_{b2} \end{bmatrix} = \begin{bmatrix} k_{11} & k_{12} \\ k_{21} & k_{22} \end{bmatrix} \begin{bmatrix} \theta_{b1} \\ \theta_{b2} \end{bmatrix} \quad (2.57)$$

where

$$k_{11} = \frac{12EI_0EI_1EI_2}{D_{et}L} (f'_{22}GAL^2 + 12EI_0EI_1EI_2) \quad (2.58)$$

$$k_{12} = k_{21} = -\frac{12EI_0EI_1EI_2}{D_{et}L} (f'_{12}GAL^2 + 12EI_0EI_1EI_2) \quad (2.59)$$

$$k_{22} = \frac{12EI_0EI_1EI_2}{D_{et}L} (f'_{11}GAL^2 + 12EI_0EI_1EI_2) \quad (2.60)$$

$$\text{and } D_{et} = GAL^2 (f'_{11}f'_{22} - f'^2_{12}) + 12EI_0EI_1EI_2 (f'_{11} + f'_{22} - 2f'_{12})$$

Flexibility coefficients for the concentrated plasticity model are obtained from the spread plasticity model by setting the yield penetration parameters α_1, α_2 equal to zero. The yielding extent is then restricted to the member ends while the interior of the member remains elastic. Inelastic zero-length rotational spring defined with parameters α_{AA} and α_{BB} are added to the member ends so that concentrated nonlinearity can be represented.

Flexibility coefficients for such model are defined as

$$f_{11} = \frac{L}{12EI_0EI_1EI_2} f'_{11} + \frac{1}{GAL} \quad (2.61)$$

$$f_{21} = f_{12} = \frac{L}{12EI_0EI_1EI_2} f'_{12} + \frac{1}{GAL} \quad (2.62)$$

$$f_{22} = \frac{L}{12EI_0EI_1EI_2} f'_{22} + \frac{1}{GAL} \quad (2.63)$$

where

$$f'_{11} = 4EI_1EI_2 + (EI_0 - EI_1)EI_2\alpha_{AA} \quad (2.64)$$

$$f'_{12} = -2EI_1EI_2 \quad (2.65)$$

$$f'_{22} = 4EI_1EI_2 + (EI_0 - EI_2)EI_1\alpha_{BB} \quad (2.66)$$

The 2x2 stiffness matrix \tilde{K}_m relating the moments M_1, M_2 and corresponding rotations θ_{b1}, θ_{b2} for a simply supported beam based on a concentrated plasticity model can be calculated using Equations (2.58), (2.59) and (2.60).

The resulting \tilde{K}_m expressions for both plasticity models can be expanded to account for shear forces using the equilibrium relationship established in Equation (2.14). Because axial effects are not coupled, they can be separately added as in the precedent sections. A final 6x6 element stiffness matrix \tilde{K}_e relating all forces and displacements can be used to assemble the global stiffness matrix using standard assembling methods based on the same DOF convention as shown in Figure 2.2.

2.6 Transformation from local to global coordinate systems

Stiffness matrix expressions for the different linear elastic and nonlinear beam-column configurations have been derived using a local coordinate system. A global coordinate system is required so that global stiffness matrix can be assembled by standard methods. Assembly can be achieved by finding a linear transformation matrix that express the components of a vector in a global coordinate system from a local coordinate system and vice versa. In reference to Figure 2.5, a vector \bar{V} can be expressed in two different coordinate systems x - y (global) and x' - y' (local) as

$$\bar{V} = V_x \bar{e}_x + V_y \bar{e}_y = V_{x'} \bar{e}_{x'} + V_{y'} \bar{e}_{y'} \quad (2.67)$$

where $\bar{e}_x = (1,0)$; $\bar{e}_y = (0,1)$, and $\bar{e}_{x'} = (\cos \theta, \sin \theta)$, $\bar{e}_{y'} = (-\sin \theta, \cos \theta)$

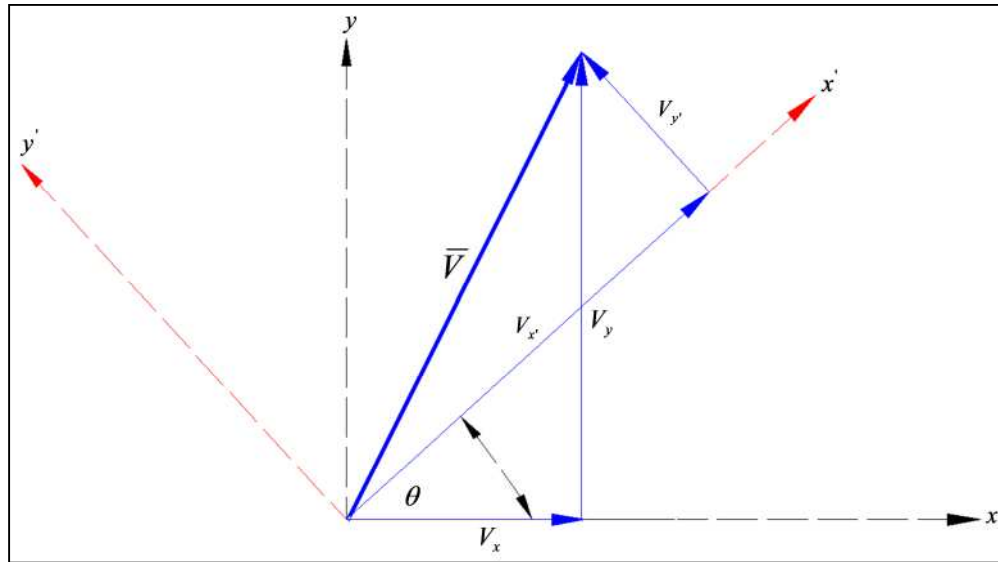


Figure 2.5: Vector \bar{V} expressed in local and global coordinate systems

Equation (2.67) is rearranged with a matrix form to relate vector components from local to global coordinates as

$$\begin{bmatrix} V_x \\ V_y \end{bmatrix} = \tilde{A} \begin{bmatrix} V_{x'} \\ V_{y'} \end{bmatrix} \quad (2.68)$$

where $\tilde{A} = \begin{bmatrix} \cos\theta & -\sin\theta \\ \sin\theta & \cos\theta \end{bmatrix}$

Consequently, a linear transformation matrix relating the vector components from global to local coordinates can be calculated by $\tilde{A}^{-1} = \tilde{A}^T$. An extension of the preceding results yields a linear transformation matrix \tilde{T} to relate the displacements and rotations from a global to a local coordinate system in a beam-column element, as

$$\tilde{T} = \begin{bmatrix} \cos\theta & \sin\theta & 0 & 0 & 0 & 0 \\ -\sin\theta & \cos\theta & 0 & 0 & 0 & 0 \\ 0 & 0 & 1 & 0 & 0 & 0 \\ 0 & 0 & 0 & \cos\theta & \sin\theta & 0 \\ 0 & 0 & 0 & -\sin\theta & \cos\theta & 0 \\ 0 & 0 & 0 & 0 & 0 & 1 \end{bmatrix} \quad (2.69)$$

where the element stiffness matrix \tilde{K}_{eg} can be expressed in global coordinates using its local coordinate representation as

$$\tilde{K}_{eg} = \tilde{T}^{-1} \tilde{K}_e \tilde{T} = \tilde{T}^T \tilde{K}_e \tilde{T} \quad (2.70)$$

where $\tilde{F}_{eg} = \tilde{K}_{eg} \tilde{u}_{eg}$ having $\tilde{u}_e = \tilde{T} \tilde{u}_{eg}$ and $\tilde{F}_e = \tilde{T}^T \tilde{F}_{eg}$.

2.7 Structural joint modeling

In the early years of frame analysis, structural joints were mainly modeled as mere points without any physical dimension, i.e. zero length elements. Later, finite-sized representation was adopted by modeling structural joints as rigid elements. However, later experimental and analytical studies demonstrated that structural joints have the capacity to deform and even dissipate energy during considerable loading conditions and therefore must be modeled with deformable body properties (Iwan, 1961; Hudson, 1961; Hudson, 1962).

Structural joints can be conceived as a combination of two components, the connection area and the panel zone. The connection area is defined as the region where frame members connect to the panel zone. The panel zone, on the other hand, is the core region where forces from adjacent frame members are transferred to each other. Several studies have been performed in the attempt to characterize the strength and stiffness configuration of structural joints (Leon, 1989; El-Tawil et al., 1999; Shiohara, 2001; Hjelmstad and Haikal, 2006).

Because the influence of the connection area has already been considered in the different beam-column element models presented in previous sections, this section mainly focuses on the selection of an adequate panel zone model for the proposed computational platform. In addition to the accuracy and the feasibility of the selected model to be implemented accordingly to any adopted frame modeling scheme, the computational efficiency within a real-time processing context is also considered for selection. Adding refined panel zone models may increase significantly the number of DOF and calculation complexity in the overall analysis, which consequently would reduce the real-time execution capabilities. Based on these criteria, a novel panel zone model proposed by Hjelmstad and Haikal (2006) is selected for the RT-Frame2D computational platform. The model is defined only by three DOF at the center of the panel zone and three

deformation modes for the panel zone itself. Moreover, DOF belonging to frame members connecting to the panel zone can be associated with the DOF and deformation modes of the panel zone via a transformation matrix that ensures equilibrium and kinematic compatibility. Therefore, the same number of DOF as the model without panel zone is used when solving the global equation of motion. Two versions are currently available in RT-Frame2D: a rigid-body version, and a linear version with bidirectional tension/compression and shear distortion effect. The derivation and corresponding formulation for both versions are presented in this section. Figure 2.6 shows the geometry of the panel zone model with corresponding nodes $1 \sim 4$ or locations where concurring beam-column elements connect to the panel zone for reference.

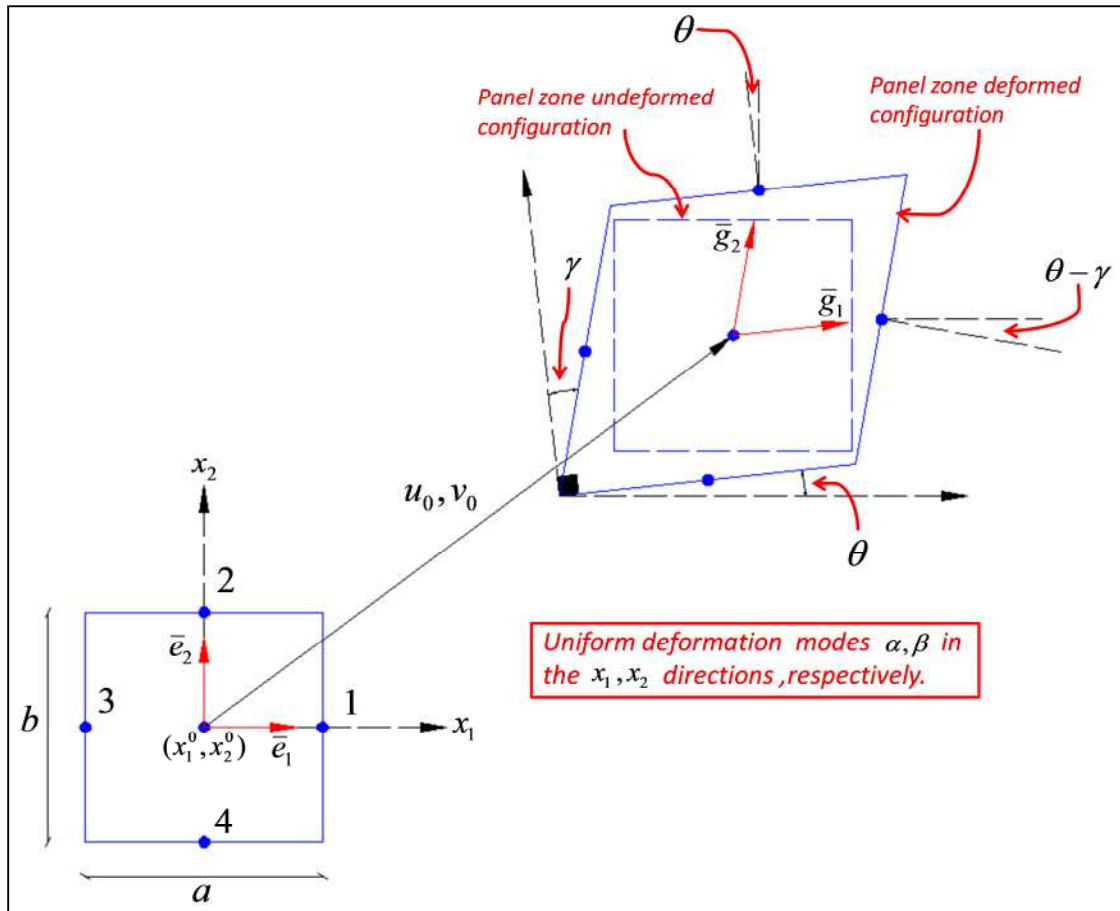


Figure 2.6: Panel zone model

The virtual work functional for a panel zone model of width "a", height "b" and thickness "t" which is subjected to in-plane deformation can be written as

$$\begin{aligned} \delta W = & -(\delta \tilde{u}_b^1)^T \tilde{F}_b^1 - (\delta \tilde{u}_b^2)^T \tilde{F}_b^2 - (\delta \tilde{u}_b^3)^T \tilde{F}_b^3 - (\delta \tilde{u}_b^4)^T \tilde{F}_b^4 + (\delta \tilde{u}_0)^T \tilde{F}_0 \\ & - \int_A (\delta \tilde{\varepsilon})^T \tilde{\sigma} t dA = 0 \end{aligned} \quad (2.71)$$

In reference to Figure 2.6, $\tilde{F}_b^i = [Fu_b^i \quad Fv_b^i \quad F\theta_b^i]^T$ is a vector of forces acting through a vector of virtual displacements, $\delta \tilde{u}_b^i = [\delta u_b^i \quad \delta v_b^i \quad \delta \theta_b^i]^T$, from a beam-column element end attached to the node "i" of the panel zone; and $\tilde{F}_0 = [Fu_0 \quad Fv_0 \quad F\theta_0]^T$ is a vector of forces acting through a vector of virtual displacements, $\delta \tilde{u}_0 = [\delta u_0 \quad \delta v_0 \quad \delta \theta]^T$, at the center of the panel zone. Furthermore, $\tilde{\sigma} = [\sigma_{x_1} \quad \sigma_{x_2} \quad \tau_{x_1 x_2}]^T$ is a stress vector acting through corresponding virtual strain vector, $\delta \tilde{\varepsilon} = [\delta \varepsilon_{x_1} \quad \delta \varepsilon_{x_2} \quad \delta \gamma_{x_1 x_2}]^T$, over the panel zone area. Additionally, the virtual strain vector $\delta \tilde{\varepsilon}$ can be expressed as function of virtual deformation modes of the panel zone $\delta \tilde{u}_{pz} = [\delta \alpha \quad \delta \beta \quad \delta \gamma]^T$ as

$$\delta \tilde{\varepsilon} = \tilde{B} \delta \tilde{u}_{pz} = \frac{\partial \tilde{\varepsilon}}{\partial \tilde{u}_{pz}} \delta \tilde{u}_{pz} \quad (2.72)$$

Here α, β, γ are deformation modes that describe uniform (constant) longitudinal and shear deformation states over the panel zone area, as shown in Figure 2.6. As implied by Equation (2.71), equations of equilibrium can be established if virtual beam-column displacements at node "i" $\delta \tilde{u}_b^i$ can be expressed in terms of virtual displacements at the center of the panel zone $\delta \tilde{u}_0$ and virtual deformation modes of the panel zone $\delta \tilde{u}_{pz}$. To

accomplish this goal, a deformation map $\bar{\varphi}(\bar{x})$ acting on a coordinate system $\bar{x} = (x_1, x_2)$ within the panel zone with coordinates at the center (x_1^0, x_2^0) is defined as

$$\bar{\varphi}(\bar{x}) = (x_1^0 + u_0)\bar{e}_1 + (x_2^0 + v_0)\bar{e}_2 + x_1(1 + \alpha)\bar{g}_1(\theta) + x_2(1 + \beta)\bar{g}_2(\theta, \gamma) \quad (2.73)$$

where $\bar{g}_1(\theta), \bar{g}_2(\theta, \gamma)$ are given as

$$\bar{g}_1(\theta) = \cos\theta\bar{e}_1 + \sin\theta\bar{e}_2 \quad (2.74)$$

$$\bar{g}_2(\theta, \gamma) = -\sin(\theta + \gamma)\bar{e}_1 + \cos(\theta + \gamma)\bar{e}_2 \quad (2.75)$$

and $\bar{e}_1 = (1, 0); \bar{e}_2 = (0, 1)$.

Note that $\bar{\varphi}(\bar{x})$ subjects the panel zone both to rigid body translation by displacements u_0, v_0 , and as previously mentioned, to deform by deformation modes α, β in the x_1 and x_2 directions, respectively. In addition, shear distortion is developed through a deformation mode γ (shown negative in Figure 2.6). Calculation of the directional derivative of the deformation map in the direction of the virtual displacements, yields the next two equations

$$\begin{aligned} \delta\bar{\varphi}(\bar{x}) = & \delta\bar{\varphi}_0 + x_1[\bar{g}_1(\theta)\delta\alpha + (1 + \alpha)\bar{g}'_1(\theta)\delta\theta] \\ & + x_2[\bar{g}_2(\theta, \gamma)\delta\beta + (1 + \beta)\bar{g}'_2(\theta, \gamma)(\delta\theta + \delta\gamma)] \end{aligned} \quad (2.76)$$

$$\delta\theta_b^i = \delta\theta + c^i \delta\gamma \quad (2.77)$$

where $c^i = 1$ when $(i=1,3)$ and $c^i = 0$ when $(i=2,4)$. After combining and algebraic manipulation of Equations (2.76) and (2.77), a direct relationship of $\delta\tilde{u}_b^i$ as function of $\delta\tilde{u}_0$ and $\delta\tilde{u}_{pz}$ can be established. However, for a geometrically linear version of the panel zone, $\bar{g}_1(\theta)$, $\bar{g}_2(\theta, \gamma)$ and the corresponding $\bar{g}'_1(\theta)$, $\bar{g}'_2(\theta, \gamma)$ can be approximated as

$$\bar{g}_1(\theta) = \bar{e}_1 + \theta\bar{e}_2 \Rightarrow \bar{g}'_1(\theta) = \bar{e}_2 \quad (2.78)$$

$$\bar{g}_2(\theta, \gamma) = -(\theta + \gamma)\bar{e}_1 + \bar{e}_2 \Rightarrow \bar{g}'_2(\theta, \gamma) = -\bar{e}_1 \quad (2.79)$$

After substitution of Equation (2.78) and (2.79) into Equation (2.76) and further elimination of high-order terms, a linear transformation matrix $\tilde{T}_{pz}(\tilde{x}^i)$ relating $\delta\tilde{u}_b^i$ at node “ i ” in terms of $\delta\tilde{u}_0$ and $\delta\tilde{u}_{pz}$ is obtained as

$$\delta\tilde{u}_b^i = \tilde{T}_{pz}(\tilde{x}^i) \begin{bmatrix} \delta\tilde{u}_0 \\ \delta\tilde{u}_{pz} \end{bmatrix} = \tilde{T}_{pz}^{11}(\tilde{x}^i)\delta\tilde{u}_0 + \tilde{T}_{pz}^{12}(\tilde{x}^i)\delta\tilde{u}_{pz} \quad (2.80)$$

where

$$\tilde{T}_{pz}(\tilde{x}^i) = \begin{bmatrix} \tilde{T}_{pz}^{11}(\tilde{x}^i) & \tilde{T}_{pz}^{12}(\tilde{x}^i) \end{bmatrix} = \begin{bmatrix} 1 & 0 & -x_2^i & \vdots & x_1^i & 0 & -x_2^i \\ 0 & 1 & x_1^i & \vdots & 0 & x_2^i & 0 \\ 0 & 0 & 1 & \vdots & 0 & 0 & c^i \end{bmatrix} \quad (2.81)$$

Because deformation modes and corresponding stress are uniformly (constantly) distributed over the panel zone area, the last term in Equation (2.71) can be re-written by the use of Equation (2.72) as

$$\int_A (\delta \boldsymbol{\varepsilon})^T \boldsymbol{\sigma} t dA = \delta \bar{\boldsymbol{u}}_{pz}^T [\tilde{\boldsymbol{B}}^T \boldsymbol{\sigma} t \int_A dA] = \delta \bar{\boldsymbol{u}}_{pz}^T [abt \tilde{\boldsymbol{B}}^T \boldsymbol{\sigma}] \quad (2.82)$$

substitution of Equation (2.82) and (2.80) into Equation (2.71) yields

$$\begin{aligned} & \delta \bar{\boldsymbol{u}}_0^T [-\tilde{\boldsymbol{T}}_{pz}^{11}(\bar{\boldsymbol{x}}^1)^T \tilde{\boldsymbol{F}}_b^1 - \tilde{\boldsymbol{T}}_{pz}^{11}(\bar{\boldsymbol{x}}^2)^T \tilde{\boldsymbol{F}}_b^2 - \tilde{\boldsymbol{T}}_{pz}^{11}(\bar{\boldsymbol{x}}^3)^T \tilde{\boldsymbol{F}}_b^3 - \tilde{\boldsymbol{T}}_{pz}^{11}(\bar{\boldsymbol{x}}^4)^T \tilde{\boldsymbol{F}}_b^4 + \tilde{\boldsymbol{F}}_0] + \\ & \delta \bar{\boldsymbol{u}}_{pz}^T [-\tilde{\boldsymbol{T}}_{pz}^{12}(\bar{\boldsymbol{x}}^1)^T \tilde{\boldsymbol{F}}_b^1 - \tilde{\boldsymbol{T}}_{pz}^{12}(\bar{\boldsymbol{x}}^2)^T \tilde{\boldsymbol{F}}_b^2 - \tilde{\boldsymbol{T}}_{pz}^{12}(\bar{\boldsymbol{x}}^3)^T \tilde{\boldsymbol{F}}_b^3 - \tilde{\boldsymbol{T}}_{pz}^{12}(\bar{\boldsymbol{x}}^4)^T \tilde{\boldsymbol{F}}_b^4 - abt(\tilde{\boldsymbol{B}}^T \boldsymbol{\sigma})] = 0 \end{aligned} \quad (2.83)$$

where matrix $\tilde{\boldsymbol{B}}$, for a geometrically linear version of the panel zone, becomes

$$\tilde{\boldsymbol{B}} = \begin{bmatrix} 1 & 0 & 0 \\ 0 & 1 & 0 \\ 0 & 0 & -1 \end{bmatrix} \quad (2.84)$$

It must be emphasized that for a geometrically nonlinear version of the panel zone, the matrix $\tilde{\boldsymbol{B}}$ is a function of the deformation modes of the panel zone, i.e. $\tilde{\boldsymbol{B}} = \tilde{\boldsymbol{B}}(\bar{\boldsymbol{u}}_{pz})$ as implied by Equation (2.72). Further substitution of matrix $\tilde{\boldsymbol{B}}$ and $\tilde{\boldsymbol{T}}_{pz}^{11}(\bar{\boldsymbol{x}}^i), \tilde{\boldsymbol{T}}_{pz}^{12}(\bar{\boldsymbol{x}}^i)$ matrices into the bracket components of Equation (2.83) yields the next set of equations as

$$\sum_{i=1:4} Fu_b^i = Fu_0 \quad (2.85)$$

$$\sum_{i=1:4} Fv_b^i = Fv_0 \quad (2.86)$$

$$\sum_{i=1:4} M_b^i = F\theta_0 \quad (2.87)$$

$$\sum_{i=1:4} F\sigma_{x_1}^i = -abt\sigma_{x_1} \quad (2.88)$$

$$\sum_{i=1:4} F\sigma_{x_2}^i = -abt\sigma_{x_2} \quad (2.89)$$

$$\sum_{i=1:4} M\tau_{x_1x_2}^i = abt\tau_{x_1x_2} \quad (2.90)$$

where

$$M_b^i = -x_2^i Fu_b^i + x_1^i Fv_b^i + F\theta_b^i \quad (2.91)$$

$$F\sigma_{x_1}^i = x_1^i Fu_b^i \quad (2.92)$$

$$F\sigma_{x_2}^i = x_2^i Fv_b^i \quad (2.93)$$

$$M\tau_{x_1x_2}^i = -x_2^i Fu_b^i + c^i F\theta_b^i \quad (2.94)$$

As a result, three equations of equilibrium associated with the DOF at the center of the panel zone and three equations of stress balance associated with the deformation modes of the panel zone are obtained for the panel zone equilibrium. Therefore, beam-column elements need to be defined in terms of the “new DOF”, i.e. DOF at the center of panel zone and corresponding deformation modes so that global equilibrium and stress balance equations can be enforced by standard assembling techniques. For instance, Figure 2.7 shows a beam-column element connected from node “*k*” at panel zone “*i*” to node “*m*” at panel zone “*j*”, respectively.

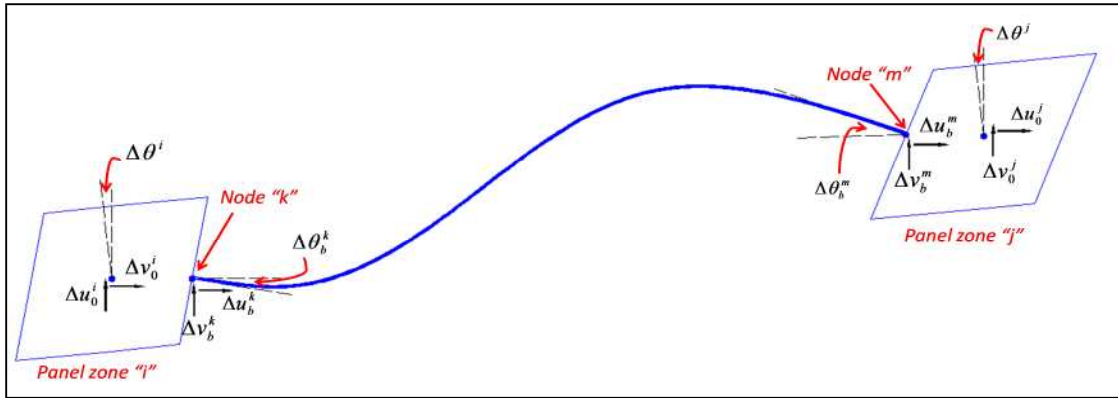


Figure 2.7: Beam-column element and panel zone connectivity

Examining Equations (2.81) and (2.83), the increment in the displacements and residual forces of the beam-column element can thus be expressed in terms of the “new DOF” associated with the panel zone as

$$\begin{bmatrix} \Delta \tilde{u}_b^k \\ \Delta \tilde{u}_b^m \end{bmatrix} = \tilde{\Gamma} \begin{bmatrix} \Delta \tilde{u}_0^i \\ \Delta \tilde{u}_0^j \\ \Delta \tilde{u}_{pz}^i \\ \Delta \tilde{u}_{pz}^j \end{bmatrix} \quad (2.95)$$

$$\begin{bmatrix} \tilde{F}^i \\ \tilde{F}^j \\ \tilde{F}\sigma^i \\ \tilde{F}\sigma^j \end{bmatrix} = \tilde{\Pi}^T \begin{bmatrix} \tilde{F}_b^k \\ \tilde{F}_b^m \end{bmatrix} \quad (2.96)$$

where

$$\Delta\tilde{u}_b = [\Delta u_b \quad \Delta v_b \quad \Delta\theta_b]^T \quad (2.97)$$

$$\Delta\tilde{u}_0 = [\Delta u_0 \quad \Delta v_0 \quad \Delta\theta]^T \quad (2.98)$$

$$\Delta\tilde{\alpha}_{\rho z} = [\Delta\alpha \quad \Delta\beta \quad \Delta\gamma]^T \quad (2.99)$$

$$\tilde{F} = [Fu_b \quad Fv_b \quad Mb]^T \quad (2.100)$$

$$\tilde{F}\sigma = [F\sigma_{x_1} \quad F\sigma_{x_2} \quad M\tau_{x_1x_2}]^T \quad (2.101)$$

and

$$\Pi^T = \begin{bmatrix} \tilde{T}_{pz}^{11^T}(\tilde{x}^k) & \tilde{0} \\ \tilde{0} & \tilde{T}_{pz}^{11^T}(\tilde{x}^m) \\ \tilde{T}_{pz}^{12^T}(\tilde{x}^k) & \tilde{0} \\ \tilde{0} & \tilde{T}_{pz}^{12^T}(\tilde{x}^m) \end{bmatrix} = \begin{bmatrix} 1 & 0 & 0 & \vdots & 0 & 0 & 0 \\ 0 & 1 & 0 & \vdots & 0 & 0 & 0 \\ -x_2^k & x_1^k & 1 & \vdots & 0 & 0 & 0 \\ \dots & \dots & \dots & \dots & \dots & \dots & \dots \\ 0 & 0 & 0 & \vdots & 1 & 0 & 0 \\ 0 & 0 & 0 & \vdots & 0 & 1 & 0 \\ 0 & 0 & 0 & \vdots & -x_2^m & x_1^m & 1 \\ \dots & \dots & \dots & \vdots & \dots & \dots & \dots \\ x_1^k & 0 & 0 & \vdots & 0 & 0 & 0 \\ 0 & x_2^k & 0 & \vdots & 0 & 0 & 0 \\ -x_2^k & 0 & c^k & \vdots & 0 & 0 & 0 \\ \dots & \dots & \dots & \vdots & \dots & \dots & \dots \\ 0 & 0 & 0 & \vdots & x_1^m & 0 & 0 \\ 0 & 0 & 0 & \vdots & 0 & x_2^m & 0 \\ 0 & 0 & 0 & \vdots & -x_2^m & 0 & c^m \end{bmatrix} \quad (2.102)$$

Therefore, the tangential stiffness matrix, $\tilde{K}_e ij$, for a beam-column element connecting from node “ k ” at panel zone “ i ” to node “ m ” at panel zone “ j ” can be expressed as

$$\tilde{K}_e ij = \tilde{\Pi}^T \tilde{K}_e \tilde{\Pi} \quad (2.103)$$

Note that an incremental formulation has been used to account for potential nonlinear behavior at the beam-column elements. As a result, global assembling will yield a system of “ $3n + 3p$ ” equations. Here “ n ” is the number of global nodes and “ p ” is the number of global nodes where panel zones are considered. These equations are represented as

$$\begin{bmatrix} \tilde{K}_{aa} & \tilde{K}_{ab} \\ \tilde{K}_{ba} & \tilde{K}_{bb} \end{bmatrix} \begin{bmatrix} \Delta \tilde{u}_o \\ \Delta \tilde{u}_{pz} \end{bmatrix} = \begin{bmatrix} \tilde{F} \\ \tilde{\sigma}_r \end{bmatrix} \quad (2.104)$$

where $a=3n$ and $b=3p$. $\Delta \tilde{u}_o = [\Delta \tilde{u}_o^1 \dots \Delta \tilde{u}_o^n]^T$ is “ $3n$ ” row vector of increments in displacement at the center of the panel zones. $\Delta \tilde{u}_{pz} = [\Delta \tilde{u}_{pz}^1 \dots \Delta \tilde{u}_{pz}^p]^T$ is the “ $3p$ ” row vector of increments in deformation modes at the panel zones. \tilde{F} and $\tilde{\sigma}_r$ are the residual global force and residual global stress, respectively, in agreement with Equations (2.104). The residual global stress vector $\tilde{\sigma}_r$ can be represented as

$$\tilde{\sigma}_r = \tilde{E}_r \Delta \tilde{u}_{pz} = \begin{bmatrix} -a_1 b_1 t_1 \tilde{B}^T \tilde{E}_1 \tilde{B} & 0 & \dots & 0 \\ 0 & -a_2 b_2 t_2 \tilde{B}^T \tilde{E}_2 \tilde{B} & \dots & \vdots \\ \vdots & \dots & \dots & 0 \\ 0 & \dots & 0 & -a_p b_p t_p \tilde{B}^T \tilde{E}_p \tilde{B} \end{bmatrix} \begin{bmatrix} \Delta \tilde{u}_{pz}^1 \\ \vdots \\ \vdots \\ \Delta \tilde{u}_{pz}^p \end{bmatrix} \quad (2.105)$$

However, in order to perform assembling of the global equation of equilibrium with standard procedures, a condensed global stiffness matrix based on DOF at the center of panel zones is required. This global stiffness matrix is defined as

$$\tilde{K} = \tilde{K}_{aa} - \tilde{K}_{ab} [\tilde{K}_{bb} + \tilde{E}_r]^{-1} \tilde{K}_{ba} \quad (2.106)$$

where the increment in the deformation modes of the panel zone can be updated from the increments of the DOF at the center of panel zones as

$$\Delta \tilde{u}_{pz} = -[\tilde{K}_{bb} + \tilde{E}_r]^{-1} \tilde{K}_{ba} \Delta \tilde{u}_o \quad (2.107)$$

The last two equations are implemented within the RT-Frame2D framework as shown later in Section 2.11 for the nonlinear dynamic analysis of frame structures with panel zone elements.

2.8 Hysteretic rules

Accurate modeling of the hysteretic relationship between stress and strain (fiber modeling) or extension of it to a resultant format such as force-displacement, moment-curvature, or moment-rotation level is one of the most important aspects of the nonlinear analysis of frame structures. However, hysteretic behaviors are not simple to characterize. Phenomena such as slip or pinching due to opening and closing of cracks are commonly observed in reinforced concrete structures when subjected to excessive loading regimes. Stiffness and strength degradation can also be present. Isotropic or kinematic hardening effects such as the Bauschinger effect in steel materials can also be present. The Bauschinger effect is evidenced by a reduction of the stress corresponding with onset of nonlinear response of the material when the direction of deformation is changed.

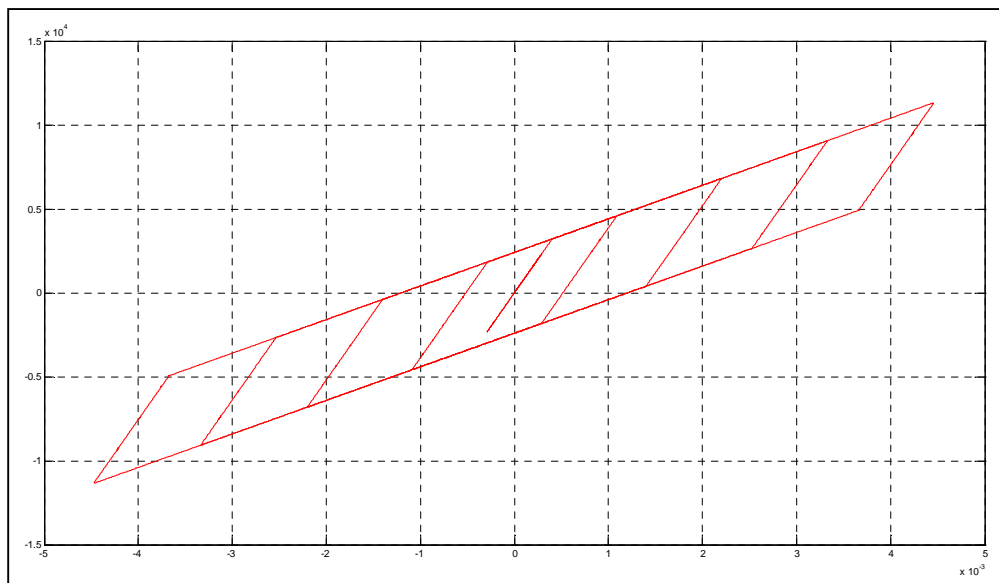


Figure 2.8: Bilinear hysteresis loop

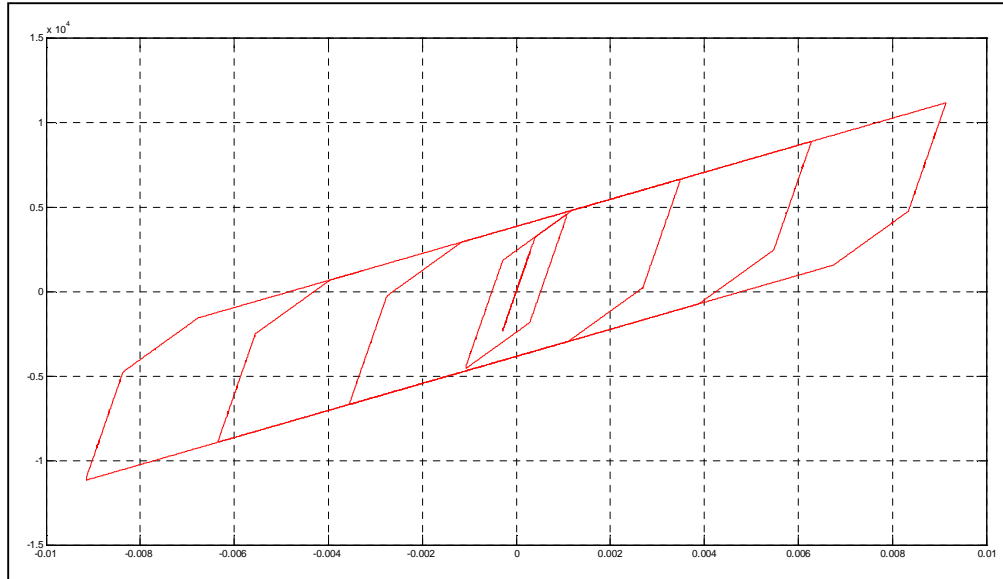


Figure 2.9: Tri-linear hysteresis loop

Hysteresis models are usually implemented by rules applied in a particular fashion where polygonal and smooth or combination of both formats can be appreciated. For instance, Popovics (1973) proposed a model with degraded linear unloading/reloading stiffness and exponential-decay tensile strength for concrete applications. Polygonal hysteretic models (Clough and Johnson, 1966; Takeda et al., 1970; Park et al., 1987) are often motivated by the actual behavior stages of structural elements where cracking, yielding and stiffness or strength degradation can be well defined. For instance, Park et al. (1987) proposed a tri-linear envelope hysteretic model where stiffness and strength deterioration with a non-symmetric development was accounted for. Conversely, smooth hysteretic models show continuous change in stiffness due to smooth yielding, or in general, sharp changes of this parameter (Bouc, 1967; Wen, 1976; Ozdemir 1976). Despite the existence of well-defined hysteretic models, the ability of these models to accurately replicate what is expected during simulation relies on the appropriate selection of parameters. Numerous efforts have recently been made to develop hysteretic models with parameters that are defined in agreement with experimental results (Sivaselvan and Reinhorn, 2000; Shi, 1997; Ibarra et al., 2002; Elwood, 2002; Mostaghel, 1999). RT-Frame2D relies on two different hysteresis models suitable for steel materials. Both a bilinear and a tri-linear

model are included with kinematic hardening to consider the Bauschinger effect. Examples of hysteresis loops of the proposed bilinear and tri-linear models are shown in Figure 2.8 and Figure 2.9, respectively; for reference. The hysteresis loops represent typical moment-curvature (or rotation) records associated a monotonically increasing input. Note the presence of the Bauschinger effect by the common space translation of the yield surface for kinematic hardening.

2.9 P- Δ effect modeling

Second order moments generated by inter-story drifts and gravity loads in building structures are commonly referred as P- Δ effects. Solution of P- Δ or second order effects in structural analysis is usually based on rigorous iterative techniques (Rutenberg, 1982). The inclusion of these approaches could be computationally inefficient when real-time execution is required.

A simpler methodology based on the lean-on column concept and the use of the geometric stiffness approach is used for representing the overall second order effect of building structures in RT-Frame2D. Lean-on columns, also known as leaning columns, have been proposed and utilized as a tool for practical stability analysis of steel un-braced frames (Galambos, 1988; Geschwindner, 1994; American Institute of Steel Construction-AISC, 2005). Lean-on columns are gravity load-type columns usually modeled as pinned end members with no lateral stability other than that provided by the frame under analysis.

The geometric stiffness matrix, also known as the initial stress stiffness matrix, defines the stiffness associated with the element stress level (Cook et al., 1989). For a beam-column or bar element, the geometric stiffness matrix accounts for the increment or reduction in the mechanical stiffness due to the tensile or compressive axial force acting on the member. This effect plays a role when the deflections are large enough to induce considerable changes in the geometry of the structure, making necessary to define the equations of equilibrium with respect to that deformed configuration.

The geometric stiffness matrix of a beam-column element can be calculated by following standard displacement-based procedures for the definition of beam-column stiffness matrix due to mechanical properties (Cook et al., 1989). However, nonlinear terms in the strain-displacement compatibility equations due to large deformation are included within the internal virtual work expressions. The resulting stiffness matrix contains both the mechanical and geometric stiffness components. The 6x6 geometric stiffness matrix for a beam-column element based on cubic-polynomial and linear displacement shape functions for inclusion of bending and axial effects, respectively; is expressed as

$$\tilde{K}_{eg} = \frac{P}{L} \begin{bmatrix} 1 & 0 & 0 & -1 & 0 & 0 \\ 0 & 6/5 & L/10 & 0 & -6/5 & L/10 \\ 0 & L/10 & 2L^2/15 & 0 & -L/10 & -L^2/30 \\ -1 & 0 & 0 & 1 & 0 & 0 \\ 0 & -6/5 & -L/10 & 0 & 6/5 & -L/10 \\ 0 & L/10 & -L^2/30 & 0 & -L/10 & 2L^2/15 \end{bmatrix} \quad (2.108)$$

where P is the compressive (when negative) or tensile (when positive) axial force acting on the member. L is the length of the beam-column element. This matrix can be used to assemble the global geometric stiffness matrix using standard assembling methods. The 4x4 geometric stiffness matrix for a bar element based on linear displacement shape function is expressed as

$$\tilde{K}_{eg} = \frac{P}{L} \begin{bmatrix} 1 & 0 & -1 & 0 \\ 0 & 1 & 0 & -1 \\ -1 & 0 & 1 & 0 \\ 0 & -1 & 0 & 1 \end{bmatrix} \quad (2.109)$$

The global P- Δ effect in the building can be accounted for using a non-iterative technique by combining the lean-on column concept and geometric stiffness approach. This procedure is accomplished using the assumption of constant weight at the building story levels and small overall structural displacements (ETABS, 1988; Wilson and Habibullah, 1987). Column elements that do not belong to the frame under analysis can be represented by a unique lean-on column component, as shown in Figure 2.10. Inertial and section properties of the lean-on column are defined as the addition of the corresponding column properties. Loads due to the accumulated weight at story levels and associated with the tributary sections under analysis can be applied as compressive axial forces to the vertical DOF of the lean-on column. The lean-on column geometric stiffness matrix is assembled from the element geometric stiffness matrix using either Equation (2.108) or Equation (2.109) and the corresponding compressive force values. The resulting lean-on column geometric stiffness matrix can be added to the global mechanical stiffness matrix to account for the P- Δ effect.

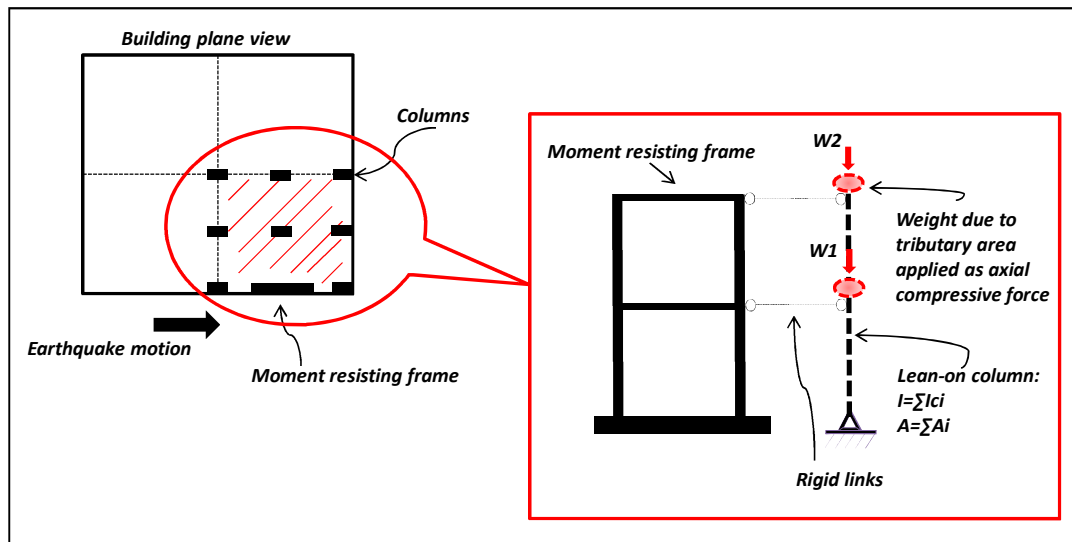


Figure 2.10: P- Δ effect in buildings using the lean-on column concept

2.10 Integration schemes for nonlinear dynamic analysis

Nonlinear dynamic analysis of building structures is usually performed by integrating temporally discretized equations of motion by the use of either explicit or implicit integration schemes (Newmark, 1959; Wilson, 1968; Hilber et al., 1977). In an explicit integration scheme, the displacement at the next time step is calculated as a function of the acceleration, velocity or displacement in the current and previous time steps. Because the displacements are known in advance, element states and the corresponding global restoring force vector are directly updated and assembled within the equation of motion from which acceleration is automatically calculated. Implicit integration schemes calculate the displacement at the next time step as function of the velocity or acceleration of the next time step, in addition to those at the current and previous steps. Consequently, element states and corresponding global restoring forces cannot be updated in advance, yielding a nonlinear equation. Thus, nonlinear solvers to calculate the displacement are required. Nonlinear algorithms from the Newton-Raphson family based on different convergence tests are frequently used in the implementation of implicit integration schemes. These algorithms are based on iterative procedures. The tangent stiffness matrix is updated at each iteration so that increment of displacements can be calculated. The procedure is repeated until global equilibrium between external and internal forces is satisfied within a certain tolerance.

Although implicit methods are usually unconditionally stable and accurate under large integration time steps, their implementation within a RTHS scenario is not practical. Iterative measurements of the experimental restoring force and updating of the tangent stiffness matrix during a RTHS may be difficult or even induce instabilities. Moreover, the allowed execution time may be exceeded due to the computational expense of the nonlinear solver or when equilibrium tolerance is not satisfied. These limitations have made explicit integration schemes more desirable for RTHS implementation because displacements are calculated in one step with no iteration. Moreover, explicit integration schemes achieve reasonable accuracy when relatively small time steps are selected for

integration. Several implementations of hybrid simulations with the use of explicit integration schemes can be found in the literature. For instance, an explicit central difference integration scheme was implemented by Takanashi et al. (Takanashi et al., 1975) for the nonlinear earthquake response analysis of structures by a computer-actuator online system. Some other applications of the central difference and the Newmark explicit methods for hybrid simulation applications can be found at (Nakashima and Masaoka, 1999; Bonnet et al., 2007). However, explicit integration schemes are usually conditionally stable. The stability limit is proportional to the smallest natural period of the computational substructure, i.e. the integration time step must be smaller than this value to guarantee stability. Therefore, in the presence of computational models with a large number of DOF, integration time steps may be too small so that real-time execution conditions can be achieved. This limitation restricts the use of traditional explicit integration schemes to analysis in which unconditional stability is guaranteed.

Therefore, the selection of an integration scheme for RTHS application must include three special requirements: it must be *fast enough* to fulfill real-time execution limits, it must have *reasonable accuracy* and it must preserve *stability*. Here, the explicit unconditionally stable Chen-Ricles (CR) algorithm (Chen and Ricles, 2008) is adopted for the proposed computational platform as the primary integration scheme. This algorithm fulfills the previous conditions and offers enough flexibility to be implemented within the RT-Frame2D framework. Additionally, the implicit unconditionally stable Newmark method (Newmark, 1959) is also available. The Newmark method is implemented in conjunction with the pseudo-force method to reach the solution in one step and avoid the use of iterations. In the following paragraphs, main aspects of these two schemes are introduced and described.

2.10.1 Explicit Chen-Ricles (CR) integration scheme

The explicit unconditionally stable Chen-Ricles (CR) integration scheme is primarily proposed here for solving the equation of motion and evaluating the dynamic linear and

nonlinear response within the RTHS. The CR algorithm enables the displacement and velocity to be calculated in explicit form. The use of an explicit form makes the CR integration scheme very convenient for RTHS applications because no stiffness matrix inversions and nonlinear solvers are required. However, the most attractive property of the CR algorithm relies on its ability to remain unconditionally stable when a linear or nonlinear-softening dynamic analysis is performed.

Let's consider how the unconditional stability condition is guaranteed within the CR algorithm using a perspective based on control theory (Franklin et al., 2002). Stability of a dynamical system can be investigated by the *poles* of the transfer function associated with the differential equation representing the dynamic system under consideration. The continuous transfer function is calculated by means of the *Laplace transform* or *s-transform*. Roots of the characteristic equation, i.e. the denominator of the transfer function are defined as poles. The location of these poles within the *s-domain* indicates the stability of the system. For instance, the system is considered stable if poles are located on the left-half plane of the *s-domain*. Conversely, the system is considered unstable if poles are located on the right-half plane of the *s-domain*. Poles located on the imaginary axis indicate a critically stable condition. The equivalent of the *s-transform* in the discrete domain is the *z-transform*, i.e. the transform of the difference equation representing the dynamic system under evaluation. The stability of the equivalent discrete system can also be investigated by the location of the *z-transform* poles within the *z-domain*. For instance, the system is considered stable if the poles have a magnitude within a unit circle of the *z-domain*. Conversely, the system is considered unstable if the poles have a magnitude out of a unit circle of the *z-domain*. Poles with a unity magnitude indicate a critically stable condition. Several discretization methodologies that approximate the *z-transform* from a continuous system are available. One of them is the bilinear transformation or Tustin's method (Franklin et al., 2002) in which stability from continuous to discrete domain is preserved. Stable poles on the *z-domain* can be approximated from stable poles on the *s-domain* by the Tustin's method as

$$z \approx \frac{1 + s.(\Delta t / 2)}{1 - s.(\Delta t / 2)} \quad (2.110)$$

where Δt is the sample period or discrete time step. In structural dynamics, an integration algorithm yields a difference equation that solves the differential equation associated with the equation of motion. Therefore, the associated z -transform and corresponding poles of the integration algorithm define its stability. Poles of the integration algorithm can be expressed in terms of certain integration parameters, which in turn, can be defined to restrict the magnitude of the poles within the unit circle in the z -domain and guarantee stability. Stable poles in the z -domain can be calculated from stable continuous poles associated to the equation of motion using Equation (2.110). As presented by Chen and Ricles (Chen and Ricles, 2008), an extension of Equation (2.110) to the multiple DOF case is defined as

$$\tilde{Z} = [\tilde{I} - \tilde{S}.(\Delta t / 2)]^{-1} . [\tilde{I} + \tilde{S}.(\Delta t / 2)] \quad (2.111)$$

where \tilde{S} is the pole matrix in the s -domain, \tilde{Z} is the pole matrix in the z -domain and \tilde{I} is the identity matrix. \tilde{S} is associated with the continuous characteristic equation

$$\tilde{M}\tilde{S}^2 + \tilde{C}\tilde{S} + \tilde{K}\tilde{S} = \tilde{0} \quad (2.112)$$

obtained from the transfer function of the differential equation of motion

$$\tilde{M}\ddot{\tilde{U}} + \tilde{C}\dot{\tilde{U}} + \tilde{K}\tilde{U} = \tilde{F} \quad (2.113)$$

Here, \tilde{M} , \tilde{C} and \tilde{K} are the global mass, damping and stiffness matrices, respectively. $\ddot{\tilde{U}}$ is the acceleration vector, $\dot{\tilde{U}}$ is the velocity vector, and \tilde{U} is the displacement vector. \tilde{F} is an input force vector. Note that the \tilde{Z} pole matrix represents stable poles in the discrete domain because they are associated with the stable \tilde{S} pole matrix. The discrete values of the displacement and velocity at time “ $t+\Delta t$ ” are explicitly calculated in the CR algorithm as

$$\dot{\tilde{U}}_{t+\Delta t} = \dot{\tilde{U}}_t + \tilde{\alpha}_1 \Delta t \ddot{\tilde{U}}_t \quad (2.114)$$

$$\tilde{U}_{t+\Delta t} = \tilde{U}_t + \Delta t \dot{\tilde{U}}_t + \tilde{\alpha}_2 \Delta t^2 \ddot{\tilde{U}}_t \quad (2.115)$$

where $\tilde{\alpha}_1$ and $\tilde{\alpha}_2$ are integration parameter matrices. The corresponding characteristic equation associated with the difference equation defined by the CR algorithm, and based on Equations (2.114) and (2.115) is defined as

$$\tilde{M}\tilde{Z}^2 + [\tilde{K}\tilde{\alpha}_2\Delta t^2 + \tilde{C}\tilde{\alpha}_1\Delta t - 2\tilde{M}]\tilde{Z} + [\tilde{K}(\tilde{\alpha}_1 - \tilde{\alpha}_2)\Delta t^2 - \tilde{C}\tilde{\alpha}_1\Delta t + \tilde{M}] = \tilde{0} \quad (2.116)$$

Therefore, $\tilde{\alpha}_1$ and $\tilde{\alpha}_2$ parameter matrices that guarantee stability can be enforced by substitution of Equation (2.111) within Equation (2.116), yielding

$$\tilde{\alpha}_1 = \tilde{\alpha}_2 = 4.(4\tilde{M} + 2\Delta t\tilde{C} + \Delta t^2\tilde{K})^{-1}.\tilde{M} \quad (2.117)$$

Acceleration at time “ $t+\Delta t$ ” can be calculated then from the discrete equation of motion as

$$\ddot{\tilde{U}}_{t+\Delta t} = \tilde{M}^{-1} \cdot (-\tilde{M}\tilde{G}\ddot{U}_{g_{t+\Delta t}} + \tilde{P}f_{t+\Delta t} - \tilde{C}\dot{\tilde{U}}_{t+\Delta t} - \tilde{R}_{t+\Delta t}) \quad (2.118)$$

Here $\ddot{\tilde{U}}_{g_{t+\Delta t}}$ is the ground acceleration vector at time “ $t+\Delta t$ ”; $f_{t+\Delta t}$ is the control force at time “ $t+\Delta t$ ” when damper devices are included in the analysis; \tilde{G} and \tilde{P} are loading vectors; $\tilde{R}_{t+\Delta t}$ is the restoring force vector measured at time “ $t+\Delta t$ ”. The restoring force vector is equal to $\tilde{K}\tilde{U}_{t+\Delta t}$ when a linear analysis is performed.

The stability condition can be verified by analyzing the magnitude of the poles when integration parameters $\tilde{\alpha}_1$ and $\tilde{\alpha}_2$ are inserted within the characteristic equation. To simplify the analysis, a single DOF system is analyzed. Reduction of Equation (2.117) to a single DOF case yields scalar values for $\tilde{\alpha}_1$ and $\tilde{\alpha}_2$ given by

$$\alpha_1 = \alpha_2 = \frac{4}{4 + 4\xi\omega_n \Delta t + \omega_n^2 \Delta t^2} \quad (2.119)$$

substitution of the previous quantities within the characteristic Equation (2.116) in the *z-domain* yields

$$[\omega_n^2 \Delta t^2 + 4\xi\omega_n \Delta t + 4]z^2 + [2\omega_n^2 \Delta t^2 - 8]z + [\omega_n^2 \Delta t^2 - 4\xi\omega_n \Delta t + 4] = 0 \quad (2.120)$$

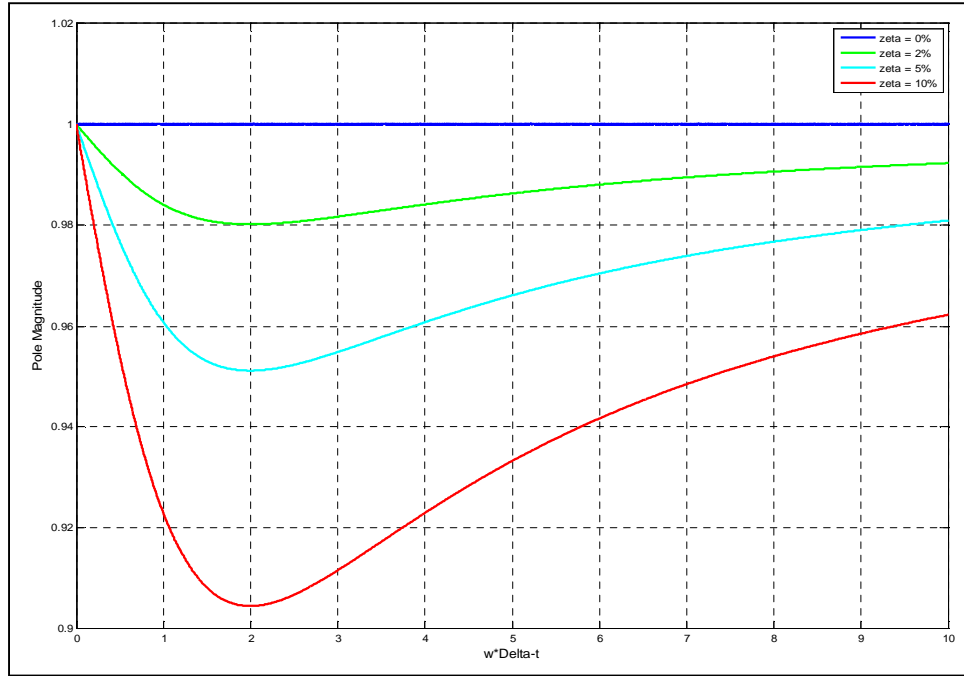


Figure 2.11: Magnitude of the poles associated to the CR integration scheme

Figure 2.11 shows the variation in the magnitude of the poles for different damping ratio values with respect to $\omega_n \Delta t$. From the Figure it is clear that stability is always guaranteed because the magnitude is always less than unity. Observe that the magnitude of the pole varies with an asymptotic behavior with respect to unity while $\omega_n \Delta t$ is increased. Moreover, Chen (2007) showed that the CR algorithm remains unconditionally stable for nonlinear structures with softening behavior. The poles of the algorithm remain within the unit circle in the z -domain when the natural frequency of the dynamic system tends to zero due to the softening behavior. Additionally, the CR algorithm has been proven to have the same accuracy as the Newmark method with constant acceleration (Newmark, 1959) and the explicit unconditionally stable Chang's algorithm (Chang, 1999; Chang, 2002). This level of accuracy is possible because the discrete transfer functions for the CR algorithm and the two previous integration schemes share the same poles leading to the same accuracy and dynamic properties.

2.10.2 Implicit-Newmark-beta integration scheme

The unconditionally-stable Newmark-type integration scheme in conjunction with the pseudo-force method (Subbaraj et al., 1989) is also available in RT-Frame2D to solve the incremental equation of motion. Here, the variation in the displacement and velocity over a time step can be defined depending on the integration parameters γ, β as

$$\tilde{U}_{t+\Delta t} = \tilde{U}_t + \Delta t \dot{\tilde{U}}_t + (\Delta t)^2 \left[\left(\frac{1}{2} - \beta \right) \ddot{\tilde{U}}_t + \beta \ddot{\tilde{U}}_{t+\Delta t} \right] \quad (2.121)$$

$$\dot{\tilde{U}}_{t+\Delta t} = \dot{\tilde{U}}_t + (\Delta t) [(1 - \gamma) \ddot{\tilde{U}}_t + \gamma \ddot{\tilde{U}}_{t+\Delta t}] \quad (2.122)$$

Because the displacement and velocity at time “ $t+\Delta t$ ” cannot be explicitly calculated from the previous quantities, an iterative nonlinear equation solver is required so that the increment of displacement can be calculated within the time step. However, this situation is prohibited when real-time execution conditions need to be fulfilled. Therefore the pseudo-force method is utilized to solve for the increment of displacement in one step. In the pseudo-force method the unbalanced force between the restoring force evaluated using the hysteresis model and the one calculated by assuming a constant linear stiffness at time t during the time interval $t \sim t+\Delta t$ is added to the equation of motion.

Following an incremental formulation, the increment of velocity and acceleration during the time interval $t \sim t+\Delta t$ can be found from Equations (2.121) and (2.122). Follow-up substitution of these quantities within the incremental equation of motion yields the increment of displacement to be calculated as

$$\Delta\tilde{U} = (\tilde{K}_D^{-1})\Delta\tilde{F}_D \quad (2.123)$$

where

$$\tilde{K}_D = \frac{1}{\beta(\Delta t)^2} \tilde{M} + \frac{\gamma}{\beta(\Delta t)} \tilde{C} + [\tilde{K}_0 + \Delta\tilde{K}] \quad (2.124)$$

$$\Delta\tilde{F}_D = -\tilde{M}\tilde{G}\Delta\ddot{U}_g + \left[\frac{1}{2\beta} \tilde{M} + \left(\frac{\gamma}{2\beta} - 1\right)\Delta t \tilde{C} \right] \ddot{\tilde{U}}_t + \left[\frac{1}{\beta\Delta t} \tilde{M} + \left(\frac{\gamma}{\beta}\right)\tilde{C} \right] \dot{\tilde{U}}_t + \tilde{P}\Delta f + \Delta\tilde{F}_{err} \quad (2.125)$$

Here $\tilde{M}, \tilde{C}, \tilde{K}_0$ are the global mass, damping and the linear portion of the stiffness matrix, respectively. $\Delta\tilde{K}$ accounts for the nonlinear portion of the global stiffness matrix. $\dot{\tilde{U}}_t, \ddot{\tilde{U}}_t$ are the velocity and acceleration vectors at time “ t ”. $\Delta\ddot{\tilde{U}}_g, \Delta f$ are the ground acceleration increment and control force increment when damper devices are included in the analysis. \tilde{G} and \tilde{P} are loading vectors. $\Delta\tilde{F}_{err}$ is the vector of unbalanced forces in agreement with the pseudo-force method. Once the increment of displacement is calculated from Equation (2.123), increment of velocity and acceleration are updated to proceed with the next time step. The increment of these quantities are calculated as

$$\Delta\dot{\tilde{U}} = (\Delta t) \left(1 - \frac{\gamma}{2\beta} \right) \dot{\tilde{U}}_t - \frac{\gamma}{\beta} \ddot{\tilde{U}}_t + \frac{\gamma}{\beta\Delta t} \Delta\tilde{U} \quad (2.126)$$

$$\Delta\ddot{U} = \left(\frac{1}{\gamma\Delta t} \right) \Delta\dot{U} - \frac{1}{\gamma} \ddot{U}_t \quad (2.127)$$

2.11 RT-Frame 2D Implementation

RT-Frame2D is implemented as a MATLAB/*embedded function*. The *embedded function* (*Embedded MATLAB* toolbox) supports efficient code generation to accelerate fixed-point algorithm execution for embedded systems. Therefore, a source code reformatting from a dynamically typed language (*MATLAB script*) to a statically typed language (*C script*) takes place. To accomplish this reformatting, the *Embedded MATLAB* inference engine requires an adequate class and size data definition in the source code so it can correctly translate the data at the compilation time.

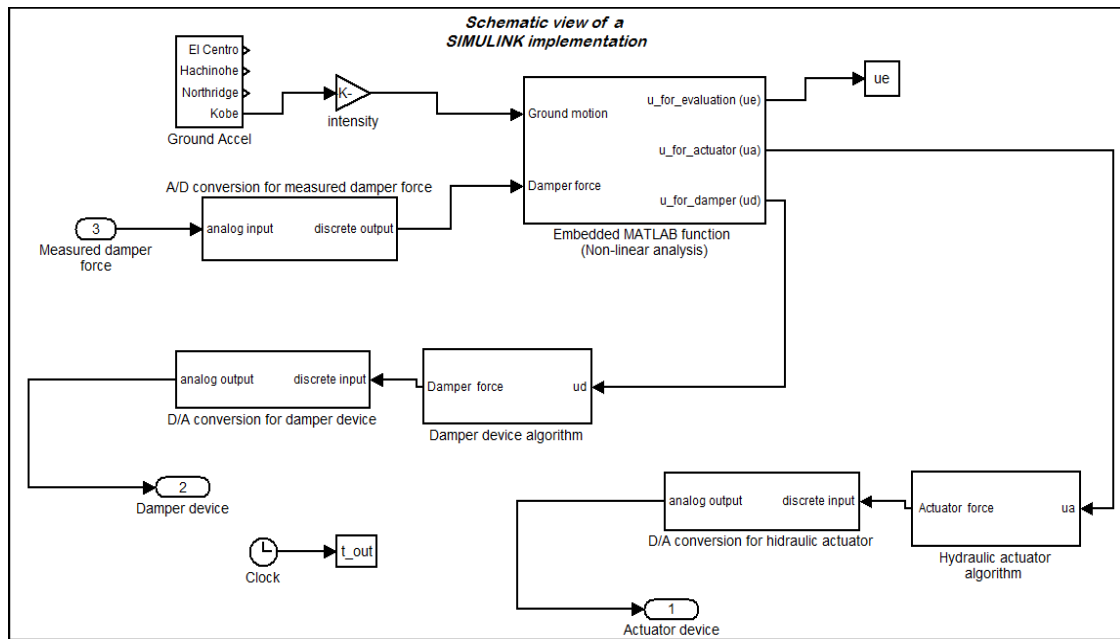


Figure 2.12: Schematic view of a *Simulink* implementation

Additionally, *Simulink* is used to integrate the computational block with the remaining RTHS components so that a unified platform can be generated and compiled for real-time execution. *MATLAB/ Simulink* is a graphical block diagramming tool for modeling, simulating and analyzing dynamic systems. Servo-hydraulic/damper controller algorithms and analog/digital (A/D-D/A) boards for data exchange between computational and experimental substructures are represented as *Simulink* block functions.

Figure 2.12 shows a schematic of a typical *Simulink* implementation. The *MATLAB/xPC* Target is used to generate and compile a C-source code from the *Simulink* model (host PC) that can be downloaded to a real-time kernel (target PC) for execution. *xPC Target* is a high performance host-target system that facilitates the integration of *Simulink* models with physical systems for real-time execution.

Table 2.1: Modeling options for RT-Frame2D executables

<i>.mdl File</i>	<i>FRAME ELEMENT</i>			<i>PANEL ZONE</i>		<i>INTEGRATION SCHEME</i>	
	<i>LBC</i>	<i>BCFC</i>	<i>NBC</i>	<i>RPZ</i>	<i>LPZ</i>	<i>NB</i>	<i>CR</i>
<i>RT_F2D_1</i>	✓		✓			✓	
<i>RT_F2D_2</i>	✓		✓				✓
<i>RT_F2D_3</i>	✓		✓	✓			✓
<i>RT_F2D_4</i>	✓		✓		✓		✓
<i>RT_F2D_5</i>	✓	✓					✓
<i>RT_F2D_6</i>	✓	✓		✓			✓
<i>RT_F2D_7</i>	✓	✓			✓		✓

LBC : Linear beam-column element
BCFC : Linear beam-column element w linear/nonlinear flexible connections
NBC : Nonlinear beam-column element
RPZ : Rigid panel zone model
LPZ : Linear panel zone model w three deformation modes
NB : Newmark-beta integration scheme
CR : Chen-Ricles integration scheme

Table 2.2: Variable definition

<i>Variables</i>	<i>Description</i>
$NSTEPS$	<i>Number of integration steps</i>
Δ	<i>“increment” variable</i>
δ	<i>Variation or change with respect to a linear-elastic state</i>
L	<i>Linear-elastic state sub-index</i>
EI_j^i	<i>Flexural stiffness at end “j” associated to element “i”</i>
α_j^i	<i>Rotational stiffness of connection “j” associated to element “i”</i>
ϕ_j^i	<i>Curvature at end “j” associated to element “i”</i>
θ_{jr}^i	<i>Rotation of connection “j” associated to element “i”</i>
$U_{e\theta j}^i$	<i>Rotation at end “j” associated to a simply supported beam element “i”</i>
M_j^i	<i>Moment at end “j” associated to a simply supported beam element “i”</i>
\mathcal{U}_e^i	<i>Displacement vector associated to element “i”</i>
$\tilde{\mathbf{u}}_{pz}^i$	<i>Vector of panel zone deformations associated to element “i”</i>
$\tilde{\Pi}^i$	<i>Linear operator to obtain displacement vector associated to element “i” from displacement at center of panel zones and panel zone deformations</i>
$\tilde{\mathbf{R}}_e^i$	<i>Restoring force associated to element “i”</i>
$\tilde{\mathbf{K}}_{te}^i$	<i>Tangent stiffness matrix of element “i”</i>
$\tilde{\mathbf{R}}$	<i>Global restoring force</i>
$\tilde{\mathbf{K}}_t$	<i>Global tangent stiffness matrix</i>
$(\tilde{\mathbf{K}}_{PZ1}, \tilde{\mathbf{K}}_{PZ2})$	<i>Matrices for updating of panel zone deformation modes</i>
$\tilde{\mathbf{u}}_{pz}$	<i>Global vector of panel zone deformations</i>

Table 2.2 Continued.

<i>Variables</i>	<i>Description</i>
$\vec{U}, \dot{\vec{U}}, \ddot{\vec{U}}$	<i>Global displacement, velocity and acceleration vectors, respectively.</i>
$\vec{M}, \vec{C}, \vec{K}$	<i>Global mass, damping and linear stiffness matrix, respectively.</i>

An RT-Frame2D computational model is executed by the combined execution of script (.m) and Simulink model (.mdl) files in MATLAB/Simulink environment. .m files are required for definition of the analysis parameters including structural model parameters, control force parameters if considered, time-history analysis parameters and input/output selection. .mdl files that contain embedded functions for both non real-time and real-time execution of a desired analysis configuration can be selected. Each .mdl executable contains coding for a specific type of analysis selected by the user. This partitioning is selected to expedite the execution time when real-time execution requirement needs to be achieved. As later shown in Chapter 3, the execution time is greatly degraded by the amount of coding that needs to be generated and compiled for execution.

Therefore, seven .mdl executables are defined, each named as *RT_F2D_k* where k=1:7 defining the type of analysis, in which only specified modeling options are included to reduce the amount of code to be generated and executed. Modeling options considered at each executable are shown in Table 2.1. Additionally, flow diagrams describing main tasks performed at each .mdl file are shown from Figure 2.13 to Figure 2.20 for understanding of the execution flow. Table 2.2 lists and explains the meaning of key variables within the flow diagrams for clarity in the understanding of the different execution flows.

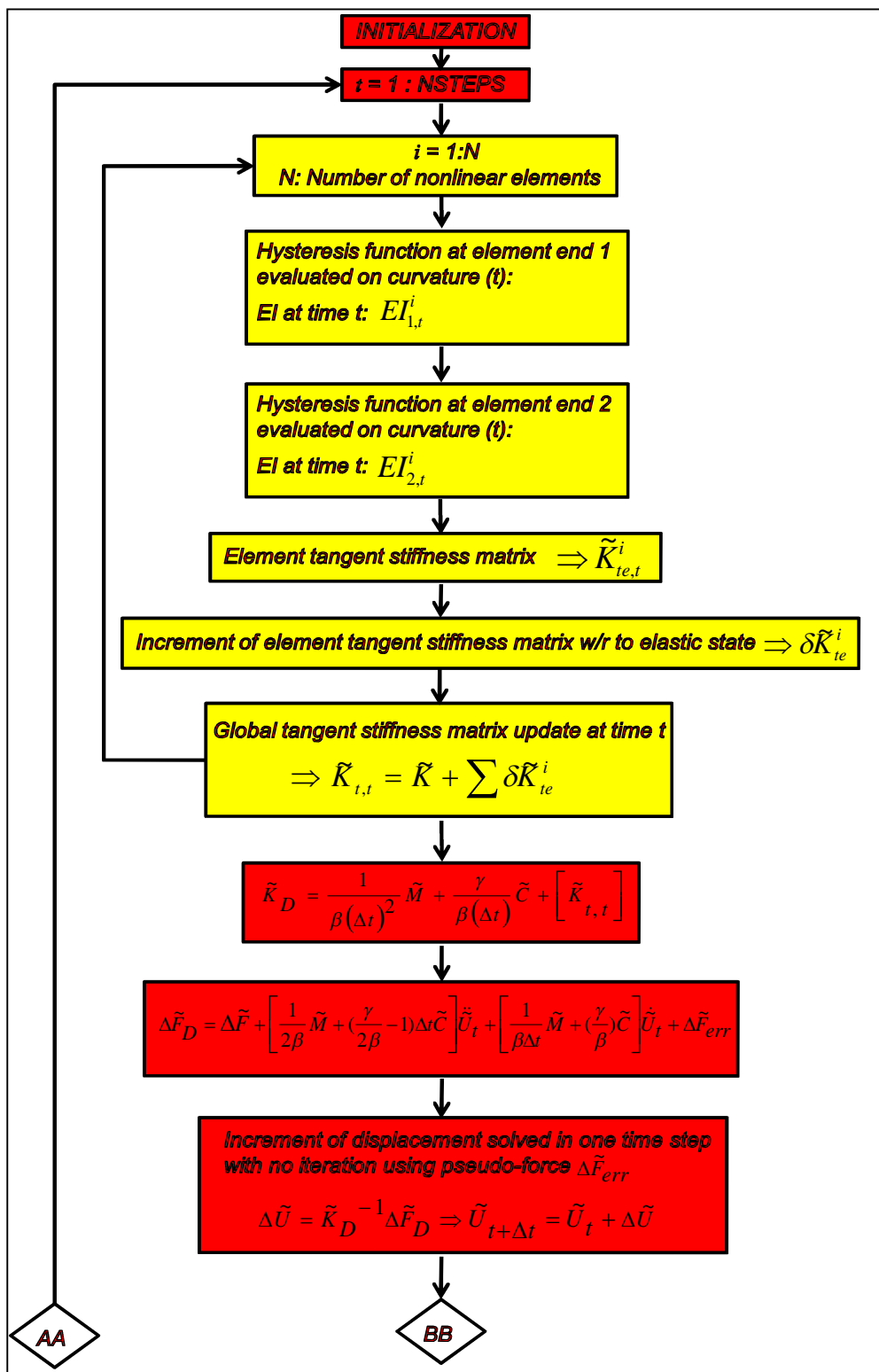


Figure 2.13: Flow diagram for executable *RT_F2D_1* (First part)

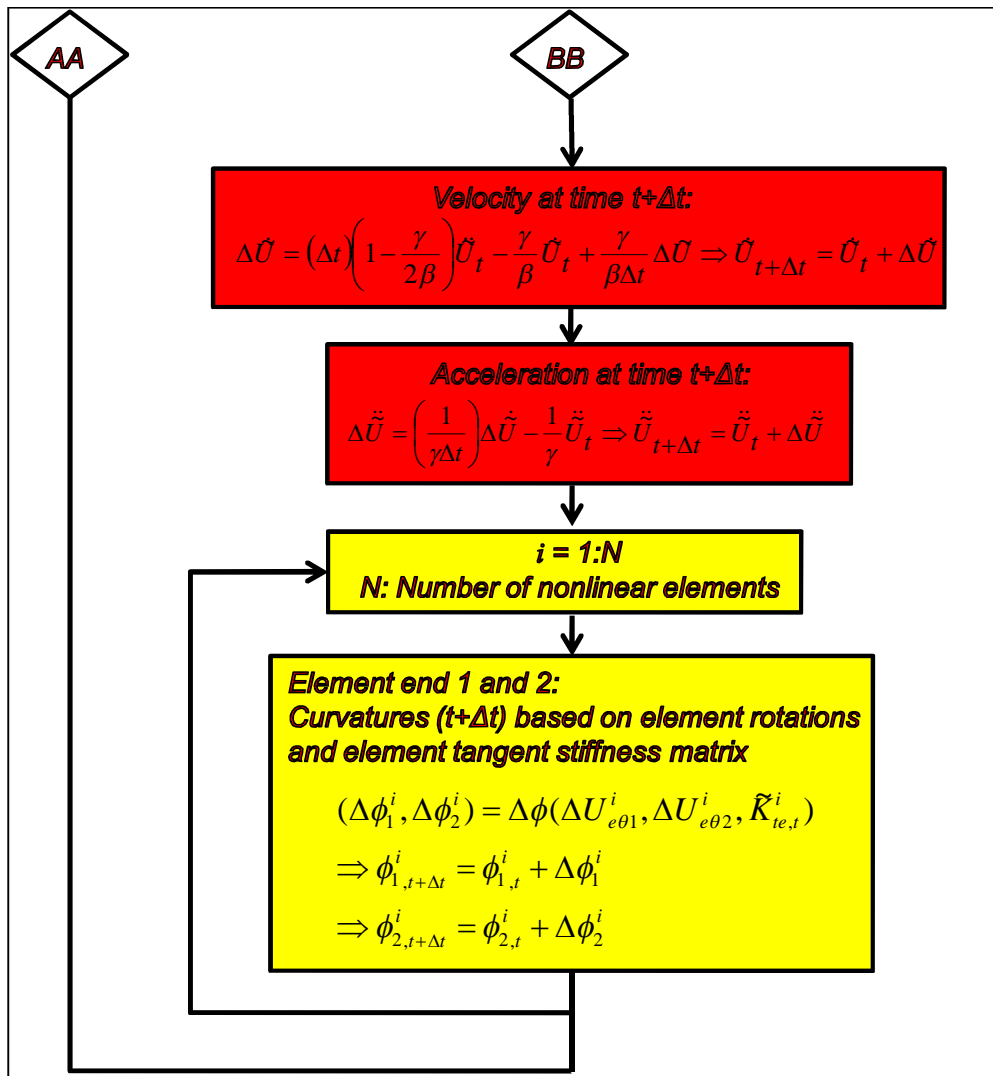


Figure 2.14: Flow diagram for executable *RT_F2D_1* (Second part)

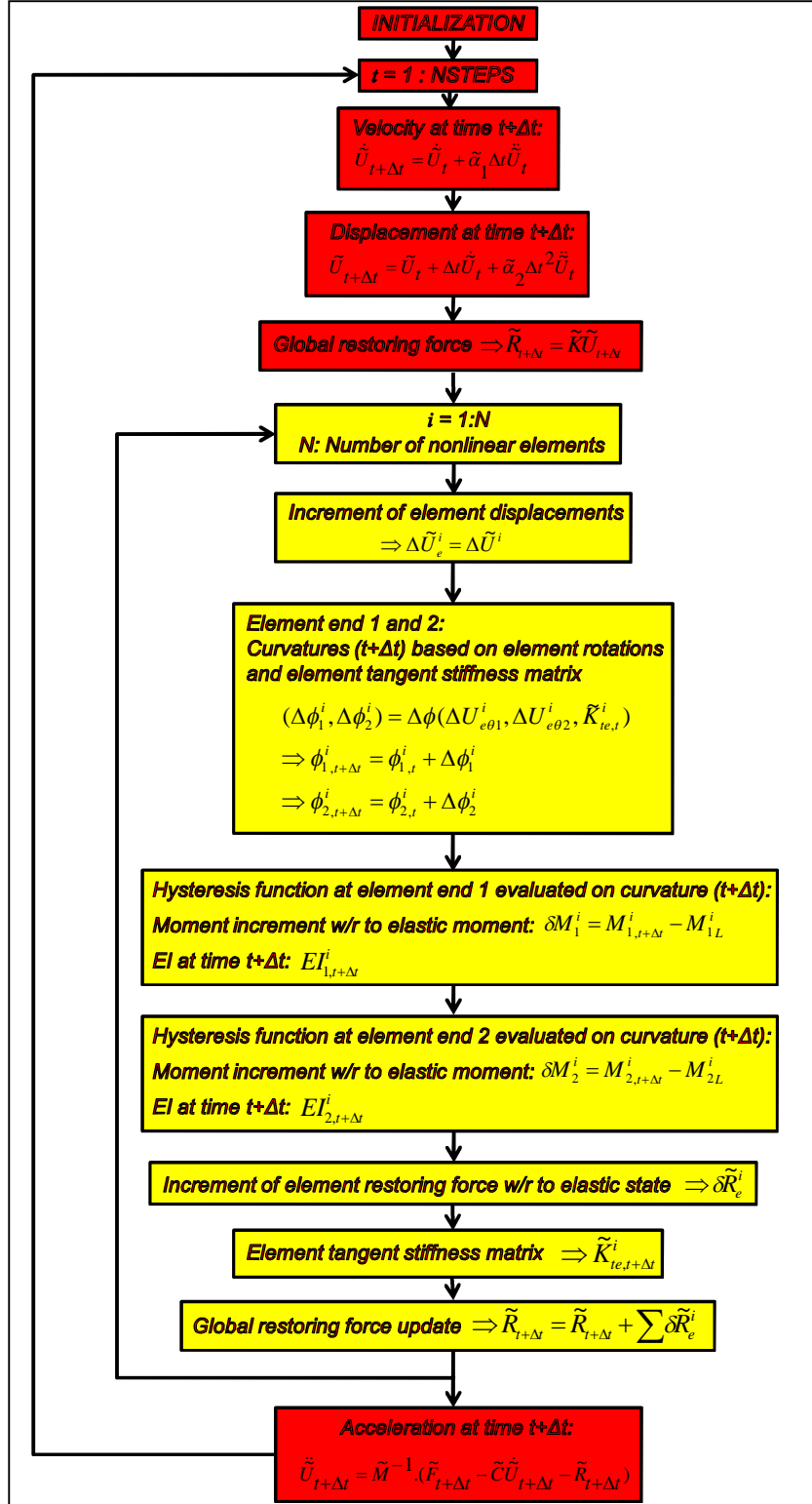


Figure 2.15: Flow diagram for executable *RT_F2D_2*

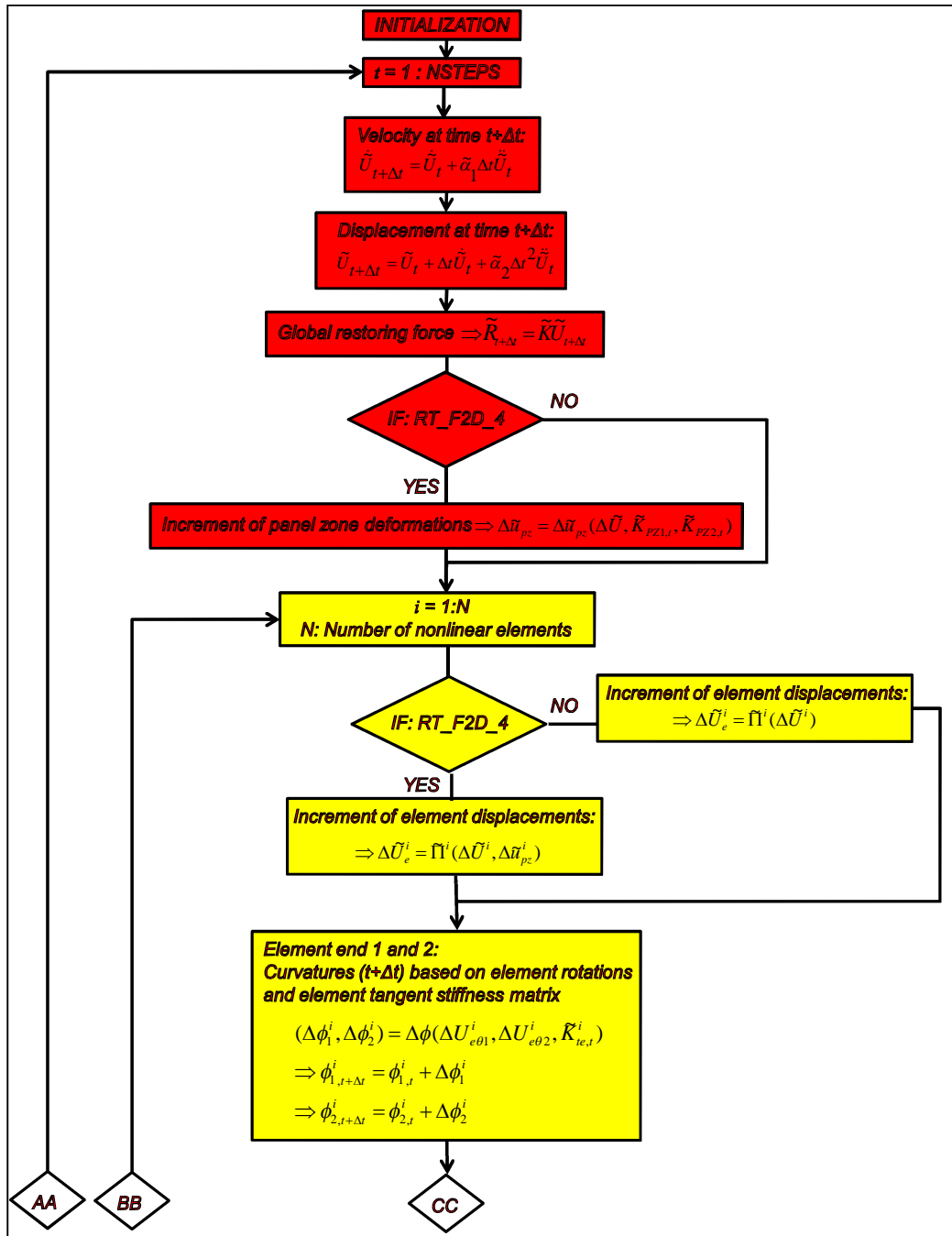


Figure 2.16: Flow diagram for executable *RT_F2D_3* and *RT_F2D_4* (First part)

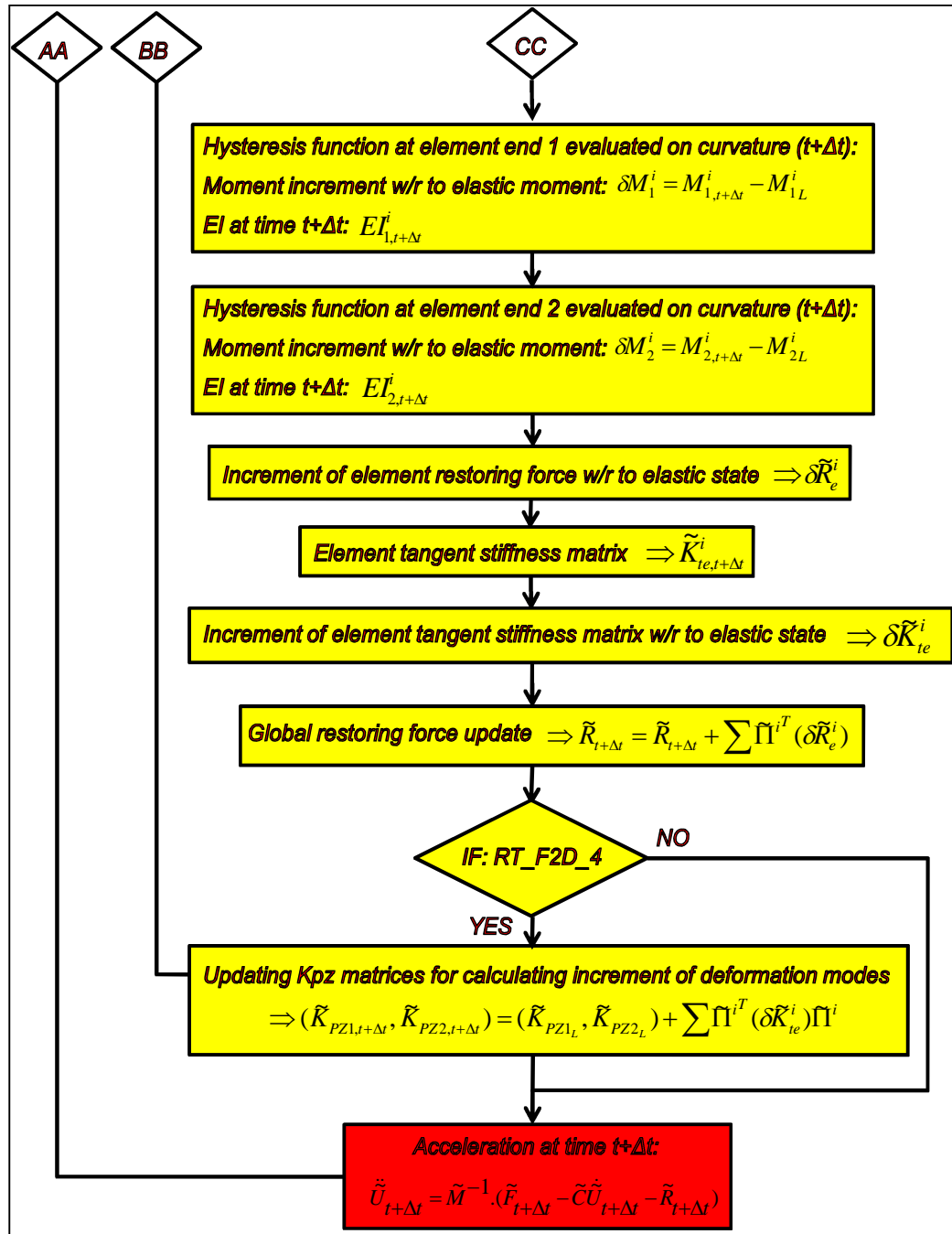


Figure 2.17: Flow diagram for executable *RT_F2D_3* and *RT_F2D_4* (Second part)

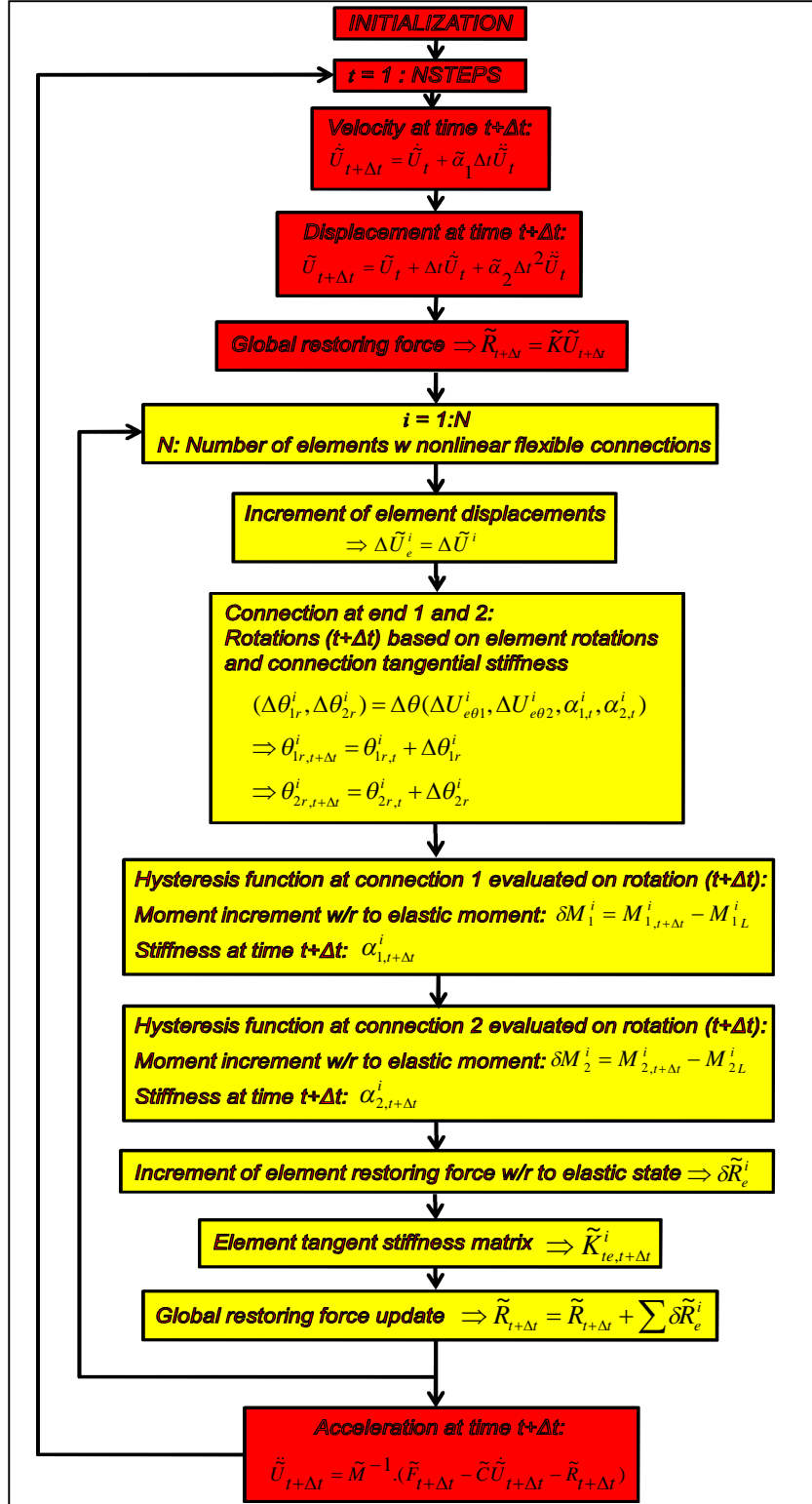


Figure 2.18: Flow diagram for executable *RT_F2D_5*

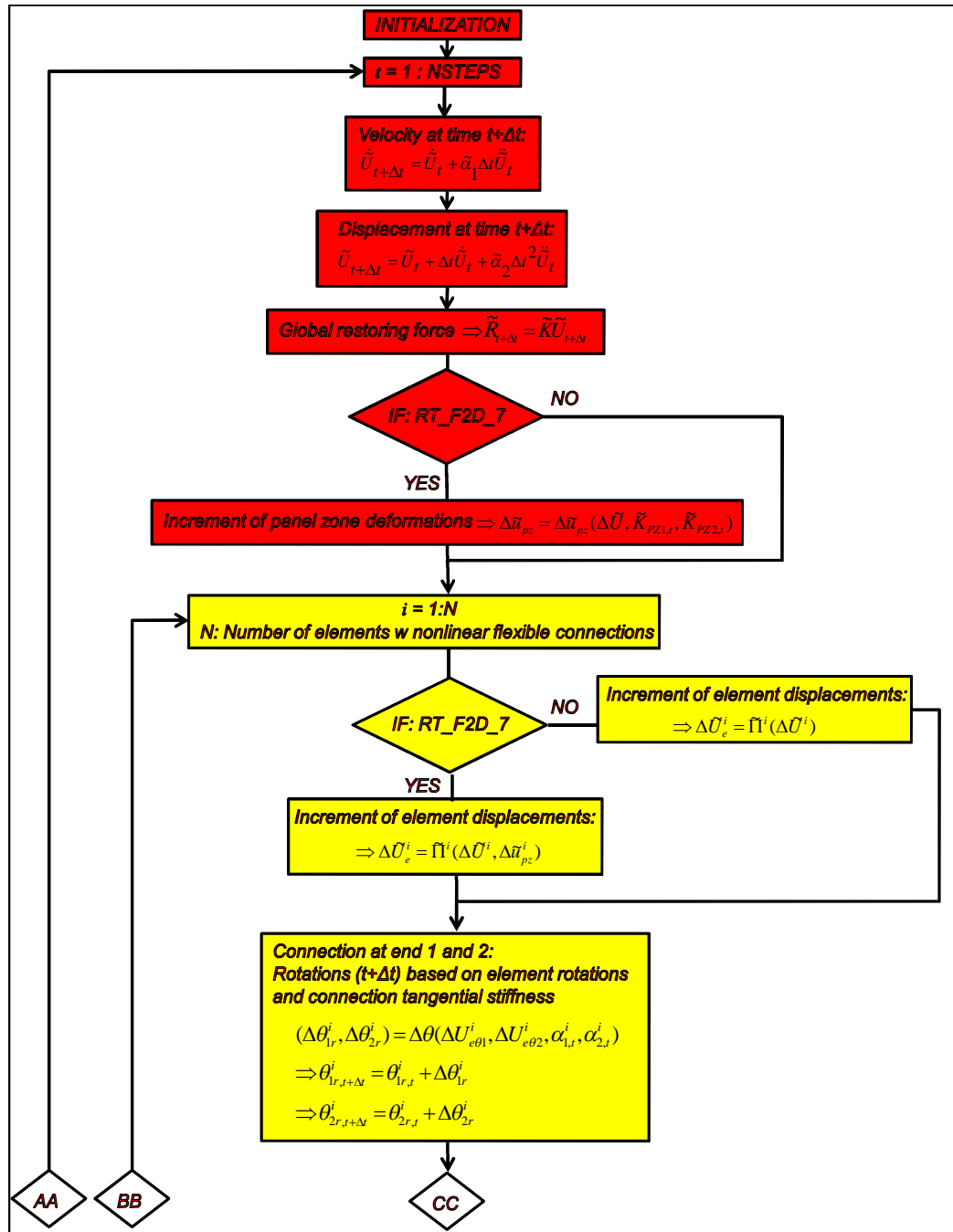


Figure 2.19: Flow diagram for executable *RT_F2D_6* and *RT_F2D_7* (First part)

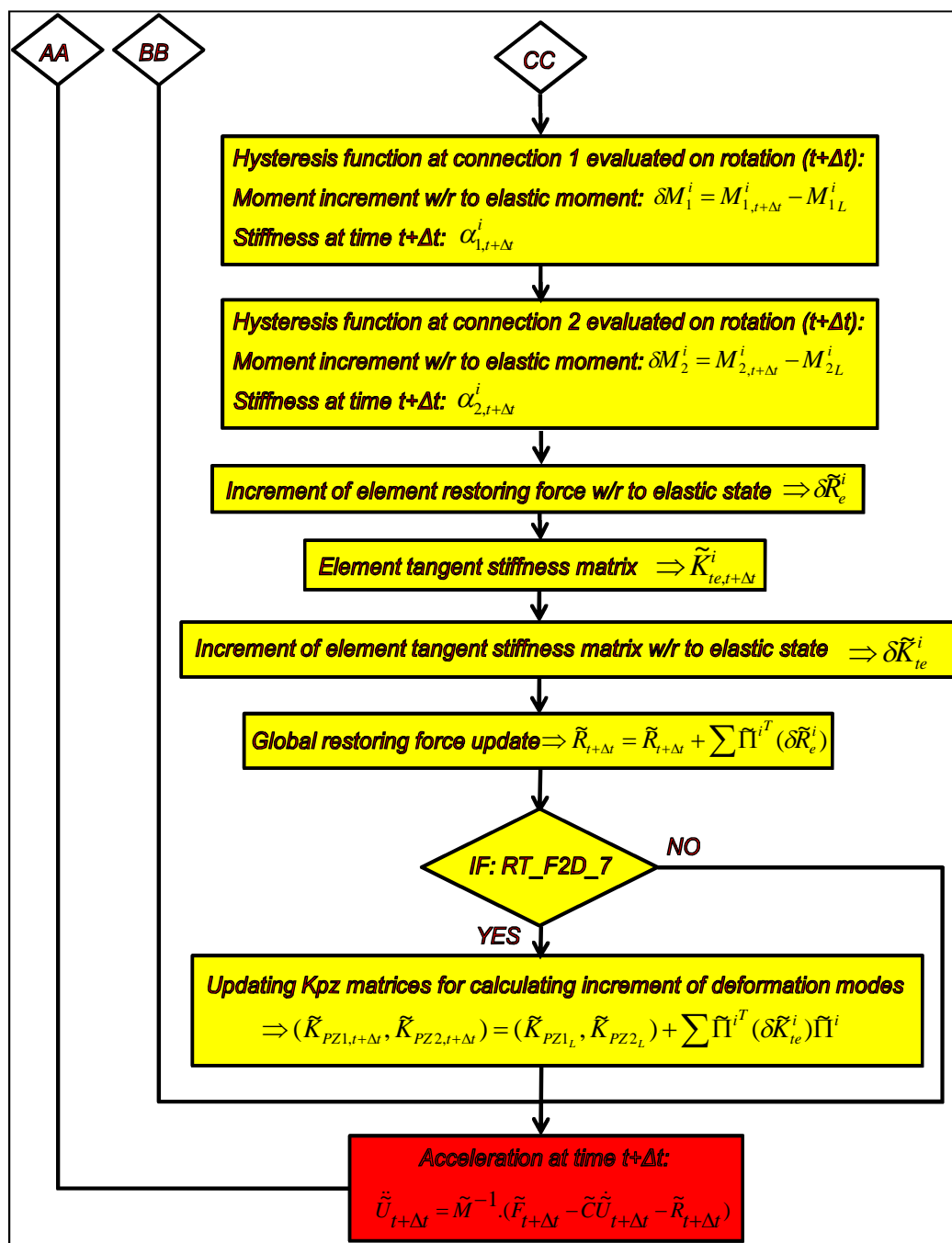


Figure 2.20: Flow diagram for executable *RT_F2D_6* and *RT_F2D_7* (Second part)

CHAPTER 3. NUMERICAL EVALUATION

The real-time execution and dynamic analysis capabilities offered by the proposed RT-Frame2D computational platform are evaluated in this chapter. Two different investigations are proposed for such evaluation herein. The first investigation focuses on the capabilities of the computational platform regarding real-time execution. Several structural configurations with an increasing number of DOF and nonlinear elements are evaluated within this investigation. The second investigation considers a qualitative comparison of the global dynamic response calculated with the RT-Frame2D and that calculated with the open source simulation package *OpenSEES*. Different analysis scenarios are performed for such comparisons.

3.1 Evaluating real-time execution capabilities

The real-time execution capabilities achievable by RT-Frame2D must be assessed. This evaluation is accomplished by measuring the average Task Execution Time (TET) that is required to complete one integration step when solving the equations of motion. In a strict sense, the TET within a RTHS must also include the time to execute calculations associated with the actuator control algorithm and the data exchange between computational and experimental substructures. However, to isolate the execution capabilities of RT-Frame2D for examination, these additional tasks are not considered in this particular section. Additionally, the execution time associated with the computational substructure is dominant when the complexity of the computational model is large. Therefore, this evaluation considers the TET as the execution time incurred only by the computational substructure.

The evaluation is performed by recording the minimum, maximum and average TET values associated to the nonlinear dynamic analysis of models of several different structures when subjected to a ground motion record. Increments in both the number of nonlinear elements and the DOF are considered in each model evaluated so that the variability in the resulting TET measurement can be studied. The N-S component recorded at the Imperial Valley Irrigation District substation in *El Centro*, California, during the Imperial Valley, California earthquake of May 18, 1940 is selected as the ground motion record for all cases. Six two dimensional structural models are proposed for the evaluation: a one-story one-bay frame structure: Model 1, a three-story one-bay frame structure: Model 2, a three-story four-bay frame structure: Model 3, a four-story four-bay: Model 4, a nine-story five-bay: Model 5, and a twenty-story five-bay: Model 6.

Structural Model 1, Model 2 and Model 4 have been designed by the Lehigh University (Bethlehem, PA) research team as a part of the NEESR research project *Performance-Based Design and Real-time, Large-scale Simulation to Enable Implementation of Advanced Damping Systems*. These structures represent extractions and scaled versions of prototype moment resisting frames (MRF) that belong to typical office buildings located upon stiff soil in Los Angeles, California. Moreover, Model 4 is designed to have a damped braced frame (DBF) to hold damper devices and uses a lean-on column to account for second order effects, as depicted in Figure 3.4. Rigid diaphragm constraints are imposed among translational DOF associated to Model 4 components ensuring equal lateral displacement and connectivity among them. Layouts for structural Model 1, Model 2 and Model 4 showing member sections are depicted in Figure 3.1, Figure 3.2 and Figure 3.4, respectively.

Structural Model 3, Model 5 and Model 6 were designed by *Brandow & Johnston Associates* for the SAC Phase II Steel Project (SAC Steel project: <http://quiver.eerc.berkeley.edu:8080>). These structures represent moment resisting frames of buildings that exemplify typical low, medium and high-rise buildings in Los Angeles, California. A layout for structural Model 3 showing member sections is also

depicted in Figure 3.3. Only general views of structural configurations for Model 5 and Model 6 are depicted in Figure 3.5 and Figure 3.6, respectively, due to their large size. Further details such as member sections and geometry definition of these models can be found at the SAC Steel project website (SAC Steel project: <http://quiver.eerc.berkeley.edu:8080>) and Ohtori et al. (2004).

To maintain consistency through the evaluation, displacement, velocity and acceleration records at each floor of the structural models are set to be simulation outputs during the analysis. Furthermore, only beam elements are considered as nonlinear elements. Therefore, Model 4 is slightly modified by adding beam elements to connect the MRF, DBF and lean-on column components and maintain consistency in the evaluation process. These beam elements are defined with the same member sections of the DBF beam elements, i.e. W10x30. Moreover, DBF beam elements with moment releases are replaced with moment resisting elements so that nonlinear flexural behavior is considered for all Model 4 beam elements.

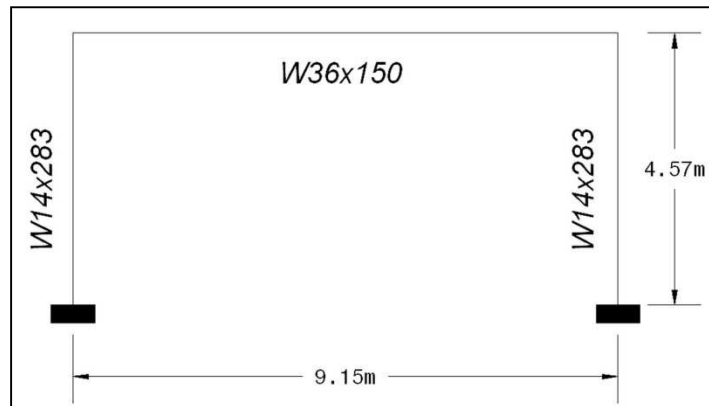


Figure 3.1: Model 1 in RT execution evaluation

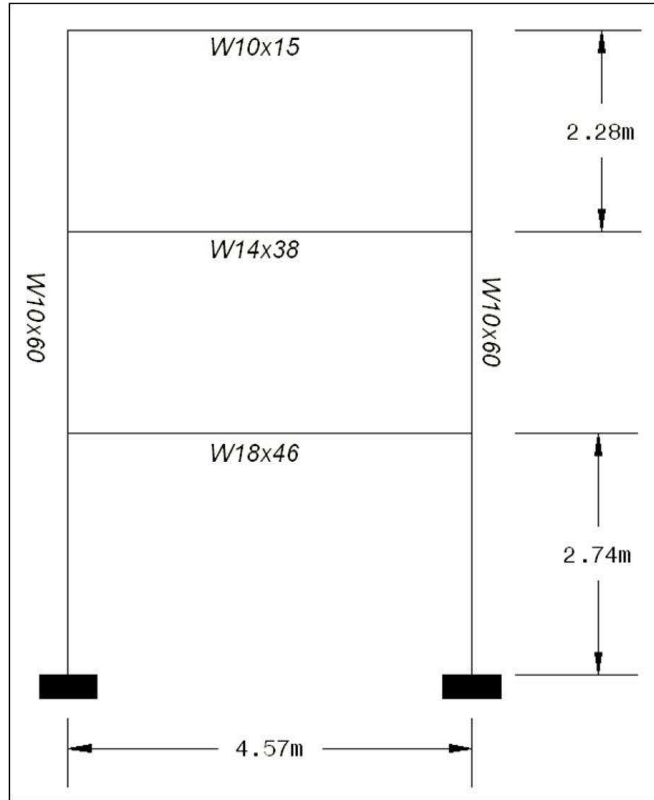


Figure 3.2: Model 2 in RT execution evaluation

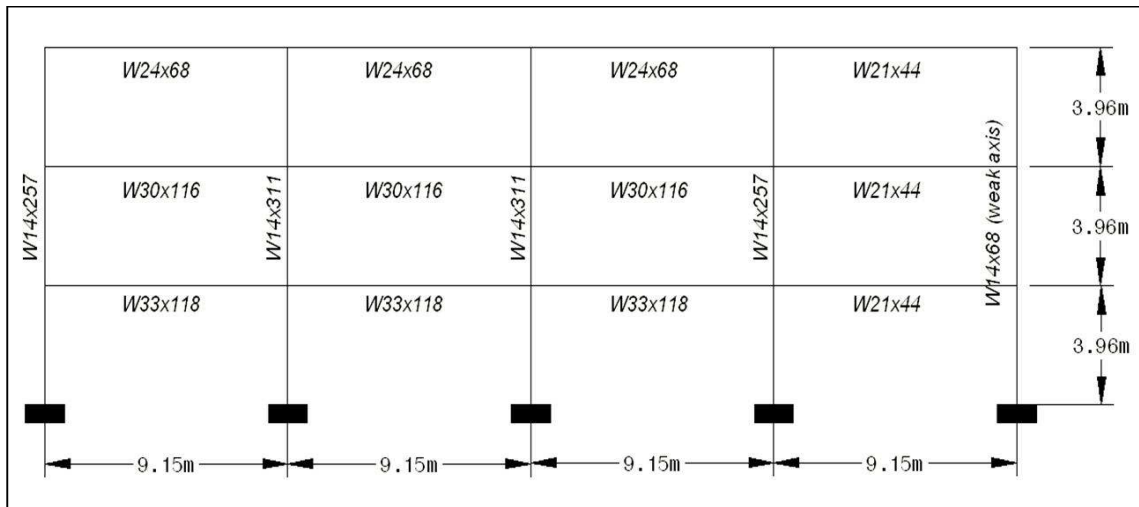


Figure 3.3: Model 3 in RT execution evaluation

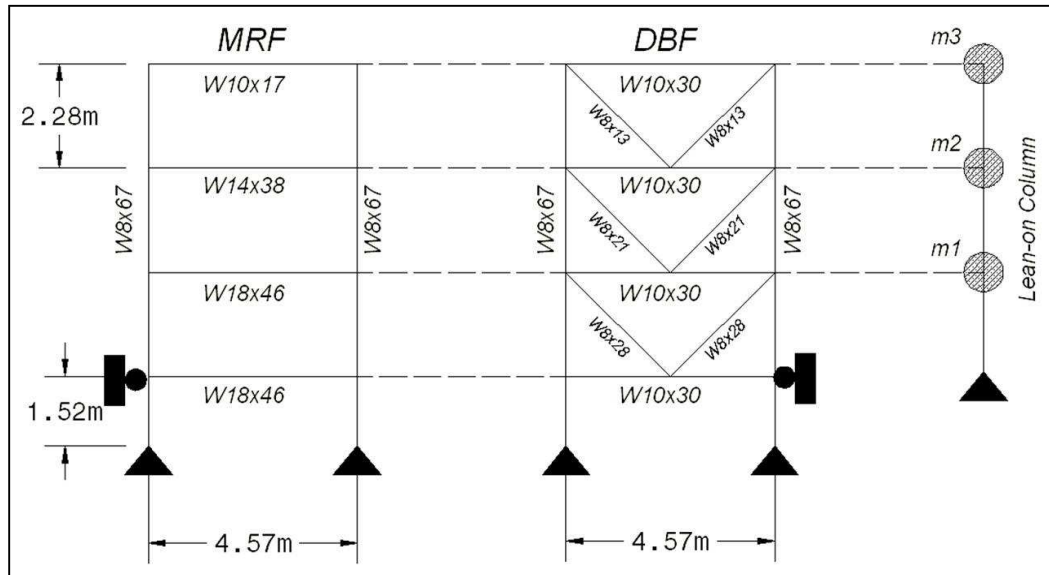


Figure 3.4: Model 4 in RT execution evaluation

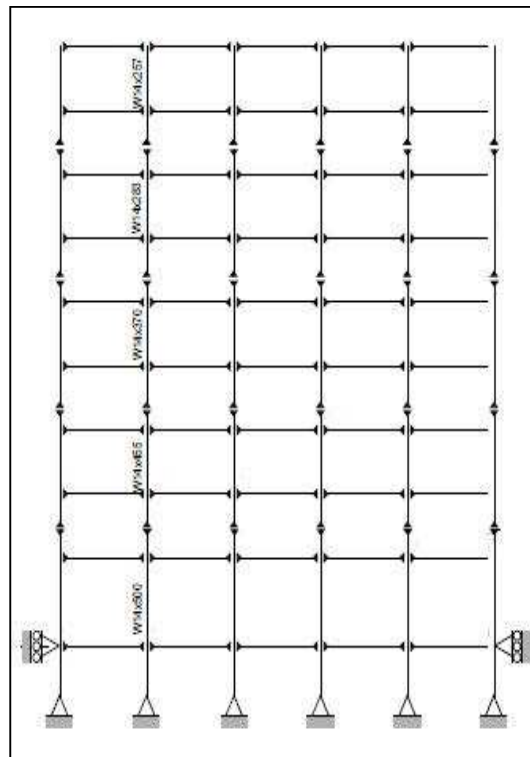


Figure 3.5: Model 5 in RT execution evaluation (after Ohtori et al., 2004)

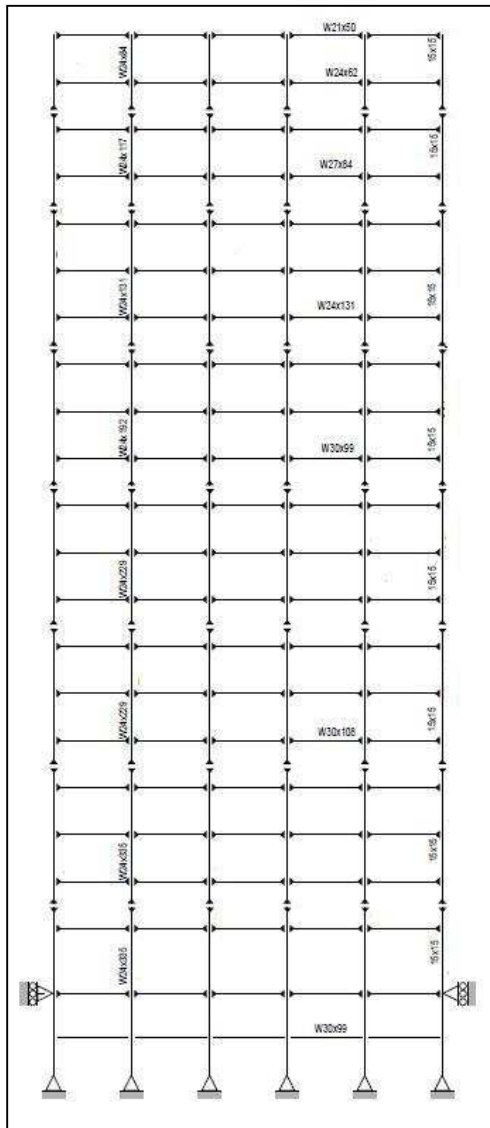


Figure 3.6: Model 6 in RT execution evaluation (after Ohtori et al., 2004)

Table 3.1 shows the number of DOF that are considered in each of the structural models. Each of the structural models is evaluated using the associated RT-Frame2D executable codes (*RT_F2D_1* ~ *RT_F2D_7*) that were introduced in Chapter 2. Modeling considerations for these executable codes were explained in Section 2.11. The *MATLAB/Real-Time Workshop* along with the high-performance *Speedgoat/xPC* real-time processor system is used to evaluate each scenario under real-time processing

conditions. As will be explained in Chapter 4, *Speedgoat/xPC* is an advanced real-time target kernel that is configured with an optimized state-of-the-art Core i5 3.6GHz processor for the processing of high-intense numerically-demanding computational models under real-time conditions. Once the input parameters for definition of the computational models are loaded within the *MATLAB/workspace*, a real-time customized executable version of the code is generated and compiled. This version is then downloaded to the *Speedgoat* target machine for real-time execution.

Table 3.1: Number of DOF at each model

<i>Model</i>	<i>NDOF</i>
Model 1	12
Model 2	24
Model 3	60
Model 4	84
Model 5	198
Model 6	414

As a result, the evaluation plan consists of 42 independent analyses, from which minimum, maximum and average TET values are recorded and presented in Table 3.2 to Table 3.7. Additionally, each table provides the corresponding allowed maximum execution frequency (F_s) achievable with each model. F_s is calculated as the inverse value of the average TET. It must be emphasized that each of the 42 analyzes were performed several times to test their degree of repeatability. Real-time processing performance is defined by confirming that the recorded F_s values are greater than a reference value $F_{s,r}$. 1024 Hz is selected for $F_{s,r}$. This value is frequently used within the RTHS community as an appropriate choice to meet the needs with respect to both computational time allowance for most reasonable well-sized structures, and guarantee enough and continuous smooth motion during the RTHS execution.

As observed, F_s values greater than F_{s_r} are achieved for evaluation models 1 ~ 4 using all of the executable versions. Model 5 is able to surpass F_{s_r} for executable versions RT_F2D_2,3,5,6, but not for RT_F2D_1,4 and 7. Model 6 cannot be simulated using the reference F_{s_r} value for any of the executable versions. Reasons for not achieving the reference F_{s_r} value may be related to the number of DOF, the extent of nonlinear response, the integration scheme and the CPU that is utilized to perform the analysis. Moreover, storage capacity for variables and the amount of code that need to be generated and compiled for execution is also considered of relevant importance. The last is more evident by checking the considerable smaller F_s values for executable versions RT_F2D_4,7 in which deformable panel zone elements are considered with respect to the other executables. This difference becomes even worse when the increment in the number of DOF is greater. For instance, the F_s value associated to executables RT_F2D_4,7 are approximately 45% and 500% slower than F_s values recorded for RT_F2D_2,3,5,6 executables in Model 1 and Model 5, respectively. This loss in speed is mainly attributable to the large matrix storage and operation requirements that are involved in the updating process of panel zone deformation modes, as shown in Figure 2.16 and Figure 2.19. More evidence of this hypothesis is observed with Model 6. Here, the generation and compilation of real-time executables RT_F2D_4,7 cannot be even completed due to the large size of the matrices that need to be saved for updating the deformation modes. Another observation is the transition from a smaller to a larger F_s value in the executable RT_F2D_2 with respect to F_s value in RT_F2D_1. As explained in Chapter 2, these two versions differ only in the type of integration scheme used. The RT_F2D_1 uses the unconditionally-implicit Newmark-beta integration scheme, while the RT_F2D_2 uses the unconditionally-explicit CR integration scheme. Therefore, the former requires the inversion of the global stiffness matrix for solving the equation of motion while the latter does not. This difference in the F_s value becomes more evident when the increment in the number of DOF is greater. For example, F_s values of approximately 60% and 235% faster than those reported for executable RT_F2D_1 can be achieved by executable RT_F2D_2 in Model 5 and Model 6, respectively.

Table 3.2: TET values for Model 1

<i>Model 1</i>	<i>min TET</i>	<i>Avg TET</i>	<i>max TET</i>	<i>Fs(Hz)</i>
<i>RT_F2D_1</i>	4.000e-06	4.000e-06	4.000e-06	250000
<i>RT_F2D_2</i>	4.000e-06	4.393e-06	5.000e-06	228000
<i>RT_F2D_3</i>	4.000e-06	4.350e-06	5.000e-06	230000
<i>RT_F2D_4</i>	6.000e-06	6.326e-06	7.000e-06	158000
<i>RT_F2D_5</i>	4.000e-06	4.400e-06	5.000e-06	227000
<i>RT_F2D_6</i>	4.000e-06	4.384e-06	5.000e-06	228000
<i>RT_F2D_7</i>	6.000e-06	6.469e-06	7.000e-06	155000

Table 3.3: TET values for Model 2

<i>Model 2</i>	<i>min TET</i>	<i>Avg TET</i>	<i>max TET</i>	<i>Fs(Hz)</i>
<i>RT_F2D_1</i>	1.600e-05	1.666e-05	1.700e-05	60000
<i>RT_F2D_2</i>	1.300e-05	1.376e-05	1.800e-05	72700
<i>RT_F2D_3</i>	1.300e-05	1.373e-05	1.400e-05	72800
<i>RT_F2D_4</i>	2.300e-05	2.455e-05	2.800e-05	40700
<i>RT_F2D_5</i>	1.300e-05	1.373e-05	1.400e-05	72800
<i>RT_F2D_6</i>	1.400e-05	1.400e-05	1.400e-05	71400
<i>RT_F2D_7</i>	2.400e-05	2.488e-05	2.900e-05	40200

Table 3.4: TET values for Model 3

<i>Model 3</i>	<i>min TET</i>	<i>Avg TET</i>	<i>max TET</i>	<i>Fs(Hz)</i>
<i>RT_F2D_1</i>	8.800e-05	9.207e-05	9.600e-05	10900
<i>RT_F2D_2</i>	6.800e-05	6.849e-05	7.200e-05	14600
<i>RT_F2D_3</i>	6.894e-05	6.900e-05	7.300e-05	14500
<i>RT_F2D_4</i>	1.340e-04	1.415e-04	1.450e-04	7070
<i>RT_F2D_5</i>	6.700e-05	6.746e-05	7.100e-05	14800
<i>RT_F2D_6</i>	6.800e-05	6.836e-05	7.300e-05	14600
<i>RT_F2D_7</i>	1.350e-04	1.426e-04	1.460e-04	7010

Table 3.5: TET values for Model 4

<i>Model 4</i>	<i>min TET</i>	<i>Avg TET</i>	<i>max TET</i>	<i>Fs(Hz)</i>
<i>RT_F2D_1</i>	1.940e-04	1.968e-04	2.020e-04	5080
<i>RT_F2D_2</i>	1.260e-04	1.270e-04	1.310e-04	7870
<i>RT_F2D_3</i>	1.260e-04	1.267e-04	1.300e-04	7890
<i>RT_F2D_4</i>	2.540e-04	2.655e-04	2.690e-04	3720
<i>RT_F2D_5</i>	1.240e-04	1.251e-04	1.280e-04	7990
<i>RT_F2D_6</i>	1.240e-04	1.254e-04	1.300e-04	7970
<i>RT_F2D_7</i>	2.550e-04	2.689e-04	2.740e-04	3710

Table 3.6: TET values for Model 5

<i>Model 5</i>	<i>min TET</i>	<i>Avg TET</i>	<i>max TET</i>	<i>Fs(Hz)</i>
<i>RT_F2D_1</i>	1.057e-03	1.070e-03	1.075e-03	935
<i>RT_F2D_2</i>	6.680e-04	6.704e-04	6.730e-04	1490
<i>RT_F2D_3</i>	6.690e-04	6.733e-04	6.780e-04	1490
<i>RT_F2D_4</i>	3.243e-03	3.345e-03	3.349e-03	299
<i>RT_F2D_5</i>	6.670e-04	6.701e-04	6.730e-04	1490
<i>RT_F2D_6</i>	6.710e-04	6.741e-04	6.780e-04	1480
<i>RT_F2D_7</i>	3.238e-03	3.340e-03	3.347e-03	299

Table 3.7: TET values for Model 6

<i>Model 6</i>	<i>min TET</i>	<i>Avg TET</i>	<i>max TET</i>	<i>Fs(Hz)</i>
<i>RT_F2D_1</i>	7.328e-03	7.338e-03	7.372e-03	136
<i>RT_F2D_2</i>	3.129e-03	3.134e-03	3.139e-03	319
<i>RT_F2D_3</i>	3.048e-03	3.048e-03	3.055e-03	328
<i>RT_F2D_4</i>	-	-	-	-
<i>RT_F2D_5</i>	3.035e-03	3.043e-03	3.049e-03	329
<i>RT_F2D_6</i>	3.043e-03	3.048e-03	3.054e-03	328
<i>RT_F2D_7</i>	-	-	-	-

Further evaluation of cases in which the only change is a modification in the number of outputs indicates that the number of outputs does not noticeably affect the achievable F_s values.

A plot showing approximate functional dependencies between the numbers of DOF at each evaluation model versus the corresponding F_s values that each RT-Frame2D executable is able to achieve are shown in Figure 3.7. A zoomed view including only the 2000 Hz bandwidth is included below for clarity and further evaluation. As expected, the execution performance for all of the executables shows an asymptotic behavior with respect to “zero” number of DOF while the F_s value increases. Another interesting observation is the approximately equal functional pattern shown between executables RT_F2D_4,7 and among executables RT_F2D_2,3,5,6. Moreover and as expected by previous discussions, executables RT_F2D_4,7 variation is always bounded by the executables RT_F2D_2,3,5,6 variation, i.e. executables RT_F2D_2,3,5,6 have a faster execution performance.

The approximate maximum number of DOF that each executable is able to achieve at the reference F_s , 1024 Hz value can be calculated from the plot below. These values are calculated from intersection points defined by the previous functions with a linear variation between definition points and the 1024 Hz abscissa, as shown in Figure 3.7. Number of DOF values of 201 is calculated for RT_F2D_1, 173 for executable RT_F2D_4,7 and 287 for executables RT_F2D_2,3,5,6. It must be emphasized that these calculated values are average values and should not be considered as strict norm values. Certain variability could be observed depending on some special modeling and analysis conditions not included in the evaluation process. However and due to the consistency in the evaluation process, they are still considered as fair indicators and can be used as good reference regarding the maximum number of DOF that can be achieved by the proposed computational platform under real-time execution conditions.

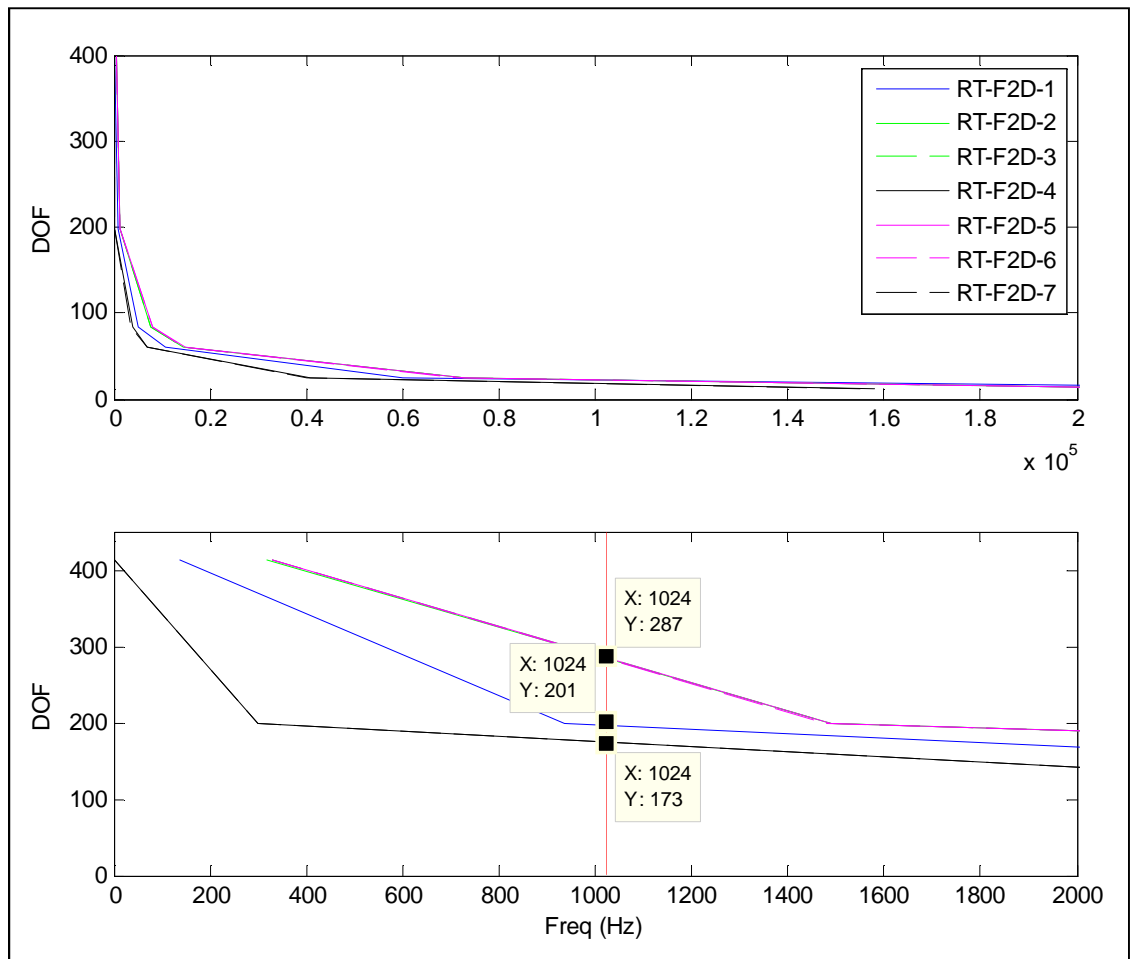


Figure 3.7: Real-time execution performance

3.2 RT-Frame2D numerical evaluation

In this section, an evaluation of the nonlinear dynamic analysis capabilities of the proposed computational platform is conducted through a qualitative comparison between RT-Frame2D and *OpenSEES: Open System for Earthquake Engineering Simulation* (Mckenna and Fenves, 2002; Mckenna et al., 2002). Although *OpenSEES* does not have the identical modeling features as RT-Frame2D, it is considered the most appropriate

selection for comparison due to the growing interest shown by the earthquake research community in its use, as introduced in Chapter 1.

The evaluation is performed by comparing the global nonlinear dynamic response of several seismically-excited frame structures. A comparison of the hysteresis loops is also performed for some of the presented models. This comparison is only presented when modeling assumptions at element level are equal or close enough for both models. Five computational models are selected for evaluation. Computational Model 1 and Model 2 are constructed based on the three-story four-bay frame structure utilized in the previous section and shown in Figure 3.3. Computational Model 3 is constructed based on a five-story two-bay frame structure. This frame structure has been designed by the Lehigh University research team as a part of the NEESR research project *Performance-Based Design and Real-time, Large-scale Simulation to Enable Implementation of Advanced Damping Systems*. Computational Model 4 and Model 5 are constructed based on a three-story one-bay frame structure. These models are based on a frame specimen that has been designed at the Seismic Test Center in the School of Civil Engineering at Harbin Institute of Technology in China. This specimen has been the subject of several studies and is being currently tested as part of the research project *Large Scale Distributed Substructure Testing for Collapse-Resistance Evaluation of Buildings and Bridges*

RT-Frame2D computational Model 1 is constructed based on the geometry and member section configuration as shown in Figure 3.3. Mass values of $4.78e5$ kg and $5.17e5$ kg distributed over beam elements at the first/second and third floor, respectively, are used to assemble the global mass matrix. Damping global matrix is defined with a Rayleigh assumption yielding a fundamental damping ratio of 4%. Column members are defined with the *linear elastic beam-column element*. Beam members are defined with the *linear elastic beam-column element with nonlinear flexible connection* element offered in the RT-Frame2D element library. The modulus of elasticity for steel is selected as 29,000 ksi. Nonlinear flexible connections for the beam elements are defined with a bilinear moment-rotation hysteresis model based on a kinematic hardening assumption and a post

yielding ratio of 5%. W33x18 members are defined with a connection stiffness value of $10e8$ N/m and a yielding rotation of 0.0015 rad. W30x16 members are defined with a connection stiffness value of $8e8$ N/m and a yielding rotation of 0.0015 rad. W24x68 members are defined with a connection stiffness value of $5e8$ N/m and a yielding rotation of 0.001 rad. W21x44 members are defined with a connection stiffness value of $4e8$ N/m and a yielding rotation of 0.001 rad. Yielding moment values for flexible connections are calculated based on the previous information. Boundary conditions are defined as shown in Figure 3.3. The unconditionally-explicit CR integration scheme is used to solve the incremental equation of motion.

The *OpenSEES* version of computational Model 1 is constructed using the same geometry and section configuration of the previous RT-Frame2D model. Moreover, global mass and damping matrices are defined with the same assumptions. Column and beam members are defined with the *elasticBeamColumn* element using the same value of modulus of elasticity for steel as 29,000 ksi. Flexible connections are defined with the *zeroLength* element offered by the *OpenSEES* element library. The *uniaxialMaterial Hardening* function is used to define a bilinear moment-rotation hysteresis model with the same parameters used in the RT-Frame2D model. Therefore, only the kinematic hardening property is included. Boundary conditions are imposed with the same considerations as in the RT-Frame2D model. The unconditionally-implicit Newmark integrator scheme with constant acceleration is used to solve the incremental equation of motion. A Newton-Raphson nonlinear solver is adopted in conjunction with the previous integrator to guarantee convergence at each integration step.

Table 3.8 shows the natural frequencies at the three first modes calculated with RT-Frame2D and *OpenSEES*. No difference in the values is observed. Next, nonlinear dynamic analyses are performed by subjecting both computational models to a 100% intensity of the N-S component recorded at the Imperial Valley Irrigation District substation in *El Centro*, California, during the Imperial Valley, California earthquake of May 18, 1940. Both analyses are performed with a time step of $9.76e-04$ sec (1024 Hz)

for duration of 75 sec leading to output vectors of 76800 points. Time history records of the displacement and absolute acceleration calculated at each floor with both simulation platforms are plotted between Figure 3.8 and Figure 3.13. Only 50 sec of the responses is included for clarity. Additional plots showing records from 1 to 10 sec and from 25 to 35 sec are also included in a zoomed view. An excellent match is obtained between the responses of the two models.

Table 3.8: Natural frequencies comparison – Model 1

	<i>NF1 (Hz)</i>	<i>NF2 (Hz)</i>	<i>NF3(Hz)</i>
<i>RT-Frame2D</i>	0.933	2.962	5.694
<i>OpenSEES</i>	0.933	2.962	5.694

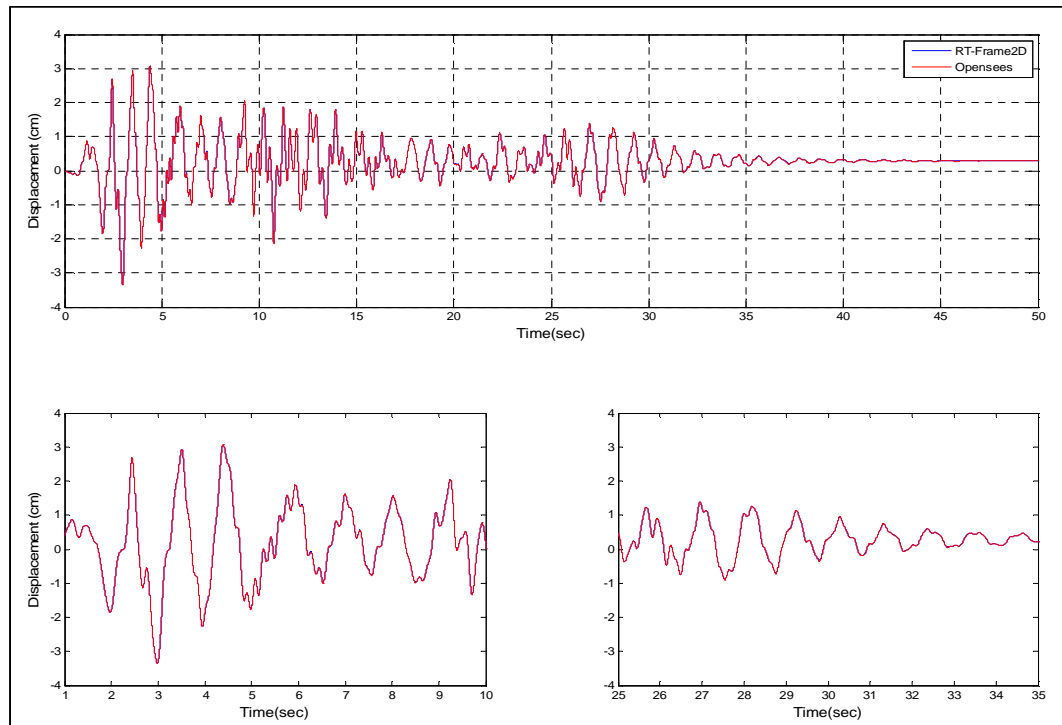


Figure 3.8: Displacement at floor 1 – Model 1

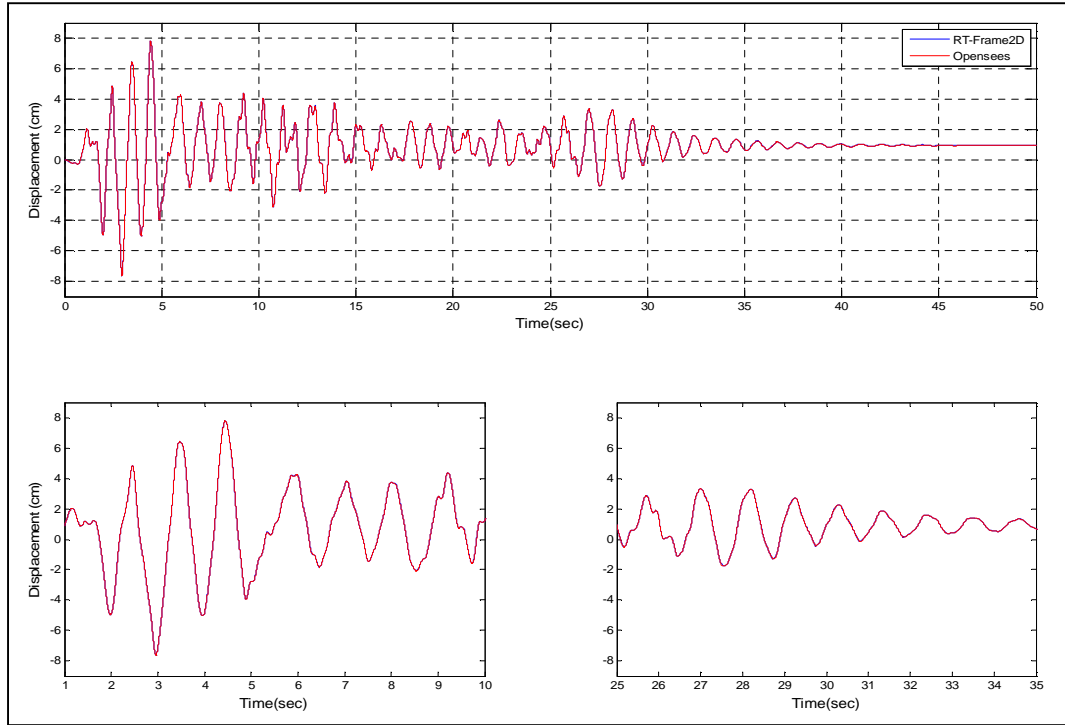


Figure 3.9: Displacement at floor 2 – Model 1

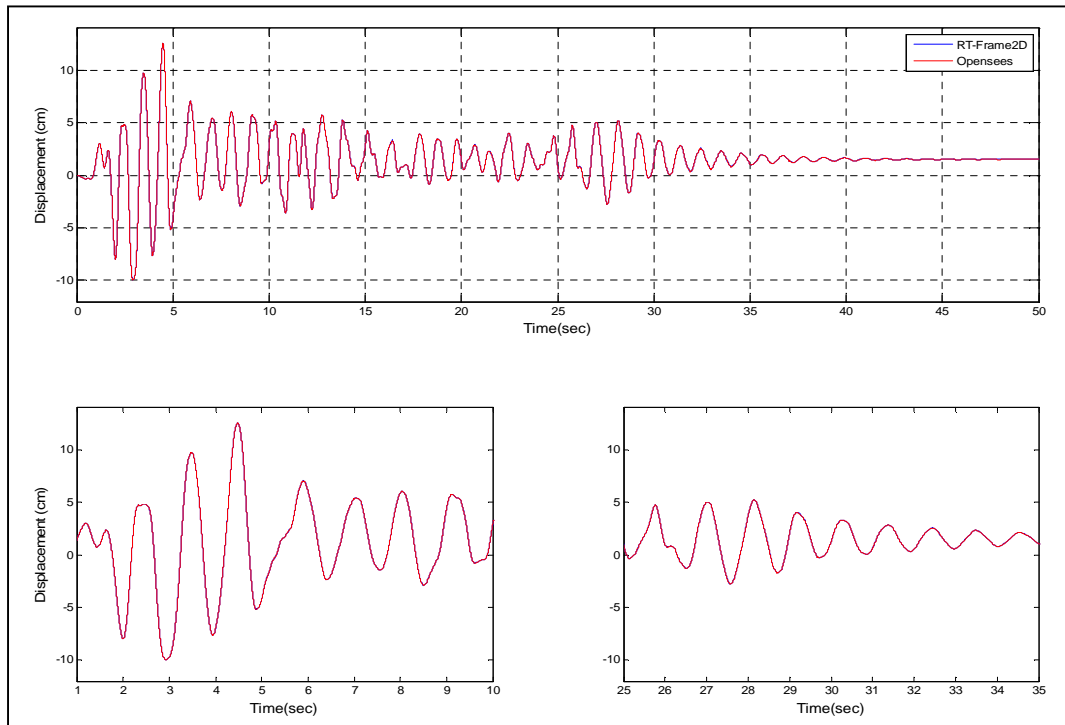


Figure 3.10: Displacement at floor 3 – Model 1

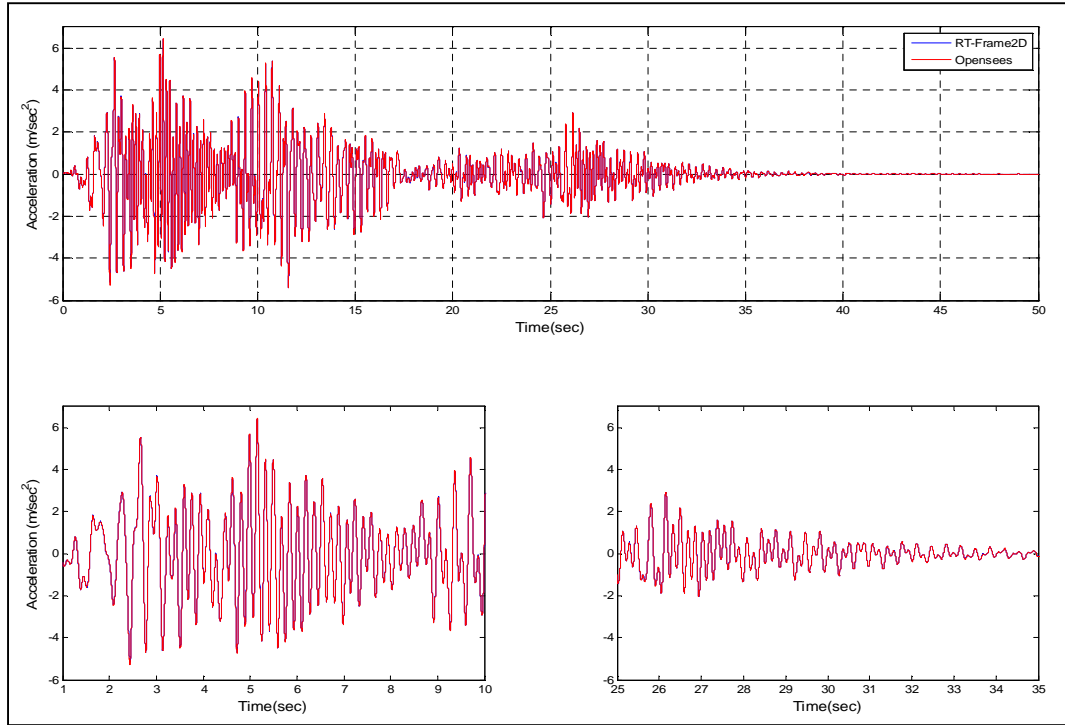


Figure 3.11: Absolute acceleration at floor 1 – Model 1

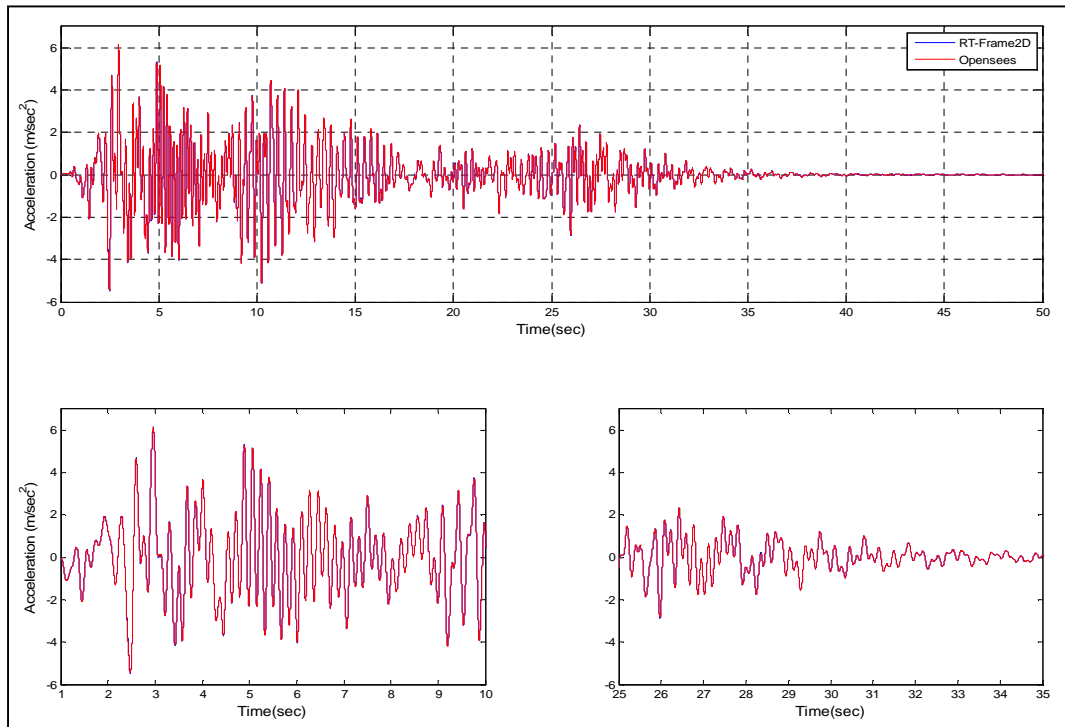


Figure 3.12: Absolute acceleration at floor 2 – Model 1

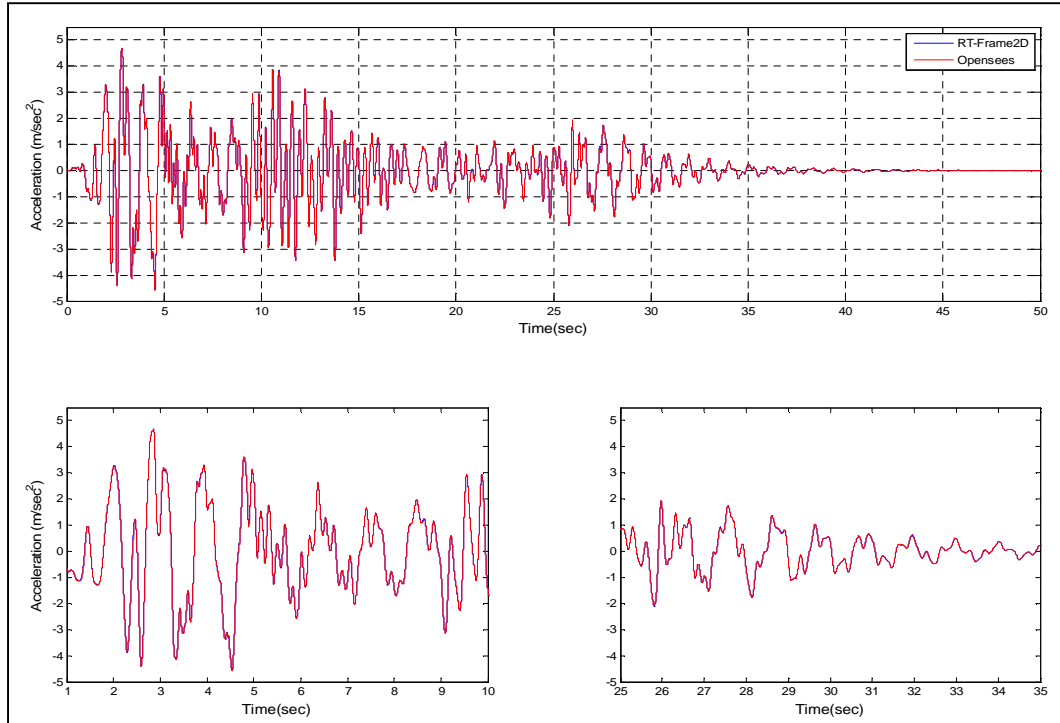


Figure 3.13: Absolute acceleration at floor 3 – Model 1

Comparison between hysteresis loops are shown in Figure 3.14. These hysteresis loops belong to the left-end flexible connection of the W33x118 member located at the first-floor and first-bay and the right-end flexible connection of the W24x68 member located at the third-floor and second-bay. Note that a fair comparison of hysteresis loops can be achieved in this model because all nonlinearity is concentrated only at the zero-length rotational springs representing the flexible connections and where the same bilinear moment-rotation hysteresis model has been adopted. Therefore, excellent match between both hysteresis loops with negligible differences due to the different integration schemes is observed. However, the RT-Frame2D computational model shows an advantage over the *OpenSEES* model because it only requires for definition the same number of DOF as a model with no connections, i.e. without zero-length rotational springs. Conversely the *zeroLength* element from *OpenSEES* requires two nodes for definition at the same location which significantly increase both the number of DOF and the execution time when compared to the RT-Frame2D model.

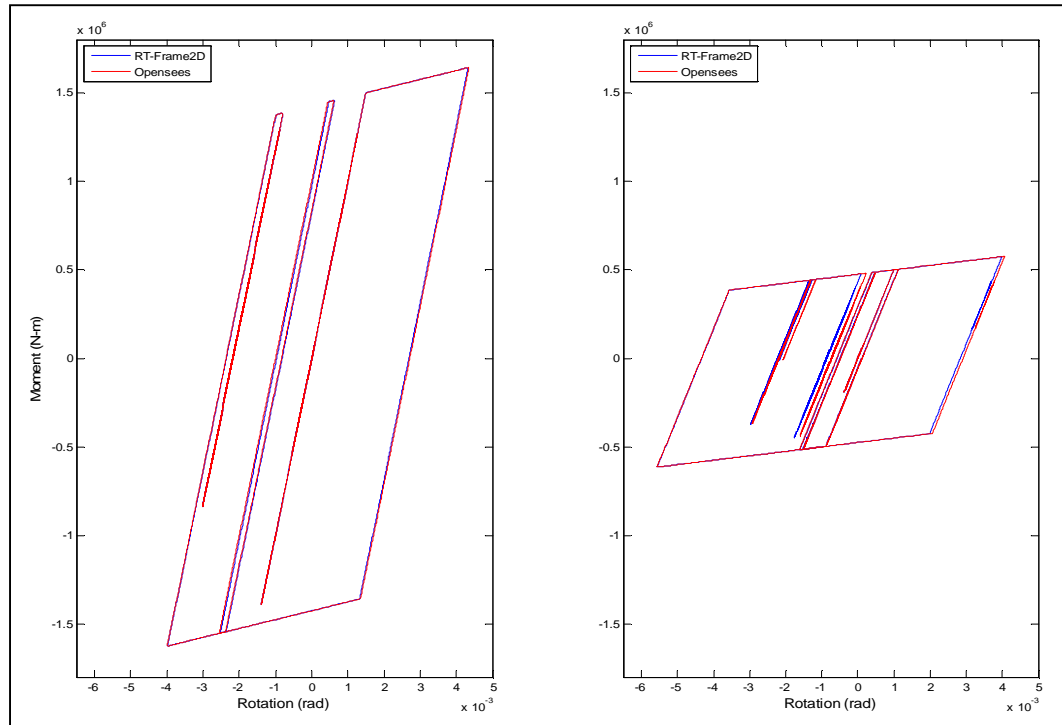


Figure 3.14: Hysteresis loops - Model 1

The geometry and member sections for the RT-Frame2D computational Model 2 are defined with the same values as in Model 1. Moreover, mass and damping properties are defined with the same assumptions. Column members are defined with the *linear elastic beam-column element*. Beam members are defined with the *nonlinear beam-column element* using the concentrated plasticity option offered by the RT-Frame2D element library. The modulus of elasticity for steel is selected as 29,000 ksi. Flexural behavior at sections of the nonlinear beam elements are defined with a bilinear moment-curvature hysteresis model based on a kinematic hardening assumption and a post yielding ratio of 2.5%. Yielding moments and corresponding yielding curvatures are calculated based on the material and flexural section properties for each member. Boundary conditions are imposed as shown in Figure 3.3. Constraints are imposed for horizontal translational DOF at each floor level ensuring a rigid diaphragm behavior. The unconditionally-explicit CR integration scheme is used to solve the incremental equation of motion.

The *OpenSEES* computational Model 2 is constructed using the same geometry and section configuration of the RT-Frame2D model. Global mass and damping matrices are defined with the same assumptions. Column members are defined with the *elasticBeamColumn* element. Beam members are defined with the *beamWithHinges* element-type (Scott and Fenves, 2006) offered by the *OpenSEES* nonlinear beam-column element library. This element restricts the plastic hinge development to a specified range at each of the member ends. Although it does not share the same characteristics as the nonlinear beam-column element in RT-Frame2D, it is considered the closest available option for purposes of this comparison. The *uniaxialMaterial Steel01* function is used to define a bilinear moment-curvature hysteresis model with the same parameters as the RT-Frame2D model. Therefore, the kinematic hardening property is only included. Flexural behavior at hinge sections for the nonlinear beam elements are defined with the hysteresis model using the *section Uniaxial* function. Boundary conditions and constraints are also imposed with the same considerations as in the RT-Frame2D model. The unconditionally-implicit Newmark integrator scheme with constant acceleration in conjunction with the Newton-Raphson nonlinear solver is used to solve the incremental equation of motion and enforce convergence.

Table 3.9 shows same values for the three first natural frequencies calculated with RT-Frame2D and *OpenSEES*.

Table 3.9: Natural frequencies comparison – Model 2

	<i>NF1 (Hz)</i>	<i>NF2 (Hz)</i>	<i>NF3(Hz)</i>
<i>RT-Frame2D</i>	1.006	3.098	5.846
<i>OpenSEES</i>	1.006	3.098	5.846

Next, nonlinear dynamic analyses are performed by subjecting both computational models to a 150% intensity of the N-S component recorded at the Imperial Valley Irrigation District substation in *El Centro*, California, during the Imperial Valley, California earthquake of May 18, 1940. Both analyses are performed with a time step of $9.76e-04$ sec (1024 Hz) for duration of 80 sec leading to output vectors of 81921 points. Time history records of the displacement and absolute acceleration calculated at each floor with both simulation platforms are plotted between Figure 3.15 and Figure 3.20. Only 50 sec of the response is included for clarity. Additional plots showing records from 1 to 10 sec and from 25 to 35 sec are included in a zoomed view. An excellent match between the two responses is observed.

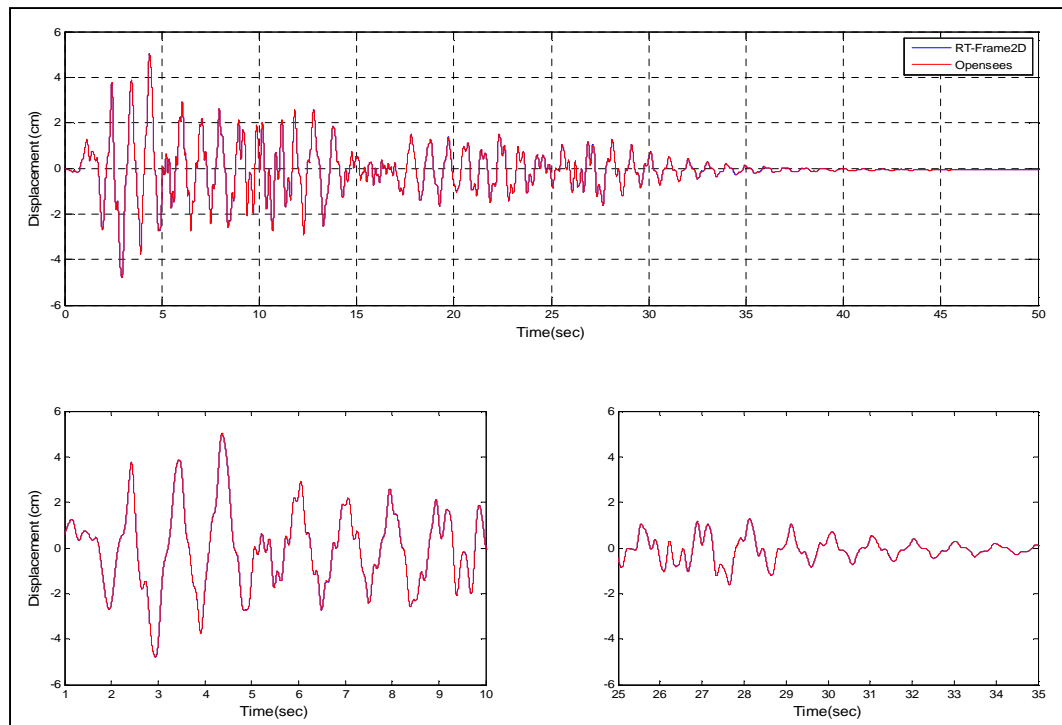


Figure 3.15: Displacement at floor 1 – Model 2

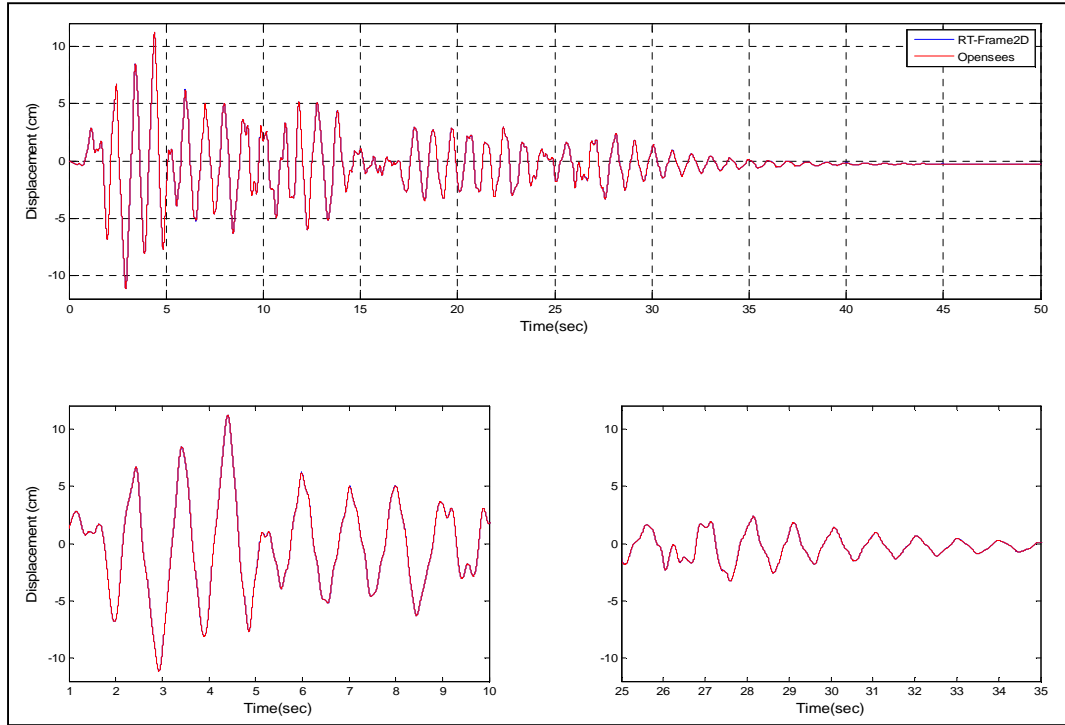


Figure 3.16: Displacement at floor 2 – Model 2

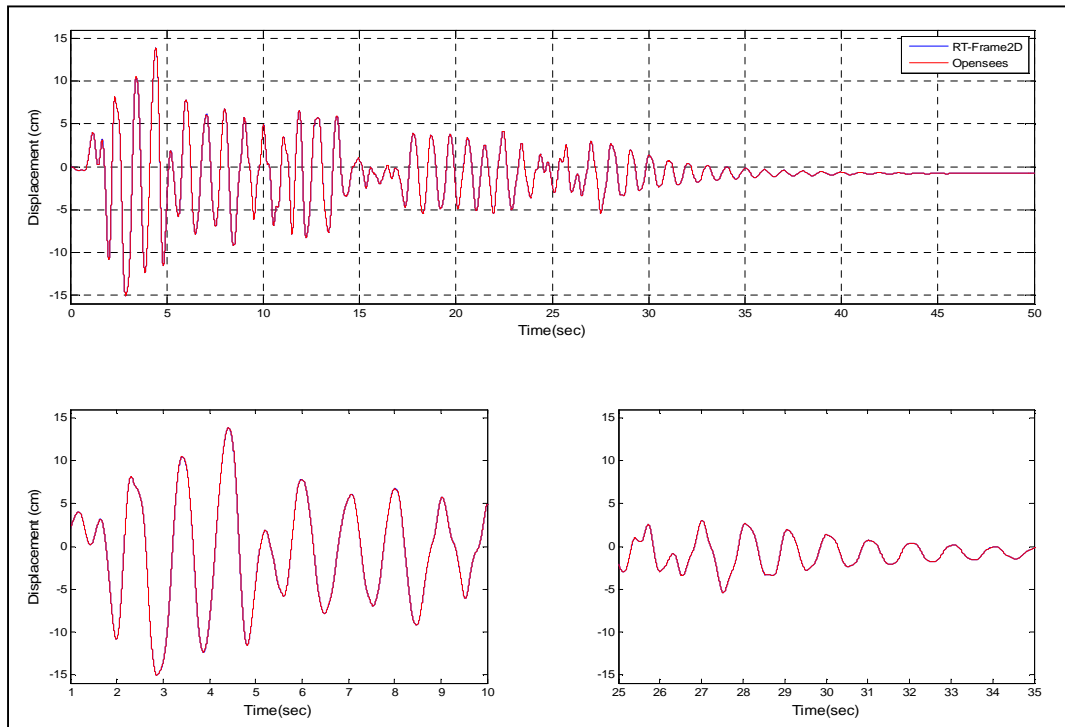


Figure 3.17: Displacement at floor 3 – Model 2

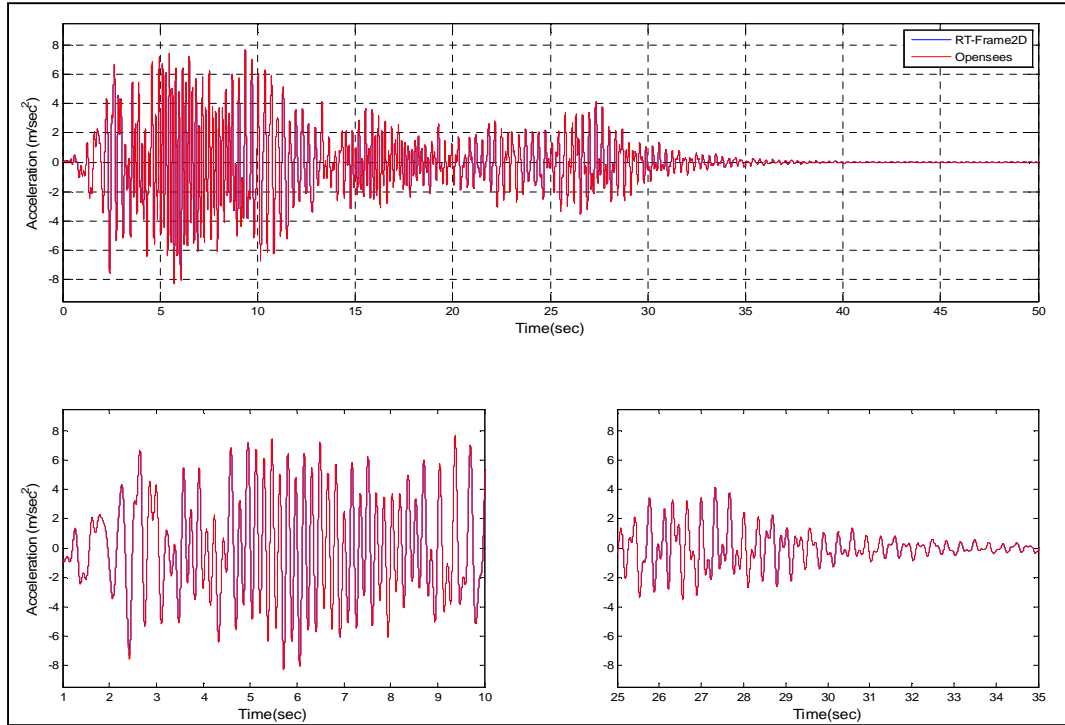


Figure 3.18: Absolute acceleration at floor 1 – Model 2

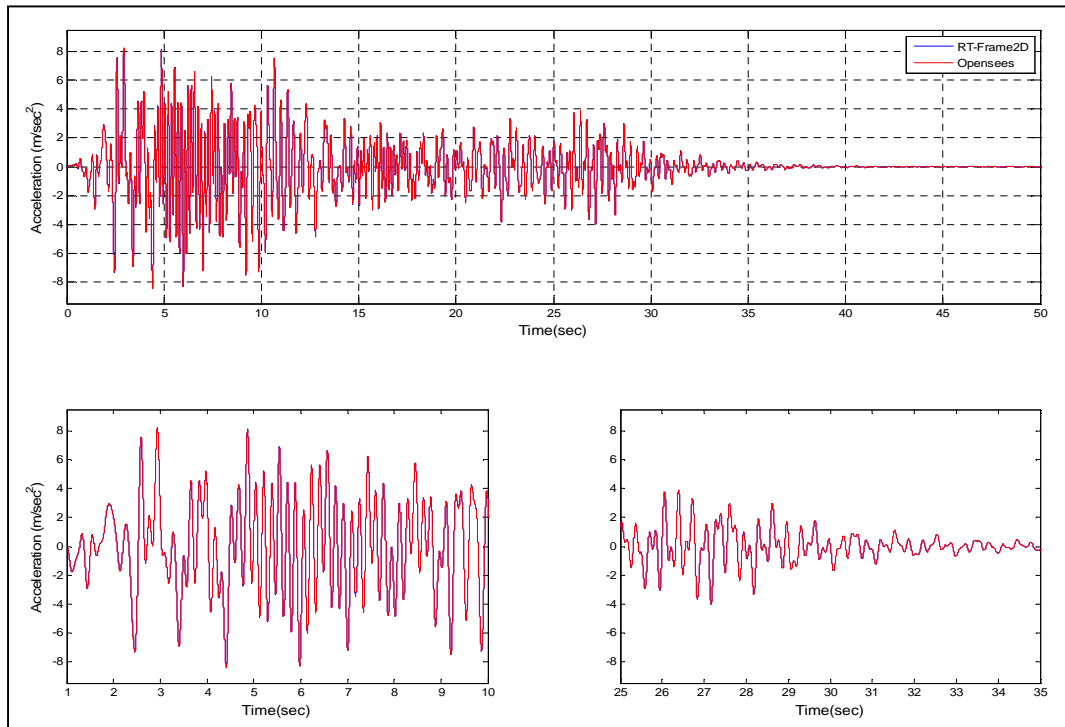


Figure 3.19: Absolute acceleration at floor 2 – Model 2

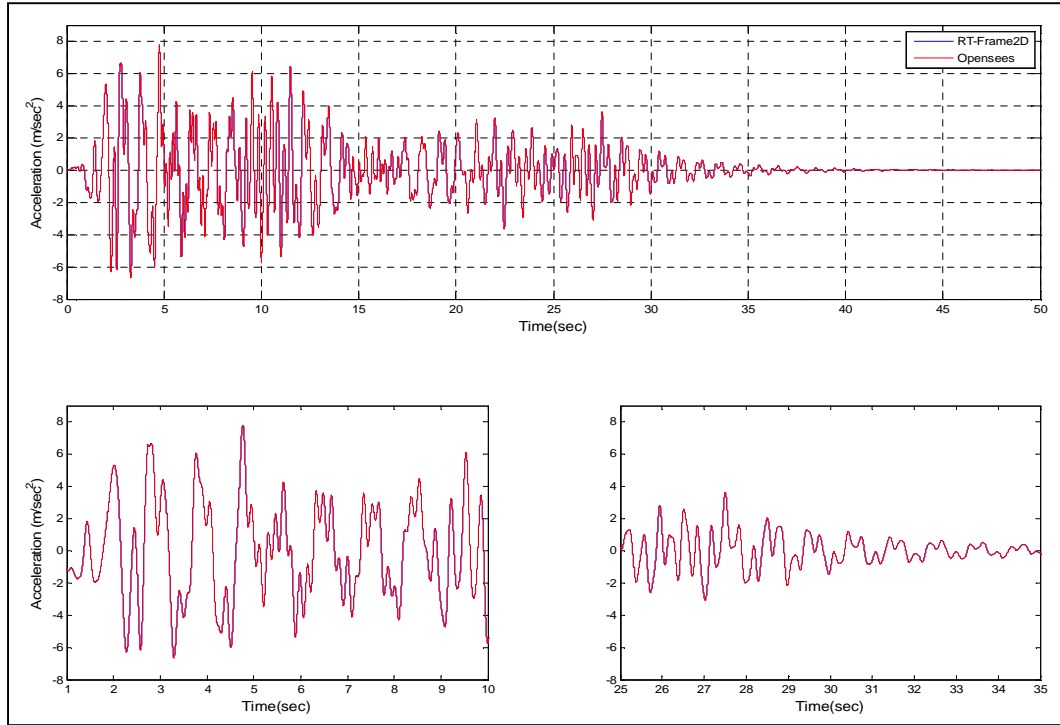


Figure 3.20: Absolute acceleration at floor 3 – Model 2

A comparison between representative hysteresis loops are shown in Figure 3.21. These hysteresis loops belong to the left-end of the W33x118 member located at the first-floor and first-bay and the left-end of the W30x116 member located at the second-floor and second-bay. Note that unfair comparison of hysteresis loops is performed in this model because of the different modeling assumptions that are adopted in both nonlinear beam-column elements. However, both hysteresis models still show good agreement. Moreover, and despite of the small differences, the global dynamic response is also in good agreement for both models. This global behavior can be explained based on an overall average effect i.e. differences in the update of one element state are compensated by the differences in the update of another.

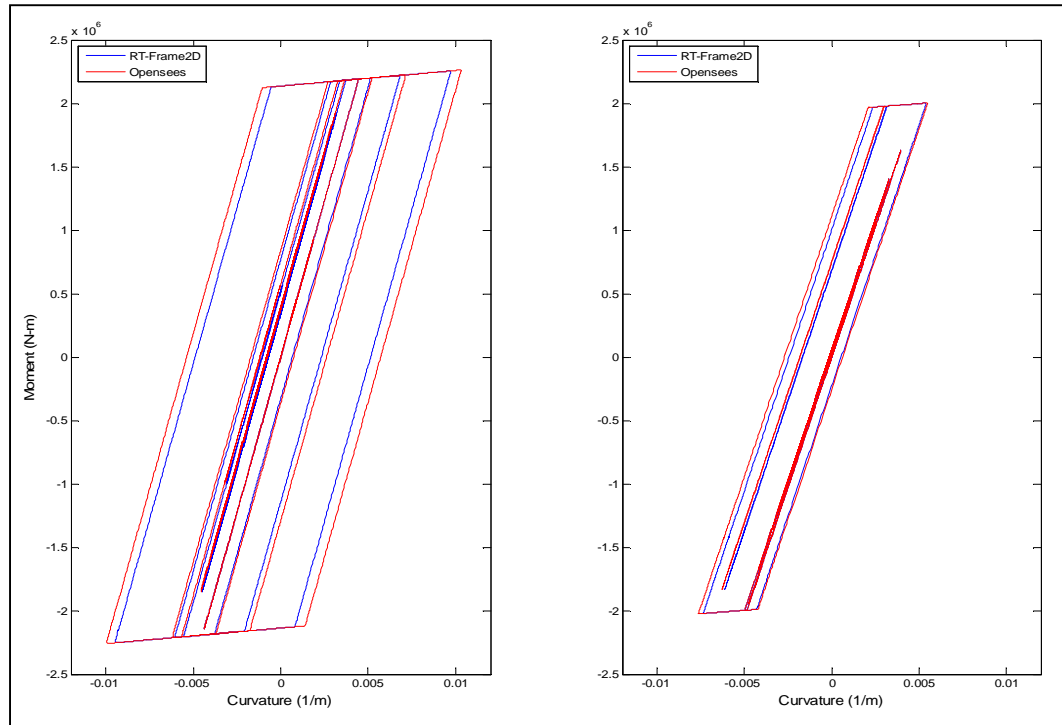


Figure 3.21: Hysteresis loops - Model 2

RT-Frame2D computational Model 3 is constructed based on the geometry and member section configuration as shown in Figure 3.22. Global mass matrix is assembled by contribution of 4.09e3 kg, 5.5e5 kg and 3.9e5 of mass distributed over beam members at the first second/third/fourth and fifth floor, respectively. Damping global matrix is defined with a stiffness proportional damping assumption yielding to a fundamental damping ratio of 2%. Column and beam members are defined with the *nonlinear beam-column element* offered by the RT-Frame2D element library using the concentrated plasticity option. The modulus of elasticity for steel is selected as 29,000 ksi. Flexural behavior at sections of the nonlinear beam-column elements are defined with a bilinear moment-curvature hysteresis model based on a kinematic hardening assumption and a post yielding ratio of 10%. Yielding moments and corresponding yielding curvatures are calculated based on the material and flexural section properties for each member. Boundary conditions are imposed as shown in Figure 3.22. Constraints are imposed for

horizontal translational DOF at each floor level, ensuring a rigid diaphragm behavior. The unconditionally-explicit CR integration scheme is used to solve the incremental equation of motion.

The *OpenSEES* computational Model 3 is constructed using the same geometry and section configuration as in the RT-Frame2D model. As before, global mass and damping matrices are defined with the same assumptions. Column and beam members are defined with the *beamWithHinges* element-type. Again this element is selected as the closest element for comparison with the one available in RT-Frame2D. The *uniaxialMaterial Steel01* function is used to define a bilinear moment-curvature hysteresis model with the same parameters as the RT-Frame2D model and also accounting for the kinematic hardening property. Hinge sections for the nonlinear beam elements are defined with this hysteresis model using the *section Uniaxial* function. Boundary conditions and constraints are also imposed with the same considerations as in the RT-Frame2D model. The unconditionally-implicit Newmark integrator scheme with constant acceleration is used to solve the incremental equation of motion with a Newton-Raphson nonlinear solver for enforcement of convergence.

Table 3.10 shows the natural frequencies of the four first modes calculated with RT-Frame2D and *OpenSEES*. No difference is observed for both records. Nonlinear dynamic analyses are performed by subjecting both computational models to a 100% intensity of the N-S earthquake record component measured at the Sylmar County Hospital parking lot during the Northridge earthquake of 1994. Both analyses are performed with a time step of $9.76e-04$ sec (1024 Hz) for duration of 100 sec, leading to output vectors of 102400 points. Time history records of the displacement and absolute acceleration calculated at each floor with both simulation platforms are plotted from Figure 3.23 and Figure 3.30. Additional plots showing records from 1 to 20 sec and from 25 to 45 sec are included for a zoomed view. Good match between both responses is observed with negligible differences at certain instances of the time history records. These differences can be attributed to not only the modeling differences between both nonlinear beam-

column elements but also to a lack of convergence at certain integration steps due to a more aggressive earthquake input. Despite these differences, peak values and permanent drift show an excellent agreement as observed from the figures.

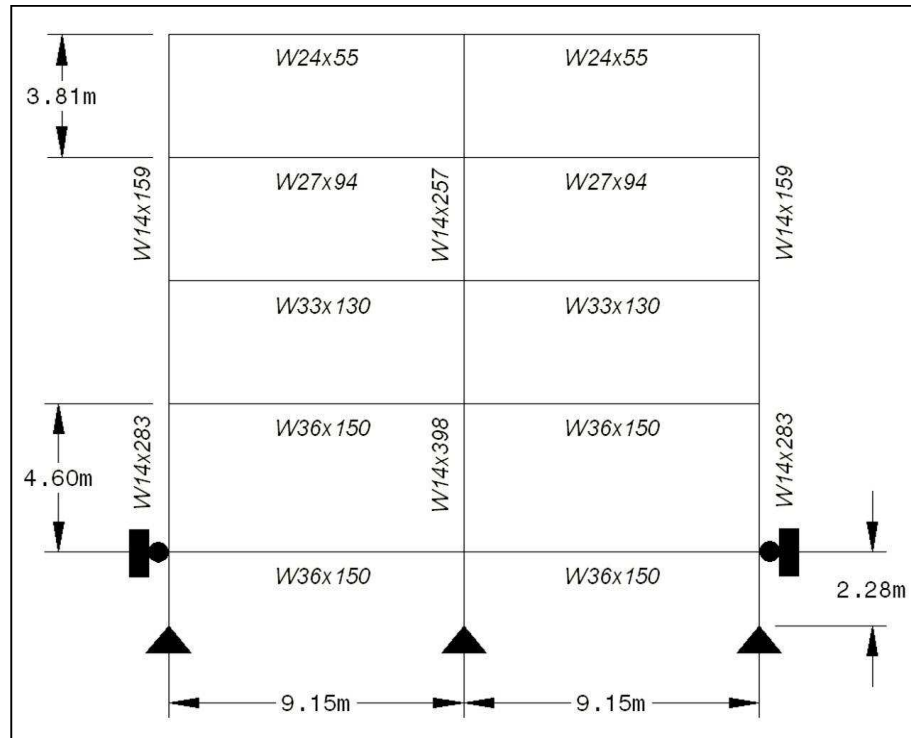


Figure 3.22: Computational model 3

Table 3.10: Natural frequencies comparison – Model 3

	<i>NF1 (Hz)</i>	<i>NF2 (Hz)</i>	<i>NF3(Hz)</i>	<i>NF4(Hz)</i>
<i>RT-Frame2D</i>	0.640	1.683	3.127	4.938
<i>OpenSEES</i>	0.641	1.683	3.127	4.938

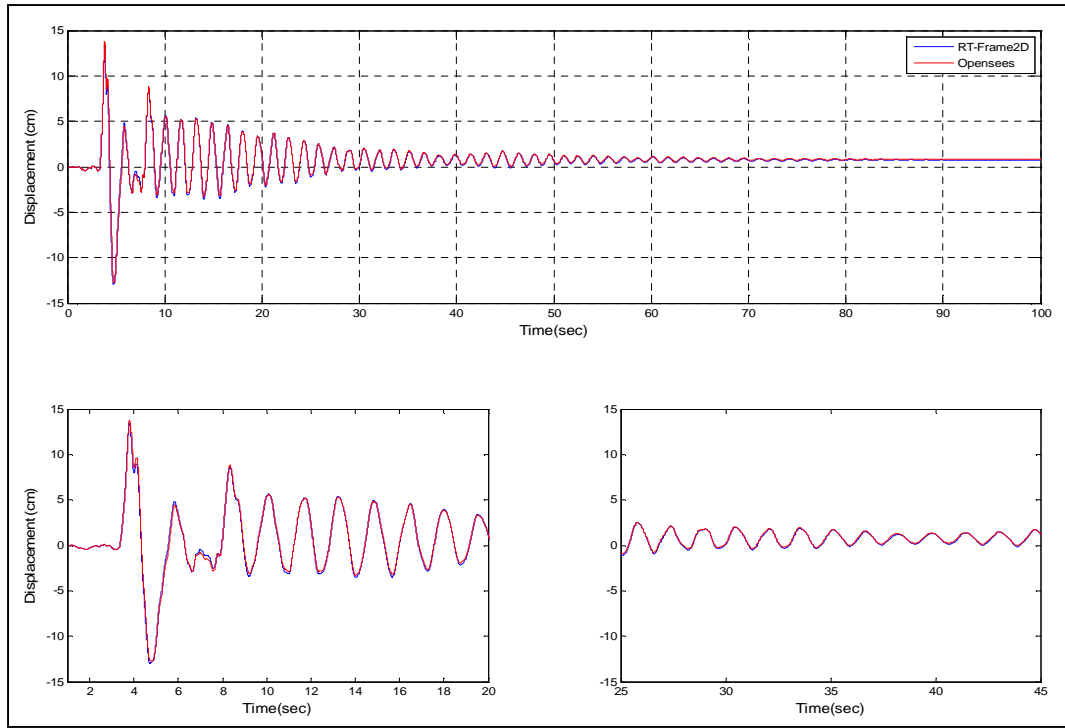


Figure 3.23: Displacement at floor 1 – Model 3

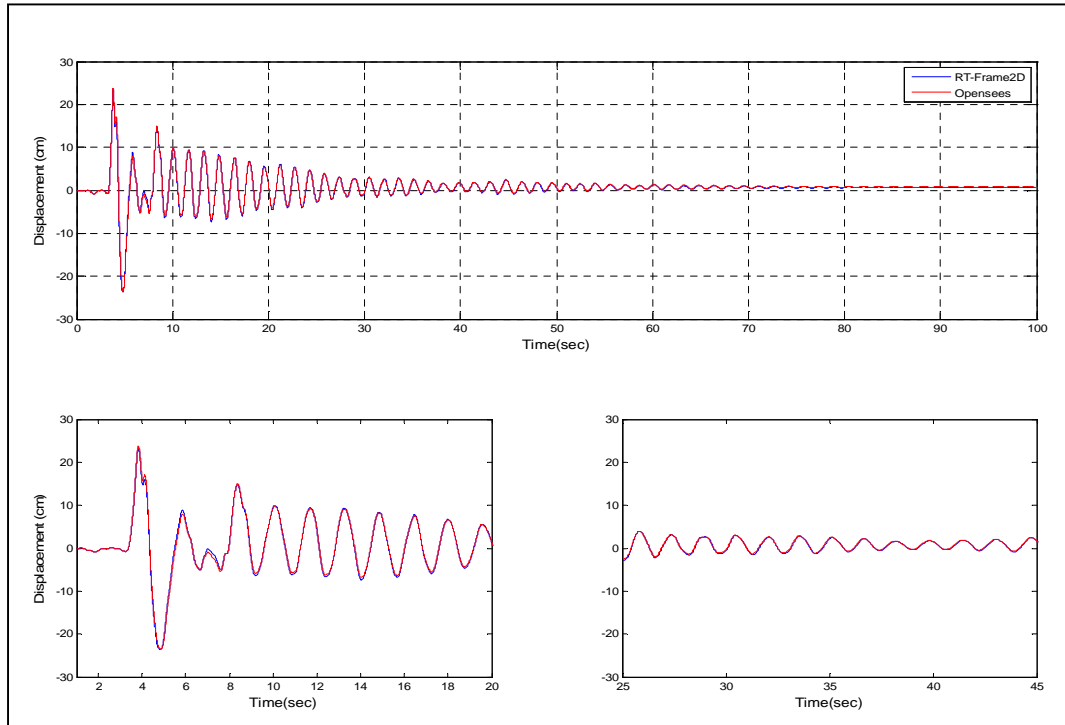


Figure 3.24: Displacement at floor 2 – Model 3

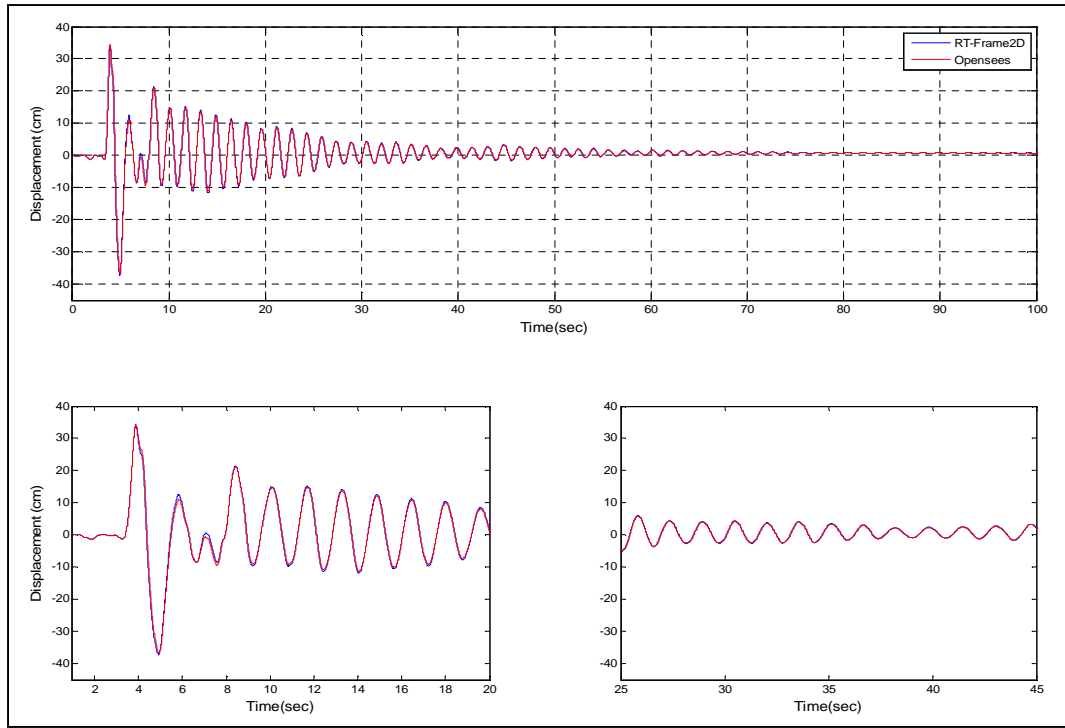


Figure 3.25: Displacement at floor 3 – Model 3

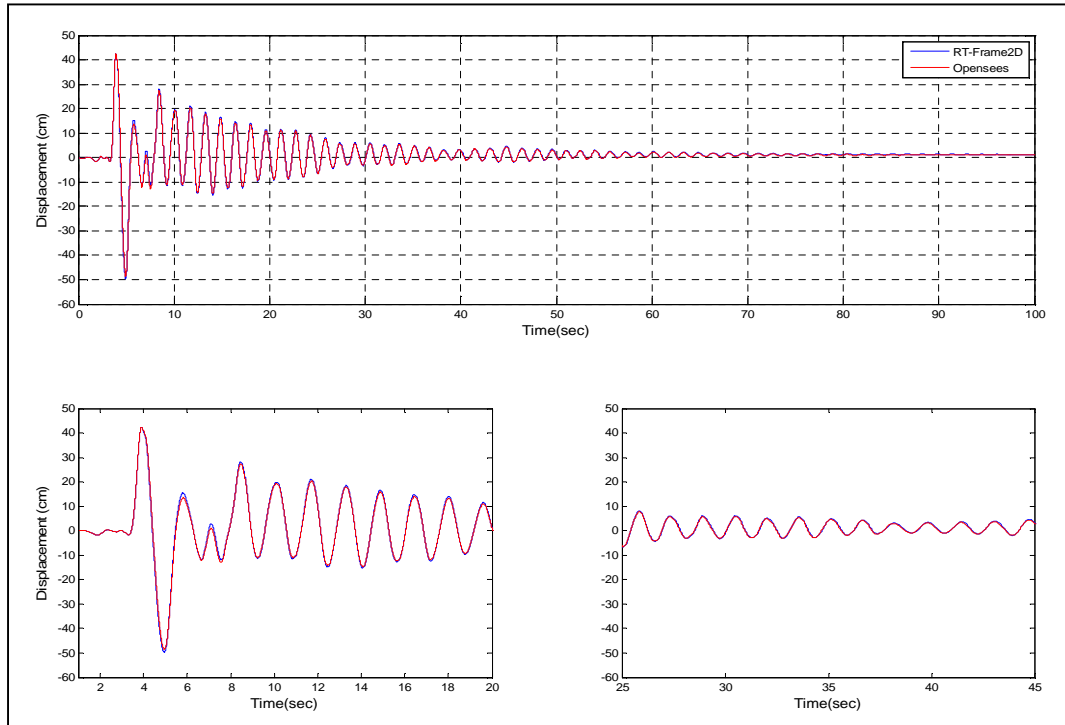


Figure 3.26: Displacement at floor 4 – Model 3

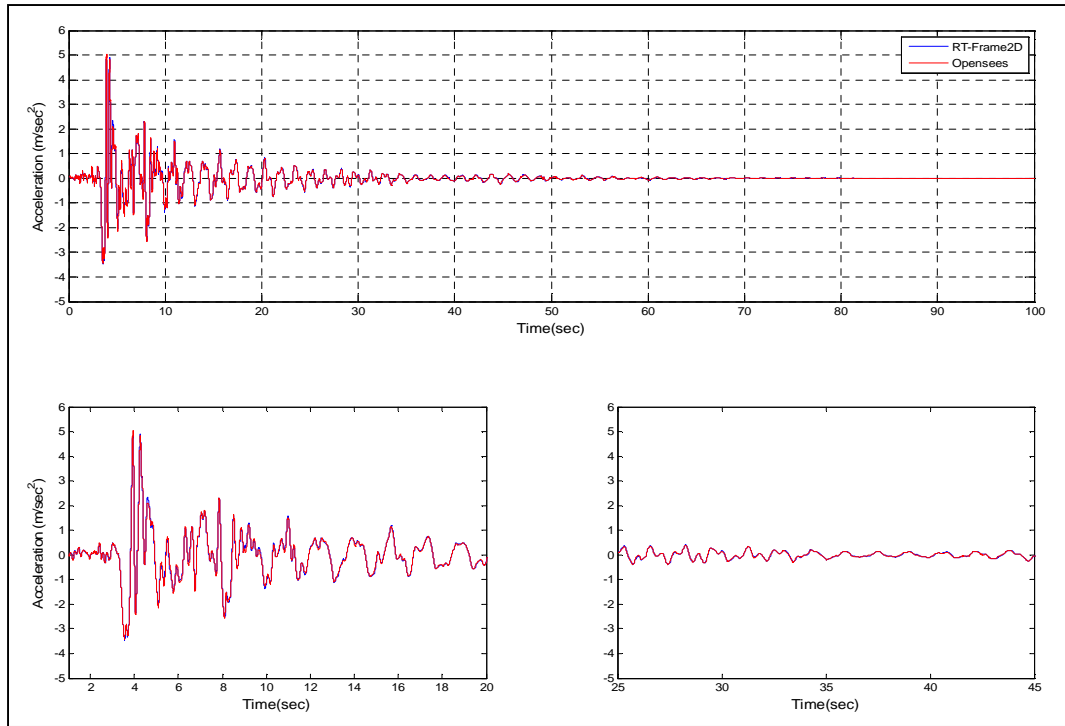


Figure 3.27: Absolute acceleration at floor 1 – Model 3

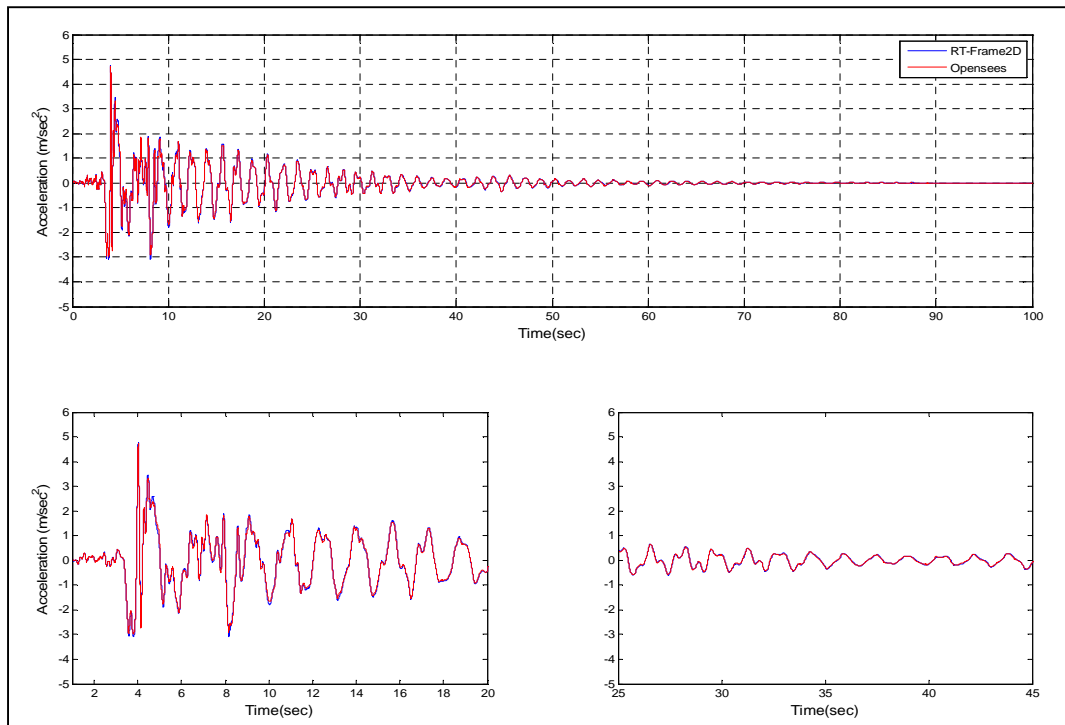


Figure 3.28: Absolute acceleration at floor 2 – Model 3

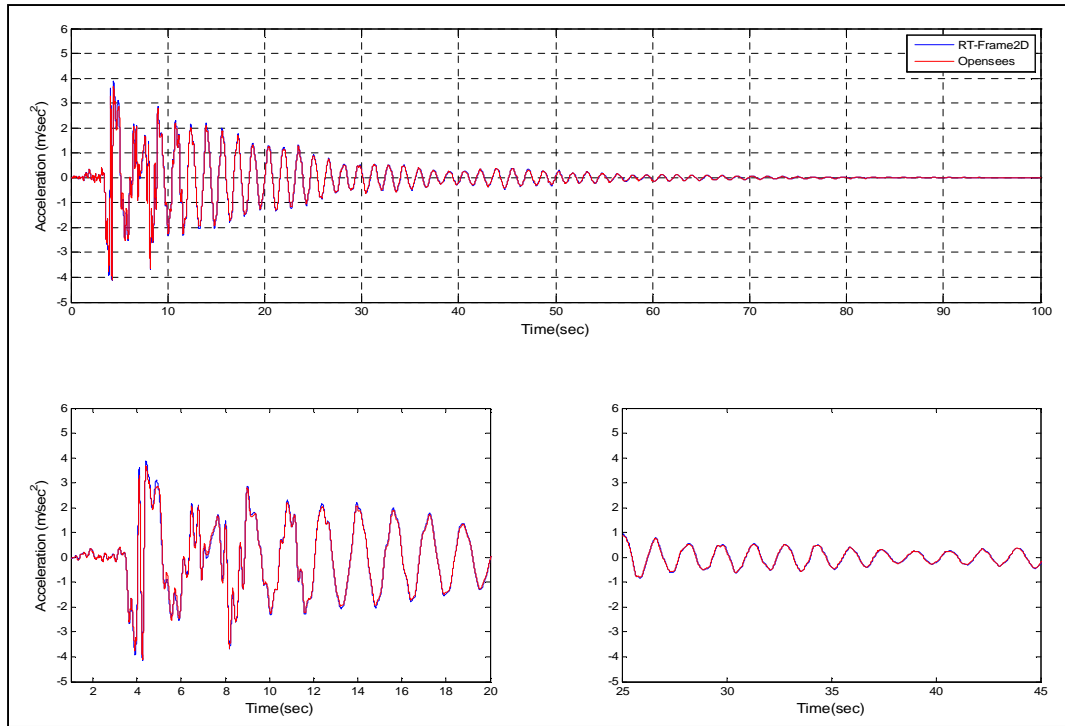


Figure 3.29: Absolute acceleration at floor 3 – Model 3

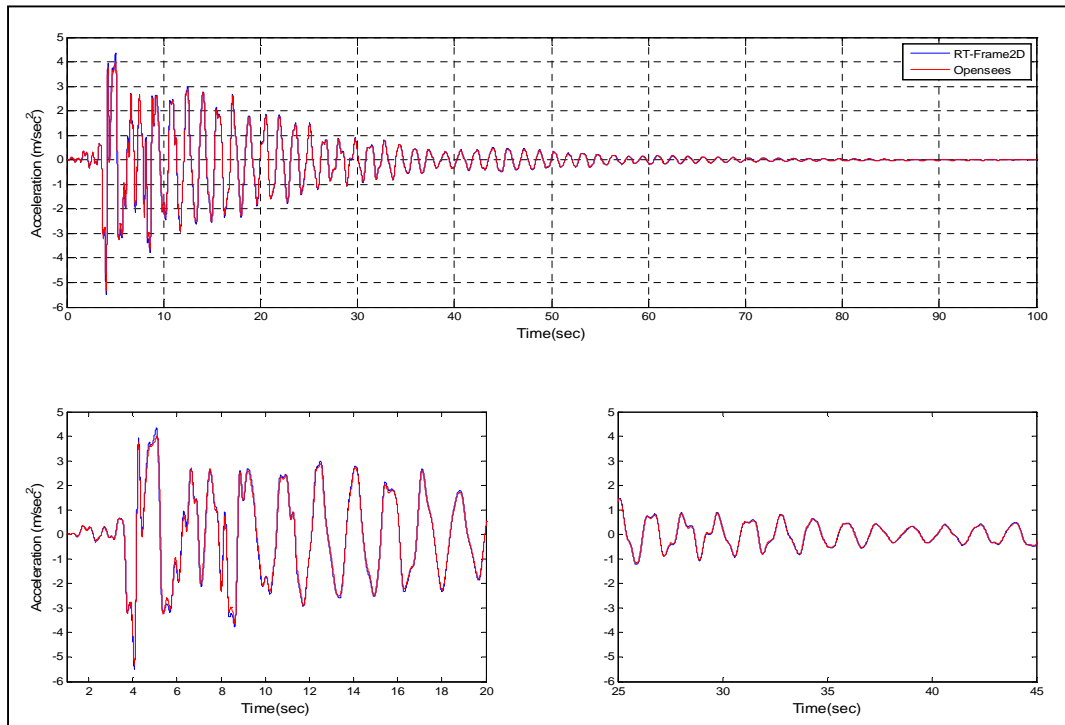


Figure 3.30: Absolute acceleration at floor 4 – Model 3

Comparison between hysteresis loops are shown in Figure 3.31. These hysteresis loops belong to the bottom-end of the W14x283 column member located at the first-floor and left side and the left-end of the W36x150 beam member located at the third-floor and second-bay. Note that an imperfect comparison of hysteresis loops is also performed in this model due to the modeling differences between both nonlinear beam-column elements. Despite the greater differences, the global dynamic response of both models is also in good agreement. This global behavior can be explained based on the overall average effect as explained in the precedent model.

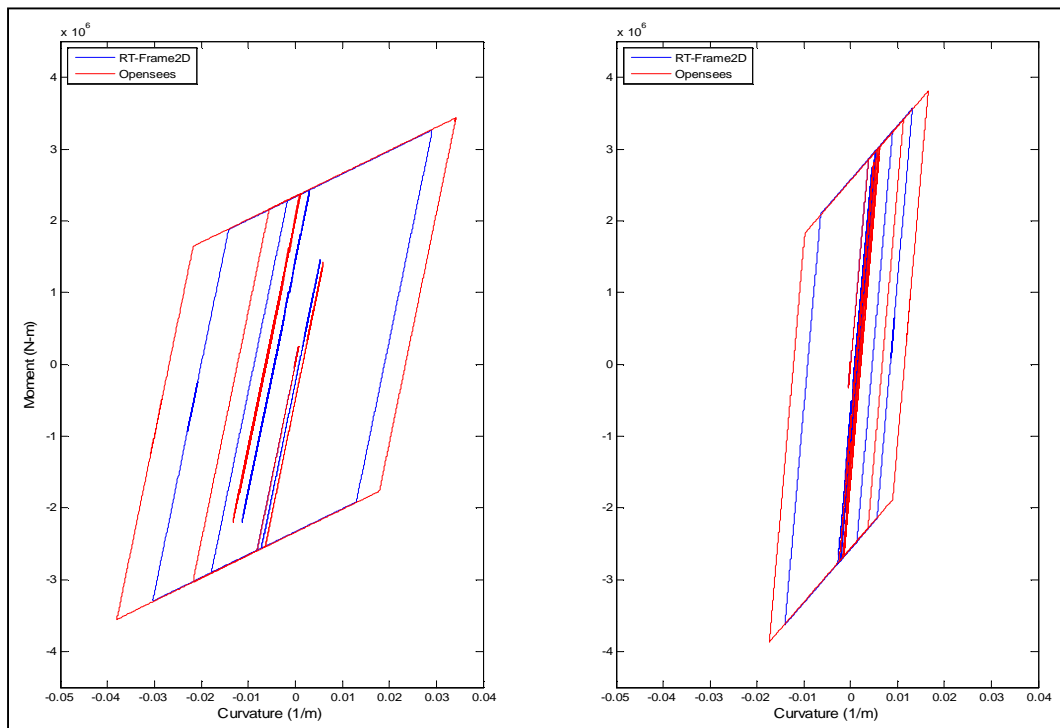


Figure 3.31: Hysteresis loops - Model 3

Figure 3.32 shows the geometry and member configuration that is used to define computational RT-Frame2D Model 4. Global mass matrix is assembled by contribution of 178 kg of self-weight distributed over beam members at each floor. Damping global matrix is defined with a Rayleigh assumption yielding a fundamental damping ratio of

1.6%. Column and beam members are defined with the *nonlinear beam-column element* using the spread plasticity option offered by the RT-Frame2D element library. The modulus of elasticity for steel is selected as 206 GPa. Flexural behavior at sections of the nonlinear beam-column elements are defined with a bilinear moment-curvature hysteresis model based on a kinematic hardening assumption and a post yielding ratio of 2.5%. Yielding moments and corresponding yielding curvatures are calculated based on the material and flexural section properties for each member. Boundary conditions are defined as indicated in Figure 3.32. The unconditionally-explicit CR integration scheme is used to solve the incremental equation of motion.

An *OpenSEES* version of computational Model 4 is constructed using the same geometry and sections as in the previous RT-Frame2D model, and include the same mass and damping configuration. Column and beam members are defined with the distributed-plasticity, displacement-based *dispBeamColumn* element type offered by the *OpenSEES* nonlinear beam-column element library. This element is selected to evaluate the performance of the force-based RT-Frame2D nonlinear beam-column element when compared with a displacement-based element. Note that displacement-based elements are more practical for implementation. Moreover, they are accurate when a refined mesh is selected. However, these elements are time consuming due to the numerical integration that is performed to update the element state. Definition of this element demands for the definition of control sections or integration points. Here, four control sections are selected for each element to ensure adequate accuracy. A bilinear moment-curvature hysteresis model comparable to the one used in the RT-Frame2D model is used. The hysteresis model is defined by the use of the *uniaxialMaterial Steel01* function. Therefore, the kinematic hardening property is only included. Because this element does not allow for direct definition of axial section properties, then material properties for axial behavior needs to be pre-defined. Definition of axial material behavior is accomplished by the use of the *uniaxialMaterial Elastic* function. Definition of section properties of nonlinear beam-column elements is accomplished by aggregating the previous material definitions with the *section Aggregator* function. Boundary conditions are enforced with the same

considerations as in the RT-Frame2D model. The unconditionally-implicit Newmark integrator scheme with constant acceleration is used to solve the incremental equation of motion. The integration scheme is also implemented with the Newton-Raphson nonlinear solver. Table 3.11 shows the natural frequencies at the three first modes calculated with RT-Frame2D and *OpenSEES*. No difference is observed.

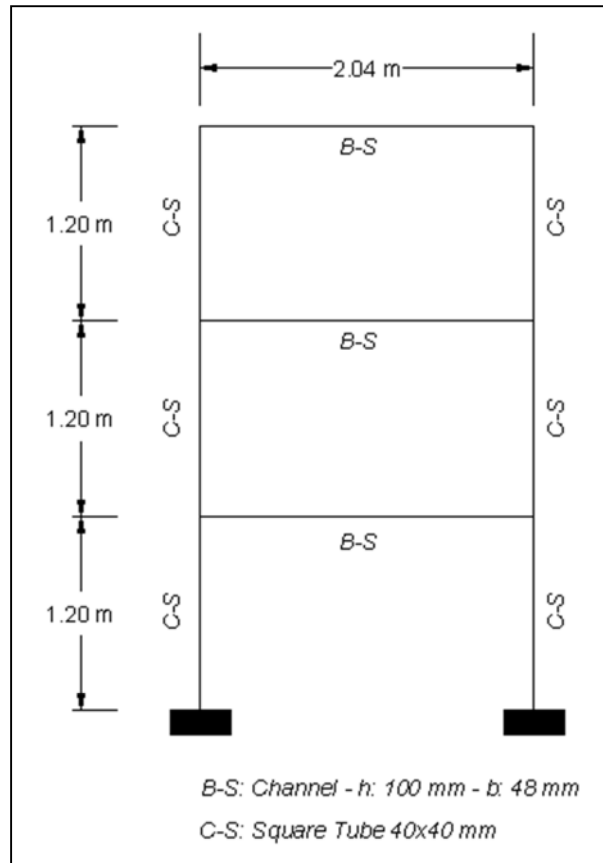


Figure 3.32: Computational model 4

Table 3.11: Natural frequencies comparison – Model 4

	<i>NF1 (Hz)</i>	<i>NF2 (Hz)</i>	<i>NF3(Hz)</i>
<i>RT-Frame2D</i>	2.708	7.748	11.495
<i>OpenSEES</i>	2.707	7.745	11.494

Nonlinear dynamic analyses are then performed by subjecting both computational models to a 100% intensity of the N-S component recorded at the Imperial Valley Irrigation District substation in *El Centro*, California, during the Imperial Valley, California earthquake of May 18, 1940. Both analyses are performed with a time step of $9.76e-04$ sec (1024 Hz) for duration of 80 sec leading to output vectors of 81921 points. Time history records of the displacement and absolute acceleration calculated at each floor with both simulation platforms are plotted from Figure 3.33 to Figure 3.38. Only 50 sec of the response is considered for clarity. Additional plots showing records from 1 to 10 sec and from 25 to 35 sec are included for a zoom view. Excellent match between both responses is observed for all displacement and absolute acceleration records.

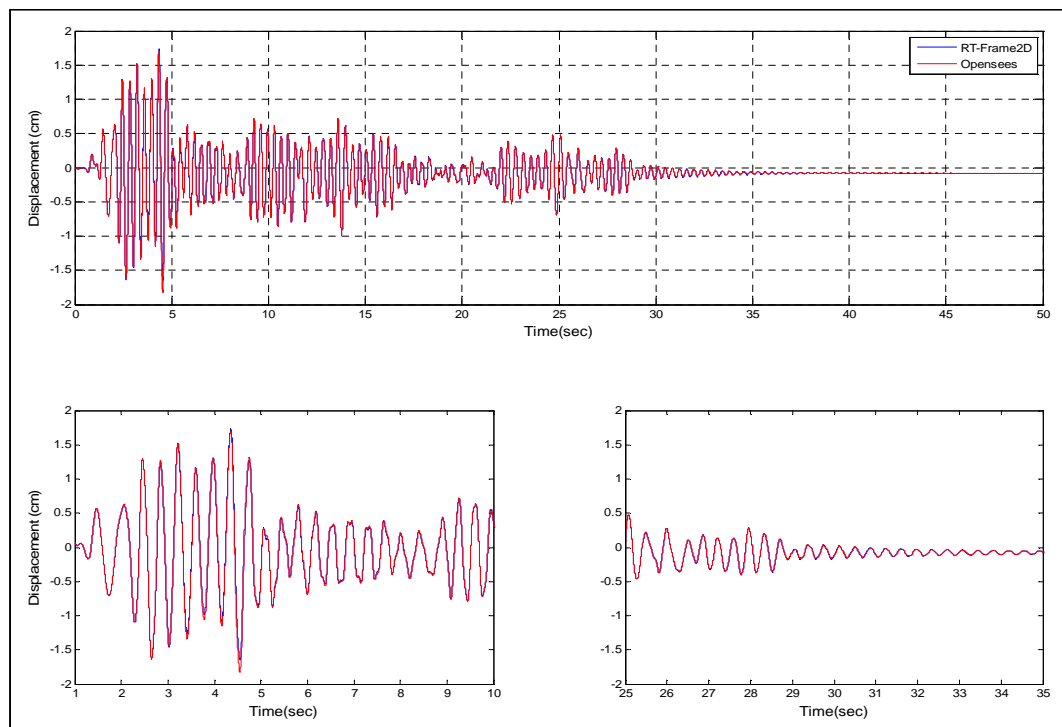


Figure 3.33: Displacement at Floor 1 – Model 4

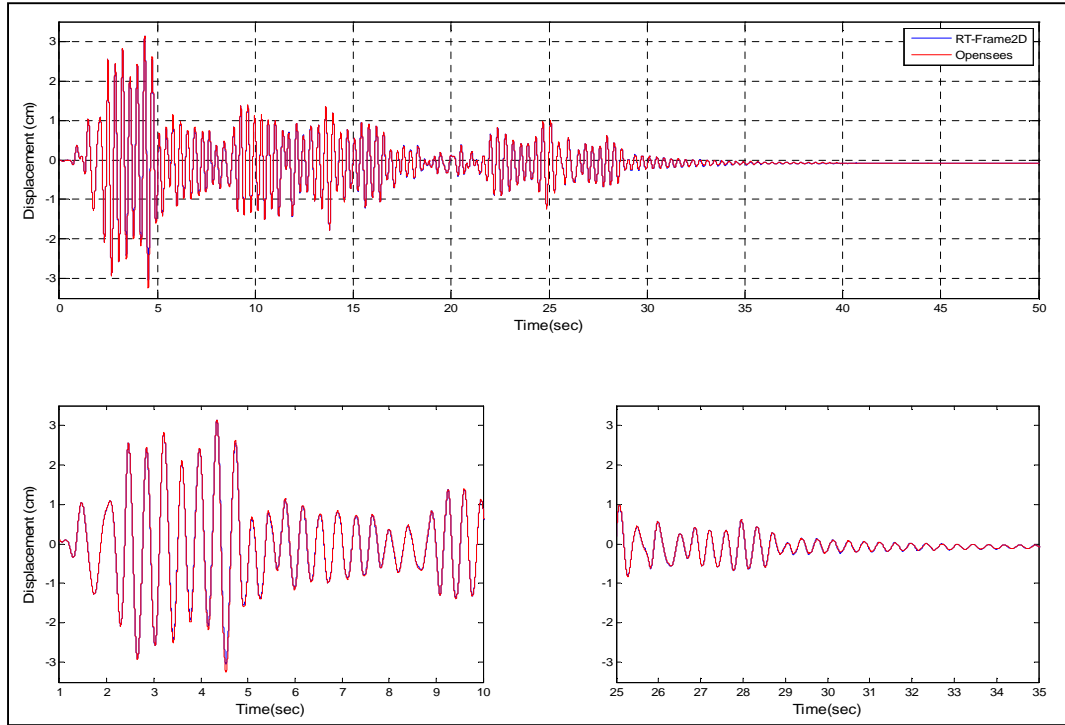


Figure 3.34: Displacement at Floor 2 – Model 4

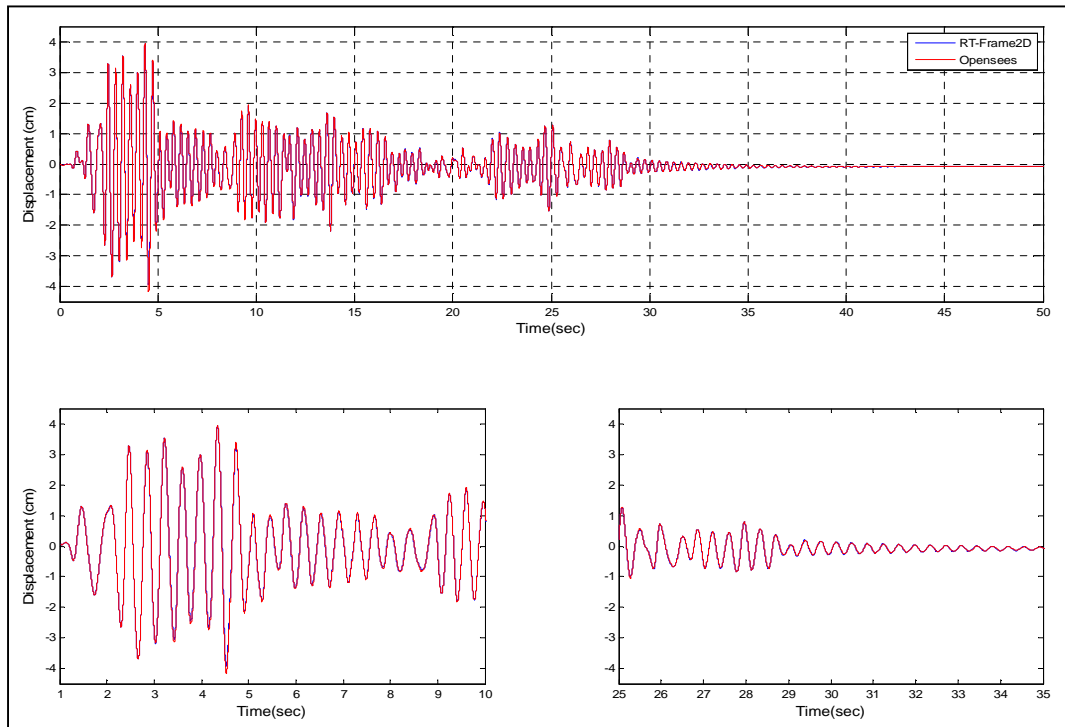


Figure 3.35: Displacement at Floor 3 – Model 4

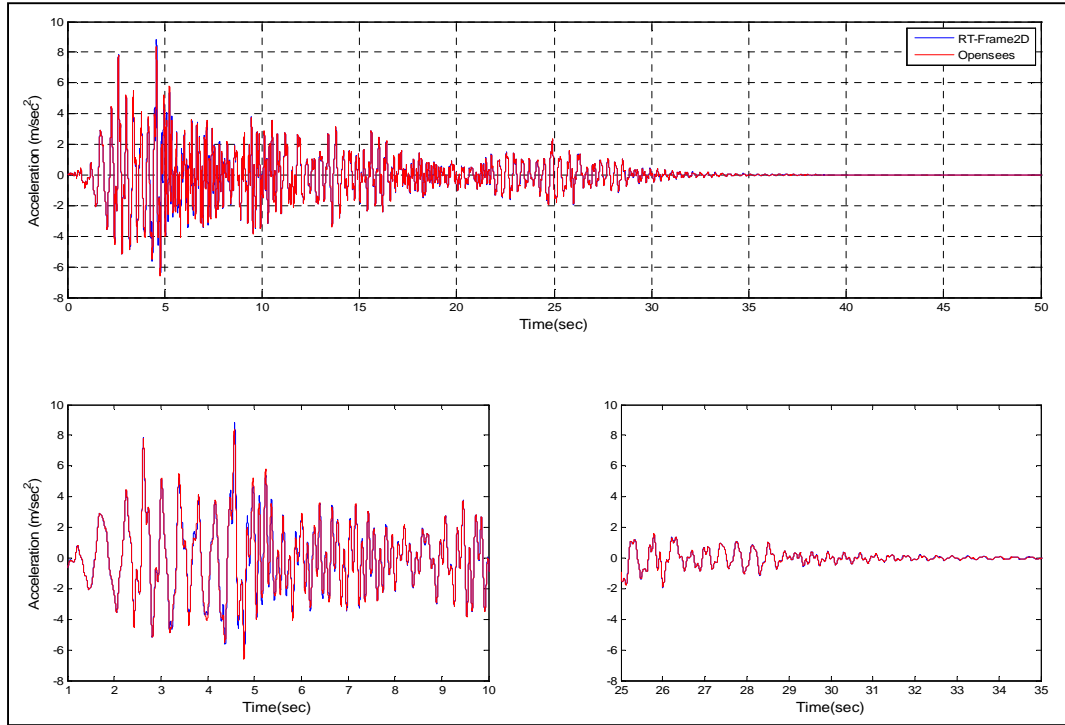


Figure 3.36: Absolute acceleration at Floor 1 – Model 4

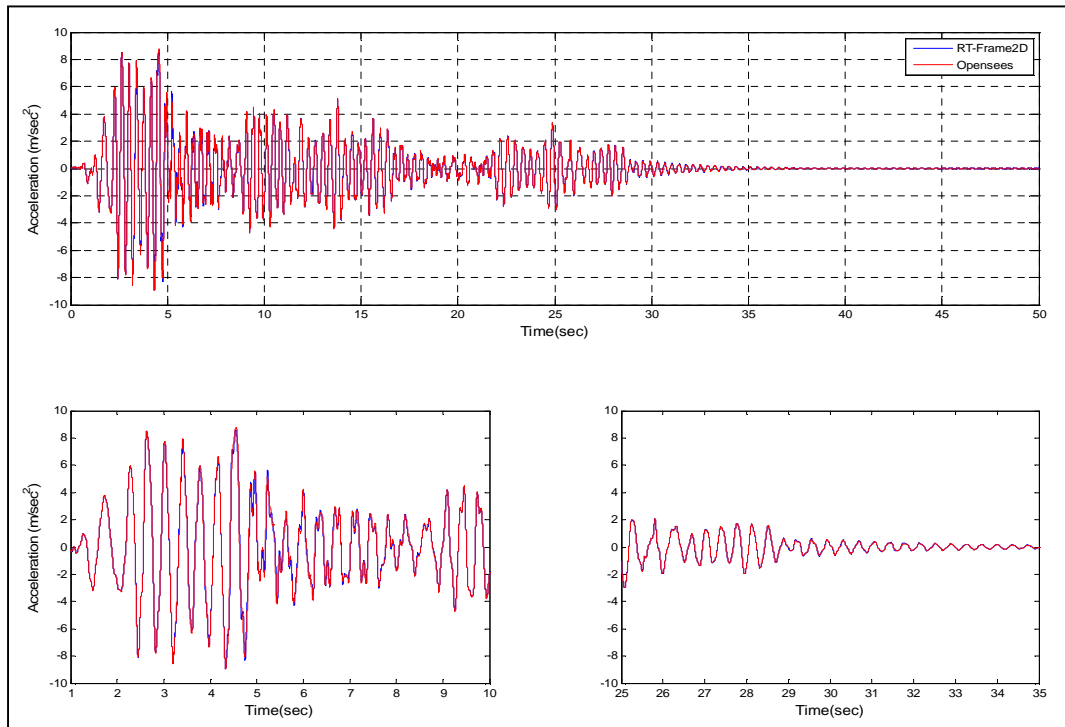


Figure 3.37: Absolute acceleration at Floor 2 – Model 4

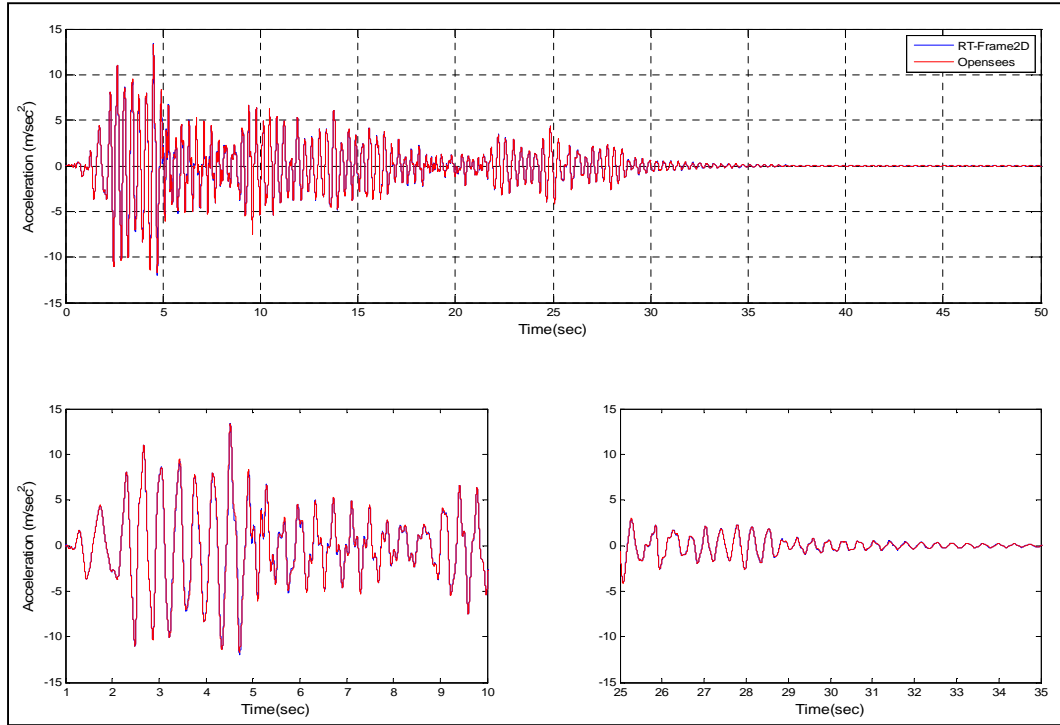


Figure 3.38: Absolute acceleration at Floor 3 – Model 4

Panel zone effect with the rigid-body modeling option is evaluated next in RT-Frame2D computational Model 5. This computational model is defined with the same geometry as Model 4. However, sections of beam members are replaced with sections of column members. The replacement is performed to yield the same reduction in element lengths due to the presence of the rigid body effect of the panel zone. Note that this reduction in the element length is proportional to the element depths connecting the panel zone. Figure 3.39 reflects the updated layout. Global mass matrix is assembled by contribution of 533 kg of mass distributed over beam members at each floor. Due to the increment in mass and reduction in the overall stiffness, a more flexible structure is obtained. This reduction in stiffness is evidenced at Table 3.12 where the natural frequencies of the three first modes are shown. The global damping matrix is defined using a Rayleigh assumption yielding a fundamental damping ratio of 4%. Column members are defined with the *linear elastic beam-column element*. Beam members are defined with the *nonlinear beam-column element* using the concentrated plasticity model option. The

modulus of elasticity for steel is selected as 206 GPa. Flexural behavior at sections of the nonlinear beam-column elements are defined with a bilinear moment-curvature hysteresis model based on a kinematic hardening assumption and post yielding ratio of 2.5%. Yielding moments and corresponding yielding curvatures are calculated based on the material and flexural section properties for each member. Panel zone members are defined with the *rigid body panel zone* element offered by RT-Frame2D. Width and height dimensions of the panel zone are defined with a value of 40 mm equal to the depth of the beam and column members connecting the panel zone. The thickness is set to 3 mm. Boundary conditions are defined in agreement with Figure 3.39. The unconditionally-explicit CR integration scheme is used to solve the incremental equation of motion.

An *OpenSEES* version of Model 5 is constructed using the same geometry and section configuration of the corresponding RT-Frame2D model including the same mass and damping. Due to the lack of a comparable panel zone model as that offered by RT-Frame2D, rigid-length zones within beam and column members are included to recreate the presence of a rigid-body panel zone. The rigid-length is defined with the same extent as the panel zone dimensions considered in the RT-Frame2D model. Therefore, linear elastic frame elements defined with the *elasticBeamColumn* element and high value of module of elasticity are considered for such rigid-length elements. Column members between rigid-length members are defined with the *elasticBeamColumn* element. Beam members between rigid-length members are defined with the *beamWithHinges* element-type. The *uniaxialMaterial Steel01* function is used to define a bilinear moment-curvature hysteresis model with the same parameters as the RT-Frame2D model. Therefore, the kinematic hardening property is only included. Sections for the nonlinear beam elements are defined with this hysteresis model using the *section Uniaxial* function. Boundary conditions are defined with the same considerations as in the RT-Frame2D model. The unconditionally-implicit Newmark integrator scheme with constant acceleration is used to solve the incremental equation of motion along with the Newton-Raphson nonlinear solver.

Table 3.12 shows the natural frequencies at the three first modes calculated with *RT-Frame2D* and *OpenSEES*. The fact that there are no difference in the natural frequency values indicates that an *OpenSEES* model based on rigid-length elements is a reasonable assumption for comparison with the rigid body panel zone model of *RT-Frame2D*.

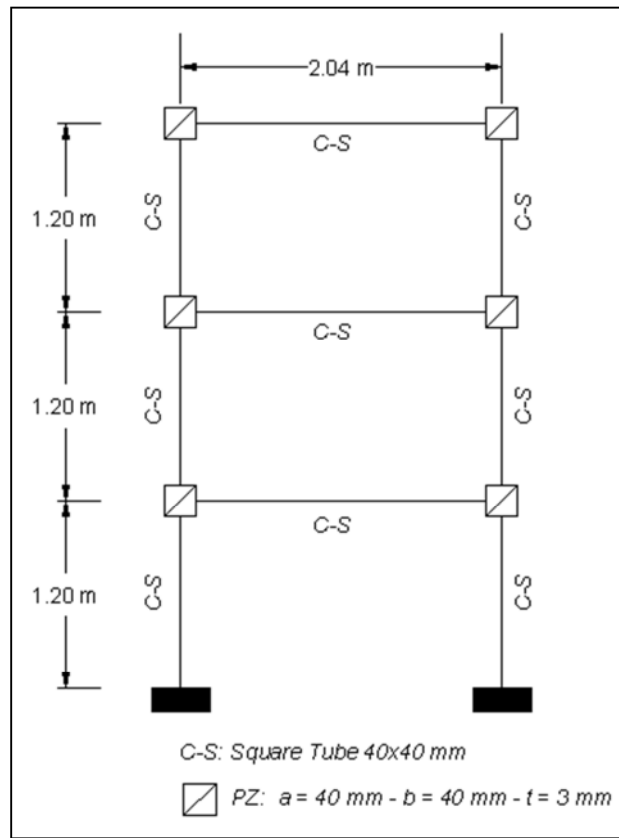


Figure 3.39: Computational model 5

Table 3.12: Natural frequencies comparison – Model 5

	<i>NF1 (Hz)</i>	<i>NF2 (Hz)</i>	<i>NF3(Hz)</i>
<i>RT-Frame2D</i>	0.990	3.380	6.332
<i>OpenSEES</i>	0.990	3.379	6.331

Next, nonlinear dynamic analyses are performed by subjecting both computational models to a 100% intensity of the N-S component recorded at the Imperial Valley Irrigation District substation in *El Centro*, California, during the Imperial Valley, California earthquake of May 18, 1940. Both analyses are performed with a time step of $9.76e-04$ sec (1024 Hz) for duration of 80 sec, leading to output vectors of 81921 points. Time history records of the displacement and absolute acceleration calculated at each floor with both simulation platforms are plotted between Figure 3.40 and Figure 3.45. Only 50 sec of the response is shown for clarity. Additional plots showing records from 1 to 10 sec and from 25 to 35 sec are included for a zoomed view.

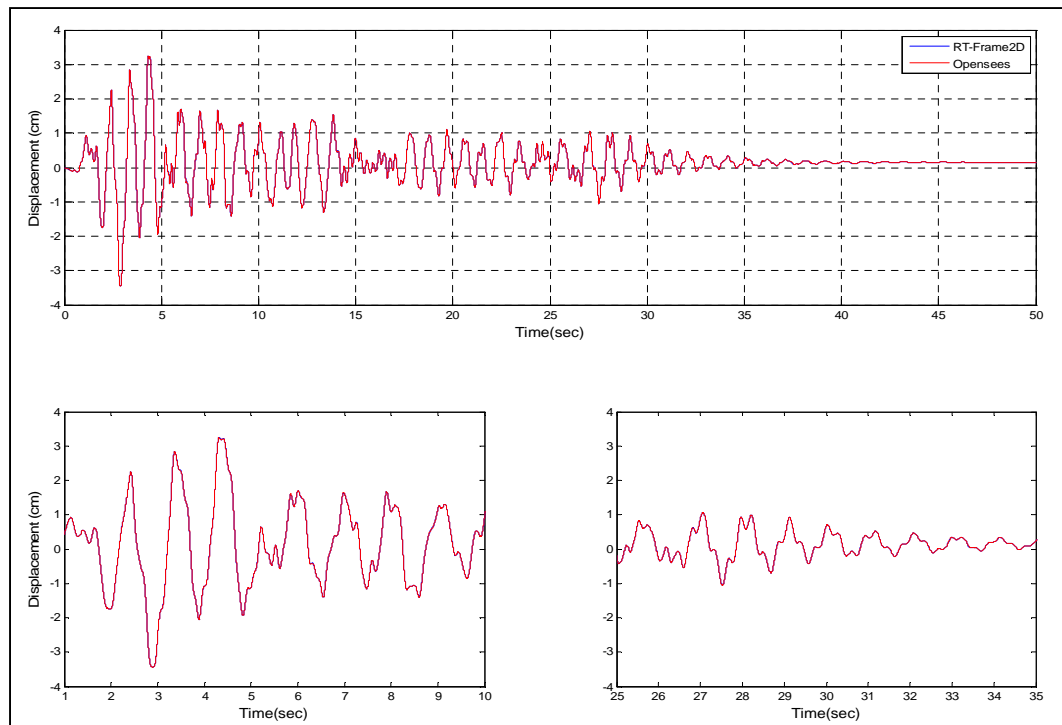


Figure 3.40: Displacement at Floor 1 – Model 5

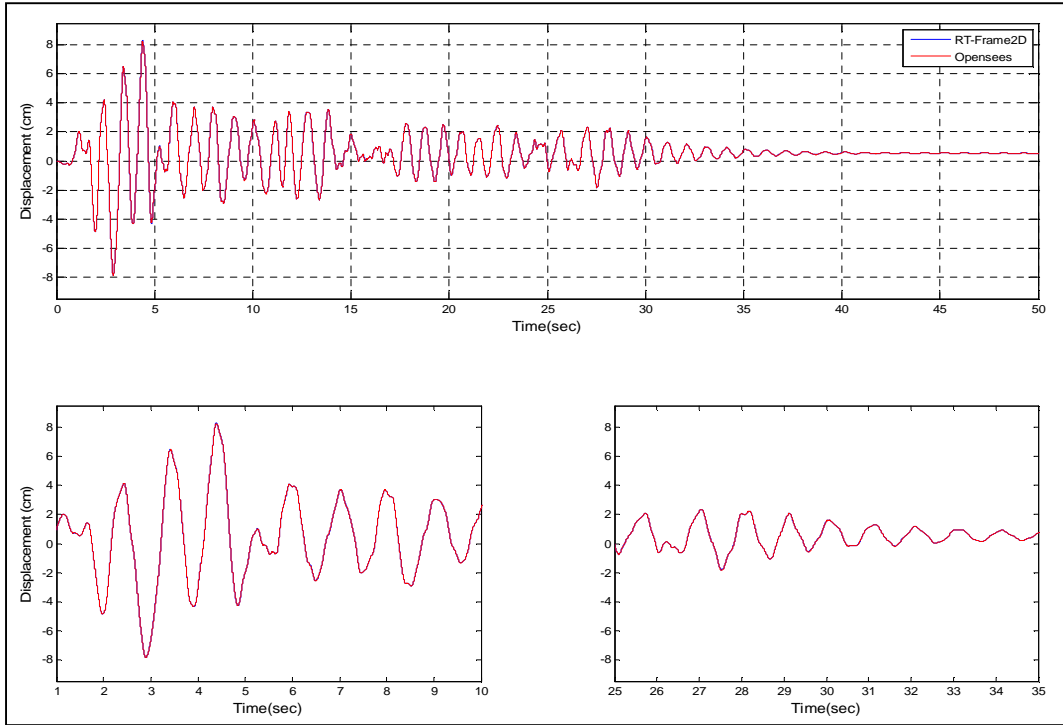


Figure 3.41: Displacement at Floor 2 – Model 5

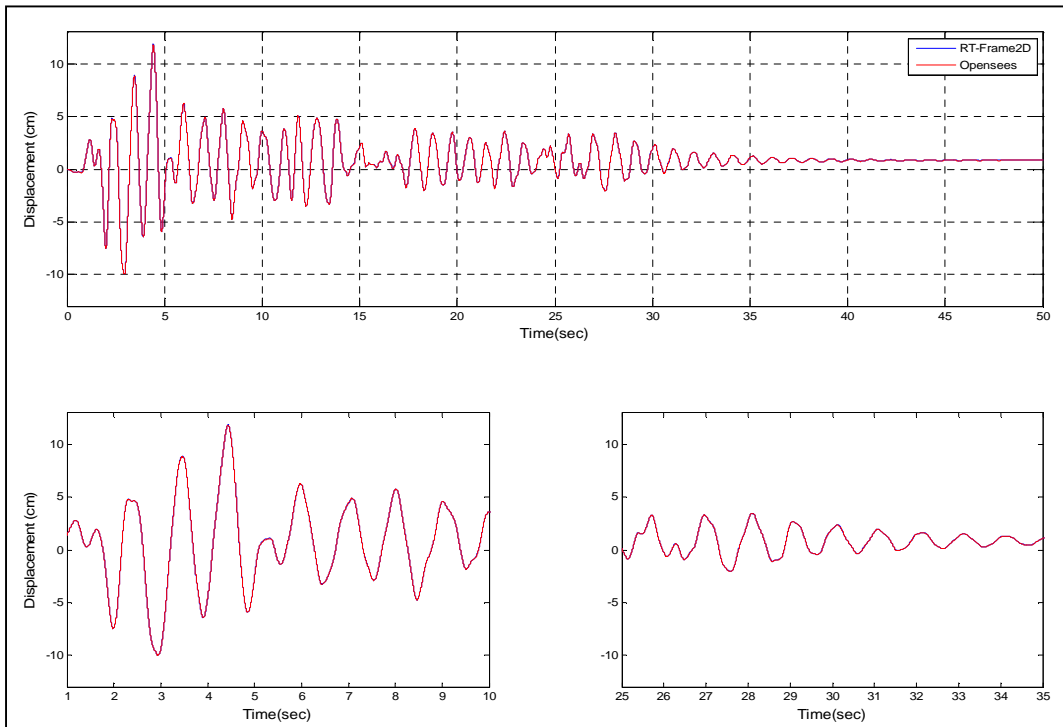


Figure 3.42: Displacement at Floor 3 – Model 5

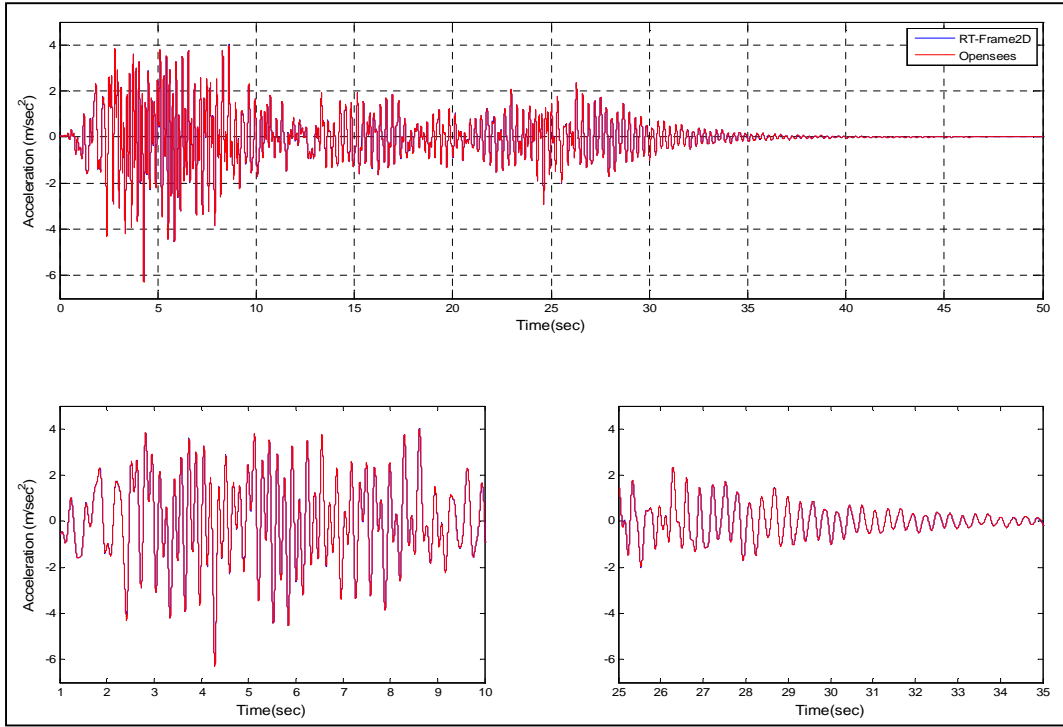


Figure 3.43: Absolute acceleration at Floor 1 – Model 5

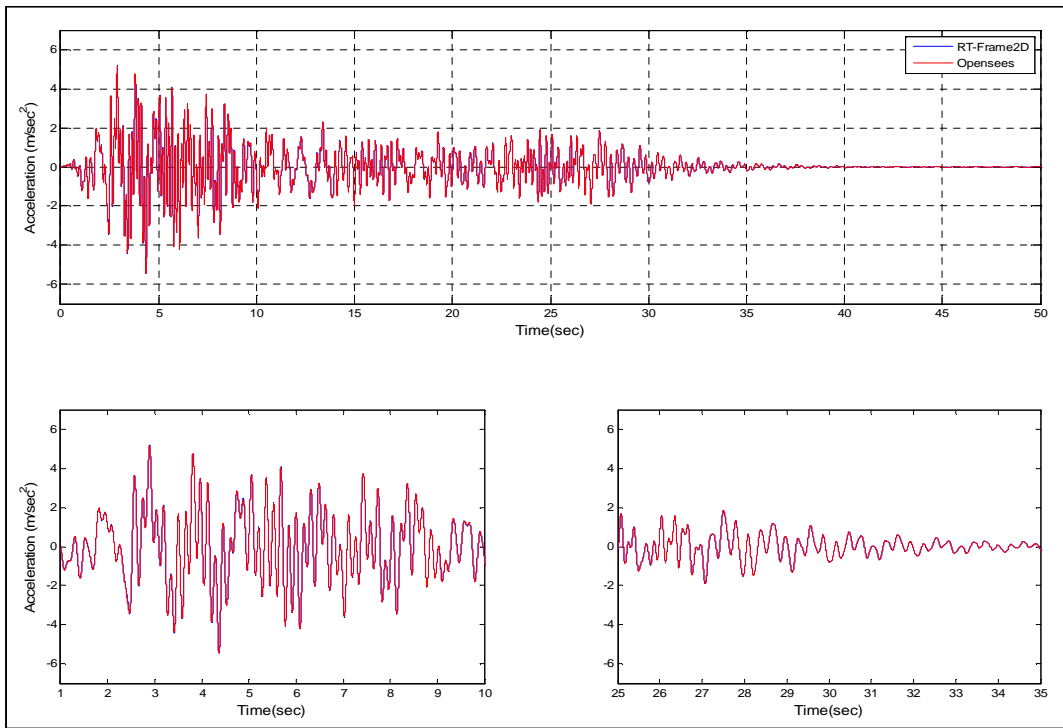


Figure 3.44: Absolute acceleration at Floor 2 – Model 5

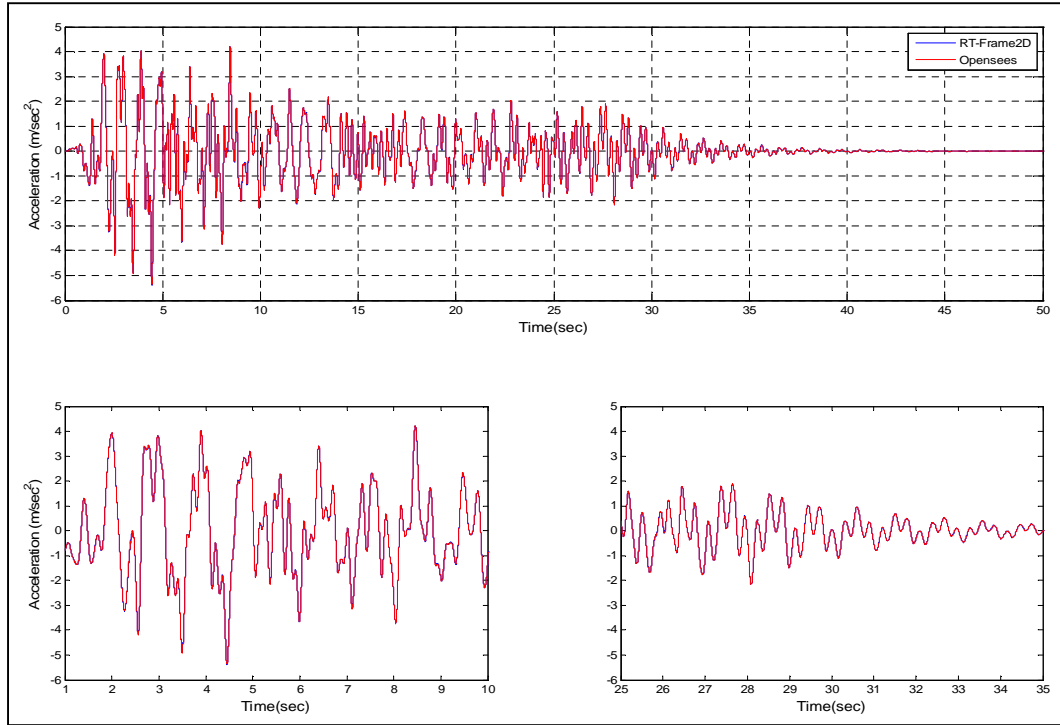


Figure 3.45: Absolute acceleration at Floor 3 – Model 5

Excellent match between both responses is observed for all displacement and absolute acceleration records. Moreover, note that the RT-Frame2D computational model possess an advantage over the *OpenSEES* model because it only requires the same number of DOF as a model defined with center-line dimensions. Conversely the *OpenSEES* model requires additional nodes for definition of rigid-length elements, significantly increasing the number of DOF and the execution time when compared to the RT-Frame2D model.

CHAPTER 4. EXPERIMENTAL VALIDATION I: REAL-TIME HYBRID SIMULATION AT THE IISL

The performance of the proposed RT-Frame2D computational platform is experimentally validated when subjected to real-time execution with several hybrid simulation scenarios. The validation is performed in the Intelligent Infrastructure Systems Laboratory (IISL) at Purdue University (<https://engineering.purdue.edu/IISL/>). An experimental plan based on different test implementations is completed for validation. Various configurations are considered in which a magneto-rheological damper (MR damper) and a modular steel frame are utilized as physical substructures. Because a test-bed is required to evaluate the experimental substructures, this chapter also includes general aspects about the development and implementation of a cyberphysical small-scale real-time hybrid simulation instrument (CIRST) recently constructed in the IISL (Gao, 2012). The proposed computational platform, RT-Frame2D is adopted here as the cyber-component for simulation of the computational counterpart during these tests. The test-bed is designed to perform RTHS of seismically-excited, steel building structures with damper devices. Thus, the experimental plan and corresponding results are aimed not only to validate the performance of the computational platform, but also to demonstrate the performance of the test-bed itself. This chapter starts with a discussion of the main aspects of the experimental plan, followed by a description of the most relevant components of the RTHS test-bed. Finally, a description of each experimental implementation with the corresponding results is presented and discussed.

4.1 Experimental plan

The experimental plan for evaluation and validation of the real-time hybrid simulation capabilities of the proposed computational platform involves the completion of four experimental implementation cases, to be named Implementations I-IV in the sequel. These cases are performed using the recently developed RTHS test-bed located in the IISL at Purdue University. The experiments are focused on replicating the dynamic response of a seismically-excited frame, equipped with and without a damper device, through two different RTHS scenarios (RTHS Phase-1 and Phase-2). Therefore, three components: mass - frame structure and a damper device are considered within the test depending on the RTHS scenario under evaluation. Figure 4.1 shows the schematic of such scenarios for reference. RTHS Phase - 1 considers the mass and frame as computational substructures while the damper device is the experimental substructure. RTHS Phase - 2 considers the mass as the computational substructure while the frame and damper device (when included) are physical substructures. Additionally, numerical simulations of the RTHS scenarios are performed so that follow-up comparisons can serve to quantitatively assess accuracy, stability and real-time performance of the proposed computational platform. Experimental counterparts of the frame and damper device are accounted for with specimens of a modular one-two story configuration steel frame and a MR damper device, respectively. Although certain experimental mass and damping associated to the experimental substructures are considered during tests, most of them are considered computationally, as implied before. Therefore, mass and damping computational values are chosen so that the dominant modal content of the hybrid system remains within the allowed operational frequency range of the test set-up. Furthermore, these values are selected so that the frequencies of the complete test specimen (i.e., the computational and experimental components combined) are comparable to those observed in large-scale frame structures.

Table 4.1 indicates the RTHS scenarios and experimental substructures that are considered at each experimental implementation. Implementations I and II evaluate the dynamic response of a seismically-excited frame with both one and two-story configurations of the frame specimen, respectively. These implementations are performed based on the RTHS Phase-2 scenario (shown in Figure 4.1) with no MR damper included during the tests. Implementation-III evaluates the dynamic response of a seismically-excited frame structure with a two-story configuration of the frame specimen. Here, the MR damper is included within the test to increase the complexity of the validation. Therefore, both RTHS Phase-1 and Phase-2 scenarios are evaluated. Implementation IV evaluates the dynamic response of a seismically-excited two-story one-bay frame structure under RTHS Phase-1 scenario, i.e. with only the MR damper device as the experimental substructure. Several computational models of the frame structure based on different modeling options offered by the computational platform are tested. A detailed description of the proposed experimental implementations including a substantial discussion of model updating, testing procedures and results is presented in the following sections.

Table 4.1: Implementations I-IV

<i>Implementation</i>	<i>RTHS Phase – 1</i>	<i>RTHS Phase – 2</i>	<i>One-story frame</i>	<i>Two-story frame</i>	<i>MR Damper</i>
I	-	✓	✓	-	-
II	-	✓	-	✓	-
III	✓	✓	-	✓	✓
IV	✓	-	-	-	✓

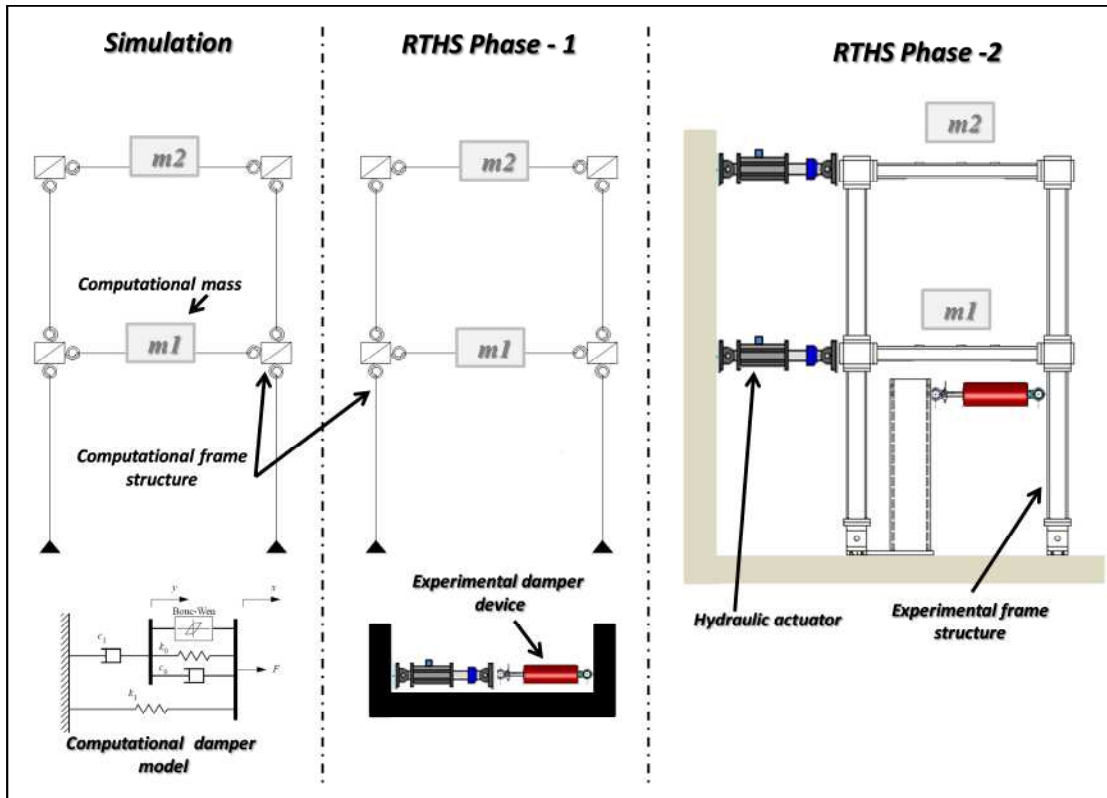


Figure 4.1: Schematic of simulation and RTHS scenarios

4.2 RTHS platform at the Intelligent Infrastructure Systems Laboratory

A general description of the main components of the cyberphysical small-scale RTHS instrument (CIRST), recently constructed in the IISL and utilized for completion of the proposed experimental plan, is presented in this section. Figure 4.2 shows a schematic of the complete test-bed and Figure 4.3 shows a photograph. The test-bed is composed of: a reinforced concrete reaction system; a set of six double-ended, dynamically-rated linear hydraulic actuators; a high precision servo-hydraulic motion control system and real-time kernel, and a six-DOF shake table.

The reinforced concrete reaction system is designed with a strong-floor strong-wall configuration that allows reconfigurable multi-axis dynamic testing, as shown in Figure 4.2 and Figure 4.3. The test-bed has dimensions 14 ft. x 10.5 ft. x 18 in. The reaction walls have dimensions of 5 ft. height - 16 in. thickness for the longitudinal and the left lateral side walls, and a 3 ft. height - 16 in. thickness for the right lateral side wall. A self-consolidating concrete mix with a compression resistance value f'_c equal to 4 ksi was employed for the reaction wall. The resistance was verified with a 28-day concrete cylinder tests, yielding average compression strength values of 9.5 ksi and 8.5 ksi for the concrete used in the floor and the wall, respectively. #5 rebar with yielding strength of 60 ksi is placed with 6 in spacing to resist flexural behavior. The design bending moment is chosen based on the case of maximum loading combination of two actuators acting in parallel at the very top of the wall height. In addition to the resistance, the design objective was to limit the maximum deflection of the reaction wall to be less than 0.01 in. Inserts and steel sleeves on a 5 in x 5 in grid format are embedded within the testing regions of the floor and walls.

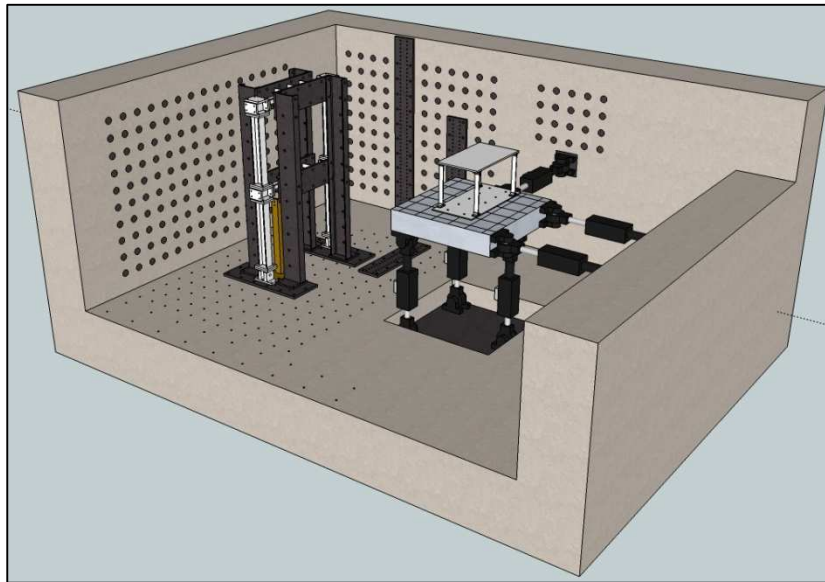


Figure 4.2: Schematic of the IISL RTHS instrument

Movable transition steel plates with mounting holes spaced over a refined grid are fixed to the wall to enable multiple hydraulic actuators to be placed in a three dimensional configuration with a minimum spacing of 1.25 in. apart. These features make the reaction system an ideal re-configurable test-bed for most types of dynamic structural testing.

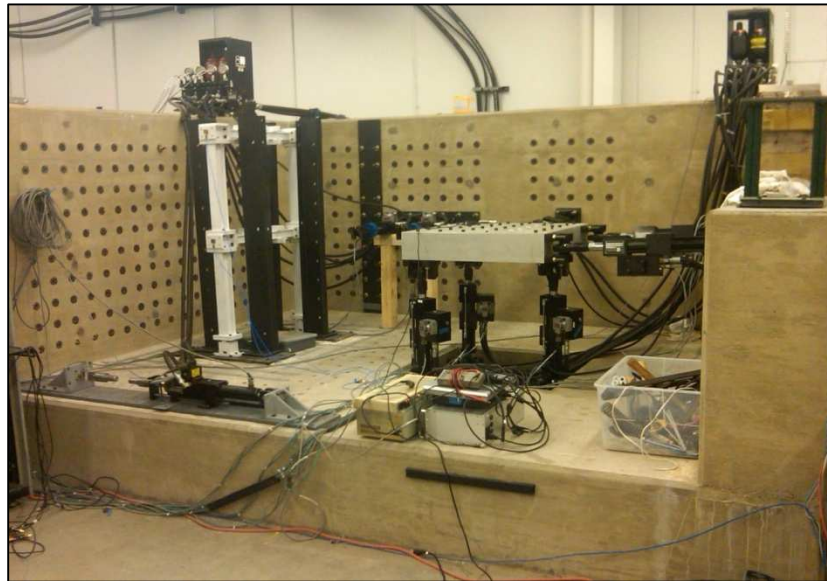


Figure 4.3: Actual view of the IISL RTHS instrument

Four of the hydraulic actuators are equipped with 10 gpm servovalves and a maximum nominal force capacity of 2.2 kips, while the remaining two with 5 gpm servovalves and 1.1 kip maximum force capacity. Each actuator is equipped with both an LVDT and a load cell, allowing for displacement, force or mixed feedback control modes. The stroke for all actuators is 4 in. 85 ft hydraulic extension lines are tied into the existing hydraulic power supply station with both pressure and return hoses of 1.25 in diameter rated at 3,000 psi. Thus, a 30-40 gpm fluid capacity can be supplied to a hydraulic service manifold with 4 independent controllable channels. This arrangement enables multiple actuators to be operated either individually or simultaneously while still meeting the nominal high force requirement.

As previously introduced in Chapter 2, *MATLAB/Simulink* is used to integrate the computational platform and the hydraulic actuator control algorithm with the remaining RTHS components so that a unified platform is generated for real-time execution. A high performance *Speedgoat/xPC* real-time system is utilized as the target PC for the proposed instrument. The *Speedgoat/xPC* is configured with an optimized state-of-the-art Core i5 3.6GHz processor for simulations with highly-intense, numerically-demanding computational models under real-time conditions. Figure 4.4 shows a photograph of the real-time kernel machine. High-resolution, high accuracy 18-bit analog I/O boards are integrated into this real-time system. This hardware supports up to 32 differential simultaneous A/D channels and 8 D/A channels, with a minimum I/O latency of less than 5 micro-seconds for all channels. This powerful component is combined with a Shore Western SC6000 analog servo-hydraulic control system to enable high precision motion control of hydraulic actuators. The succesful experimental results to be discussed in the remainder of this study indicate that the proposed instrument is appropriate for the RTHS of seismically-excited steel building structures equipped with damper devices.

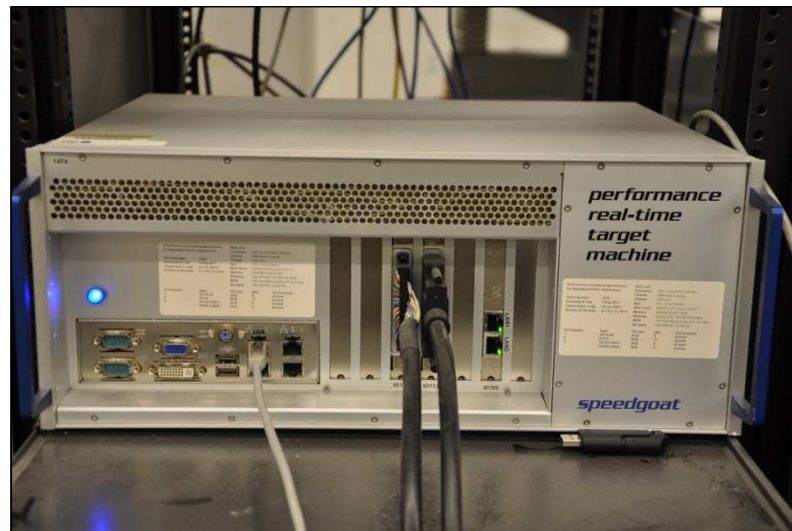


Figure 4.4: High performance *Speedgoat/xPC* real-time system

4.3 Experimental set-up

This section introduces relevant aspects in the design and modeling of the experimental components, i.e. the steel frame specimen and the MR damper specimen.

4.3.1 2D Steel frame specimen

The main provisions in the design of the steel frame specimen are presented in this section. A side view of the frame structure specimen (in white) and a bracing system (in black) to restrict out-of-the plane movement during testing is shown in Figure 4.5.

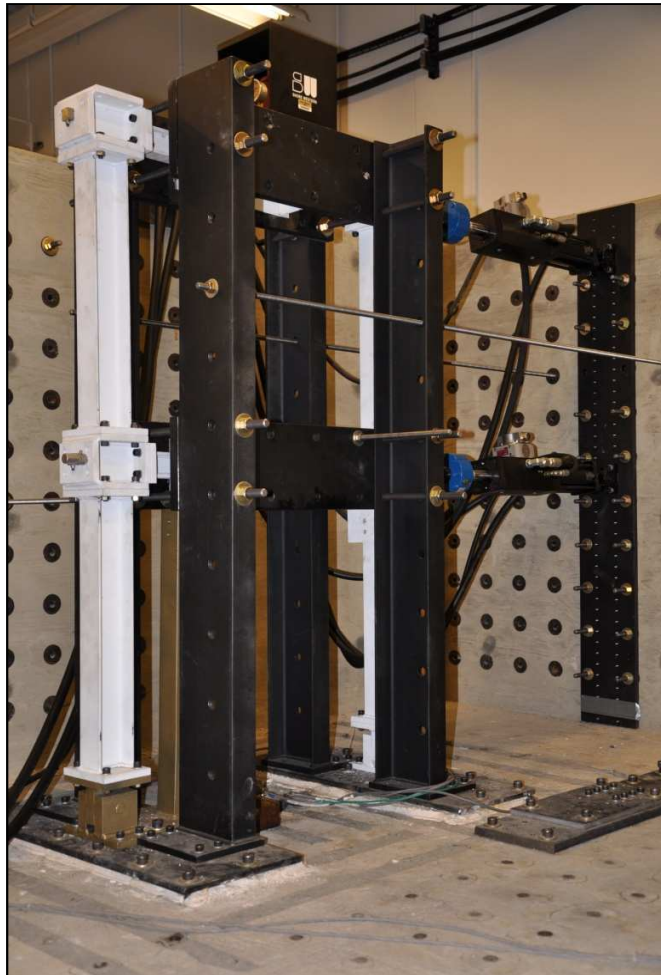


Figure 4.5: Side view of frame specimen

In order to maintain the integrity of the frame during testing, the specimen is designed with a modular approach consisting of sets of horizontal beams, vertical columns and joint block panel zone elements that can be replaced and easily re-assembled if any structural damage occurs. Moreover, a strong-column, weak-beam configuration is adopted in the design to limit the extent of damage to only beam members if the allowed overall deformation is exceeded during the test. Load demands for design purposes are selected based on regulated dynamic response criteria in addition to the force limits for the hydraulic actuators and damper device.

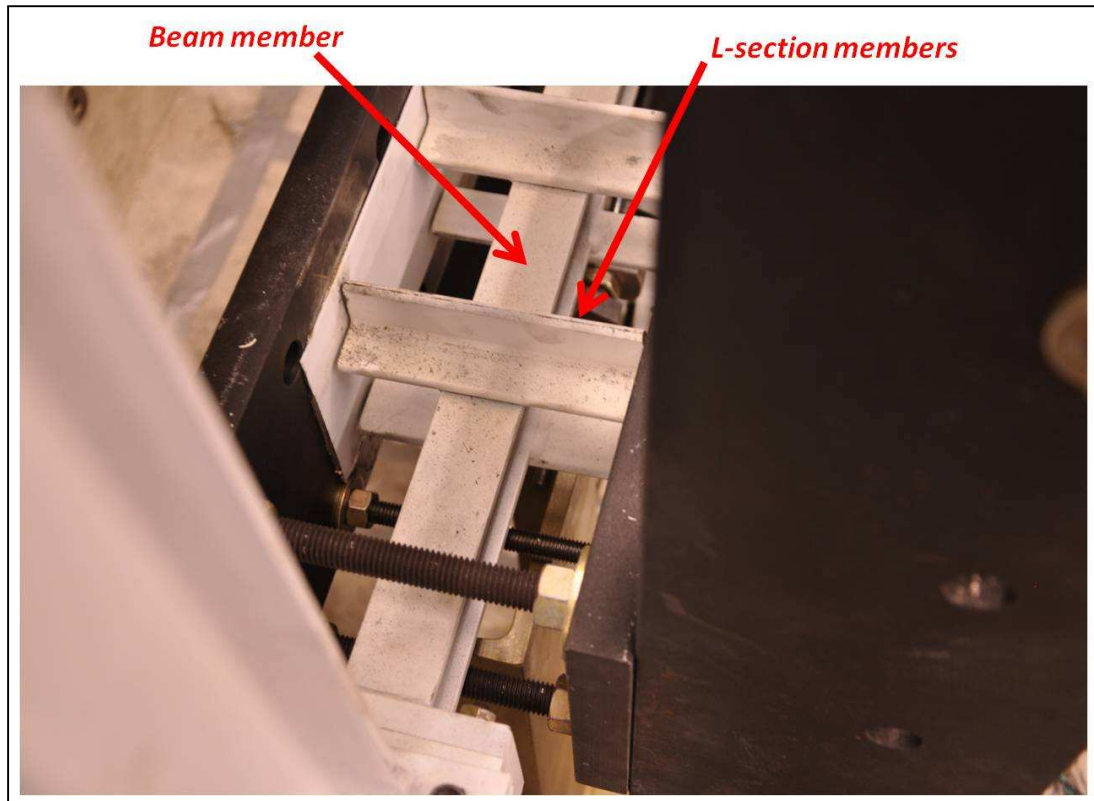


Figure 4.6: View of L-shape section and beam member attachment

Beam-column member sections are designed in accordance with AISC provisions to guarantee plastic moment failure rather than failure due to local or lateral-torsional instability. Therefore, web local buckling (WLB) and flange local buckling (FLB) are

controlled by selecting compact sections for the beam-column elements. Because beam members are expected to fail before columns due to their lower capacity, lateral-torsional buckling (LTB) is further controlled by reducing their un-braced effective length with the use of L-shape section members, as observed in Figure 4.6 and Figure 4.7. Moreover, web stability for appropriate shear design is also evaluated. As a result, capacity with respect to the previously defined loading demand is satisfied, including the moment-axial force interaction demands for column elements. Therefore, a resulting oversized column section and under designed beam section for a maximum hydraulic actuator action is obtained to guarantee failure localized to the beam members only if the loading demand is exceeded during testing, either accidentally or intentionally with the goal to impart nonlinear behavior. A S3x5.7 commercial section is selected for columns, while beams are welded from steel bars defining a section of 2x1/8 in. web and 1-1/2x1/4 in. flanges. Core regions of the panel zones are designed with steel plates of 4x3 in. and a conservative thickness of 0.75 in. to avoid any instability. Column elements are designed with a height of 21 in. and beam elements with a length of 25 in.

The final assembly defines a height to width aspect ratio of approximately $H/W=1.75$, which in conjunction to an appropriate mass preserves realistic dynamic properties of large scale building frame structures. Supports are designed to have free rotation and avoid moment actions in column members at the ground level. This behavior is achieved by the design of a special support connection with enough axial and shear strength but free rotation as shown in Figure 4.10. All components are connected through the use of anti-lock, high-strength steel bolts. This component imposes special provisions in the modeling of the frame specimen due to the flexibility induced by the presence of the bolts. Design details of main components are shown in Figure 4.7 through Figure 4.10. A final assembly drawing of the frame specimen is shown in Figure 4.11.

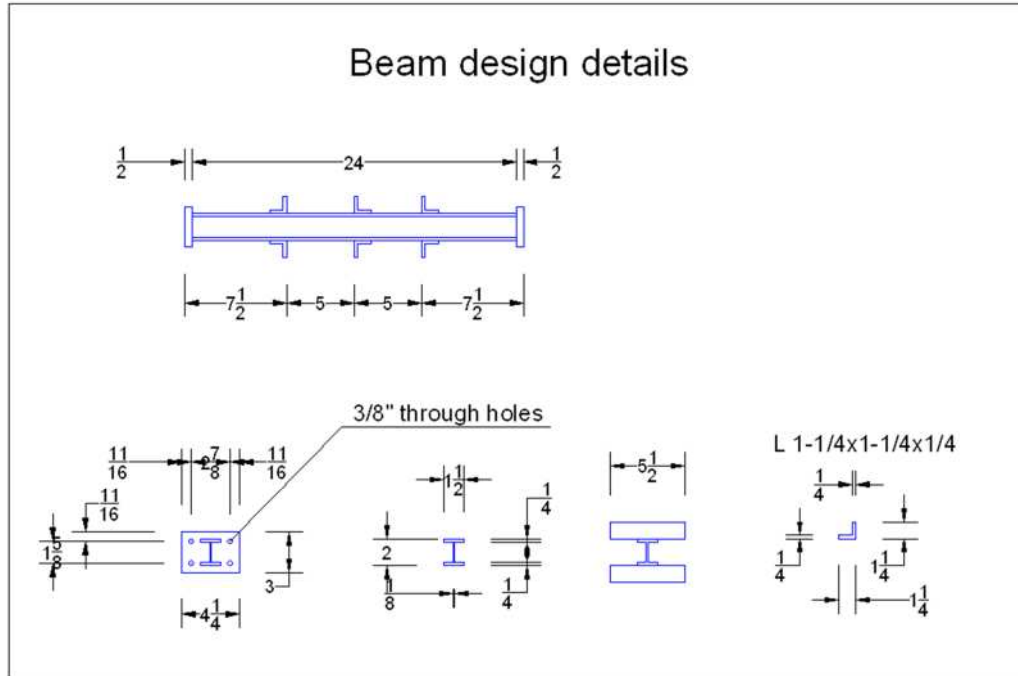


Figure 4.7: Beam design

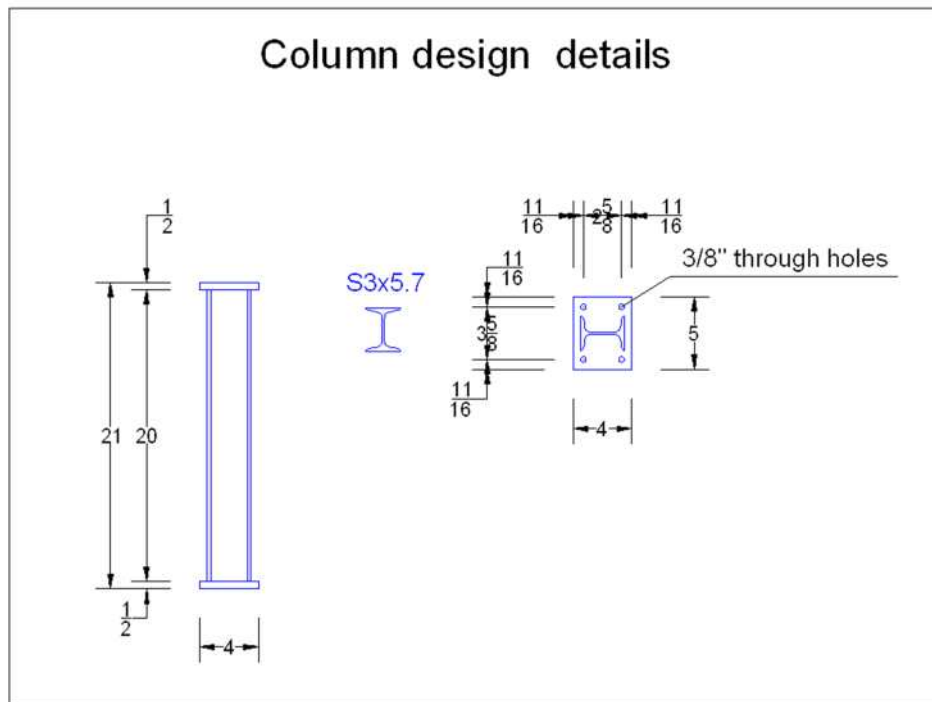


Figure 4.8: Column design

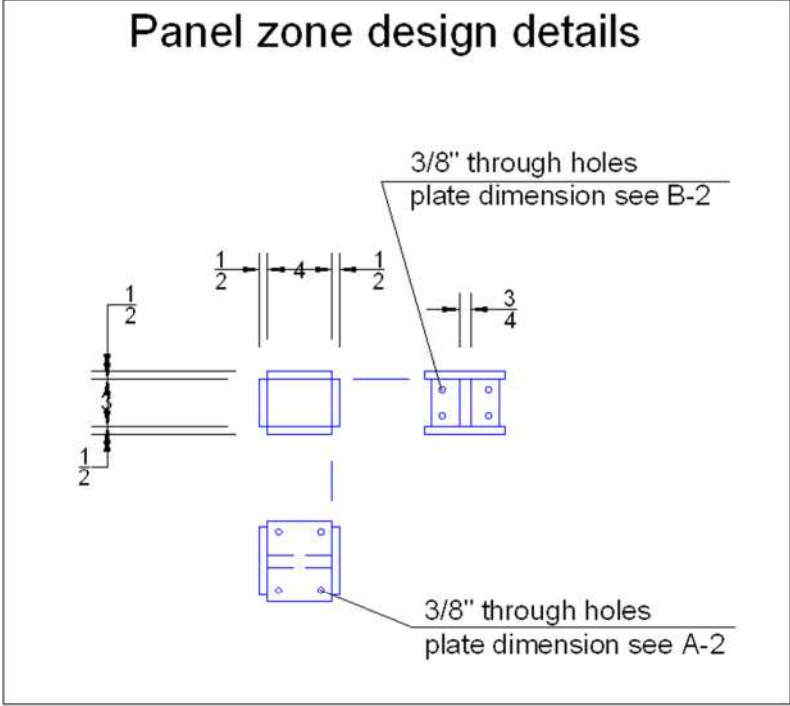


Figure 4.9: Panel zone design

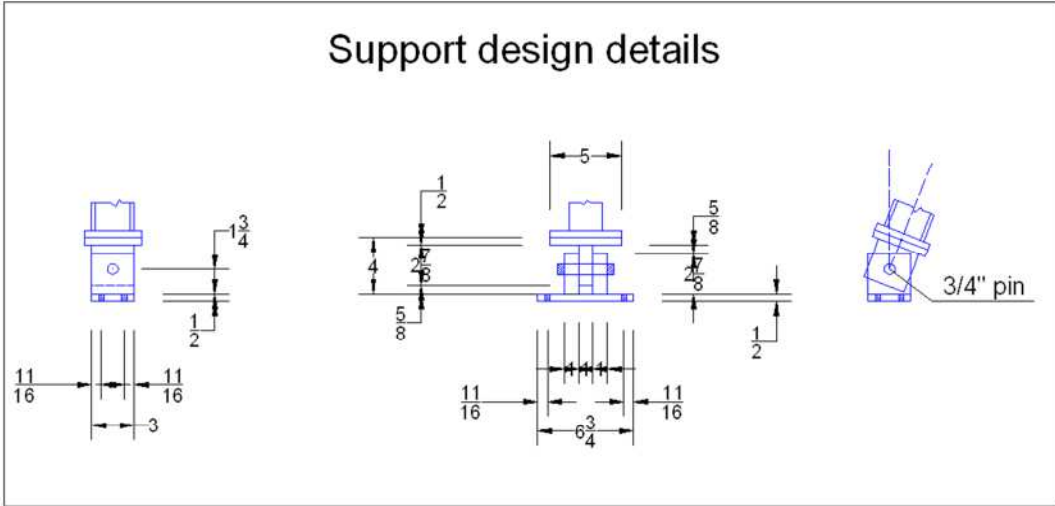


Figure 4.10: Support design

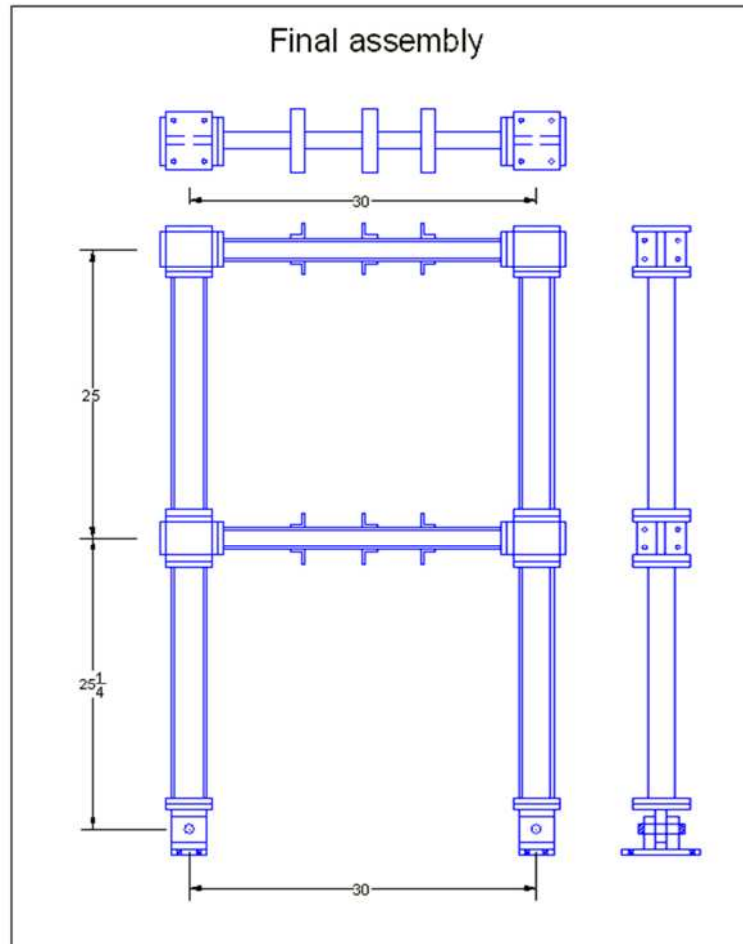


Figure 4.11: Frame structure specimen

4.3.2 Magneto-rheological (MR) damper device

This section presents relevant information for the small-scale, magneto-rheological (MR) damper utilized as the other experimental substructure in the proposed experimental plan. An MR damper is one specific class of semi-active control devices. Semi-active control devices have shown great potential for hazard mitigation in civil infrastructure due to their reduced energy demands and inherent stability nature (in the bounded input – bounded output sense) when compared to active control devices. Moreover, semi-active control devices have the potential to match the dynamic reduction performance of active

systems under strong seismic solicitations. MR damper operation is based on controllable MR fluids which are equivalent to electro-rheological fluids also considered in structural applications. MR fluids have the capacity to modify their free-flowing, linear, viscous fluid condition to a semi-solid condition in milliseconds when exposed to a magnetic field. Therefore, the MR damper force can be modified by varying the magnetic field intensity allowing for several operational control-based strategies. This behavior enables MR dampers to be very attractive for structural control applications. A view of the MR damper device currently available in the IISL at Purdue University and utilized in this experimental validation is depicted in Figure 4.12. The damper has a length of 21.5 cm in its extended position with an operational stroke of ± 2.5 cm. The main cylinder, with a diameter of 3.8 cm, contains the piston, the magnetic circuit, the accumulator and the MR fluid. The magnetic field can be varied from 0 to 200kA/m for currents of 0 to 1 amp in the electromagnet coil, which has a resistance of 4 Ω . A maximum of 10 watts is required for operation of this device. Maximum forces of 3000 N can be generated within this device with small variations over a broad temperature range (less than 10%).

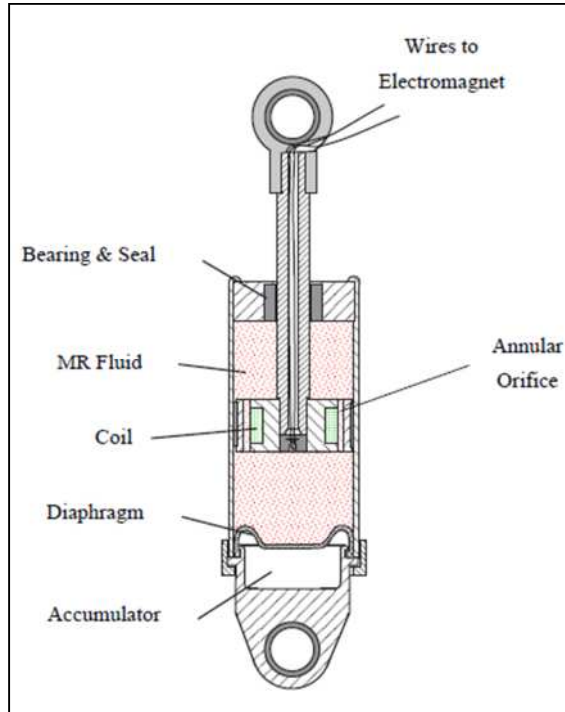


Figure 4.12: MR Damper specimen (after Dyke, 1997).

In order to perform simulation of hybrid implementations and follow-up comparison with RTHS results, a mathematical model for the MR damper is required. A well-known mathematical model for MR damper is presented in the following section.

4.3.3 Phenomenological Bouc-Wen model

Several mathematical models for replicating MR dampers behavior are proposed in the literature (for example, see: Jiang et al., 2010, Jiang and Christenson, 2012). In this study, the complex nonlinear dynamics of the MR damper mechanics are characterized using a phenomenological Bouc-Wen mechanical model (Spencer et al, 1997; Dyke et al., 1997). Figure 4.13 shows a schematic view of the mechanical analogy of the proposed model for reference.

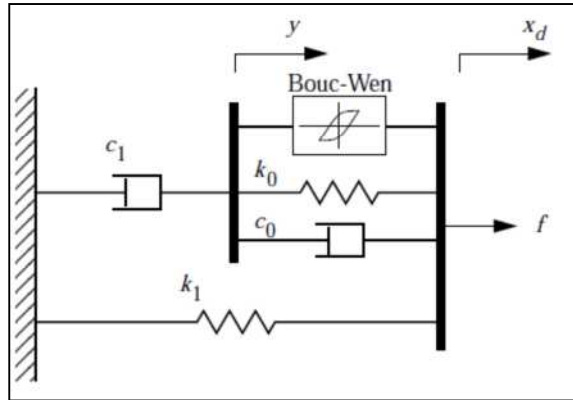


Figure 4.13: Bouc-Wen mechanical model (after Dyke, 1997).

The MR damper force is calculated in the phenomenological Bouc-Wen model with the following equations

$$f = \alpha z + c_0(\dot{x}_d - \dot{y}) + k_0(x_d - y) + k_1(x_d - x_0) \quad (4.1)$$

where the evolutionary variable z and the state variable y can be found by solving the nonlinear state equations

$$\dot{z} = -\gamma \left| \dot{x}_d - \dot{y} \right| \bullet z \bullet |z|^{n-1} - \beta (\dot{x}_d - \dot{y}) |z|^n + A (\dot{x}_d - \dot{y}) \quad (4.2)$$

$$\dot{y} = \frac{1}{(c_0 + c_1)} [\alpha z + c_0 \dot{x}_d + k_0 (x_d - y)] \quad (4.3)$$

Here, γ, β and A are parameters that control the linearity in the unloading and the smoothness of the transition from the pre-yield to the post-yield region. The spring k_1 represents the accumulator stiffness with an initial displacement x_0 , while k_0 controls the stiffness at large velocities. c_0 is the viscous damping observed at large velocities, while the dashpot c_1 is included to produce a force roll-off effect observed in experimental data at low velocities. These parameters are calibrated based on experimental data with an optimization procedure explained in the next section.

4.3.4 MR Damper device characterization

Parameters of the proposed Bouc-Wen model are calibrated using experimental data. The data is acquired with a test that measures the damper response under various operating conditions. Characterization testing is performed by subjecting the MR damper to a sinusoidal displacement input with fixed amplitude-frequency and a constant input voltage. The test is accomplished with a hydraulic actuator load frame, and is repeated for various frequencies and control voltage values. A wonder box device is used to generate and control the current signal that is applied to the MR damper based on a linearly proportional voltage. This voltage can be directly set to a defined value or externally controlled from a power supply unit. In this study, the MR damper is characterized using

a 2.5 Hz sinusoid displacement signal with amplitude of 0.2 in under four constant voltage levels, 0V, 1V, 2V, and 3V. Because there is a functional dependency of the MR damper with the magnetic field, some of the parameters in the proposed mathematical model are defined as a function of the applied voltage (or current). Dyke (1996) showed that for this MR damper device, the parameters α, c_0 and c_1 vary linearly with the applied voltage over the region of interest. These parameters are calibrated based on two sub-parameters defining linear voltage dependence as

$$c_0 = c_{0a} + c_{0b}u \quad (4.4)$$

$$c_1 = c_{1a} + c_{1b}u \quad (4.5)$$

$$\alpha = \alpha_a + \alpha_b u \quad (4.6)$$

where the dynamics in the MR fluid is defined in terms of the voltage v applied to the current driver as

$$\dot{u} = -\eta(u - v) \quad (4.7)$$

All of the model parameters are then identified based on the experimental data using a constrained nonlinear optimization. The optimization is performed using the curve fit tool *lscurvefit* available in *MATLAB*. The resulting calibrated Bouc-Wen model parameters are shown in Table 4.2.

Table 4.2: Identified Bouc-Wen model parameters

<i>Parameter</i>	<i>Value</i>	<i>Unit</i>
α_a	10.97	<i>lb/in</i>
α_b	33.59	<i>lb/in-V</i>
c_{0a}	3.72	<i>lb-sec/in</i>
c_{0b}	5.96	<i>lb-sec/in-V</i>
c_{1a}	11.93	<i>lb-sec/in</i>
c_{1b}	82.14	<i>lb-sec/in-V</i>
k_0	11.08	<i>lb/in</i>
k_1	0.01	<i>lb/in</i>
γ	23.44	<i>in⁻²</i>
β	23.44	<i>in⁻²</i>
A	155.32	-
x_0	0.00	<i>in</i>
n	2	-
η	60.00	<i>sec⁻¹</i>

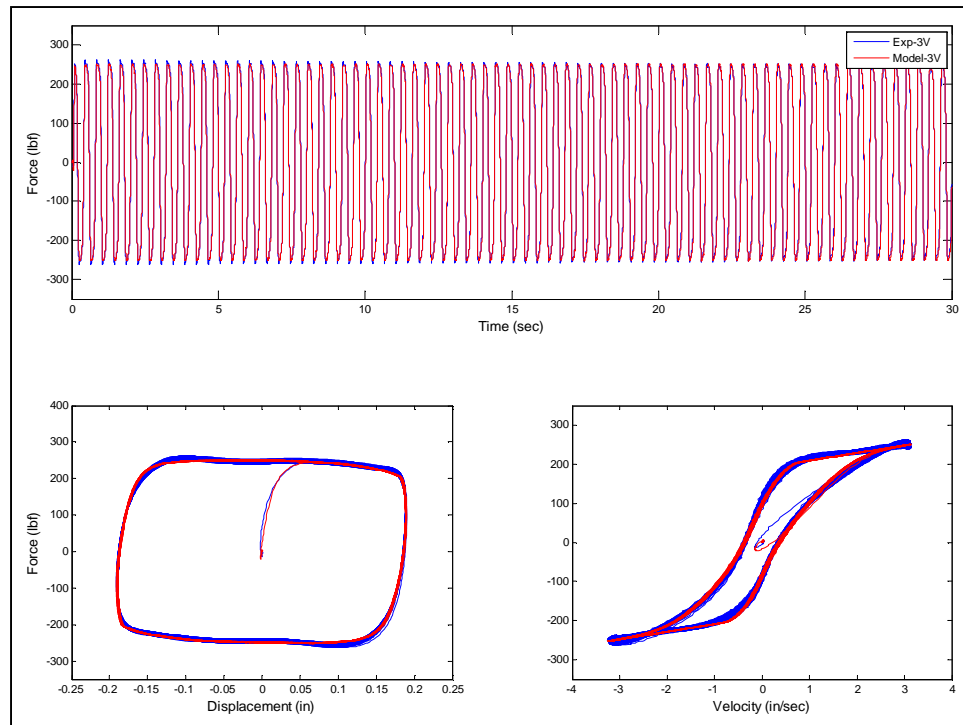


Figure 4.14: Comparison of calibrated MR Damper model

A comparison between the MR damper response predicted with the updated Bouc-Wen model and experimental MR damper response is shown in Figure 4.14. Both records are acquired when the MR damper is subjected to 3V control voltage. Good agreement is observed between the model and experiment, indicating that the updated model is sufficiently accurate for simulation and follow up comparison.

4.3.5 Hydraulic actuator compensation scheme

The H_∞ control strategy (Glover and McFarlane, 1989), designed and implemented by Gao (2012) for the RTHS test-bed at the IISL, is adopted for the compensation of hydraulic actuator dynamics in the proposed experimental plan. A summary of the proposed control strategy and design philosophy are discussed in this section. An adequate hydraulic actuator control methodology is a key component to achieving accurate RTHS performance and guaranteeing stability as shown previously. The control strategy must enforce the requirement that computed displacements are applied precisely to the experimental substructures under real-time execution. A block diagram representation of the controller structure is depicted in Figure 4.15.

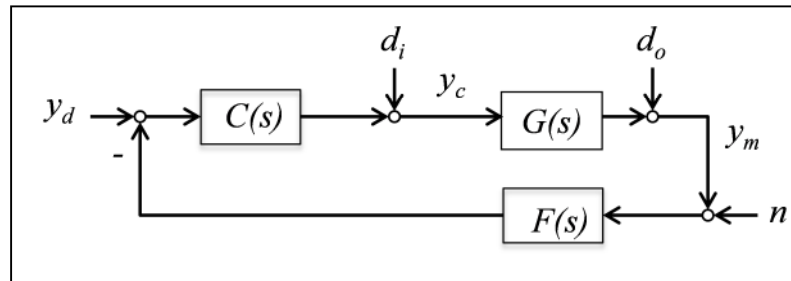


Figure 4.15: Tracking control system formulation (after Gao et. al., 2012)

Here, the plant, G , contains the overall dynamics including the inner-loop servo-hydraulic actuation and control system. The design objective is to develop a stable outer-loop controller C that facilitates the best tracking of the desired trajectory y_d

(calculated from the computational substructure) as evaluated through the measured response y_m (measured from the experimental substructure). A unity gain low pass filter, F , is inserted into the feedback path for practical implementation to reduce the effect of measurement noise n , where d_i and d_o are generalized input and output disturbances respectively. System output sensitivity and complementary sensitivity are defined, respectively, as

$$S_o = (I + GC)^{-1} \quad (4.8)$$

$$T_o = I - S_o = GC(I + GC)^{-1} \quad (4.9)$$

where the dynamical output is then calculated as

$$y_m = T_o(y_d - n) + S_o G d_i + S_o d_o \quad (4.10)$$

From the previous equation, a high performance tracking controller, i.e. $y_m \rightarrow y_d$, with strong disturbance rejection can be achieved by setting T_o close to unity and S_o to zero. This performance is achieved by selecting a large open loop gain GC , as implied by Equations (4.8) and (4.9). As presented by Gao et al. (2012), the loop gain is defined as the maximum singular value of a generalized multi-input, multi-output (MIMO) system that is equivalent to the magnitude of the transfer function in the special case of a single-input, single-output (SISO) system. However, an aggressive controller with an unrealistically large loop gain may cause system instabilities. Such instability would be due to the un-modeled dynamics and unstructured uncertainties of the plant that are present in high frequency ranges and usually not considered in the plant identification. The last leads to a trade-off design philosophy between a large loop gain for accurate

tracking on low frequency range and a small loop gain for robust performance at high frequency range. Moreover; an undesirable high loop gain at high frequency ranges may cause noise being passed through the system and even result in actuator saturation. The actuator control design can be visualized in Figure 4.16 where a typical transfer function of the hydraulic actuator plant with the proposed control strategy is depicted. A transfer function (black color) obtained when a unity gain low pass filter is considered to reduce the noise effect in the actuator control performance is also added. Note that the insertion of the unity gain low pass filter further improves the phase-lag tracking. Despite the nearly perfect tracking performance achieved with this control strategy, certain degree of magnitude amplification in the resulting closed-loop transfer function is observed due to the presence of the filter. Therefore, certain provisions must be considered for evaluating RTHS applications under specific operational bandwidths or considerable noise content.

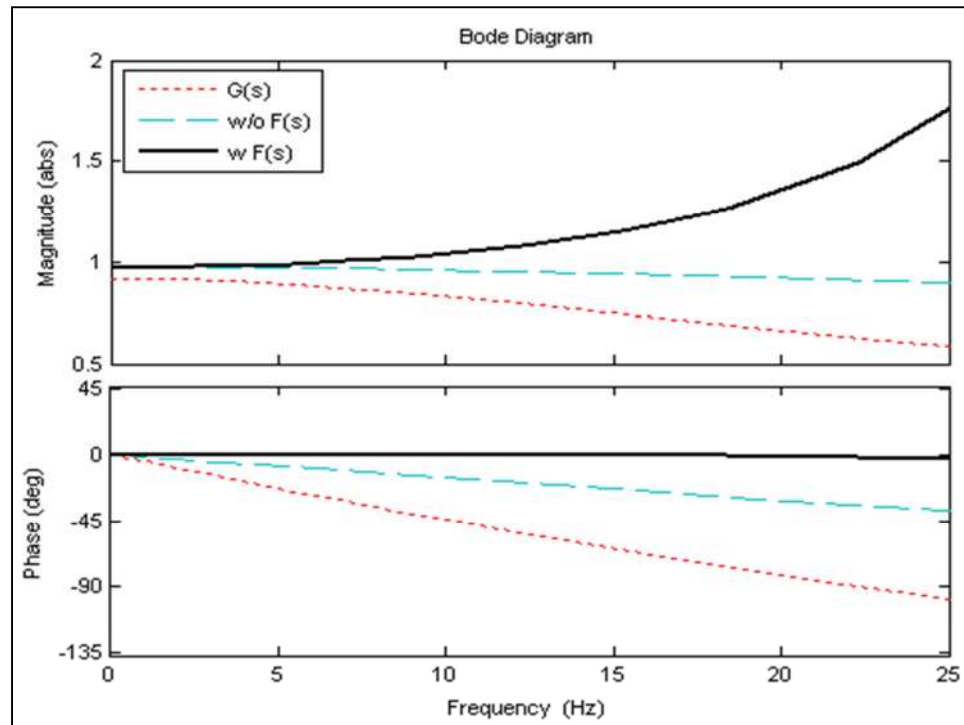


Figure 4.16: Hydraulic actuator transfer functions (after Gao et al., 2012)

Figure 4.16 also shows the transfer function of the hydraulic actuator plant without compensation for comparison purposes. A more complete description of the control design and system evaluation can be found in (Gao et al., 2012) where extensive experimental evidence is provided to demonstrate both the controller effectiveness and robustness to accommodate large system uncertainties in the plant.

4.4 Performance evaluation of RTHS

The main sources of error during RTHS execution and definition of validation norms for performance evaluation are summarized in this section. Errors induced by dynamical feedback systems such as those representing a real-time hybrid simulation are cumulative and can significantly affect the accuracy or exceed the stability limits of the test (Shing and Mahin, 1987). Sources of RTHS errors are mainly due to inaccurate computational restoring force calculations, inaccurate experimental feedback restoring force measurements, and potential instabilities in the integration scheme when solving the equation of motion. This cumulative pattern of error effects is evident in Figure 4.17 where a conceptual schematic of RTHS architecture is depicted.

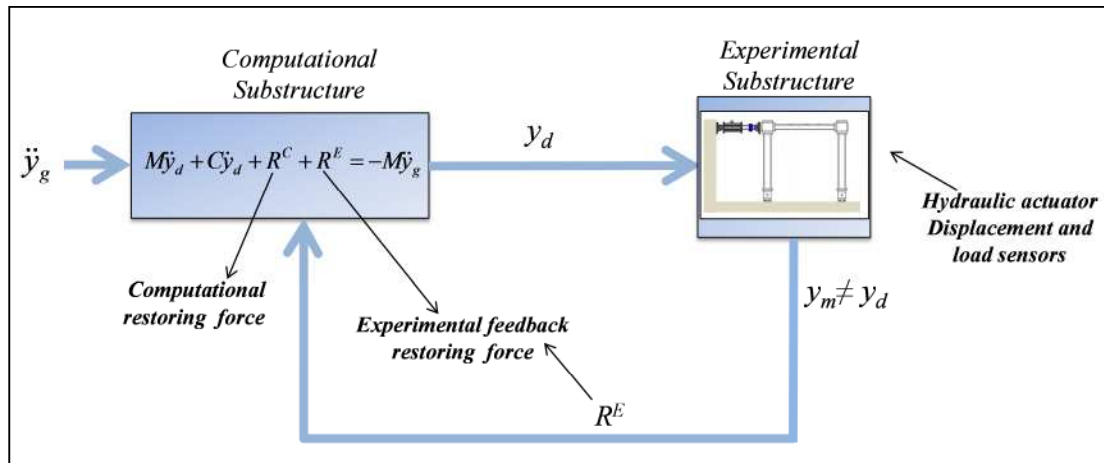


Figure 4.17: Proposed RTHS platform architecture.

As observed, calculation of desired displacements y_d at the computational substructure block is compromised by the error from the computational restoring force R^C and the experimental feedback restoring force R^E while the equation of motion is solved in terms of a ground motion record \ddot{y}_g and computational mass and damping. Note that measured displacement y_m is typically different than the desired displacement y_d due mainly to the hydraulic actuator dynamics, leading to errors in R^E measurement and possibly compromising the RTHS system stability, as explained in Chapter 1.

Errors in the computational restoring force calculation can occur due to inaccurate updating of the nonlinear restoring force and tangent stiffness matrix states at the element level. For instance, the state determination for certain nonlinear displacement-based beam-column elements that are defined with a reduced order mesh could become inaccurate under highly nonlinear responses. However, a more refined mesh would significantly increase the execution time and potentially exceed the real-time timing constraints. State determination for elements with pre-convergence demands based on fixed iteration nonlinear solvers to achieve real-time constraints can also lead to inaccuracies.

In RTHS, inappropriate selection and setup of the integration scheme for solving the equations of motion can also lead to inaccurate results and potential instabilities. For instance, reduce order convergence demands for a nonlinear solver with a fixed iteration pattern for enforcing global equilibrium in implicit integration schemes could not only induce inaccuracies but also instabilities. Moreover, conditionally-stable explicit integration schemes can trigger stability limits in the RTHS execution when large time steps are used. Conversely, when small time steps are selected, real-time execution constraints can be compromised. The impact of the integration scheme selection on RTHS performance has been extensively studied (Shing and Mahin, 1984; Shing et al., 1991, Shing and Vannan, 1991). Criteria for selection of appropriate numerical modeling

schemes along with an adequate integration scheme for performing accurate and stable RTHS implementations have been extensively discussed in Chapter 2.

Errors in the experimental feedback restoring force could be due to hardware and incorrect alignment in the experimental set-up but mainly to the inevitable delays during RTHS execution. These delays may result due to the time elapsed in the calculation of desired displacements at the computational substructure, data exchange between computational and experimental substructures and more importantly from the phase lag induced by the hydraulic actuator dynamics when desired displacements are applied to the experimental substructures. Because of this dynamic phase lag, desired displacements are not imposed on time to the experimental substructures producing incorrect restoring force measurements. Moreover, stability limits for the overall closed-loop RTHS dynamics can be triggered by the presence of this phase-lag, as discussed in Chapter 1.

An error index is proposed for evaluation and validation of accuracy and stability of the results when using RT-Frame2D computational platform in a real-time hybrid simulation. This index is defined as the RMS value of the normalized RTHS error. The RTHS error at time “ k ” is defined as the difference between simulated response $y_{sim,k}$ of the RTHS implementation and the RTHS computed (desired) response $y_{d-RTHS,k}$, calculated with the computational platform block during the RTHS execution. The RTHS error index is defined as

$$E_{RTHS} = \sqrt{\frac{\frac{1}{N} \sum_{k=1}^N (y_{Sim,k} - y_{d-RTHS,k})^2}{\frac{1}{N} \sum_{k=1}^N (y_{Sim,k})^2}} \times 100\% \quad (4.11)$$

Additionally, a tracking command error index is also considered for reference. This index is defined as the RMS value of the normalized tracking error. The tracking error at time “ k ” is defined as the difference between the computed (desired) response $y_{d-RTHS,k}$ from the computational model block and the measured response $y_{m-RTHS,k}$ acquired from the load cell at the hydraulic actuator. The tracking error index is defined as

$$E_{Tracking} = \sqrt{\frac{\frac{1}{N} \sum_{k=1}^N (y_{d-RTHS,k} - y_{m-RTHS,k})^2}{\frac{1}{N} \sum_{k=1}^N (y_{d-RTHS,k})^2}} \times 100\% \quad (4.12)$$

4.5 Implementation – I

Implementation-I evaluates the dynamic response of the one-story, one-bay configuration of the frame structure when subjected to ground motion through the RTHS Phase-2 scenario. No damper device is considered in this implementation.

As established in the experimental plan, the simulated responses of the hybrid system are required for evaluation of the performance of the computational platform. Therefore, an updated full-DOF computational model of the frame structure is developed using RT-Frame2D. The model is constructed based on the geometry and member section properties of the one-story one-bay configuration of the frame structure specimen introduced in Section 4.3.1. Columns and beams are modeled with *linear elastic beam-column element with flexible connections* element. These elements are selected to account for the flexibility induced by the connection bolts between the beam-column and panel zone members. The *linear deformable panel zone* model with three deformation modes is used to model the joint block panel zone members under a plane stress assumption. The

modulus of elasticity and Poisson's ratio values for steel are selected as 29,000 ksi and 0.3, respectively. These values are assumed to be equal for all of the specimen members. Damping is determined based on a Rayleigh damping assumption with a critical modal damping ratio of 2%. Boundary conditions are defined in agreement with the specimen supports, i.e. fixed translation and free rotation. Global constraints of equal translational horizontal DOF at the story level is also considered. Therefore, the resulting computational model has 4 nodes – with 8 active global DOF.

Model updating is performed by identification of a parameter k defined as the stiffness value for the zero-length rotational springs that model the flexible connections at beam-column ends. This parameter is identified based on the one-DOF experimental stiffness value of the frame specimen determined based on a push-over test. Only a one-DOF experimental stiffness value is considered because only one actuator is utilized.

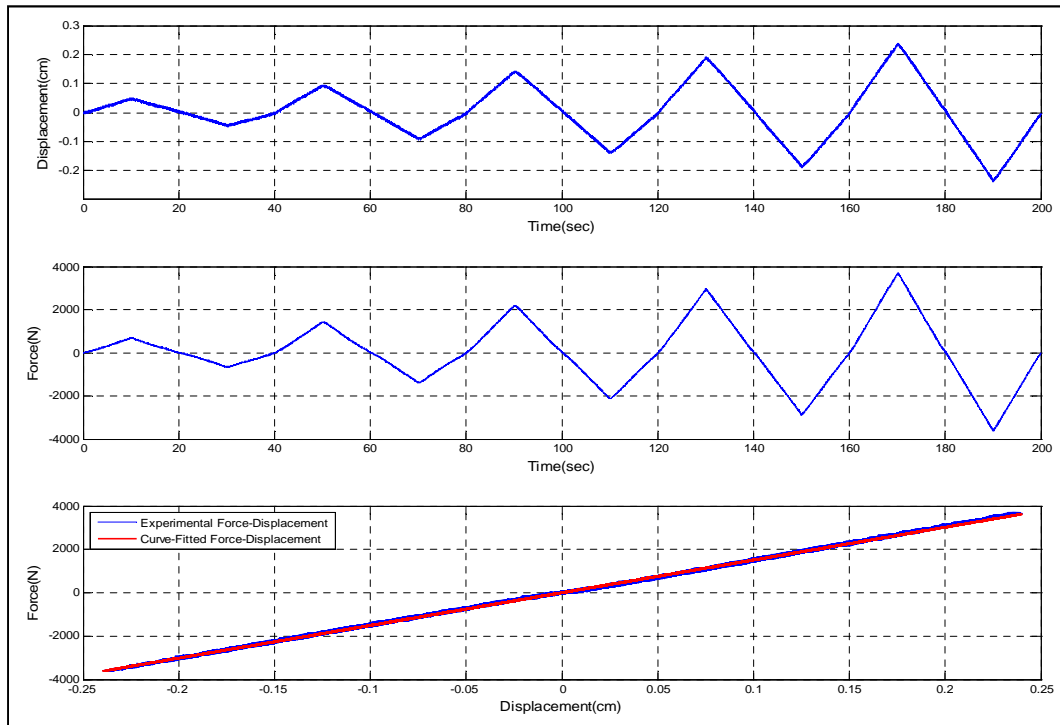


Figure 4.18: Push-over test results

The push-over test is also used to check the linear state and adequate assembling of the frame structure before testing. Therefore, force and displacement are measured continuously while a monotonically increasing force is applied to the specimen by the hydraulic actuator. A well-defined linear correlation between measured values is obtained, thus ensuring an adequate condition for testing as observed in Figure 4.18. A resulting experimental stiffness value of 1.5e4 N/cm (8.6 kip/in) is obtained from the previous measurements using a curve fit and used for model updating. The model updating is performed by an optimization procedure based on the minimization of the *Frobenius* norm of the difference between the experimental stiffness matrix and the computational stiffness matrix, defined as function of unknown model updating parameters p , i.e. k in this case. The objective function is expressed as

$$\tilde{K}a(p) \Leftrightarrow \min_p \left(\|A(p)\|_F^2 \right) \quad (4.13)$$

where $A(p)$ is calculated as

$$A(p) = \tilde{K}s - \tilde{K}ac(p) \quad (4.14)$$

Here $\tilde{K}a(p)$ is the full-DOF computational stiffness matrix in terms of the unknown model updating parameters p . $\tilde{K}ac(p)$ is the condensed stiffness matrix of $\tilde{K}a(p)$ and $\tilde{K}s$ is the identified experimental stiffness matrix (one-DOF value in this case). The optimization problem is solved using the MATLAB function *fmincon*, from which a minimum value of k equal to 2.4e6 N-m is obtained for the objective function. Therefore, the dimensions for the computational model are defined in agreement with the frame specimen specifications. Panel zone members are modeled using a 4x3 in. dimensions and 0.75 in. thickness. The height H is set to 25.25 in. and the width L is set to 30 in. Figure 4.19 shows the computational model of the frame structure indicating the updated variables, i.e. the location for the flexible connections along with other elements.

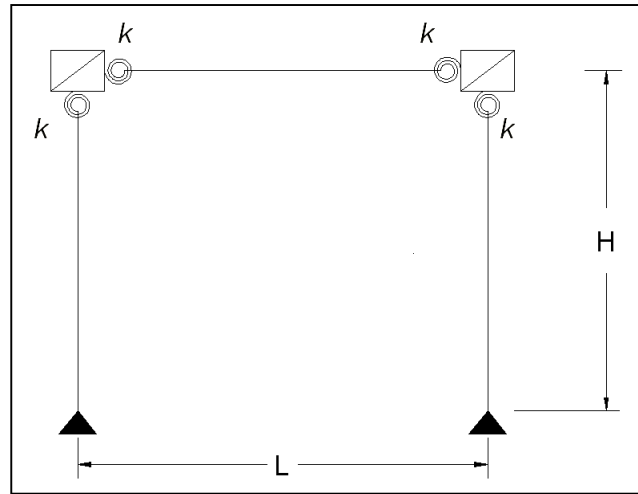


Figure 4.19: Computational model for Implementation-1

As further verification, experimental natural frequency of the frame specimen based on only self-weight is compared to the one calculated with the updated model. The peak-picking technique in the frequency domain is used to identify the corresponding natural frequency from measured system transfer function of an impulse test and a band-limited white noise (BLWN) test. The BLWN test is performed by applying a broad-band excitation signal with a bandwidth of 0-500 Hz to the hydraulic actuator. Experimental natural frequency values of 42.8 Hz for the impulse test and 37.2 Hz for the BLWN test are identified. These values are compared with the natural frequency values calculated with the updated computational model an equal to 42.6 Hz and 35.1 Hz, respectively. Good agreement is observed between both sets with only a small discrepancy in the BLWN results due to the uncertainty of the actual mass contribution by the hydraulic actuator when attached to the frame.

Two RTHS scenarios are tested using the N-S component recorded at the Imperial Valley Irrigation District substation in *El Centro*, California, during the Imperial Valley, California earthquake of May 18, 1940. Mass selections, frequency content and earthquake intensities at each scenario are shown in Table 4.3.

Table 4.3: Testing scenarios description

<i>Test</i>	<i>EQ Intensity</i>	<i>Mass (kg)</i>	<i>Frequency (Hz)</i>	E_{RTHS}	$E_{Tracking}$
1	0.05	20000	1.40	24.22	8.00
2	0.40	2000	4.40	16.43	5.75

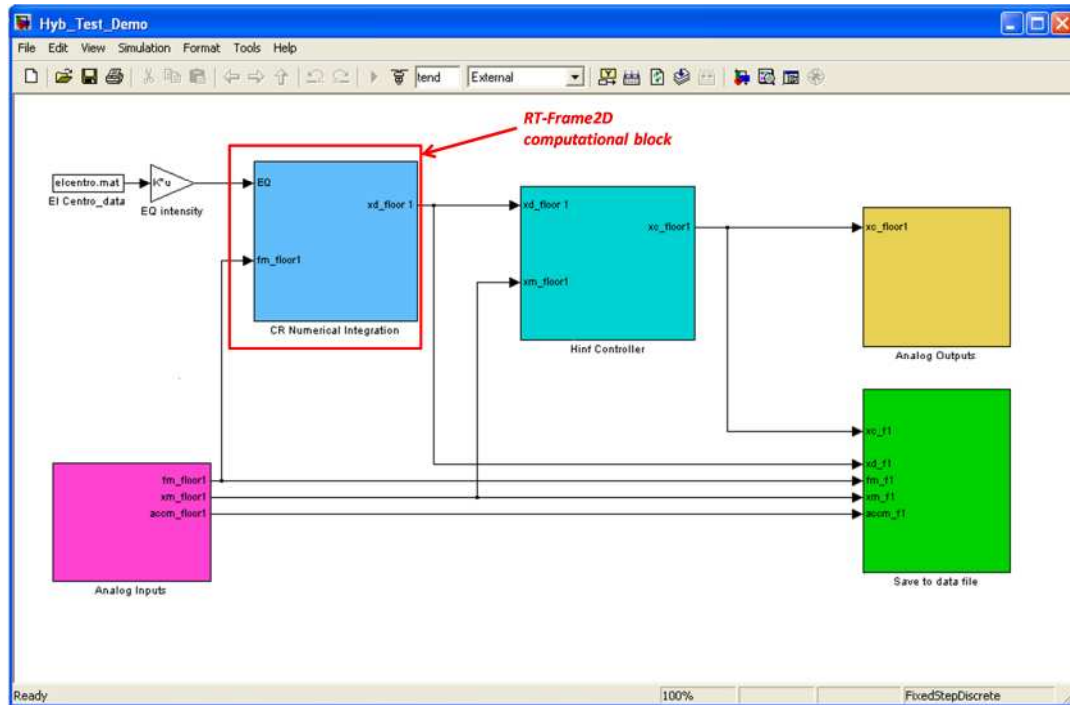


Figure 4.20: *Simulink* platform for Implementation I

The frame structure specimen is considered as the one-DOF experimental substructure and the associated mass as the computational substructure within Implementation-I. Damping is considered to be the same as that defined for the simulation and comparison, i.e. a 2% fundamental damping ratio. Therefore, a one-DOF RT-Frame2D computational block solves the equation of motion within the *Simulink* implementation using the CR integration scheme and two inputs. These inputs include the restoring force exerted by the frame specimen when is being continuously displaced and the ground motion record. Therefore, displacements computed at 1024 Hz are imposed onto the frame specimen by the use of a hydraulic actuator. The experimentally measured restoring force, used for

feedback, is measured with the load cell attached to the hydraulic actuator. The same hydraulic actuator control design is used for both tests since the same physical substructure is utilized. A view of the *Simulink* platform showing the computational block used for implementation I is depicted in Figure 4.20.

Time history records of the displacement of the RTHS and corresponding simulation outputs are plotted simultaneously in Figure 4.21 and Figure 4.22 for each RTHS case. Only 50 sec of the response is included for visibility. Additional plots showing zoomed views of records in early stages of the motion are also included. As observed, good overall agreement between both RTHS and simulated displacement responses is achieved for each case demonstrating the accuracy and stability of the proposed computational RT-Frame2D platform as well as the hydraulic actuator control.

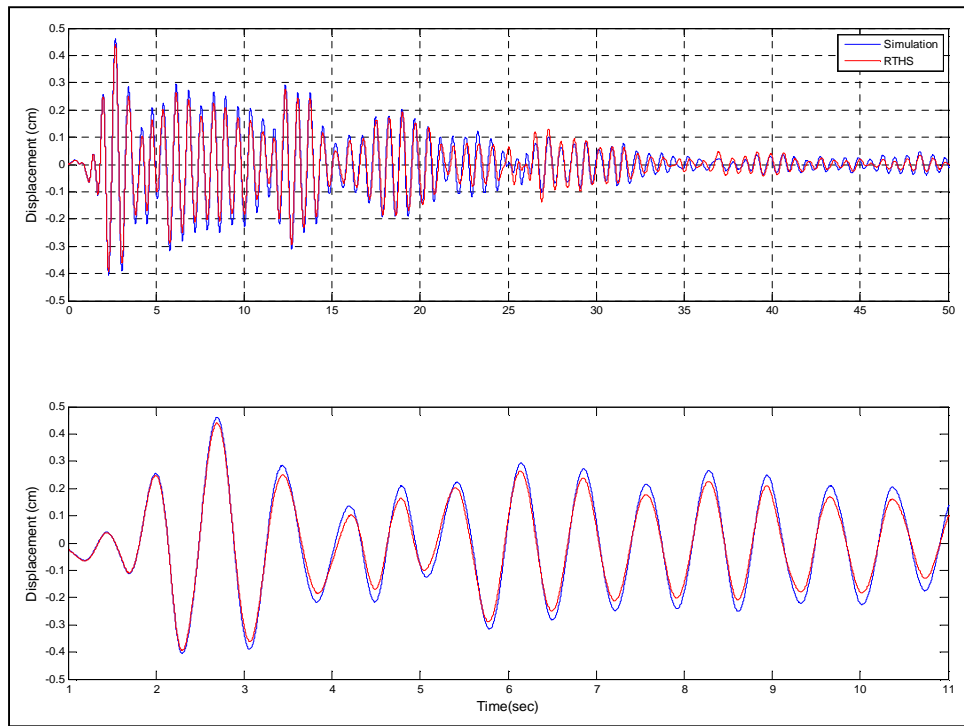


Figure 4.21: Comparison for the 20000 Kg-mass case

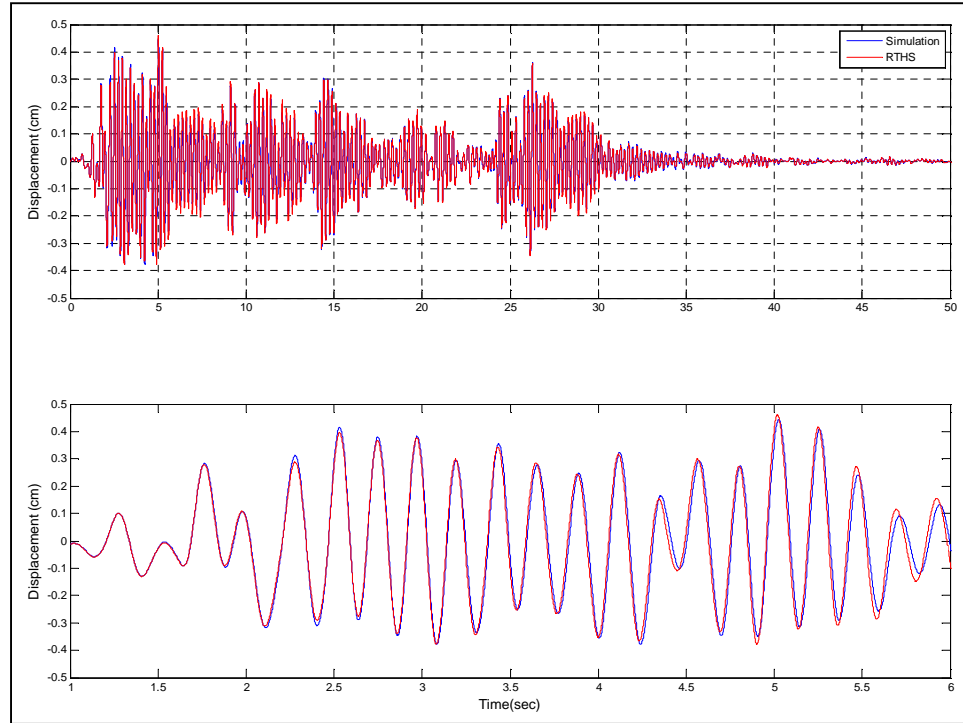


Figure 4.22: Comparison for the 2000 Kg-mass case

RTHS error values calculated Equation (4.11) for both testing scenarios are listed in Table 4.3. Note that these values represent a measure of the error for the entire time history. Therefore, minor differences at certain intervals of the displacement records may have significant impact in the calculation of the error. This observation becomes more evident in later experimental results. Table 4.3 also lists error values for actuator tracking control. These error values show the same tendency as the RTHS error values, i.e. greater value for the 20000-Kg mass case.

Error for the RTHS performance in Implementation-I may be mostly attributed to the stability in the integration scheme and the influence of noise in both the measured displacement for actuator tracking control and experimental restoring force used within the computational block. Computational restoring forces are not included in this selection because most of it comes from the experimental counterparts. The stability of the CR integration scheme during tests is verified based on the bounded nature of the time

history records and guaranteed by the stable poles associated to the discrete transfer function of the integration scheme. The last observation validates the adequate selection of the CR integration scheme for the proposed computational platform. However, the noise effect is slightly amplified due to the magnitude of the closed-loop transfer function associated to the actuator tracking control, as explained in Section 4.3.5. This effect becomes more pronounced in displacement signals with small amplitude yielding greater noise ratios. The last observation is the case for Implementation I in which displacement records with small amplitude are evaluated to avoid exceeding the linear-elastic state of the frame specimen. In addition to the previous considerations, RTHS error could be also attributed to the incorrect alignment in the experimental set-up and uncertainty in the experimental mass and damping.

4.6 Implementation - II

Implementation-II is performed with an equivalent hybrid scenario of Implementation-I, i.e. the RTHS Phase-2 scenario. However, a more complex case with a two-story one-bay configuration of the frame structure specimen is considered.

An updated full-DOF computational model of the frame specimen is required for performing a simulation of the hybrid system and follow-up evaluation of the computational platform performance. Thus, a computational model is constructed based on the geometry and member sections of the two-story one-bay configuration of the frame specimen introduced in Section 4.3.1. Frame specimen components are modeled with the RT-Frame2D modeling options selected in the previous section, i.e. *linear elastic beam-column element with flexible connections* and the plane-stress *linear deformable panel zone* model with a Poisson's ratio of 0.3. A damping ratio of 2% value is defined for the two first modes based on a Rayleigh damping assumption. Boundary conditions and global DOF constraints are defined as in the previous section leading to a computational model with 6 nodes and 12 active global DOF.

A more comprehensive model updating procedure is followed in this implementation. Model updating parameters are defined as the stiffness values for the flexible connections at beam-column ends, and the modulus of elasticity for each of the frame components, representing a correction in the stiffness. These nine parameters are identified based on the two-DOF experimental stiffness matrix of the frame specimen using the optimization procedure presented in the previous section. Because a two-DOF stiffness matrix needs to be identified, a dynamic parameter based identification methodology would be a natural choice. However, the accuracy of the hybrid implementation is sensitive to the feedback restoring forces measured by the load cells located at the hydraulic actuators. Therefore, a combined methodology based on three experimental quantities is utilized to identify a unique and representative stiffness matrix instead. These quantities are defined as: the stiffness value km_1 measured from a push-over test when one actuator is attached at the first floor of the specimen while the other actuator is not attached, the stiffness value km_2 measured from a push-over test when one actuator is attached at the second floor of the specimen while the other actuator is not attached, and the Frobenius norm of the identified stiffness matrix $\tilde{K}d$ of the frame specimen using a dynamic parameter based method. This approach allows for refined experimental stiffness matrix identification that preserves not only the accuracy in the restoring force measurement but also the dynamic and modal content information of the system. The previous conditions are represented by the next set of equations to calculate the entries of the experimental stiffness matrix as

$$ks_{11} - \frac{(ks_{12})^2}{ks_{22}} = km_1 \quad (4.15)$$

$$ks_{22} - \frac{(ks_{12})^2}{ks_{11}} = km_2 \quad (4.16)$$

$$\left\| \tilde{\mathbf{K}}_S \right\|_F^2 = \left\| \tilde{\mathbf{K}}d \right\|_F^2 \quad (4.17)$$

where

$$\tilde{\mathbf{K}}_S = \begin{bmatrix} k_{S11} & -k_{S12} \\ -k_{S12} & k_{S22} \end{bmatrix} \quad (4.18)$$

Here $\tilde{\mathbf{K}}_S$ is the identified experimental stiffness matrix and used for model updating using Equations (4.13) and (4.14) as explained previously. The dynamic stiffness matrix $\tilde{\mathbf{K}}d$ is identified based on the modal content information of the two-DOF experimental system (two-story frame configuration). Natural frequencies and corresponding mode shapes are extracted using the Eigensystem Realization Algorithm (ERA) (Juang and Pappa, 1985), a time domain modal identification technique. Impulse response records of acceleration data calculated through an inverse fast Fourier transform (IFFT) of impulse and BLWN transfer functions are used as input for evaluation of ERA. The impulse test is performed with an input force applied at the second level of the frame structure. The BLWN test is performed with a 0-500 Hz broad-band excitation signal applied with the hydraulic actuator at the second level.

Figure 4.23 shows the measured transfer functions from the impulse force to the first (left) and second (right) floor accelerations. Figure 4.24 shows the measured transfer functions from the actuator force to first (left) and second (right) floor accelerations. The resulting natural frequencies and normalized mode shapes identified using the ERA are shown in Table 4.4. Because of the uncertainty in the hydraulic actuator mass, modal identification results from the impulse test are selected for $\tilde{\mathbf{K}}d$ identification. However, modal results obtained with the BLWN test are used as further verification and reference.

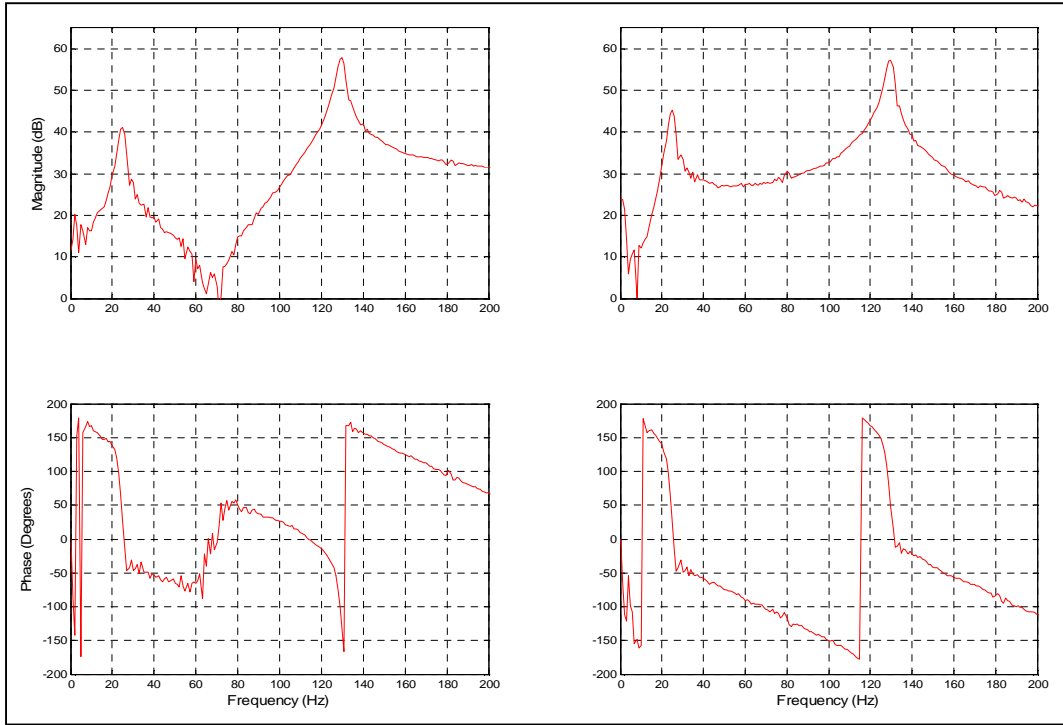


Figure 4.23: Measured transfer functions (from impulse tests)

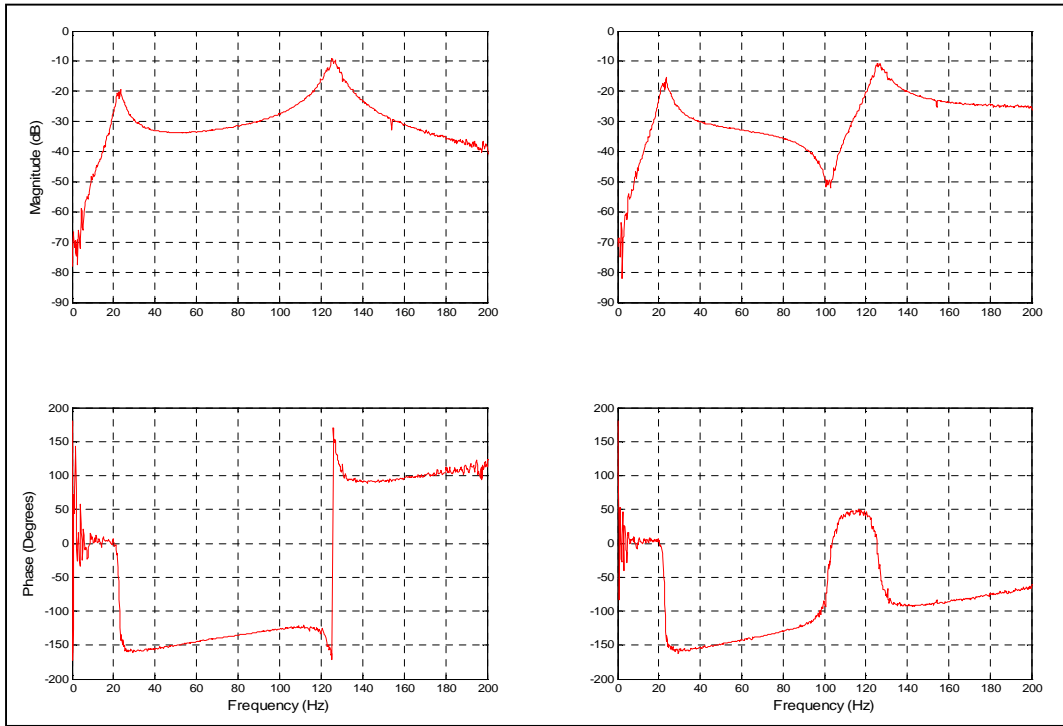


Figure 4.24: Measured transfer functions (from BLWN tests)

Table 4.4: Modal parameters identified with ERA

<i>Freq (Hz)</i>	<i>Mode Shape 1</i>	<i>Mode Shape 2</i>
<i>Impulse Test</i>		
24.70	0.42	1.00
129.20	1.00	-0.94
<i>BLWN</i>		
23.00	0.64	1.00
126.00	1.00	-0.83

The dynamic stiffness matrix, $\tilde{K}d$ is then obtained by minimizing an objective function (Zhang et. al., 2008) defined as function of $\tilde{K}d$ entries, i.e. $p = kd_{11}, kd_{12}, kd_{22}$. The objective function is defined as

$$\tilde{K}d(p) \Leftrightarrow \min_p \left(\sum_{i=1}^N \|f_i(p)\|_2^2 \right) \quad (4.19)$$

$f_i(p)$ is calculated as

$$f_i(p) = \eta [1 - \text{MAC}(\Phi_{ID,i}, \Phi_{FE,i}(p))] + \beta \left\| \frac{\omega_{ID,i} - \omega_{FE,i}(p)}{\omega_{ID,i}} \right\| \quad (4.20)$$

where

$$\text{MAC}(\Phi_{ID,i}, \Phi_{FE,i}(p)) = \frac{(\Phi_{FE,i}^T, \Phi_{ID,i}^T)^2}{(\Phi_{FE,i}^T, \Phi_{FE,i}^T)(\Phi_{ID,i}^T, \Phi_{ID,i}^T)} \quad (4.21)$$

Here N is the number of modes to be considered. η and β are weighting constants whose values are selected as 0.1 and unity, respectively. MAC is the modal assurance criteria factor (Allemang and Brown, 1982) computed between the experimentally

identified i -th mode shape $\Phi_{ID,i}$ and the computationally calculated i -th mode shape $\Phi_{FE,i}$. $\omega_{ID,i}$ and $\omega_{FE,i}$ are the experimentally identified and computationally calculated natural frequencies at the i -th mode, respectively. The previous optimization problem is solved with the *MATLAB* function *fmincon*, from which $\tilde{K}d$ is calculated. The corresponding Frobenius norm $\|\tilde{K}d\|_F^2$ is then calculated yielding a value of $1.96e7$ N/m (112.2 kip/in). Next, a km_1 value of $1.86e4$ N/cm (10.64 kip/in) and a km_2 value of $8.31e3$ N/cm (4.75 kip/in) are obtained through a curve-fit using the continuously recorded force and displacement measurements while a monotonically increasing force is applied to the specimen by the hydraulic actuator. Force-displacement records are shown in Figure 4.25 for both floors. As in the previous study, this test is also used to confirm the linear behavior and correct assembly of the frame structure prior to any testing.

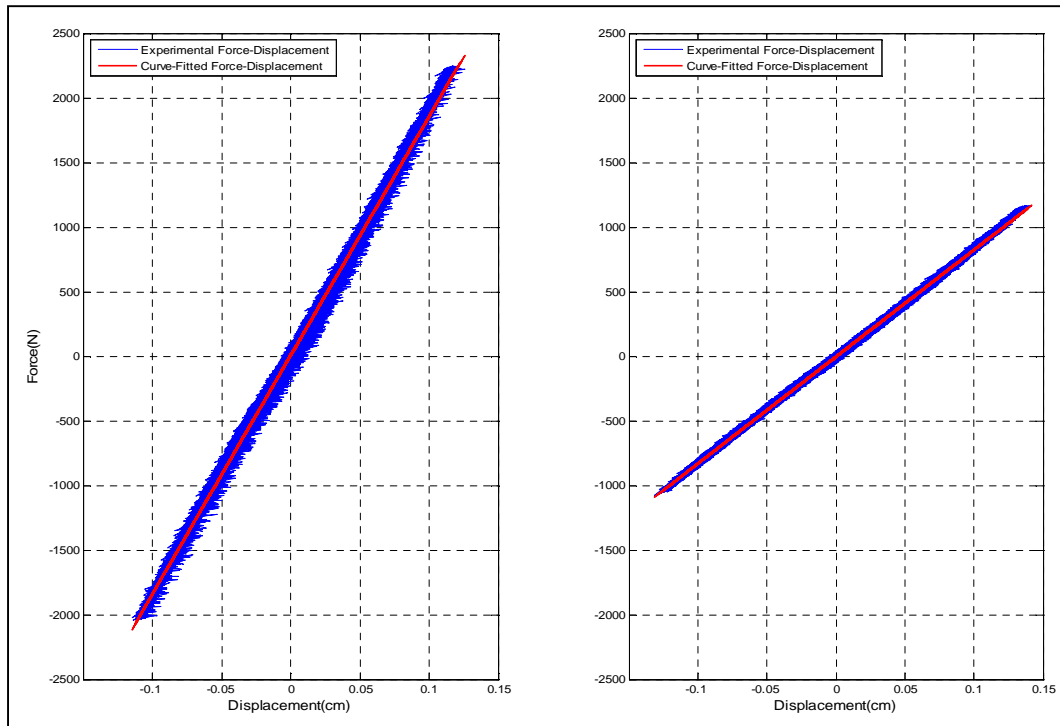


Figure 4.25: Data to obtain values of km_1 (left) and km_2 (right) stiffness parameters.

Solving Equations (4.15), (4.16) and (4.17) yields the experimental stiffness matrix \tilde{K}_S as

$$\tilde{K}_S = \begin{bmatrix} 1.39 \times 10^7 & -8.69 \times 10^6 \\ -8.69 \times 10^6 & 6.23 \times 10^6 \end{bmatrix} N/m$$

Optimal values for model updating parameters are calculated using the previous quantity in Equations (4.13) and (4.14). The final values of each parameter are shown in Table 4.5. Dimensions for the computational model are defined in agreement with the frame specimen specifications, i.e. Section 4.3.1. Therefore, panel zone members are modeled with 4x3 in dimensions and 0.75 in thickness. Height H1 is set to 25.25 in while H2 is set to 25 in. The width L is set to 30 in. Figure 4.26 shows the computational model of the frame structure indicating the updated variables, i.e. the location for the flexible connections along with other elements.

Table 4.5: Values for model updating parameters

<i>Parameter</i>	<i>Value</i>	<i>Unit</i>
<i>k1</i>	3.669e6	<i>N-m</i>
<i>k2</i>	3.661e6	<i>N-m</i>
<i>k3</i>	8.654e6	<i>N-m</i>
<i>k4</i>	8.617e6	<i>N-m</i>
<i>k5</i>	1.212e6	<i>N-m</i>
<i>k6</i>	5.436e6	<i>N-m</i>
<i>Epz</i>	29380	<i>ksi</i>
<i>Ec</i>	28500	<i>ksi</i>
<i>Eb</i>	31000	<i>ksi</i>

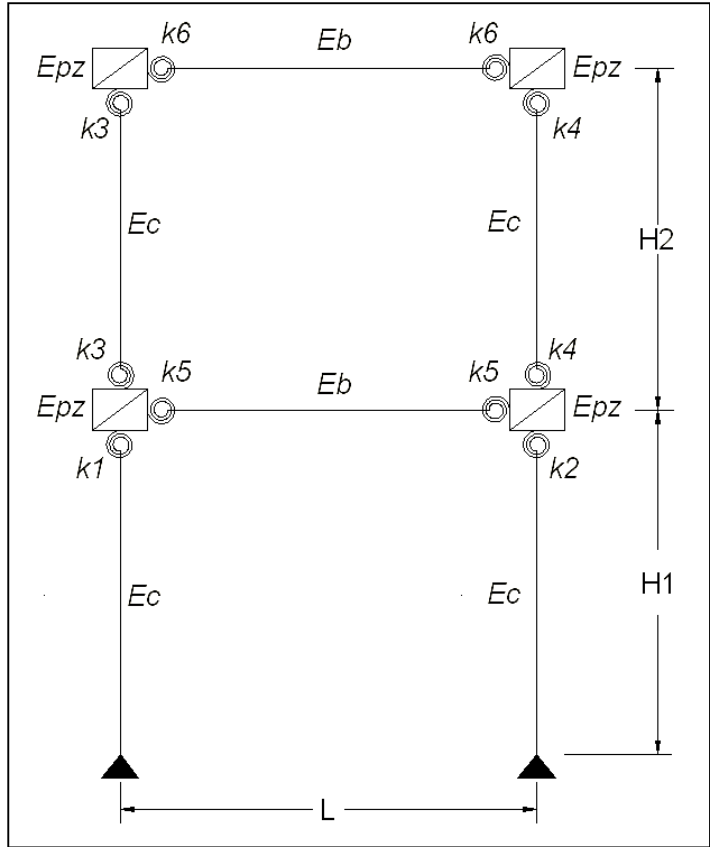


Figure 4.26: Computational model for Implementation-II

Four RTHS scenarios are tested using the N-S component recorded at the Imperial Valley Irrigation District substation in *El Centro*, California, during the Imperial Valley, California earthquake of May 18, 1940. Mass configurations at first and second floor and earthquake intensities at each scenario are shown in Table 4.6. Natural frequencies are also included for reference.

Implementation-II considers the frame specimen as a two-DOF experimental substructure with the associated mass at both levels as computational substructure components within the hybrid implementation. Damping is considered to be the same as the one defined for simulation and comparison, i.e. a 2% damping ratios for the two first modes.

Table 4.6: Testing scenarios description

<i>Test</i>	<i>EQ Intensity</i>	<i>Story</i>	<i>Mass (kg)</i>	<i>Frequency (Hz)</i>	E_{RTHS}	$E_{Tracking}$
1	0.15	1	2000	2.73	17.74	7.71
		2	2000	15.76	17.25	4.98
2	0.15	1	4000	2.39	19.03	4.35
		2	2000	12.71	18.98	3.28
3	0.10	1	4000	1.93	12.04	4.14
		2	4000	11.14	11.15	3.25
4	0.07	1	8000	1.36	8.80	4.50
		2	8000	7.88	8.00	3.33

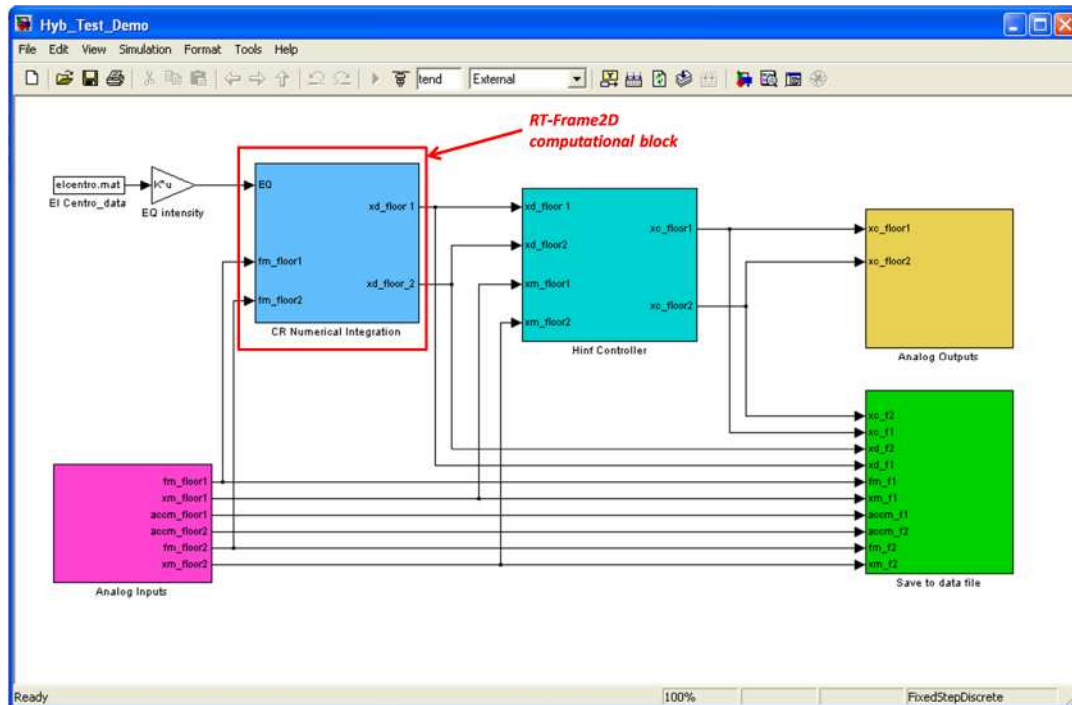


Figure 4.27: Simulink platform for Implementation II

Therefore, a two-DOF RT-Frame2D computational block solves the equation of motion within the *Simulink* implementation based on the CR integration scheme using three inputs. These inputs are defined as the restoring forces exerted by the frame specimen when displaced at each floor level and the ground motion record. Therefore, displacements computed at 1024 Hz are imposed on the frame specimen with the two hydraulic actuators. The experimental restoring forces are measured from the load cells located at the hydraulic actuators for feedback. The same hydraulic actuator control design is used for all tests because the same physical substructure is utilized. A view of the *Simulink* platform showing the computational block is depicted in Figure 4.27.

Time history records of the displacement of each floor in the RTHS, and corresponding simulation outputs, are plotted simultaneously in Figure 4.28 and Figure 4.35 for each RTHS case. 50 sec of the response is included for clarity. Additional plots showing records at the early stages of the motion are also included as a zoomed view. As observed, excellent agreement between both RTHS and simulated responses can be observed in each case, demonstrating both the accuracy and stability of the proposed computational RT-Frame2D platform as well as the hydraulic actuator control. Moreover, peak values at different stages of the motion are well captured.

Error values for RTHS performance and actuator tracking control calculated with displacement records from both floors are listed in Table 4.6. Because no computational restoring force calculation is performed in this implementation either, stability in the integration scheme performance and noise content in the experimental measurements are considered as the most probable sources of error. The stability of the CR integration scheme is still guaranteed by the stable poles of the integration block and evidenced by the bounded trend in the results. However, more evidence of the noise content influence in the RTHS results is further observed. For instance, slightly better results for both RTHS and actuator tracking control performance are observed in the second floor outputs with respect to the first floor at all testing cases. This tendency is explained because displacement outputs at the second level are larger and thus yielding smaller noise ratios.

However and despite excellent agreement between responses is shown at the different testing scenarios, error values are significant for some of them. This observation agrees with that stated in the previous implementation, i.e. differences at certain intervals of the records may have significant impact in the calculation of the error. For instance, the smallest RTHS error values are obtained for test scenarios 3 and 4 in which better agreement between records is observed. For the remaining test scenarios, considerable differences are located towards the end of the records in which amplitudes are smaller yielding greater noise ratios and leading to these differences, as previously discussed. Another interesting observation is made regarding the frequency dependency of the overall RTHS performance dynamics. Testing scenarios with close frequency content show comparable RTHS performance. Additionally, RTHS error could be also attributed to the incorrect alignment in the experimental set-up and uncertainty in the experimental mass and damping.

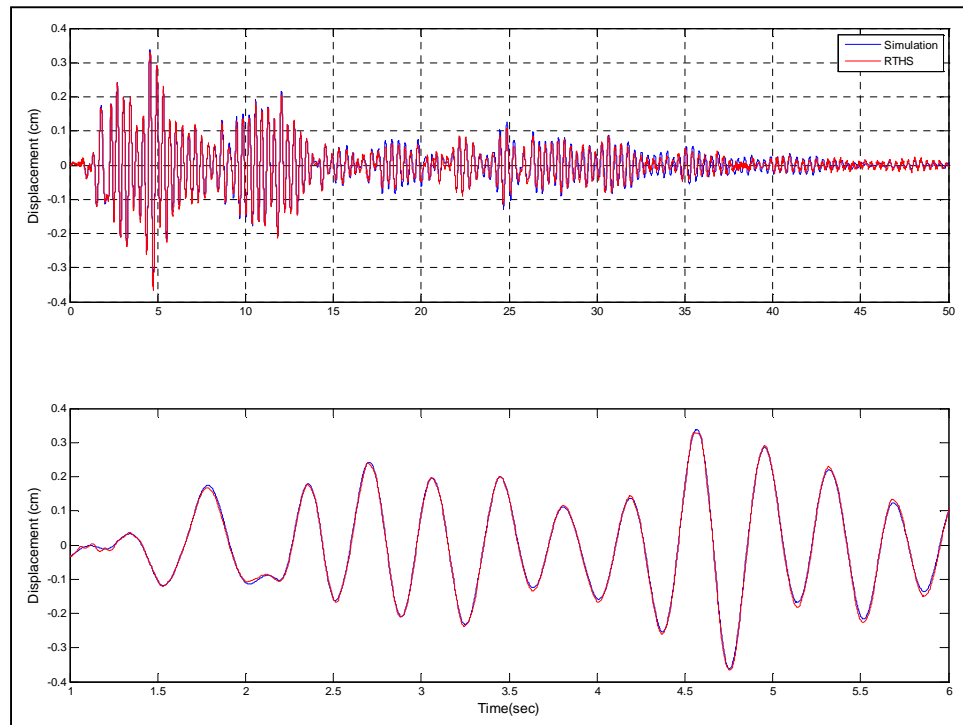


Figure 4.28: 2000/2000 Kg-mass case – Displacement first floor

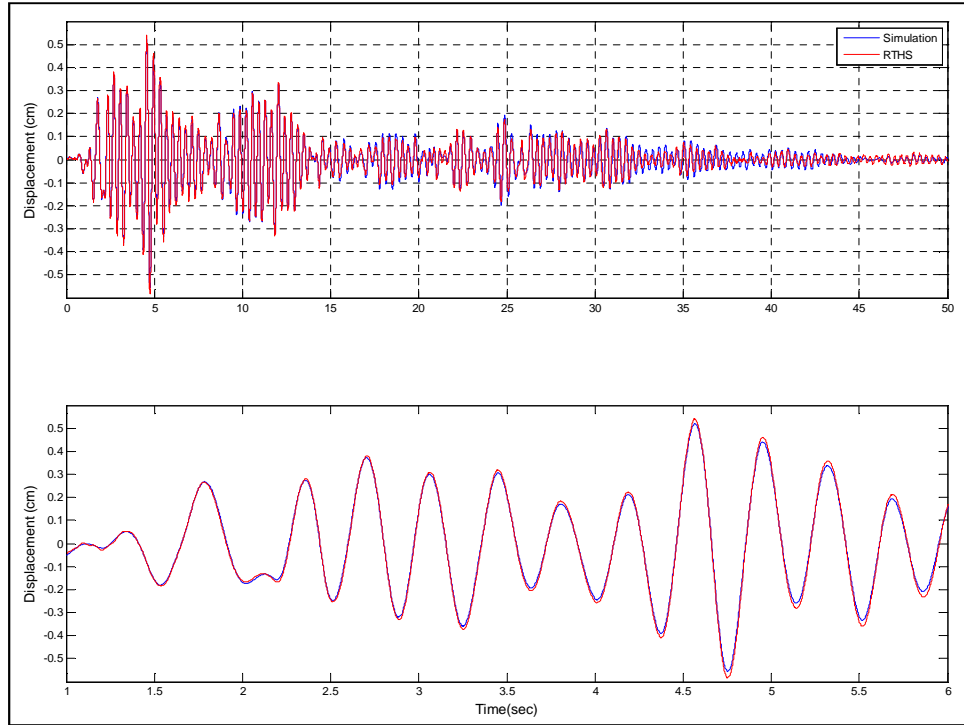


Figure 4.29: 2000/2000 Kg-mass case – Displacement second floor

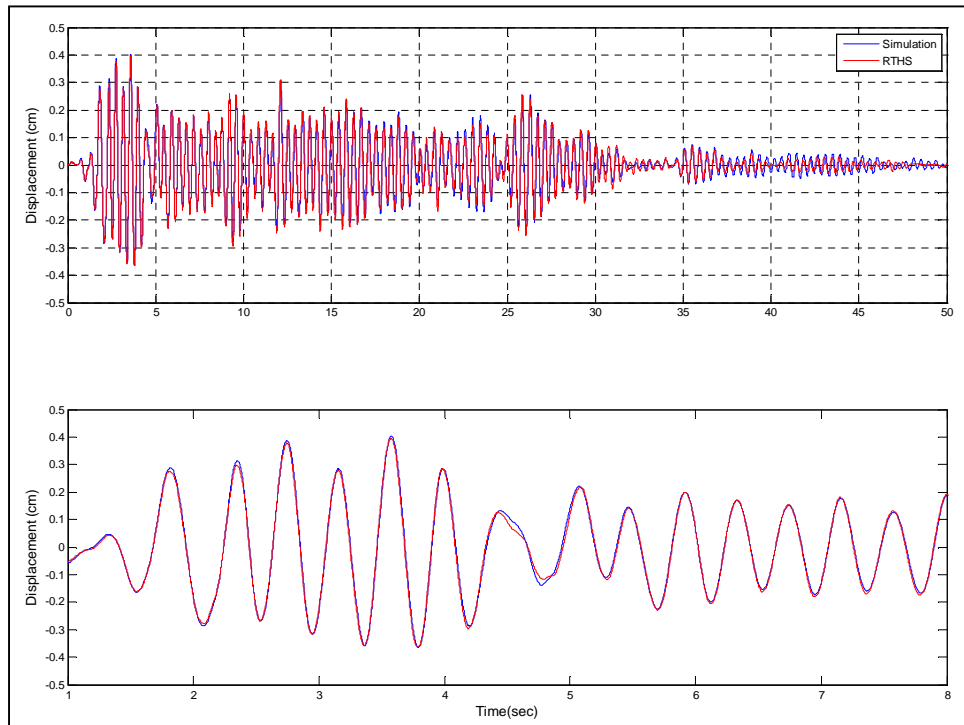


Figure 4.30: 4000/2000 Kg-mass case – Displacement first floor

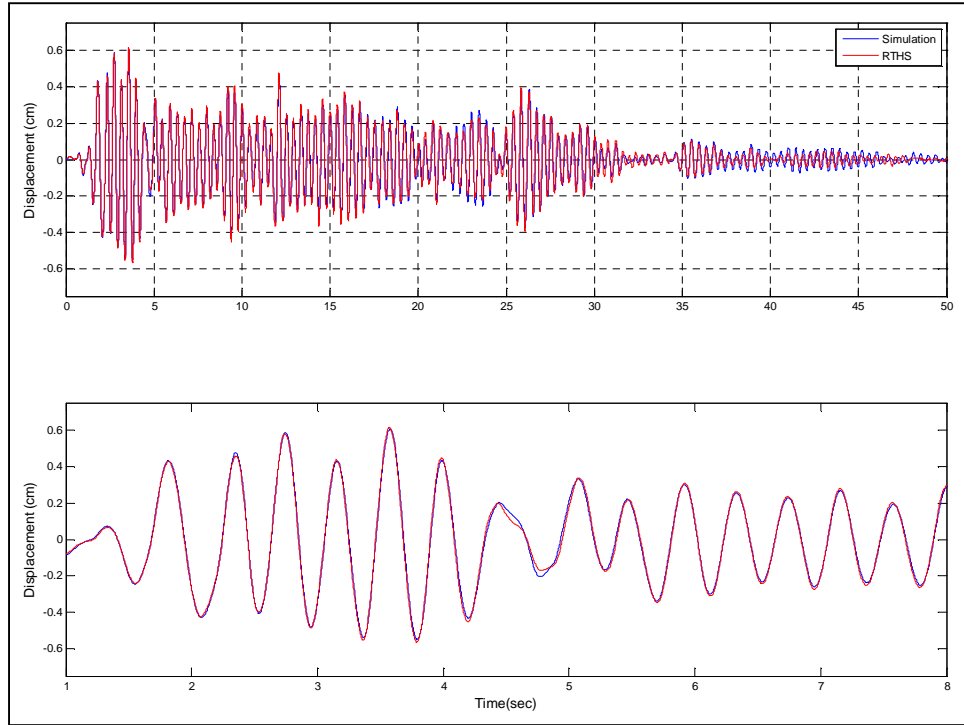


Figure 4.31: 4000/2000 Kg-mass case – Displacement second floor

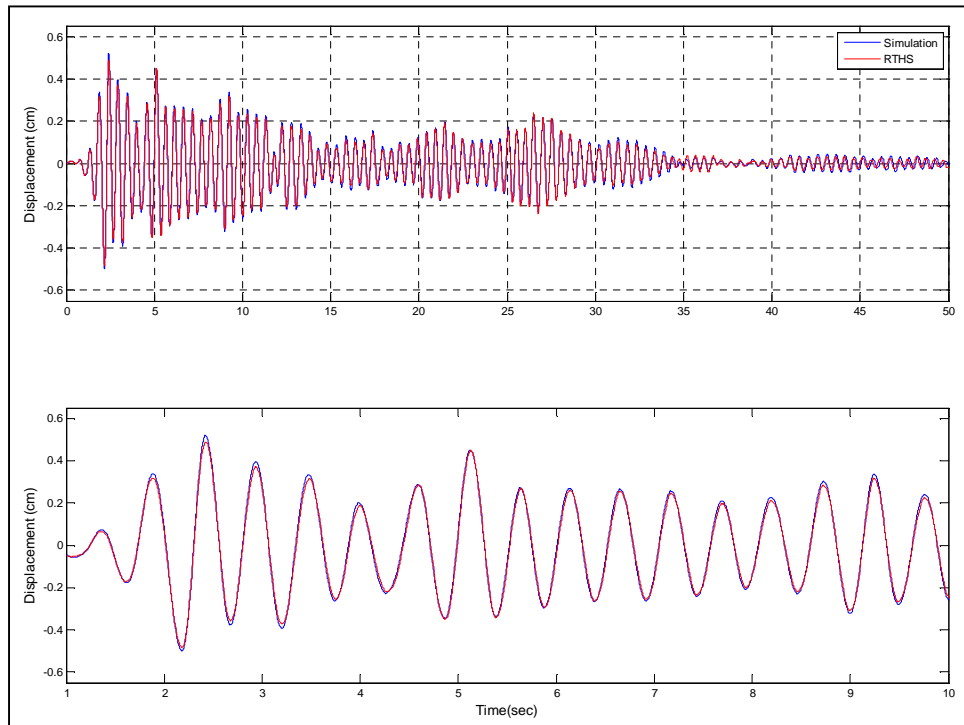


Figure 4.32: 4000/4000 Kg-mass case – Displacement first floor

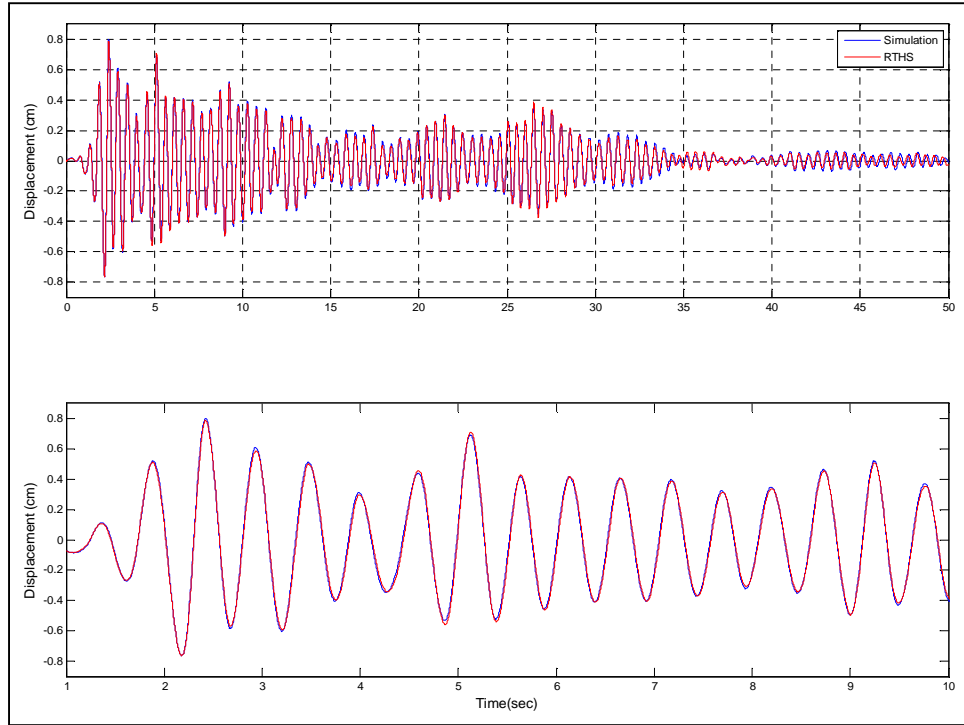


Figure 4.33: 4000/4000 Kg-mass case – Displacement second floor

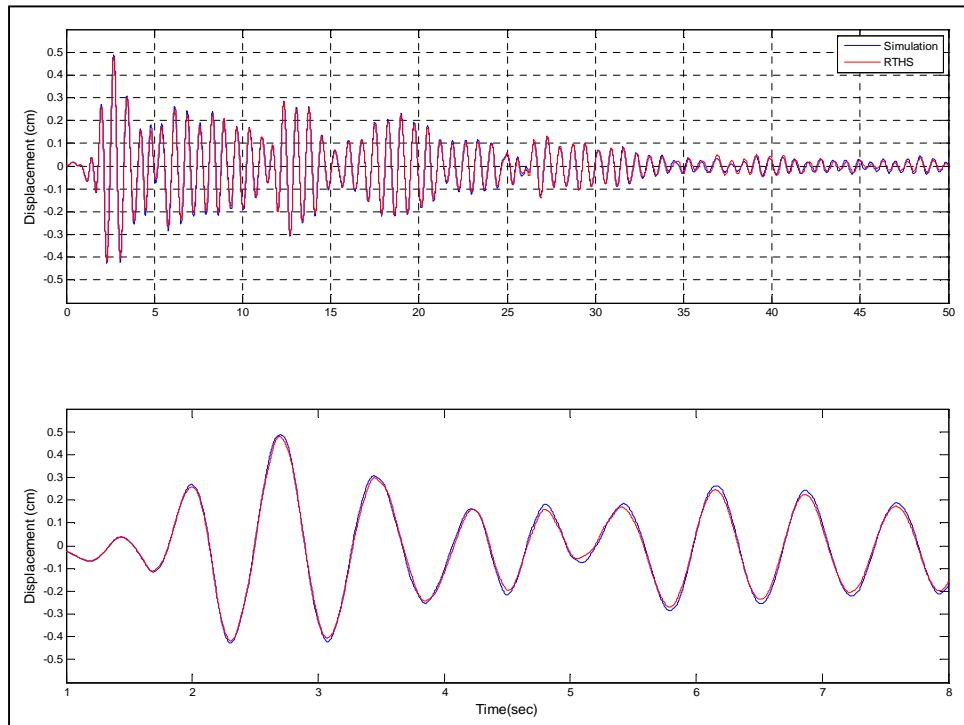


Figure 4.34: 8000/8000 Kg-mass case – Displacement first floor

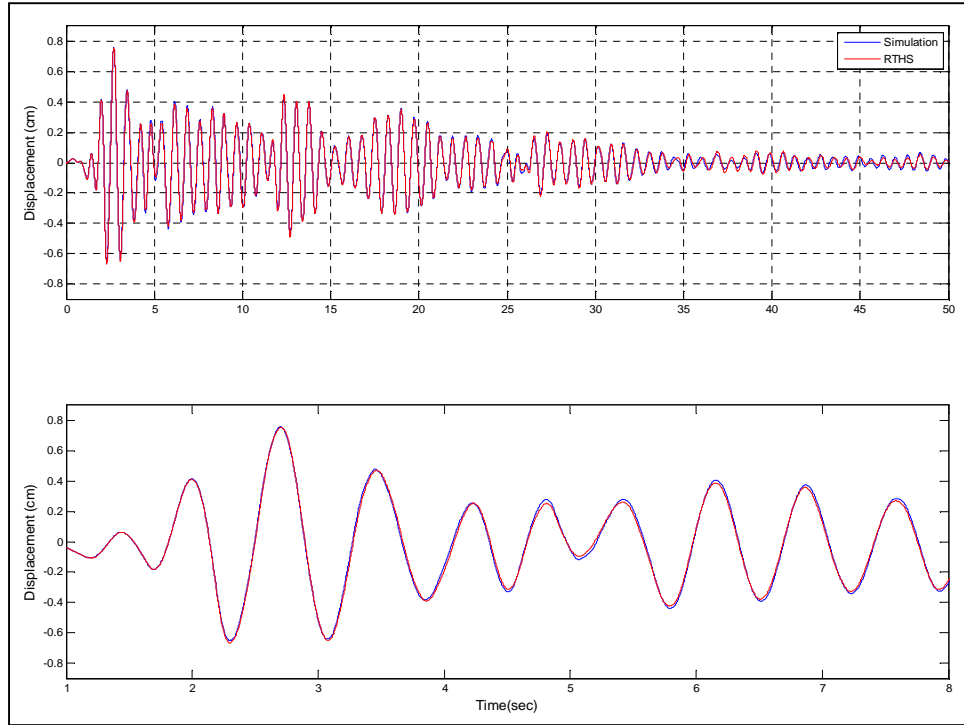


Figure 4.35: 8000/8000 Kg-mass case – Displacement second floor

4.7 Implementation - III

Implementation-III is performed using the two-story one-bay configuration of the frame specimen as in Implementation-II. However, here the MR damper device is included in the frame as an additional physical substructure component. Therefore, both RTHS Phase-1 and RHTS Phase-2 scenarios are evaluated for validation of the proposed RT-Frame2D. The MR damper is placed at the first floor of the frame specimen. Figure 4.36 shows two views of the attachment between the MR damper with the reaction floor and the frame specimen by the use of a C-shape member and a steel plate, respectively.

Simulated responses of the different RTHS scenarios are required for evaluation of the computational platform performance. A mathematical model for the MR damper based on the phenomenological Bouc-Wen model is used for the proposed simulation (Spencer

et al, 1997). Updated parameters for this model appropriate for the device used here were presented in Section 4.3.4. The updated RT-Frame2D computational model of the frame specimen used in Implementation-II is also utilized here.

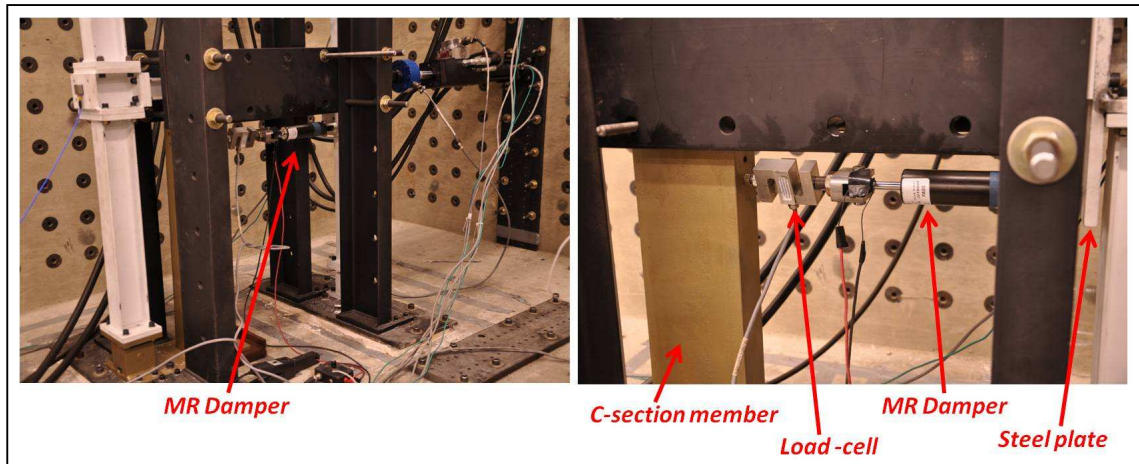


Figure 4.36: MR damper and frame specimen attachment

Implementation-III is performed considering the identical RTHS testing scenarios as Implementation-II, i.e. mass and earthquake intensities in agreement with Table 4.6, with same ground motion record.

For RTHS Phase-1, the MR damper specimen is utilized as the entire experimental substructure. The updated full-DOF computational model of the frame as well as the mass associated with levels one and two are used as computational substructures. Therefore, a full-DOF version of the RT-Frame2D computational block is used to solve the equation of motion using two inputs. These inputs are the restoring force exerted by the MR damper when displaced by the hydraulic actuator, and the ground motion record. Therefore, displacements computed at 1024 Hz and outputted from the first floor are imposed on the MR damper specimen by the use of the hydraulic actuator. The experimental restoring force from the MR damper is measured from the load cell located at the hydraulic actuator for feedback. In all testing cases, the MR damper is operated

with a semi-active controller. The same hydraulic actuator motion controller is used for all tests scenarios because the same physical substructure, i.e. the MR damper, is utilized. A view of the *Simulink* platform showing the computational block for RTHS Phase-1 is depicted in Figure 4.37.

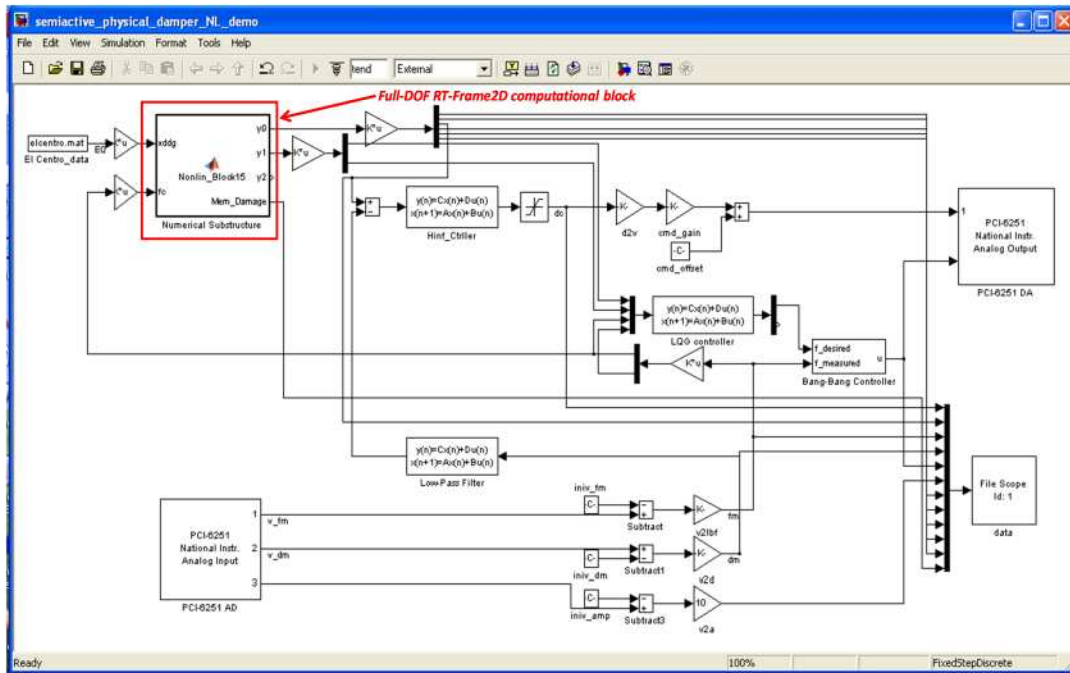


Figure 4.37: *Simulink* platform for Implementation III – RTHS Phase - 1

RTHS Phase-2 considers the two-DOF frame specimen with the MR damper as the experimental substructure. The mass associated with levels one and two are considered as the computational substructure. Damping is set to the value defined in Implementation-II. The two-DOF RT-Frame2D computational block utilized in Implementation-II is also used here. The computational block is used to solve the equation of motion using three inputs. These inputs are defined as the two restoring forces exerted by the frame specimen and the ground motion record. However, note that the measured restoring forces already account for the effect of the MR damper force in this implementation. Displacements computed at 1024 Hz are imposed on the frame specimen with the MR

damper using two hydraulic actuators. The experimental restoring forces are measured with load cells located at the hydraulic actuators, and used for feedback in the RTHS. The same hydraulic actuator motion controller is used for all tests because the same physical substructure is utilized. A view of the *Simulink* platform showing the computational block for RTHS Phase-2 is depicted in Figure 4.38.

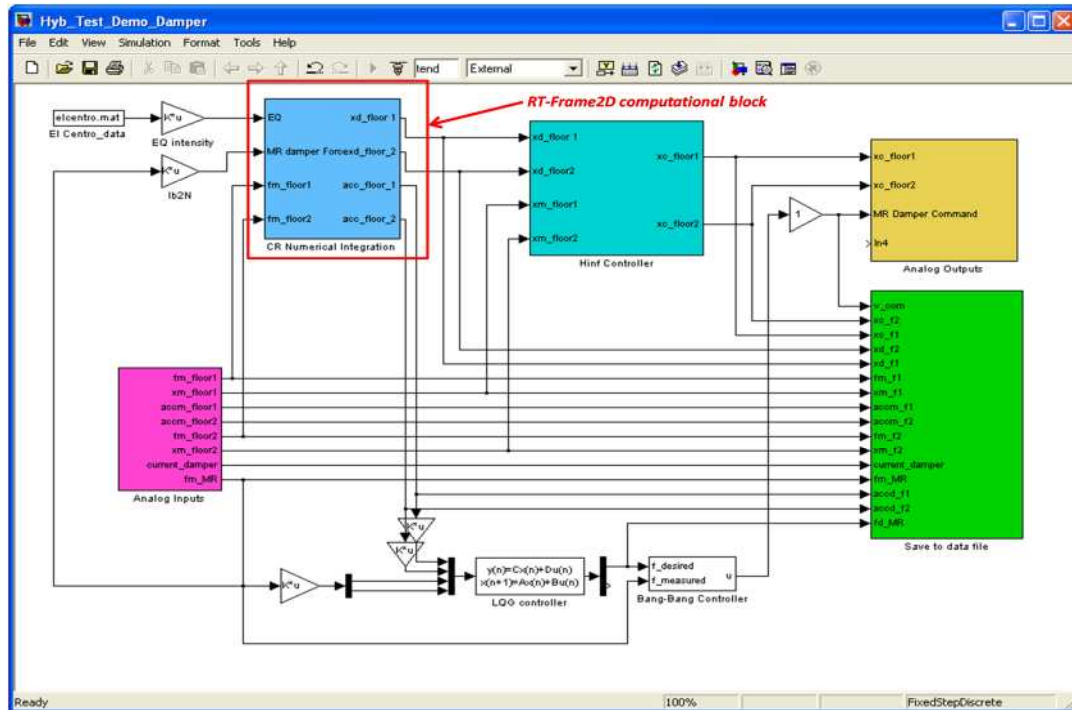


Figure 4.38: *Simulink* platform for Implementation III – RTHS Phase - 2

Time history records of the displacement at each floor for the controlled RTHS Phase-1 and RTHS Phase-2, along with corresponding simulation outputs are plotted in Figure 4.39 and Figure 4.46 for each RTHS case. Only 50 sec of the response is included for clarity. Additional plots showing zoomed records at early stages of the motion are also included. As observed, an excellent match between both RTHS Phase-1 and simulated responses are observed in each case. Moreover, peak values at different stages of the

motion are well captured. However, some discrepancies can be observed between RTHS Phase-2 and simulation.

Table 4.7: Error table for RTHS Phase - 1

<i>Test</i>	<i>Story</i>	E_{RTHS}	$E_{Tracking}$
1	1	15.91	19.93
	2	14.66	-
2	1	11.86	11.93
	2	11.77	-
3	1	9.34	9.42
	2	9.07	-
4	1	11.33	6.32
	2	10.32	-

Table 4.8: Error table for RTHS Phase - 2

<i>Test</i>	<i>Story</i>	E_{RTHS}	$E_{Tracking}$
1	1	38.67	21.02
	2	39.08	14.20
2	1	36.10	8.99
	2	36.64	7.46
3	1	32.70	7.83
	2	31.72	6.91
4	1	43.19	5.90
	2	41.94	5.04

Error values associated to the RTHS and actuator tracking control for both RTHS phases and calculated with records from both floors are shown in Table 4.7 and Table 4.8. RTHS errors between responses at the first case, i.e. comparison between simulation and RTHS Phase-1 could be attributed to inaccurate calculation in the computational restoring force, inaccuracy or instability induced by the integration scheme or inadequate measurement of

the experimental feedback restoring force exerted by the MR damper. Moreover, a full-DOF computational model is being evaluated here leading to computational time closer to real-time execution limits. Because of the linear nature of the test, minor contribution in the RTHS error induced by the calculation of computational restoring forces is expected. Stability in the integration scheme remains guaranteed as explained in the precedent implementations. However, the degree of noise content in the feedback experimental measurements still plays a critical role. The noise effect is even more relevant in this case because of the presence of the damper device yielding displacement records with smaller amplitudes than in previous implementations. RTHS errors between responses at the second case, i.e. comparison between simulation and RTHS Phase-2 are attributed to the same aspects discussed in Implementation II and the greater noise effect due to smaller amplitudes of displacement records. However, the test set-up seems to have a greater influence in this case.

As observed in Figure 4.36 (right view), flexibility induced by the steel plate used to connect the MR damper device and the frame specimen yields damper force measurements different than those obtained in simulation and the RTHS Phase-1 set-up (shown in Figure 4.47). This flexibility is mainly induced because of the offset between the action point of the damper force (lower side of the steel plate) and the attachment point between steel plate and the frame specimen. Moreover, in simulation, an infinity rigid connection between MR damper and the frame specimen is considered and the action point of the damper force is at the floor level, i.e. no offset effect. Additional flexibility due to the C-section member to attach the other end of the MR damper may also exist. However and due to the high stiffness (it is placed in the strong axis direction), this flexibility is considered to be less relevant. Due to the greater discrepancies between RTHS and simulated outputs in this case, large RTHS error values are recorded. However, good overall agreement between responses is still achieved.

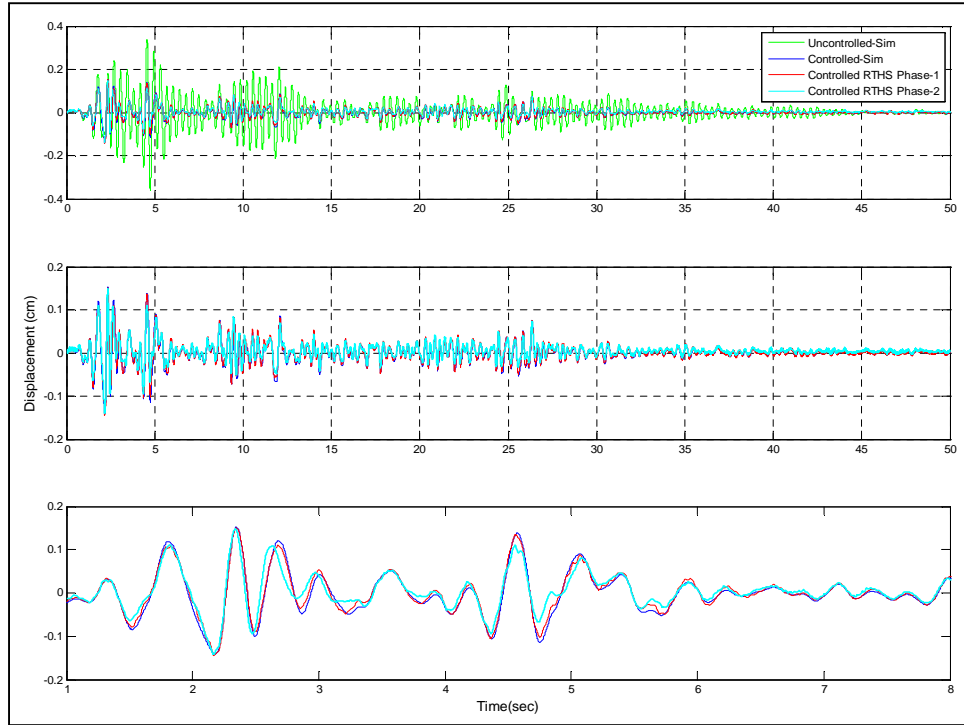


Figure 4.39: 2000/2000 Kg-mass case – Displacement first floor

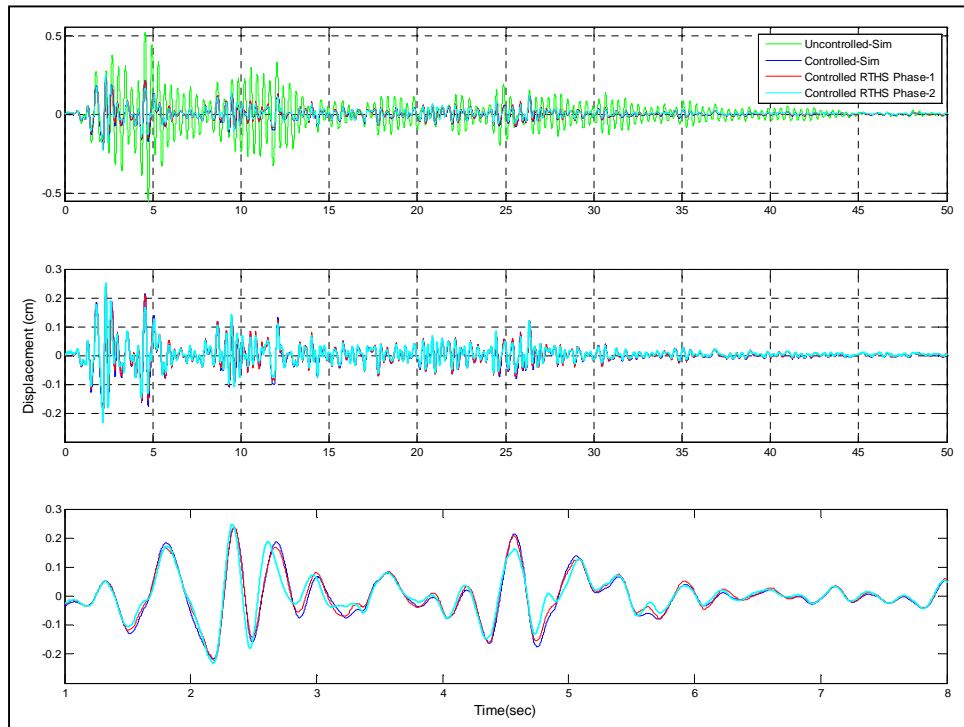


Figure 4.40: 2000/2000 Kg-mass case – Displacement second floor

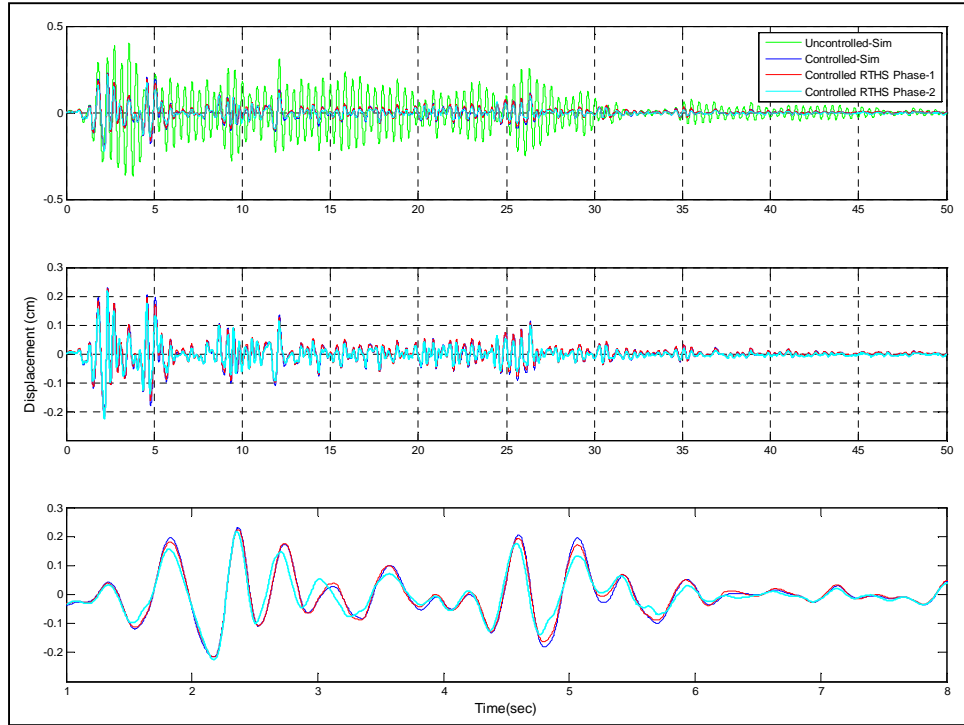


Figure 4.41: 4000/2000 Kg-mass case – Displacement first floor

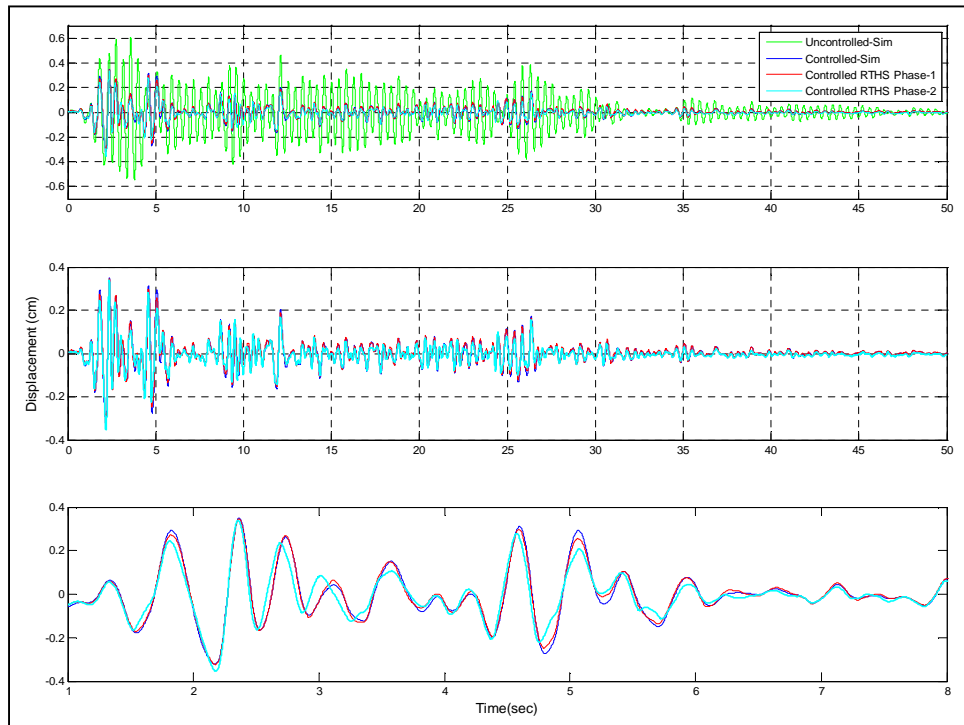


Figure 4.42: 4000/2000 Kg-mass case – Displacement second floor

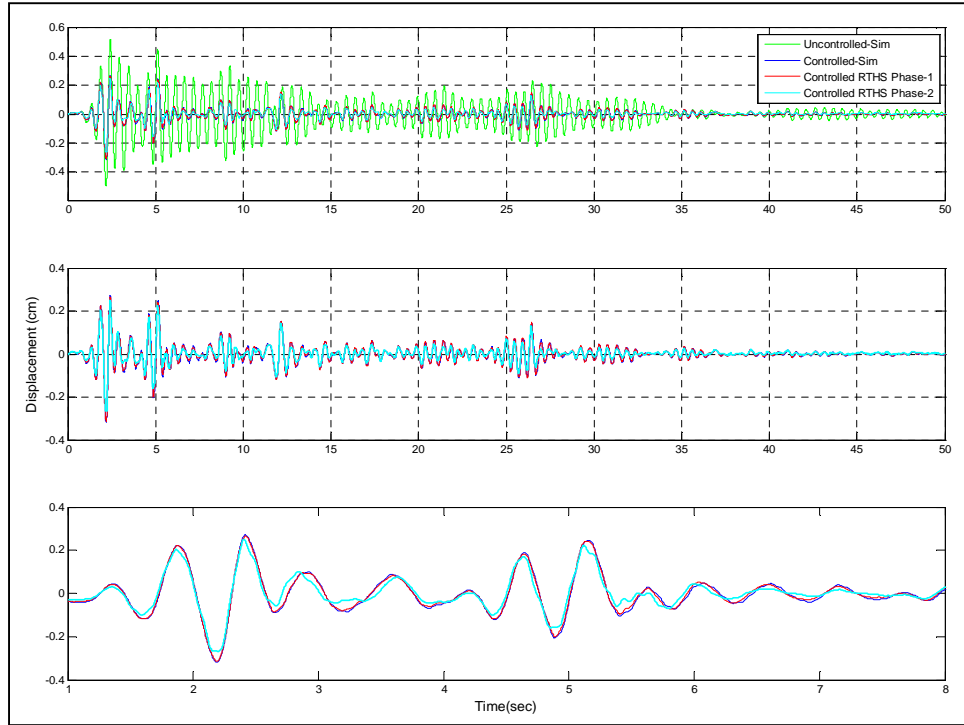


Figure 4.43: 4000/4000 Kg-mass case – Displacement first floor

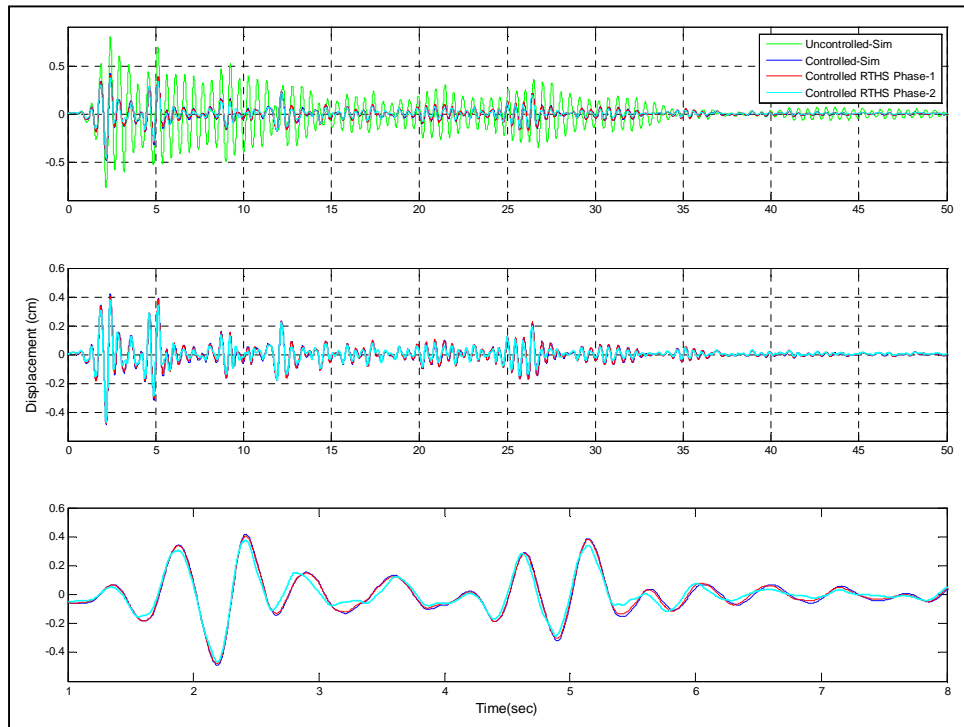


Figure 4.44: 4000/4000 Kg-mass case – Displacement second floor

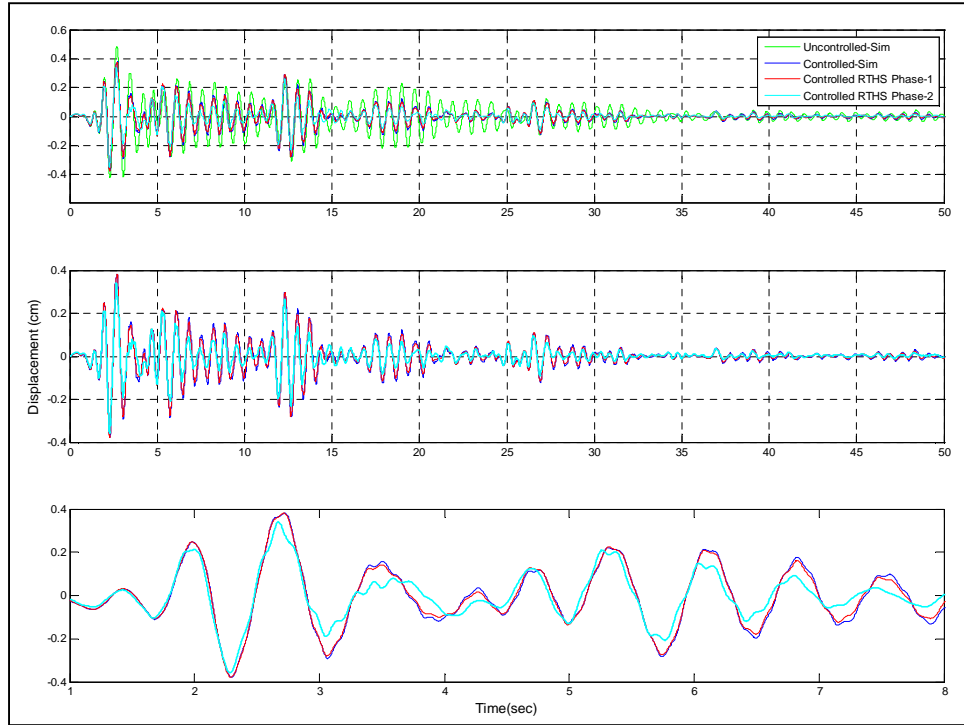


Figure 4.45: 8000/8000 Kg-mass case – Displacement first floor

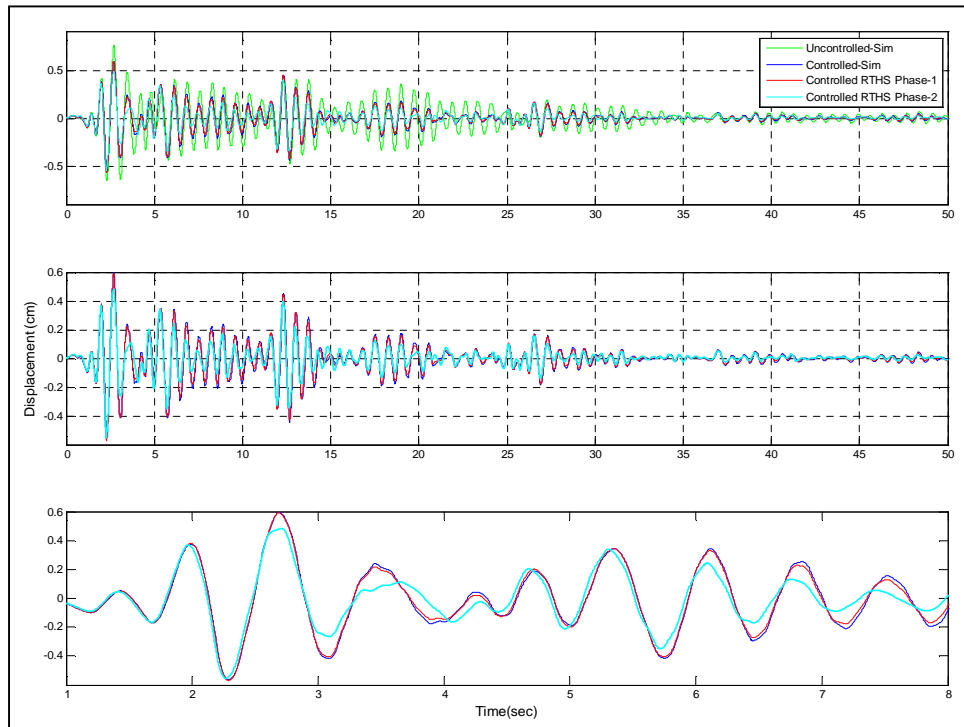


Figure 4.46: 8000/8000 Kg-mass case – Displacement second floor

4.8 Implementation - IV

Various RTHS scenarios using different modeling options offered by RT-Frame2D are tested in Implementation IV. The tests are focused on the RTHS of a seismically-excited two-story one-bay frame structure that is equipped with a MR damper device. Therefore, the RTHS Phase - 1 scenario is adopted for all cases in this implementation. Computational models of the frame structure and associated mass are utilized as computational substructures. An MR damper specimen, introduced at Section 4.3.2, is utilized as the experimental substructure for all tests.

As in previous implementations, simulated responses of the different RTHS scenarios are used for evaluation of the computational platform performance. A mathematical model of the MR damper based on a phenomenological Bouc-Wen model is used for the simulations. Updated parameters and calibration of this model were presented in Section 4.3.4. Eighteen RTHS scenarios are to be tested in Implementation IV, described subsequently. Therefore, eighteen computational models of the frame structure, with varying levels of complexity, are developed using different RT-Frame2D modeling capabilities. All models are constructed based on the same geometry and member section configuration of the two-story one-bay frame specimen, i.e. Section: 2D Steel frame specimen. Masses of 4000 kg and 2000 kg are assigned at the first and second floors, respectively. This mass configuration is used to assemble the global mass matrix, which is repeated for all testing cases. A global damping matrix is defined using a stiffness proportional damping assumption, yielding a fundamental damping ratio of 2%. This damping configuration is also used in all tests. The modulus of elasticity and Poisson's ratio for steel are selected as 29,000 ksi and 0.3, respectively. These values are assumed for all members.

Table 4.9 provides the modeling options considered in the computational models used in each RTHS test. Columns are modeled for all cases with the *linear elastic beam-column element*, identified with the tag LBC. Three choices of beam members are considered:

linear elastic beam-column element (LBC), nonlinear beam-column element (NBC) and the linear elastic beam-column element with flexible connections (BCFC). Yielding moments and curvature values for NBC elements are calculated based on the member section properties and a steel yielding stress value $F_y=50$ ksi. Flexible connections for the BCFC element are defined with a stiffness value of $8e6$ N-m and a yielding rotation value of 0.004 rad. These connections are considered in the test matrix with either a linear or nonlinear option. Therefore, corresponding yielding moment values are calculated based on the connection properties. Panel zone members are defined with the *rigid-body panel zone* version (RPZ) or the *linear deformable panel zone* version (LPZ) with three deformation modes under a plane stress assumption, also depending on the test under consideration.

Table 4.9: Modeling options used in each RTHS scenario

<i>Test</i>	<i>Column</i>	<i>Beam</i>	<i>Flexible Connection</i>	<i>Panel Zone</i>	<i>Hysteresis</i>	$EI_2 - k_{C2}$	$EI_3 - k_{C3}$	$\phi_r - \theta_r$
1	LBC	LBC	-	-	-	-	-	-
2	LBC	NBC	-	-	Bilinear	0.02	-	-
3	LBC	NBC	-	-	Tri-linear	0.50	0.02	1.50
4	LBC	BCFC	Linear	-	-	-	-	-
5	LBC	BCFC	Nonlinear	-	Bilinear	0.25	-	-
6	LBC	BCFC	Nonlinear	-	Tri-linear	0.25	0.10	3.00
7	LBC	LBC	-	RPZ	-	-	-	-
8	LBC	NBC	-	RPZ	Bilinear	0.02	-	-
9	LBC	NBC	-	RPZ	Tri-linear	0.50	0.02	1.50
10	LBC	LBC	-	LPZ	-	-	-	-
11	LBC	NBC	-	LPZ	Bilinear	0.02	-	-
12	LBC	NBC	-	LPZ	Tri-linear	0.50	0.02	1.50
13	LBC	BCFC	Linear	RPZ	-	-	-	-
14	LBC	BCFC	Nonlinear	RPZ	Bilinear	0.10	-	-
15	LBC	BCFC	Nonlinear	RPZ	Tri-linear	0.10	0.02	3.00
16	LBC	BCFC	Linear	LPZ	-	-	-	-
17	LBC	BCFC	Nonlinear	LPZ	Bilinear	0.25	-	-
18	LBC	BCFC	Nonlinear	LPZ	Tri-linear	0.10	0.05	3.00

The type of hysteresis and corresponding parameter values for definition of nonlinearity on beam members at each RTHS scenario is also included in Table 4.9. The type of hysteresis is defined for the hysteresis models depending on the nonlinear beam element under consideration. Specifically, a bilinear or tri-linear moment-curvature hysteresis model based on kinematic hardening is used for the case of NBC elements; a bilinear or tri-linear moment-rotation hysteresis model under the same hardening assumption is considered for the nonlinear flexible connections of BCFC elements. Table 4.10 shows the variables and corresponding description for definition of post-yielding ratios used at each test. For instance, the variable EI_2 defines the ratio between the value of the flexural rigidity constant $EI_{Bilinear}$ used in the second branch of the bilinear model with respect to the linear value. Similarly, the variable k_{c3} defines the ratio between the value of the flexible connection stiffness $k_{cTrilinear}$ used in the third branch of the tri-linear model with respect to the linear value. It is noted that EI values are used for NBC beam elements based on moment-curvature hysteresis, while the k_c values are used for BCFC elements based on moment-rotation hysteresis for connections. These values are shown in Table 4.9. Additionally, variable definition for ratios between 1st and 2nd yielding curvature (or rotation) are also included. For instance, φ_r variable defines the ratio between the yielding curvatures to reach the third branch with respect to the second branch in the tri-linear model.

Boundary conditions are defined in agreement with the frame specimen supports, i.e. fixed translation and free rotation as presented in Section 4.3.1. Global constraints ensuring equal values for the translational horizontal DOF at each story level is also considered. This constraint is considered to ensure rigid diaphragm behavior. The same boundary conditions and constraints are considered for all cases. The unconditionally-explicit CR integration scheme is used to solve the incremental equations of motion. Because, the MR damper can handle a larger stroke, larger earthquakes intensities are selected leading to larger deformations and highly nonlinear behavior in the

computational models. The CR integration scheme is thus selected for all testing cases due to its improved convergence ability under strong nonlinear conditions.

Table 4.10: Hysteresis parameters

<i>Hysteresis Parameters</i>	<i>Description</i>
EI	<i>Flexural rigidity constant</i>
$EI_2 = \frac{EI_{Bilinear}}{EI}$	<i>EI ratio for 2nd-branch of bilinear model</i>
$EI_3 = \frac{EI_{Trilinear}}{EI}$	<i>EI ratio for 3rd-branch of tri-linear model</i>
k_c	<i>Flexible connection stiffness</i>
$k_{c2} = \frac{k_{cBilinear}}{k_c}$	<i>k_c ratio for 2nd-branch of bilinear model</i>
$k_{c3} = \frac{k_{cTrilinear}}{k_c}$	<i>k_c ratio for 3rd-branch of tri-linear model</i>
$\varphi_r = \frac{\varphi_{Trilinear}}{\varphi_{Bilinear}}$	<i>Curvature ratio between 2nd and 1st yielding</i>
$\theta_r = \frac{\theta_{Trilinear}}{\theta_{Bilinear}}$	<i>Rotation ratio between 2nd and 1st yielding</i>

Eighteen RTHS scenarios are tested using the N-S component recorded at the Imperial Valley Irrigation District substation in *El Centro*, California, during the Imperial Valley, California earthquake of May 18, 1940. The type of analysis and earthquake intensities in each RTHS scenario is shown in Table 4.11.

Table 4.11: Testing scenarios

<i>Test</i>	<i>EQ Intensity</i>	<i>Analysis Type</i>	<i>Story</i>	<i>Frequency (Hz)</i>	E_{RTHS}	$E_{Tracking}$
1	0.50	Linear	1	2.28	4.34	3.36
			2	11.98	4.32	-
2	0.30	Nonlinear	1	2.28	4.63	4.96
			2	11.98	4.59	-
3	0.50	Nonlinear	1	2.28	3.58	3.48
			2	11.98	3.58	-
4	0.50	Linear	1	2.24	3.94	3.10
			2	11.90	3.93	-
5	0.30	Nonlinear	1	2.24	5.56	4.67
			2	11.90	5.57	-
6	0.50	Nonlinear	1	2.24	3.47	3.13
			2	11.90	3.47	-
7	0.50	Linear	1	2.69	4.31	4.45
			2	13.94	4.28	-
8	0.50	Nonlinear	1	2.69	4.64	4.49
			2	13.94	4.61	-
9	0.50	Nonlinear	1	2.69	4.69	4.64
			2	13.94	4.69	-
10	0.70	Linear	1	2.67	3.14	3.26
			2	13.88	3.12	-
11	0.70	Nonlinear	1	2.67	3.32	3.40
			2	13.88	3.35	-
12	0.70	Nonlinear	1	2.67	4.21	3.30
			2	13.88	4.27	-
13	0.50	Linear	1	2.65	4.58	4.21
			2	13.81	4.55	-
14	0.50	Nonlinear	1	2.65	4.20	4.24
			2	13.81	4.19	-
15	0.50	Nonlinear	1	2.65	4.20	4.21
			2	13.81	4.17	-
16	0.50	Linear	1	2.62	4.97	4.27
			2	13.76	4.96	-

Table 4.11 Continued.

<i>Test</i>	<i>EQ Intensity</i>	<i>Analysis Type</i>	<i>Story</i>	<i>Frequency (Hz)</i>	E_{RTHS}	$E_{Tracking}$
17	0.45	Nonlinear	1	2.62	5.27	4.61
			2	13.76	5.28	-
18	0.50	Nonlinear	1	2.62	6.26	4.12
			2	13.76	6.29	-

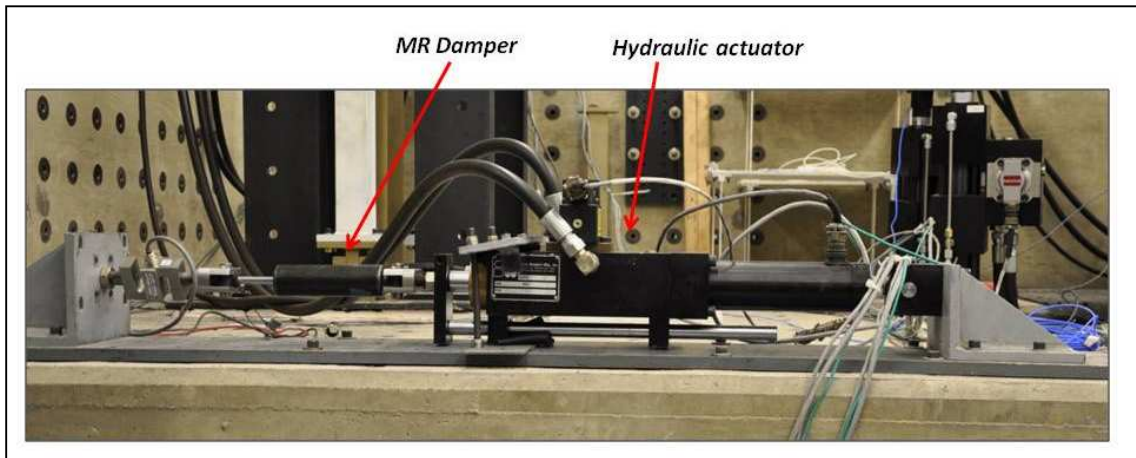


Figure 4.47: Experimental set-up for Implementation IV

Figure 4.47 shows a photograph of the test setup. In agreement with the RTHS Phase-1 configuration, the MR damper specimen is the experimental substructure. Computational models of the frame structure developed for simulation and comparison at each RTHS scenario, and including appropriate mass distribution are used as the computational substructures. Because the frame structure is computational, a full-DOF version of RT-Frame2D is used for evaluation of all testing cases. A view of the *Simulink* platform showing the computational block for Implementation IV is depicted in Figure 4.37. Thus, in each case the RT-Frame2D computational block solves the equations of motion at 1024 Hz using two inputs. These inputs are defined as the restoring force provided by the MR damper and the ground motion record.

The MR damper is assumed to be located at the first floor of the frame specimen, with no compliance between the device and structure. Therefore, the computed 1st floor frame displacements are applied to the MR damper with the hydraulic actuator. The experimental restoring force from the MR damper is measured using the load cell and used for feedback in the RTHS. In all cases, the MR damper is operated in a semi-active mode. The same hydraulic actuator motion controller is used for all tests scenarios because the same physical substructure, i.e. the MR damper, is utilized.

Time histories of the displacements of the controlled structure during the RTHS are shown in the odd-numbered figures between Figure 4.48 and Figure 4.83. The controlled and uncontrolled simulated response is also included for comparison in the response reduction. Only 50 sec of the response is included for clarity, with a zoomed view of the early stages of the response. An excellent match is observed between the RTHS and simulated responses in each case, demonstrating the accuracy and stability of the nonlinear modeling capabilities of the proposed computational RT-Frame2D platform. Moreover, the excellent performance, robustness and stability of the hydraulic actuator control are also validated based on these results.

As an additional point of evaluation, the comparison between moment-curvature and moment-rotation records are also shown in the even-numbered figures between Figure 4.48 and Figure 4.83. These records correspond to the right-end of the beam members located at the first floor. Uncontrolled records, shown on the left-side of the figures, are also included for a comparison to the controlled cases. RTHS controlled cases and corresponding simulations are shown at the right-side of each figure. As expected, test with nonlinear modeling assumptions yield hysteresis loops depending on the earthquake intensity. Therefore, linear records are still observed for tests in which the plastic limits for beam members have not been exceeded. Excellent agreement between both RTHS and simulated responses is also achieved.

The RTHS error values calculated with simulation and RTHS displacement outputs at both floors are shown in Table 4.11. These values are calculated with Equation (4.11) yielding an approximate mean value of 4.5% and clearly demonstrating the accuracy of the results. Additionally, error values for the actuator control tracking error are included for reference. Note that in contrast to the previous implementations, here nonlinear computational restoring forces for a full-DOF model are calculated within the computational block. Thus the accuracy and performance of the computational platform in the updating of the nonlinear restoring force and tangent stiffness matrices under real-time execution is directly evaluated. Moreover, the risk for potential instabilities or large errors in the results can be more significantly attributed to this fact. As before, stability performance of the integration scheme is verified based on the bounded nature of the responses at each testing case. However, magnitude of the poles associated to the discrete transfer function of the CR integration scheme is no longer fixed, i.e. it can vary depending on the degree of nonlinearity in the model and yielding to potential instabilities. However, all of the nonlinear testing cases are subjected to softening behavior and thus still preserving the unconditionally-stable condition as explained in Section 2.10.1. These excellent experimental results further validate the adequate selection of both accurate and stable nonlinear beam-column models and the CR integration scheme for implementation within the RT-Frame2D platform.

As discussed before, the RTHS performance is influenced by the noise content in the experimental measurements. Because displacement signals with higher amplitudes are tested in this implementation to induce nonlinear response, the noise ratio is expected to have less impact. This observation becomes evident based on the much smaller RTHS error values than those calculated in previous implementations. Moreover, because the MR damper is considered the only experimental substructure, errors in the experimental restoring force measurements have less impact in the RTHS performance.

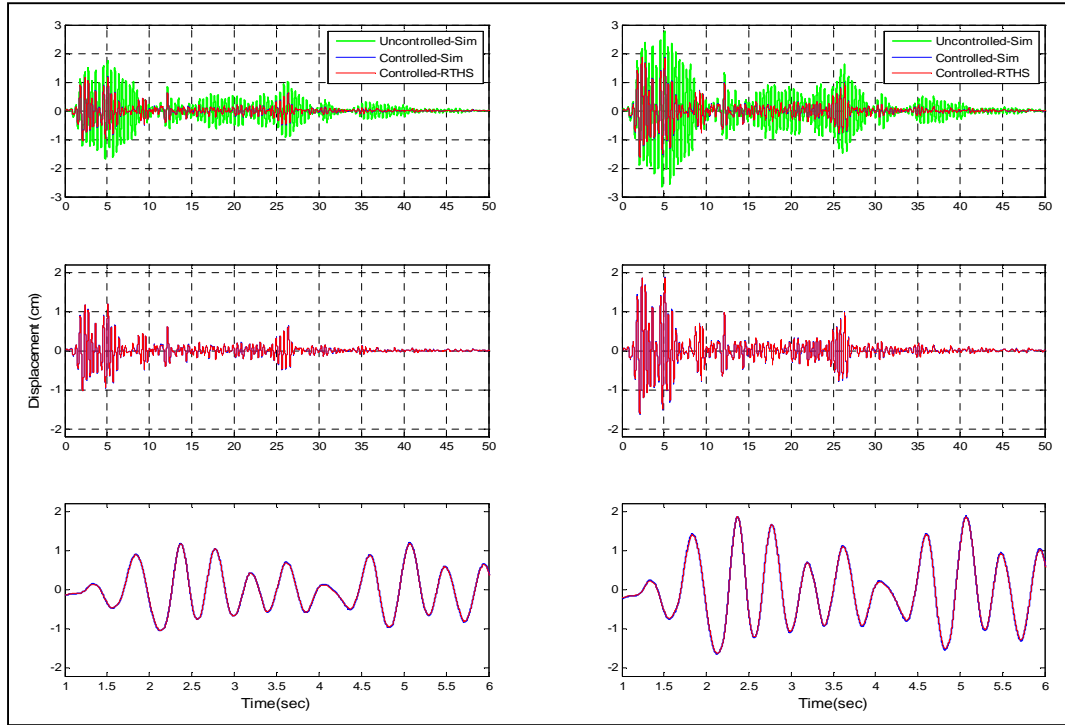


Figure 4.48: Displacement records based on Test 1

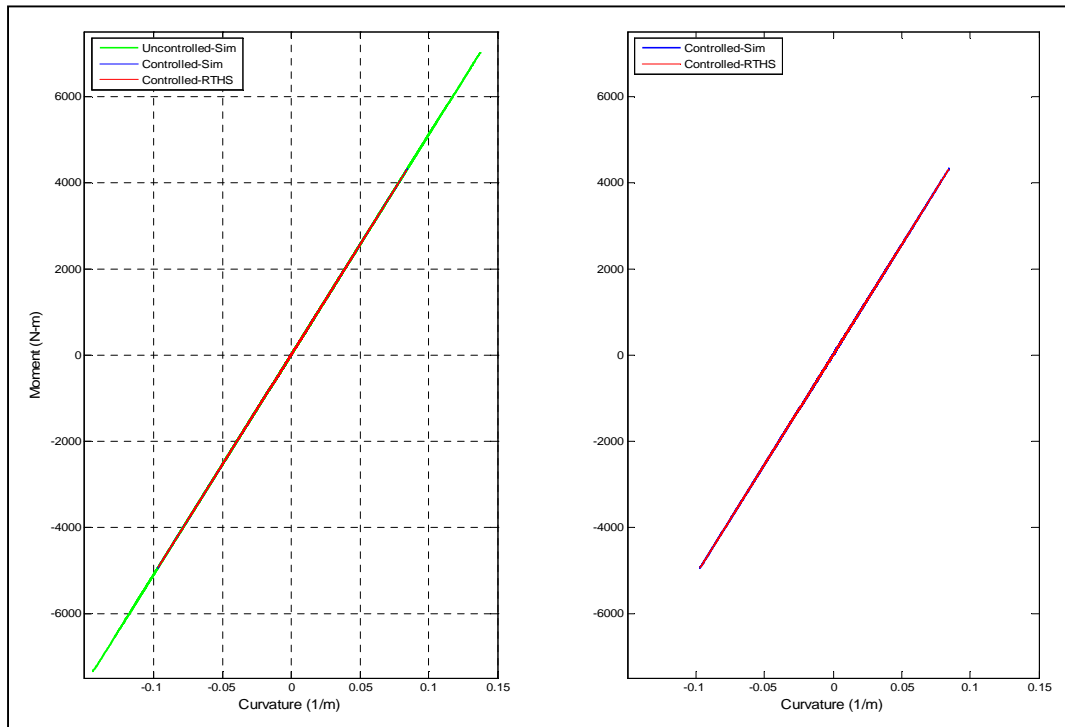


Figure 4.49: Hysteresis loops based on Test 1

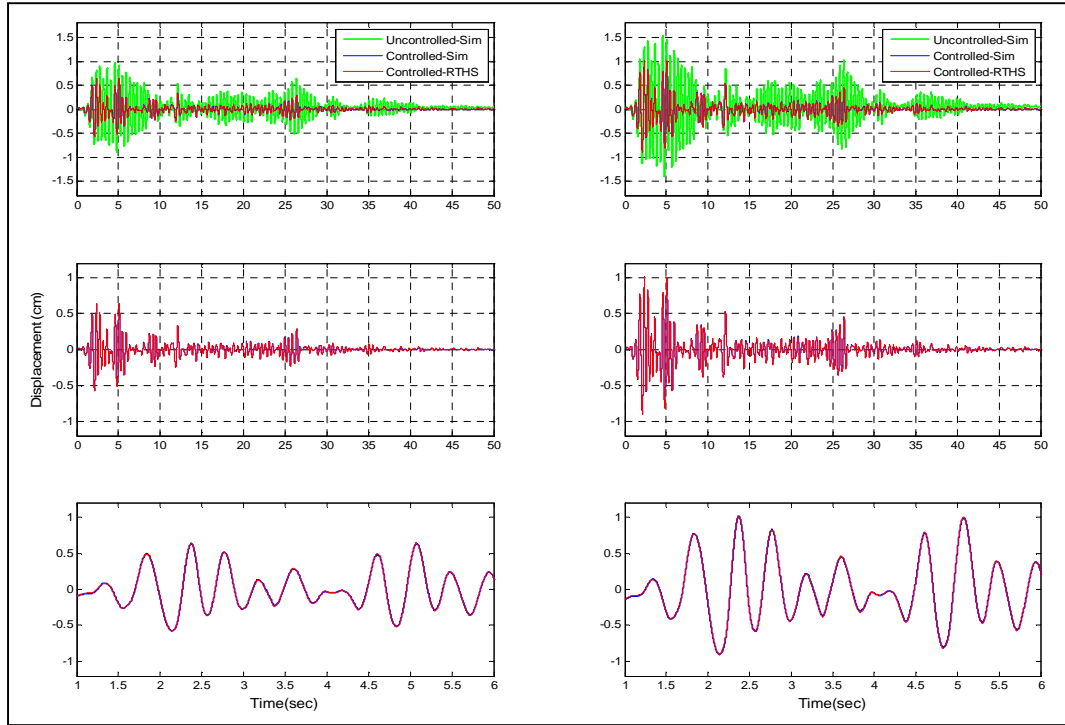


Figure 4.50: Displacement records based on Test 2

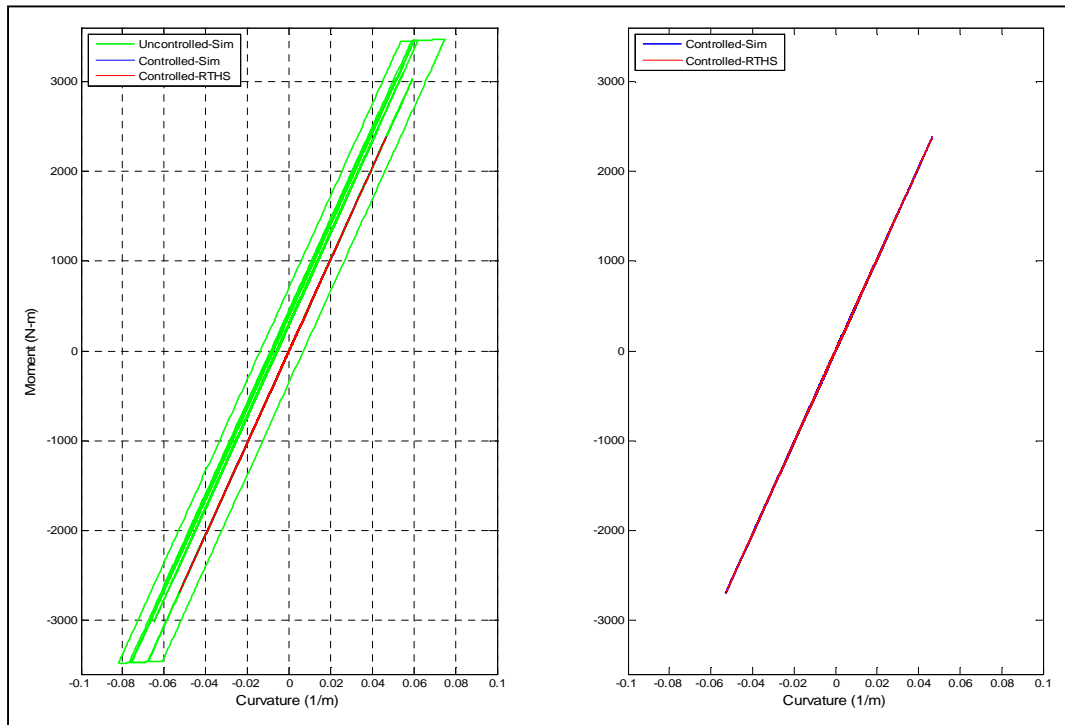


Figure 4.51: Hysteresis loops based on Test 2

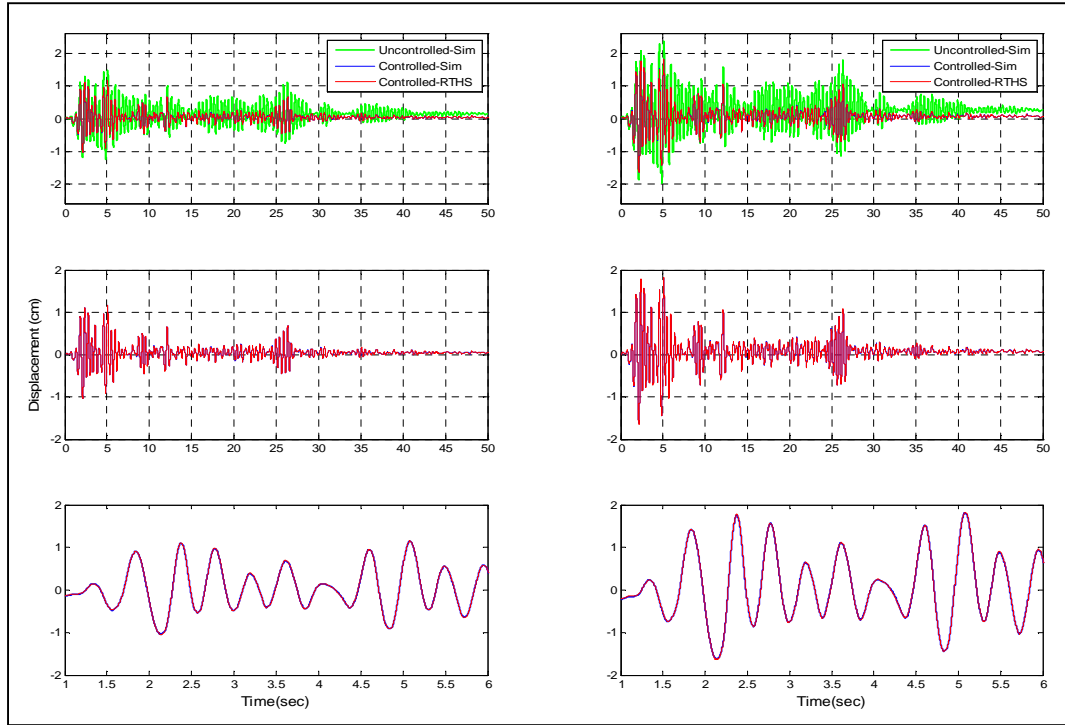


Figure 4.52: Displacement records based on Test 3

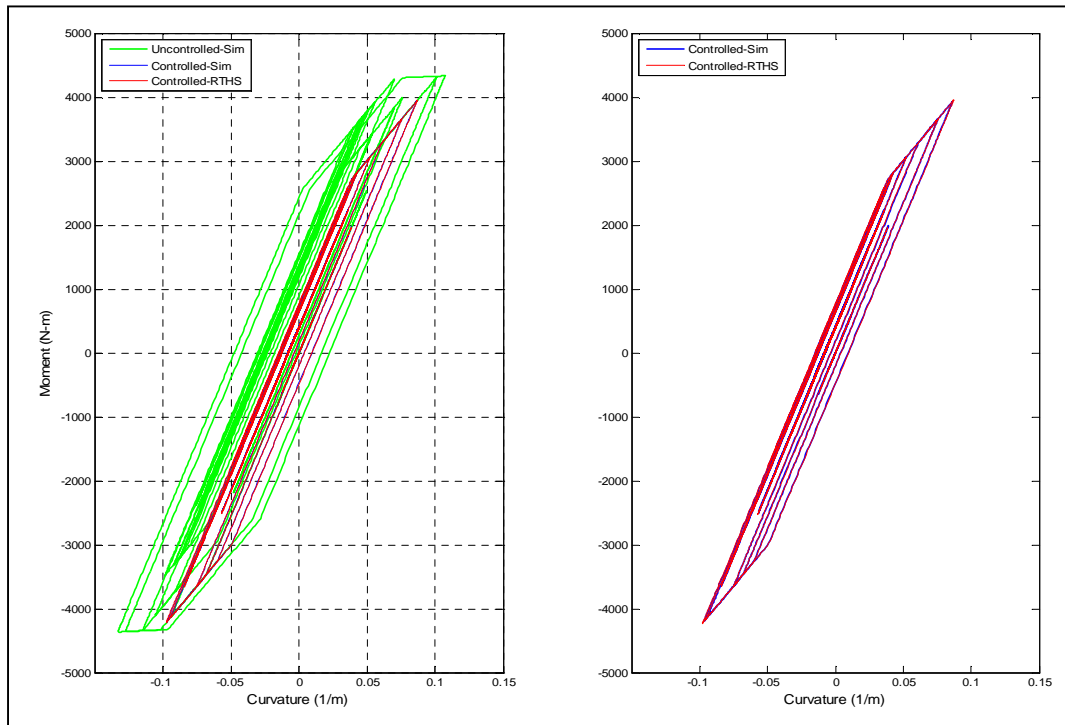


Figure 4.53: Hysteresis loops based on Test 3

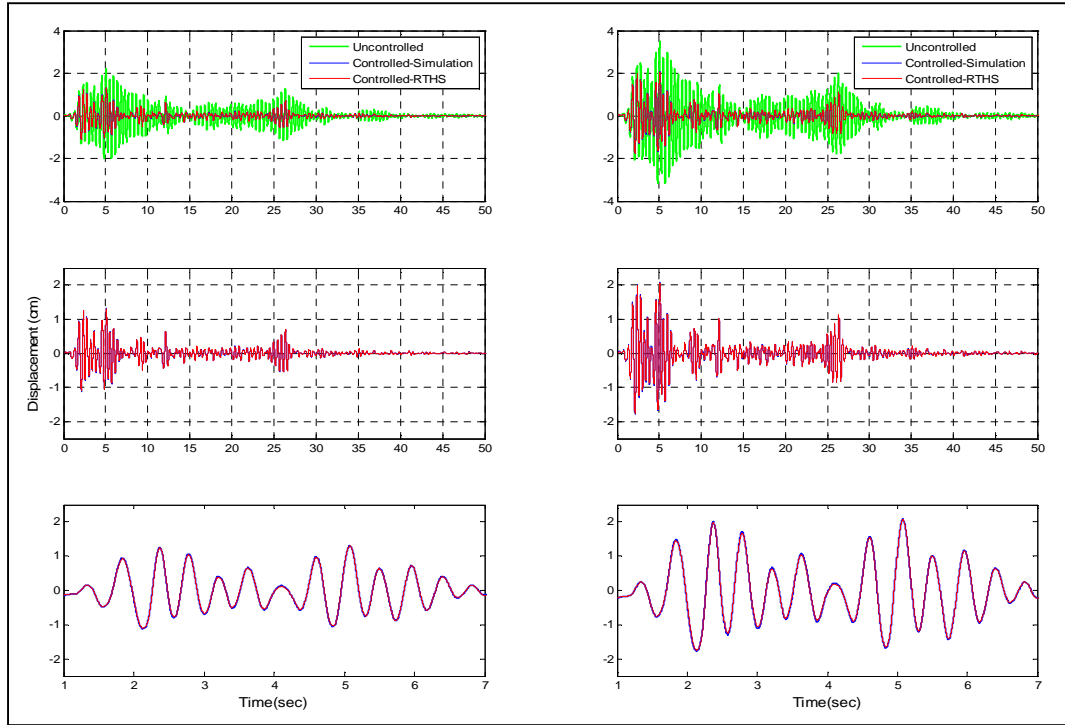


Figure 4.54: Displacement records based on Test 4

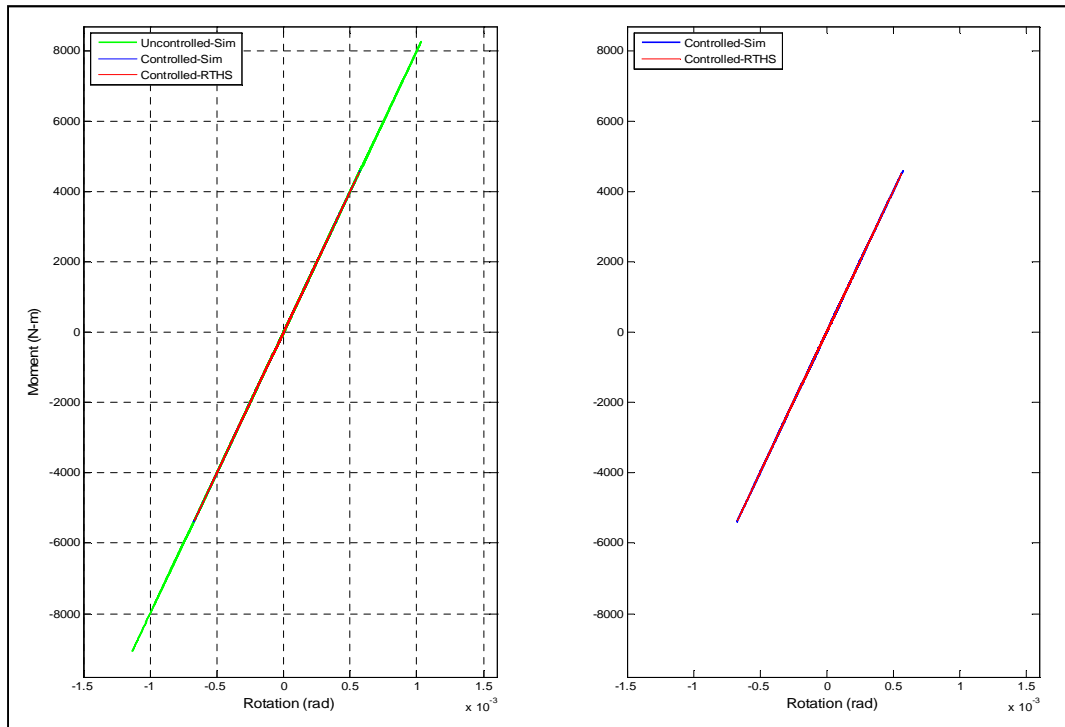


Figure 4.55: Hysteresis loops based on Test 4

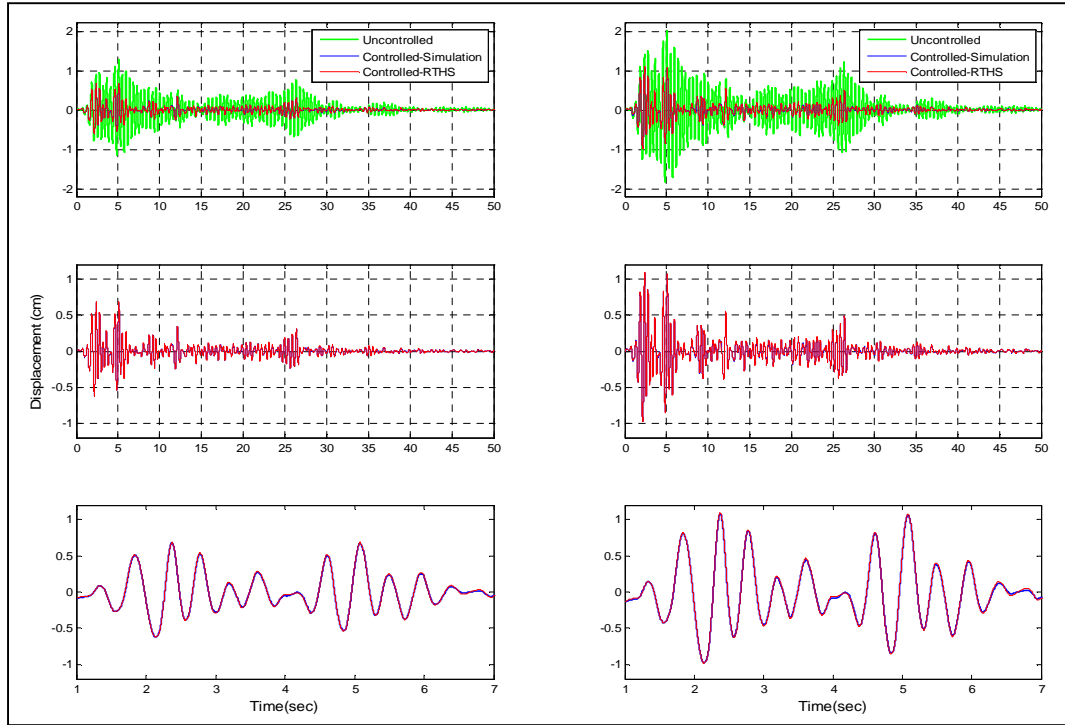


Figure 4.56: Displacement records based on Test 5

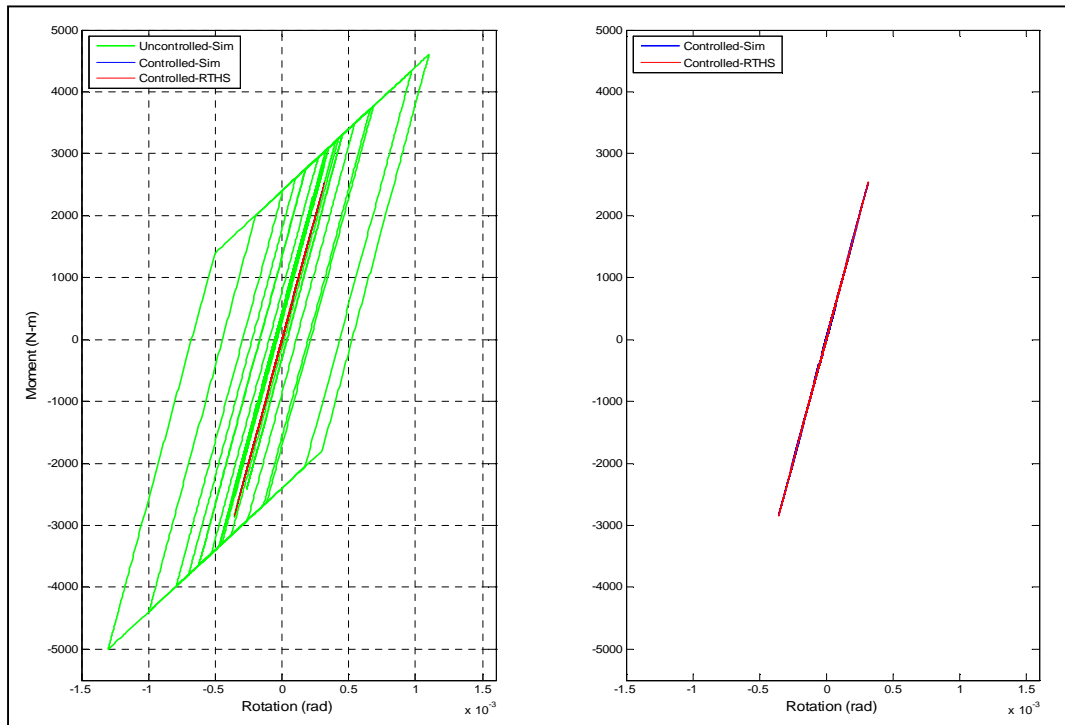


Figure 4.57: Hysteresis loops based on Test 5

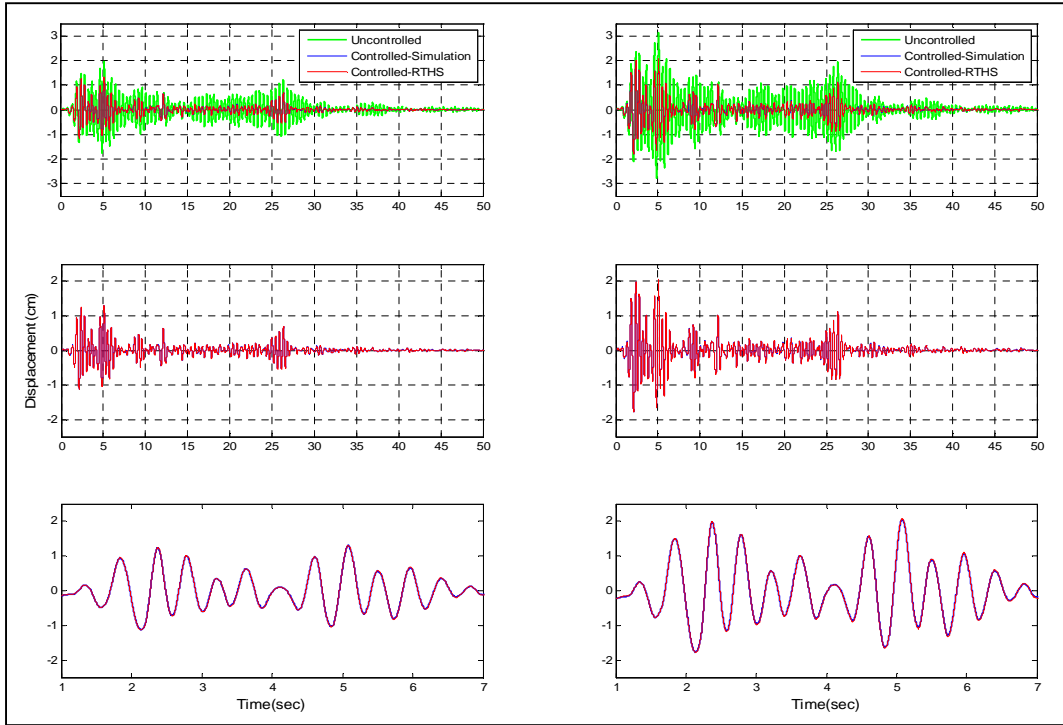


Figure 4.58: Displacement records based on Test 6

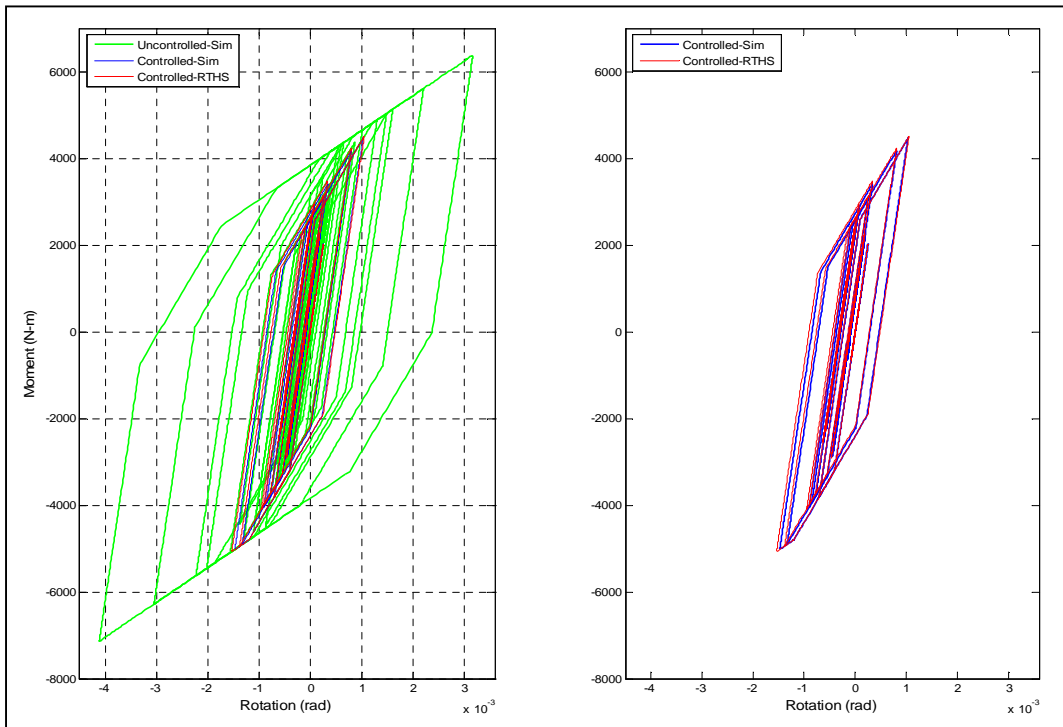


Figure 4.59: Hysteresis loops based on Test 6

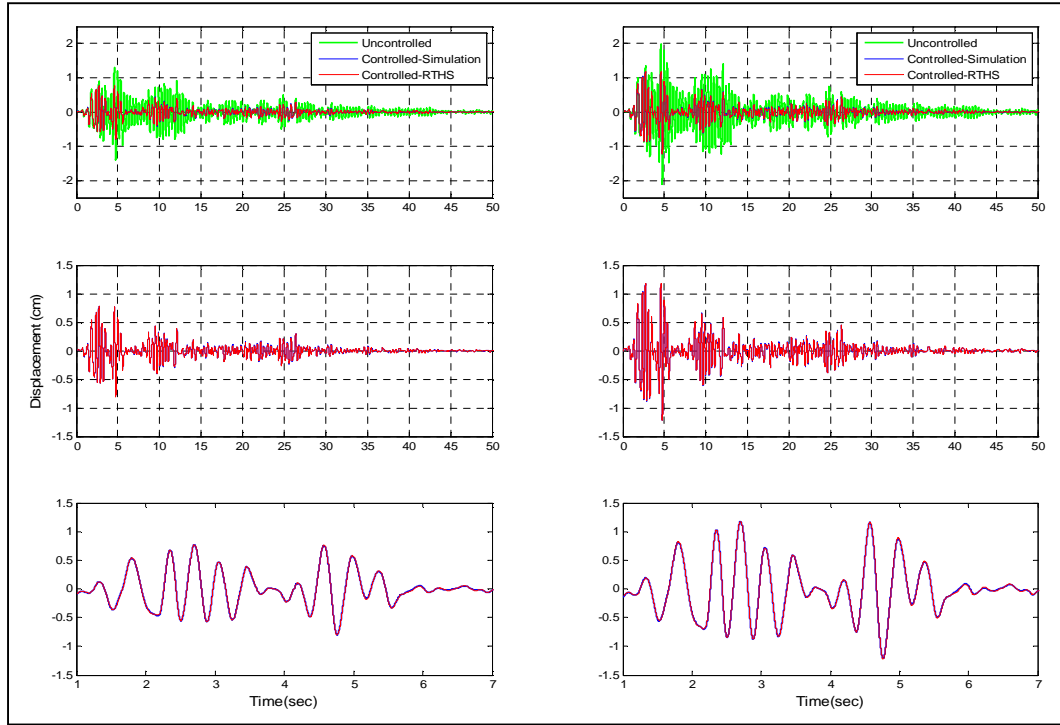


Figure 4.60: Displacement records based on Test 7

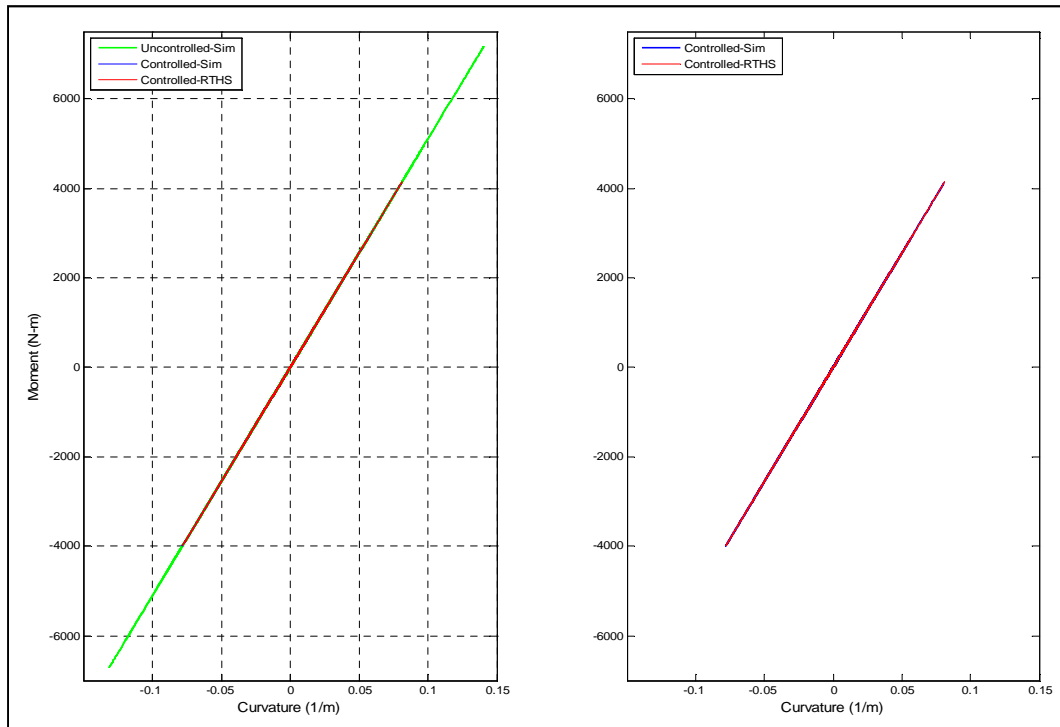


Figure 4.61: Hysteresis loops based on Test 7

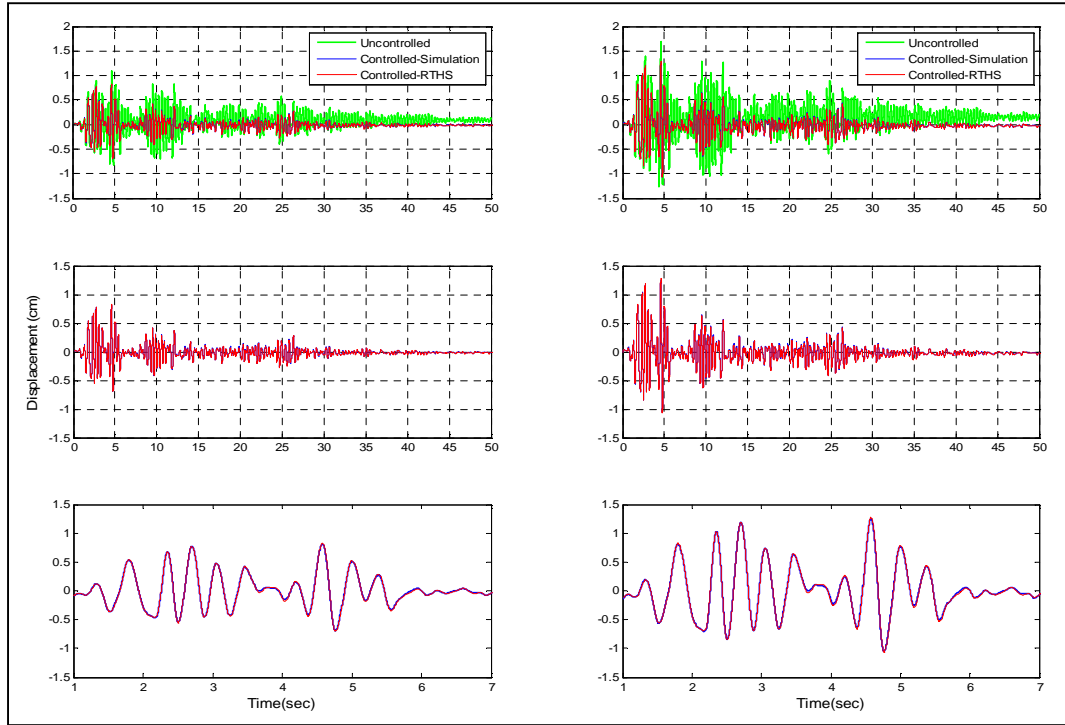


Figure 4.62: Displacement records based on Test 8

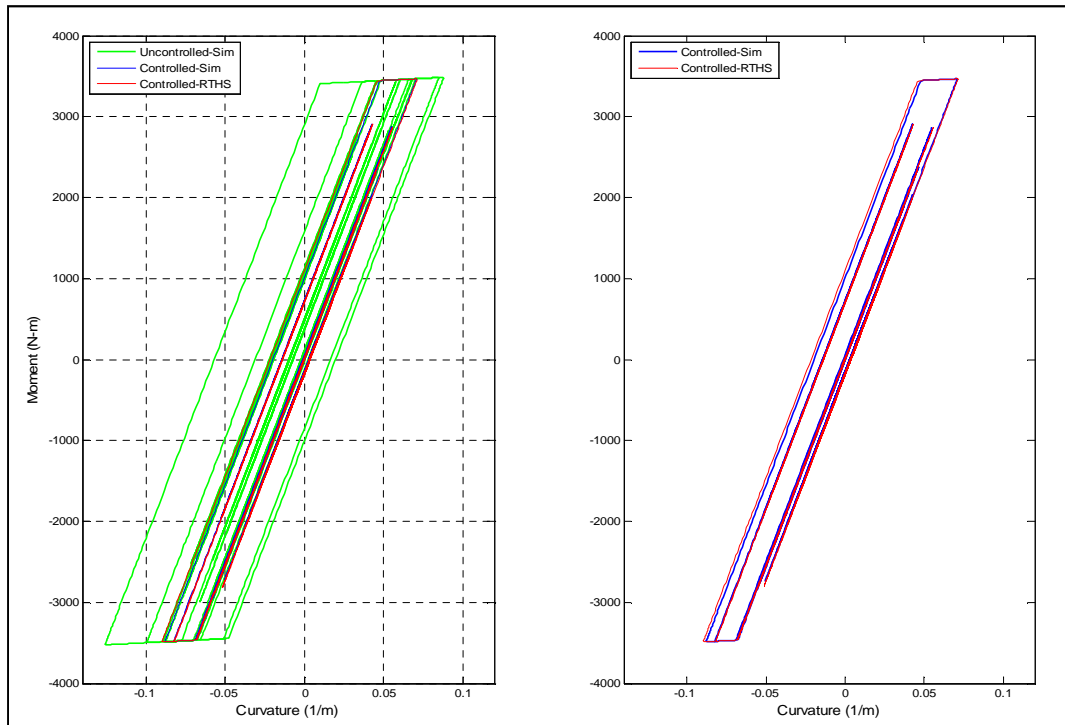


Figure 4.63: Hysteresis loops based on Test 8

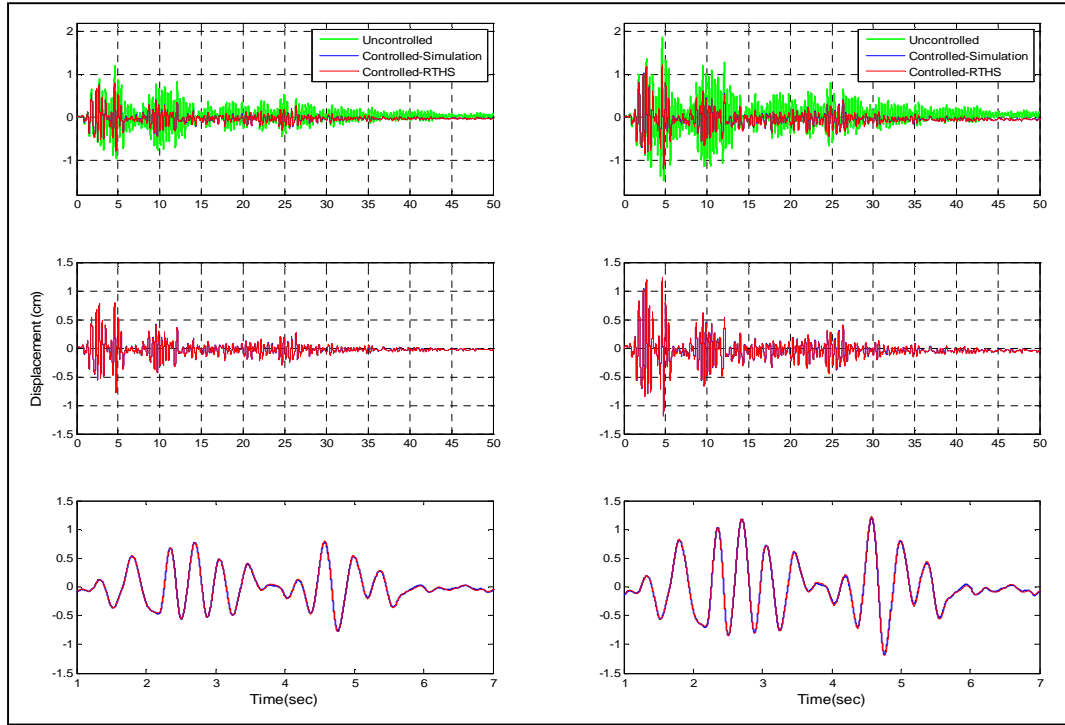


Figure 4.64: Displacement records based on Test 9

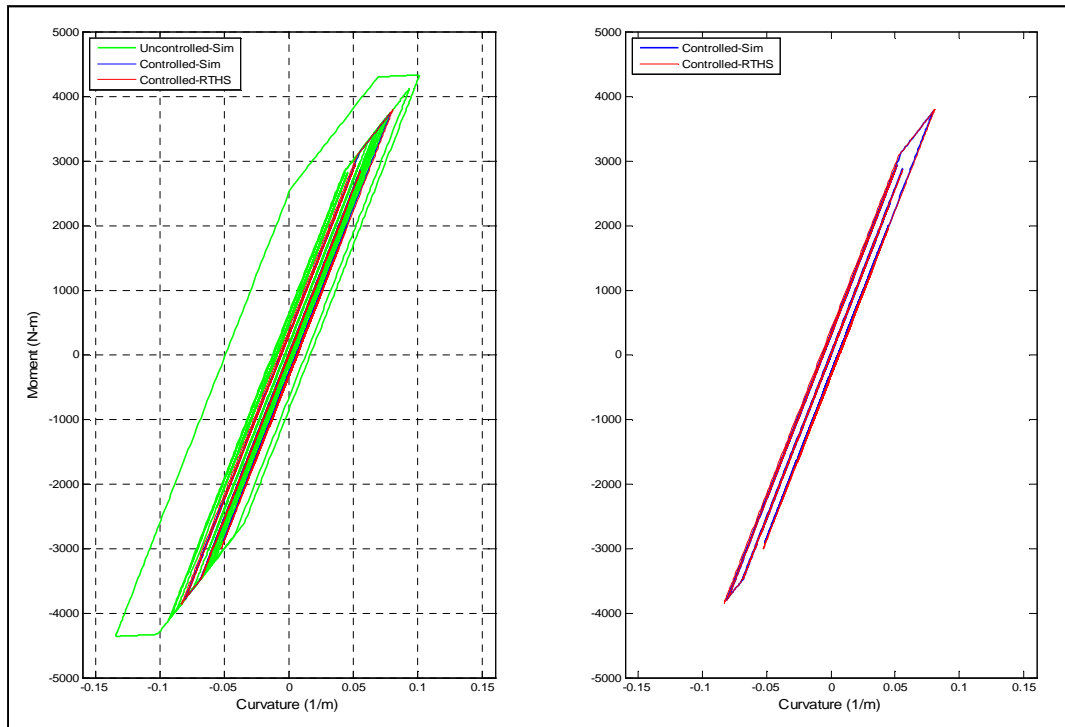


Figure 4.65: Hysteresis loops based on Test 9

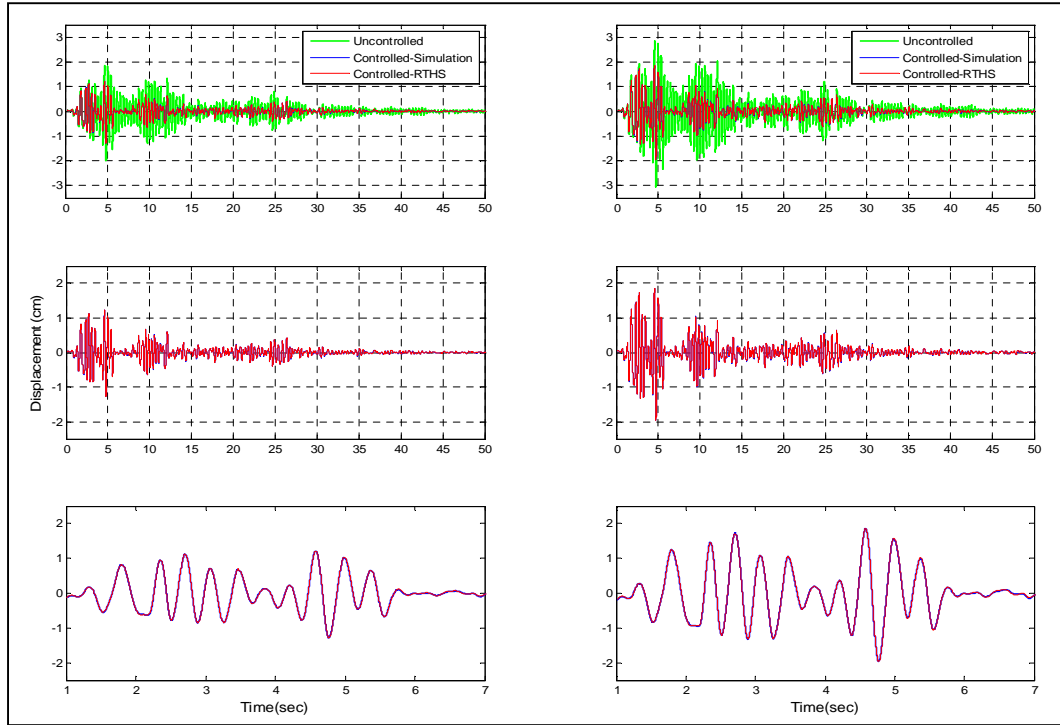


Figure 4.66: Displacement records based on Test 10

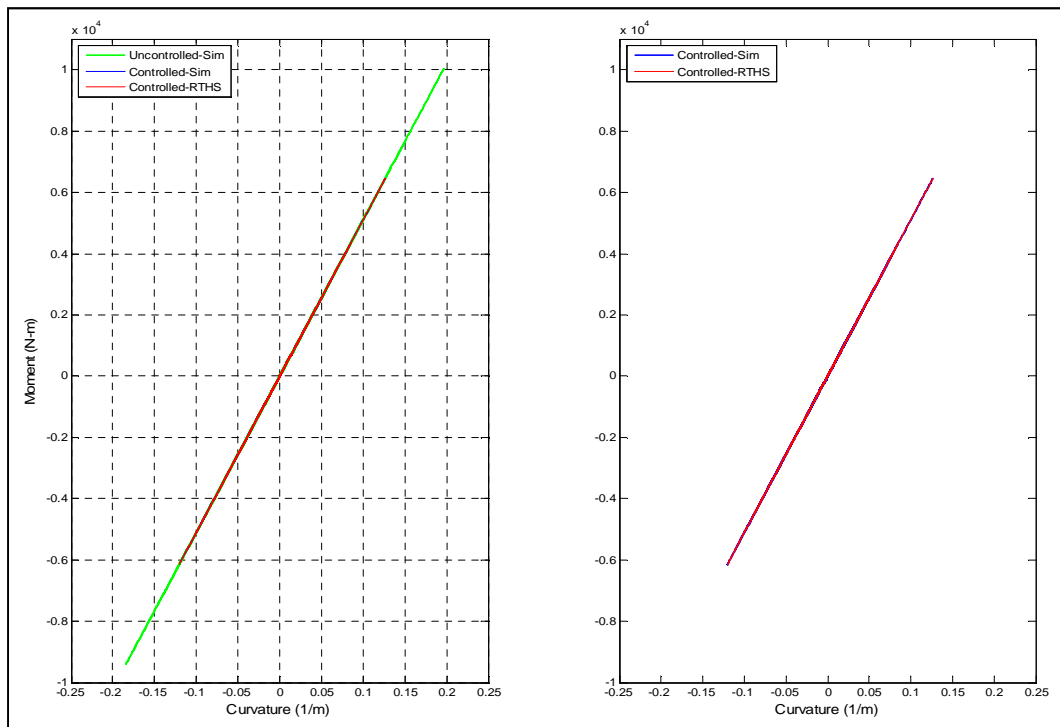


Figure 4.67: Hysteresis loops based on Test 10

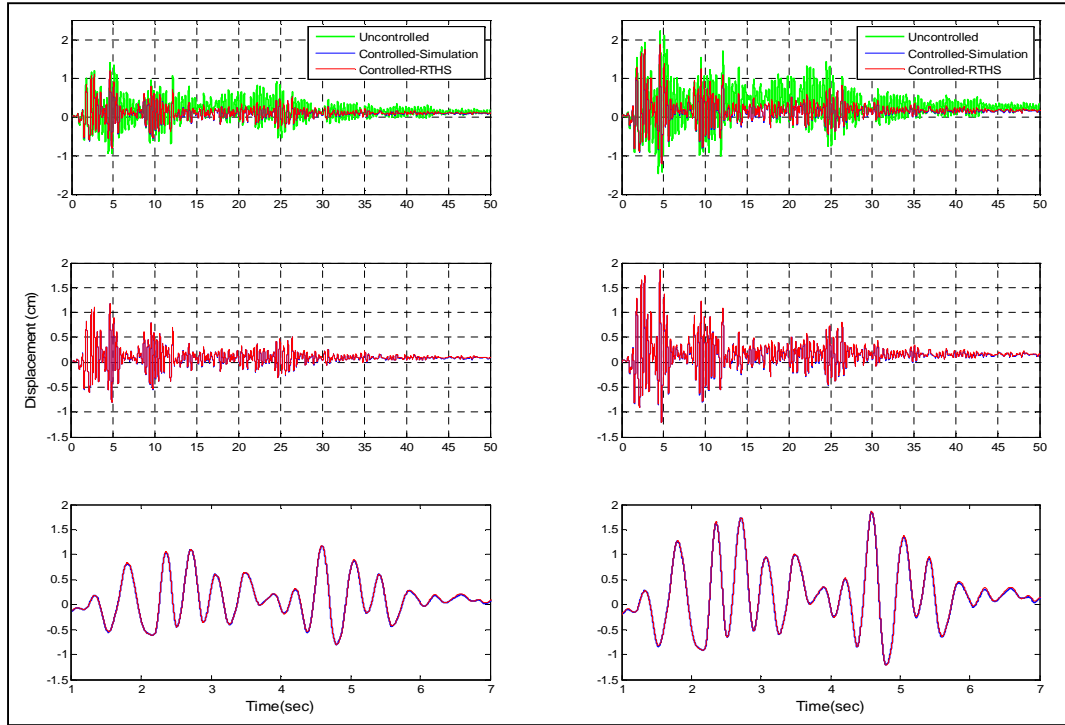


Figure 4.68: Displacement records based on Test 11

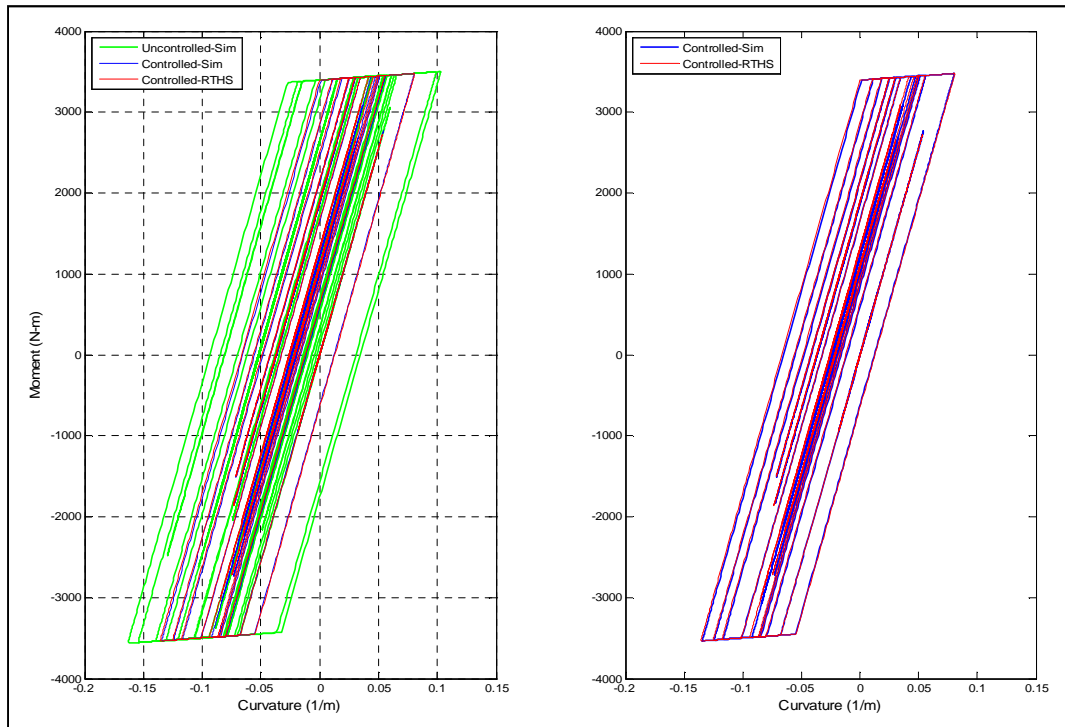


Figure 4.69: Hysteresis loops based on Test 11

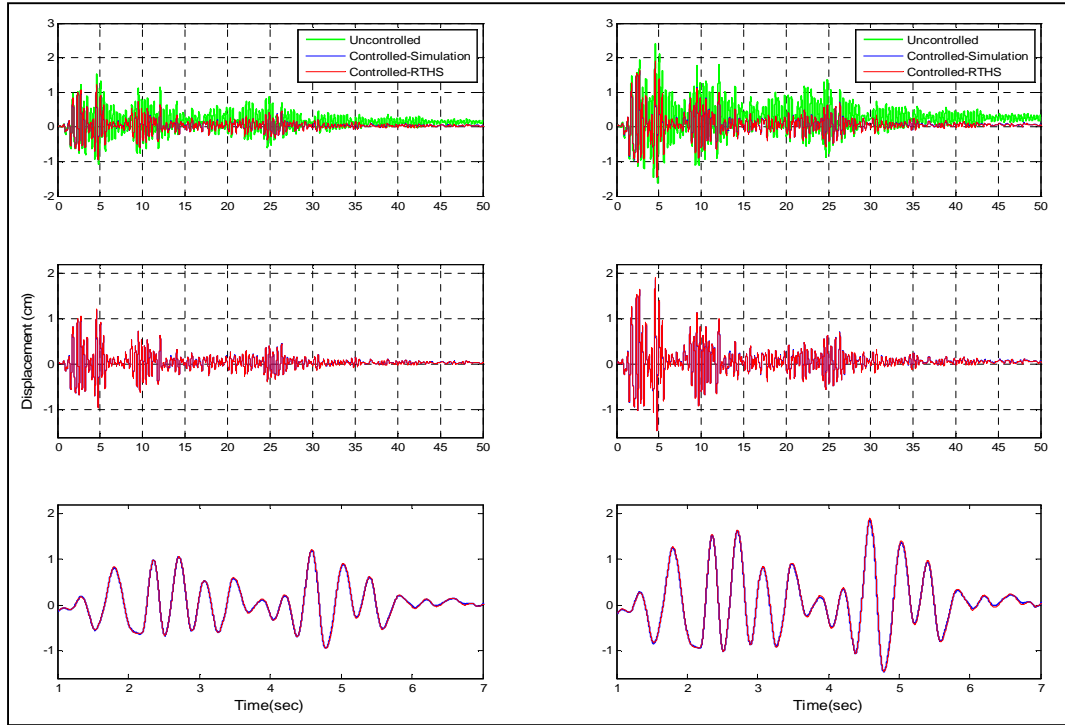


Figure 4.70: Displacement records based on Test 12

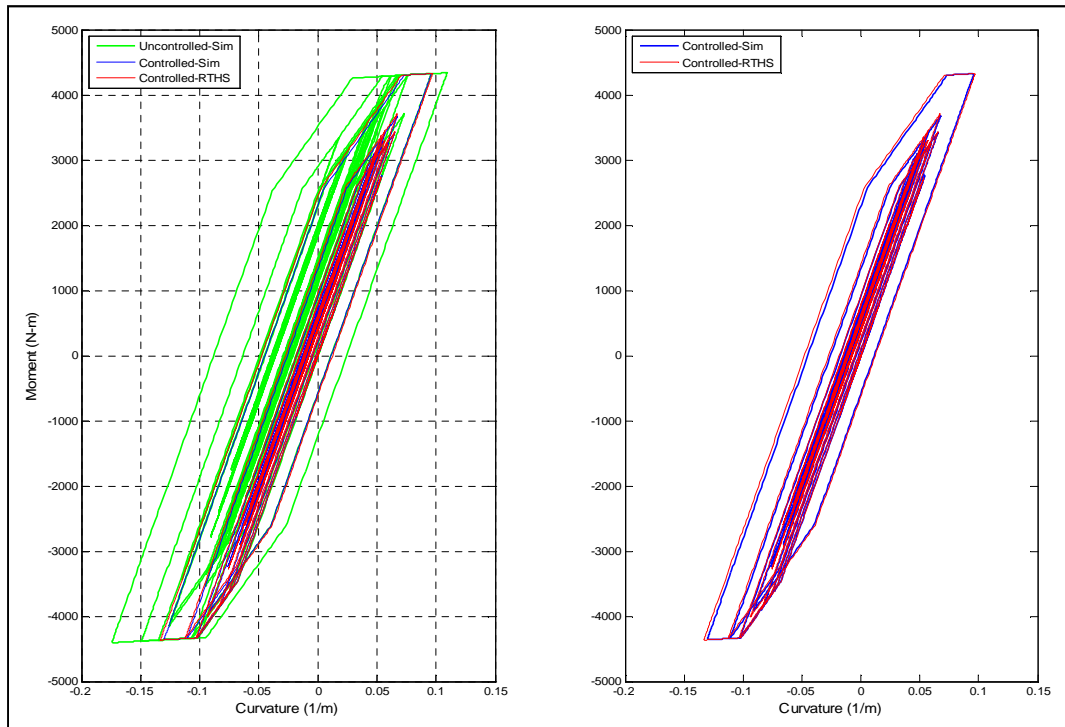


Figure 4.71: Hysteresis loops based on Test 12

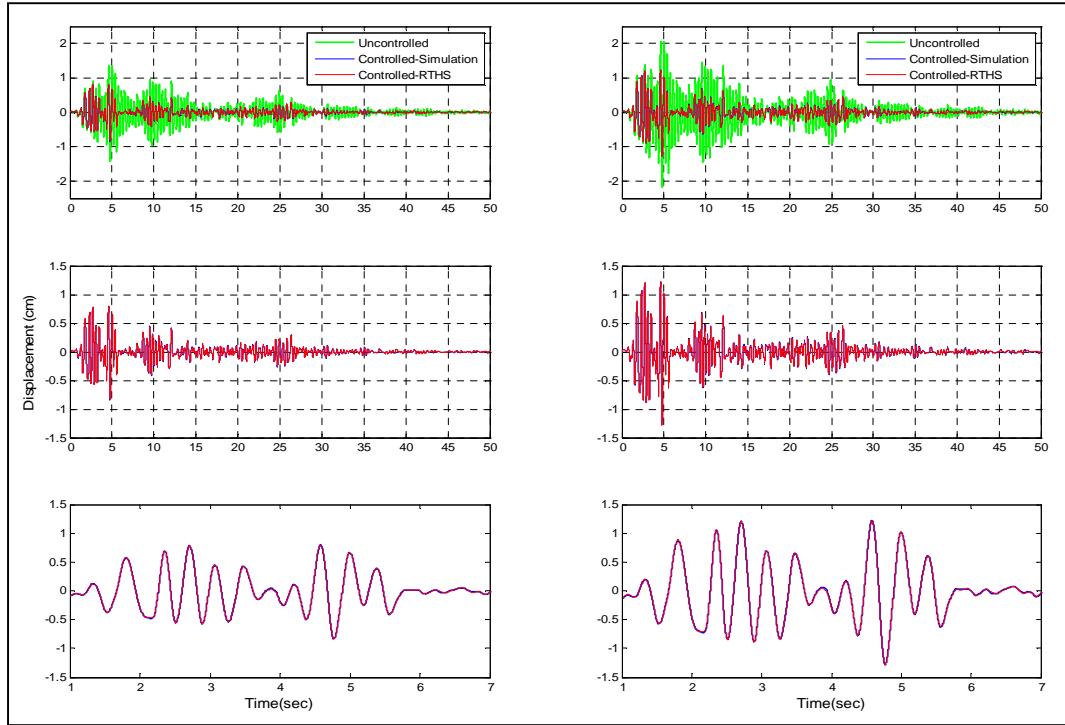


Figure 4.72: Displacement records based on Test 13

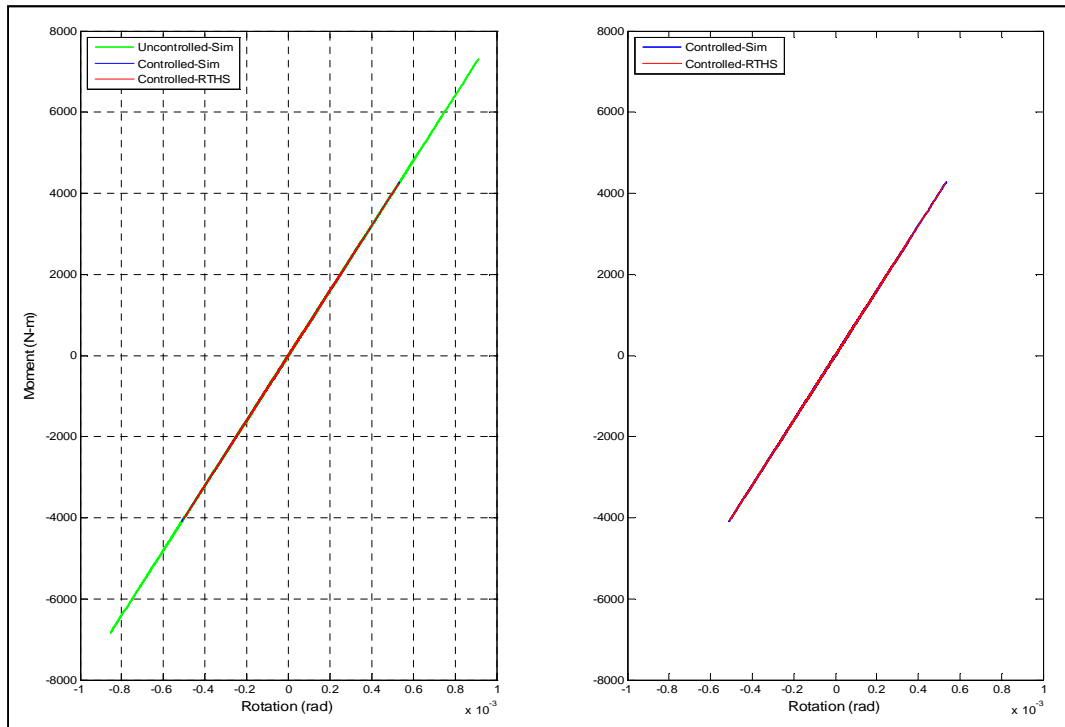


Figure 4.73: Hysteresis loops based on Test 13

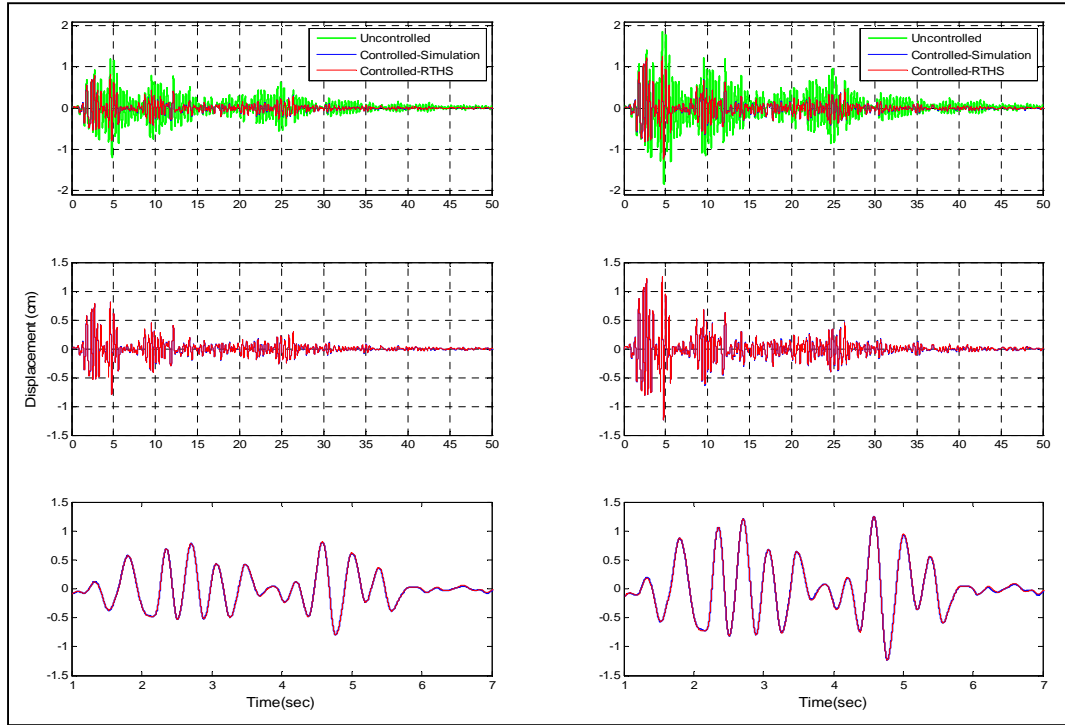


Figure 4.74: Displacement records based on Test 14

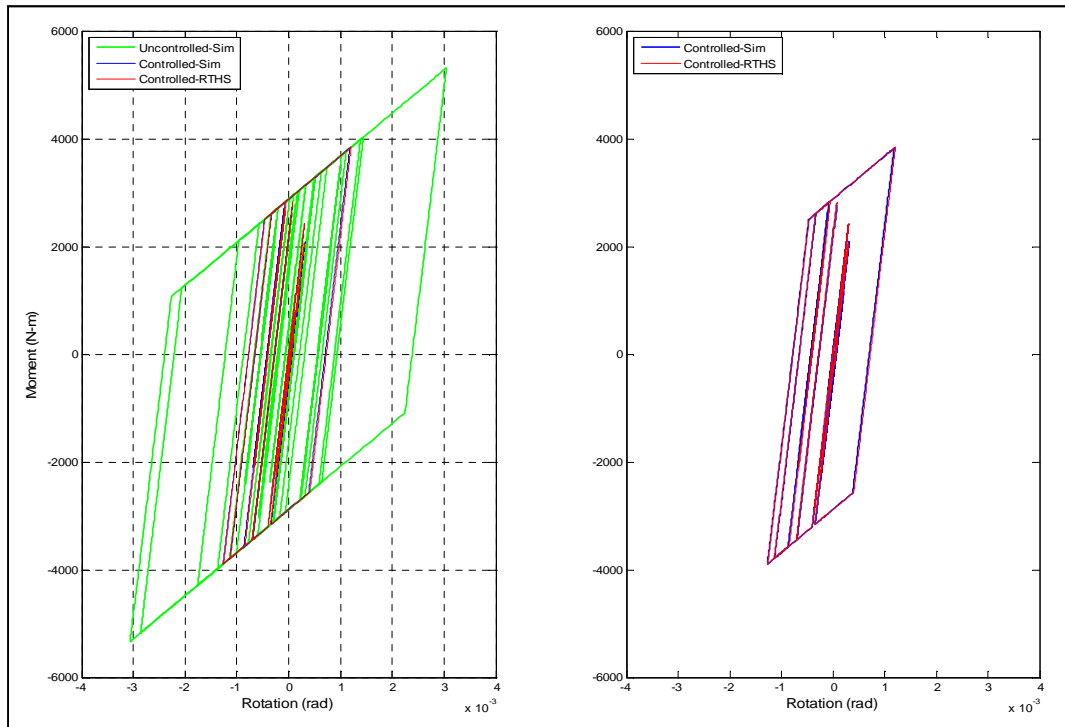


Figure 4.75: Hysteresis loops based on Test 14

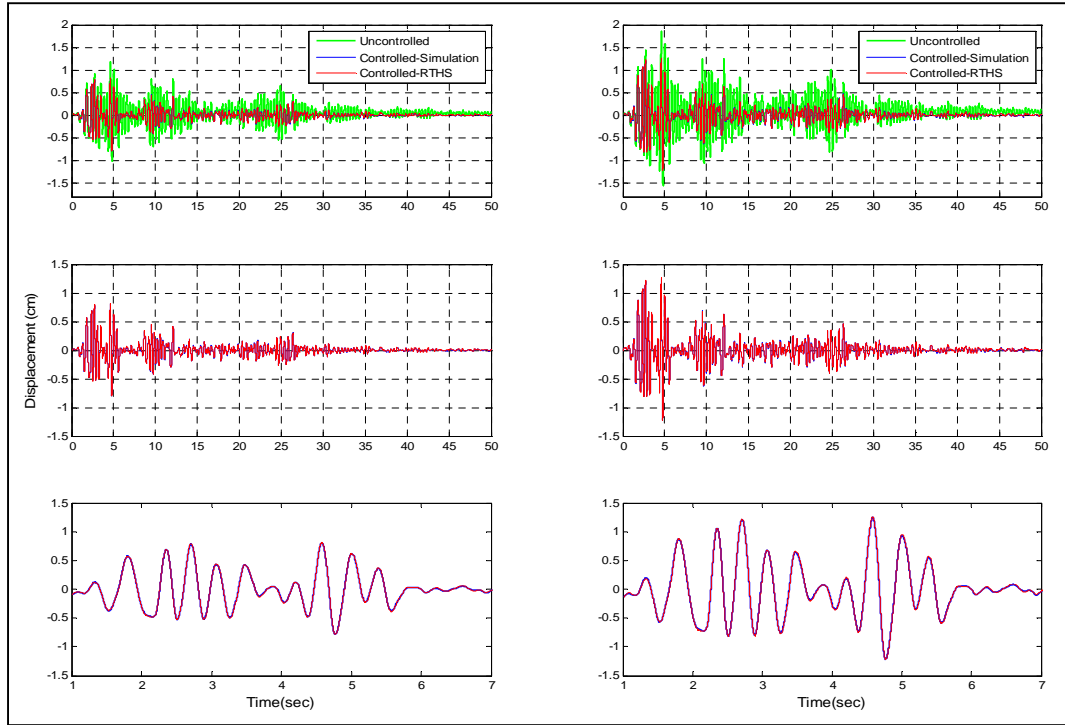


Figure 4.76: Displacement records based on Test 15

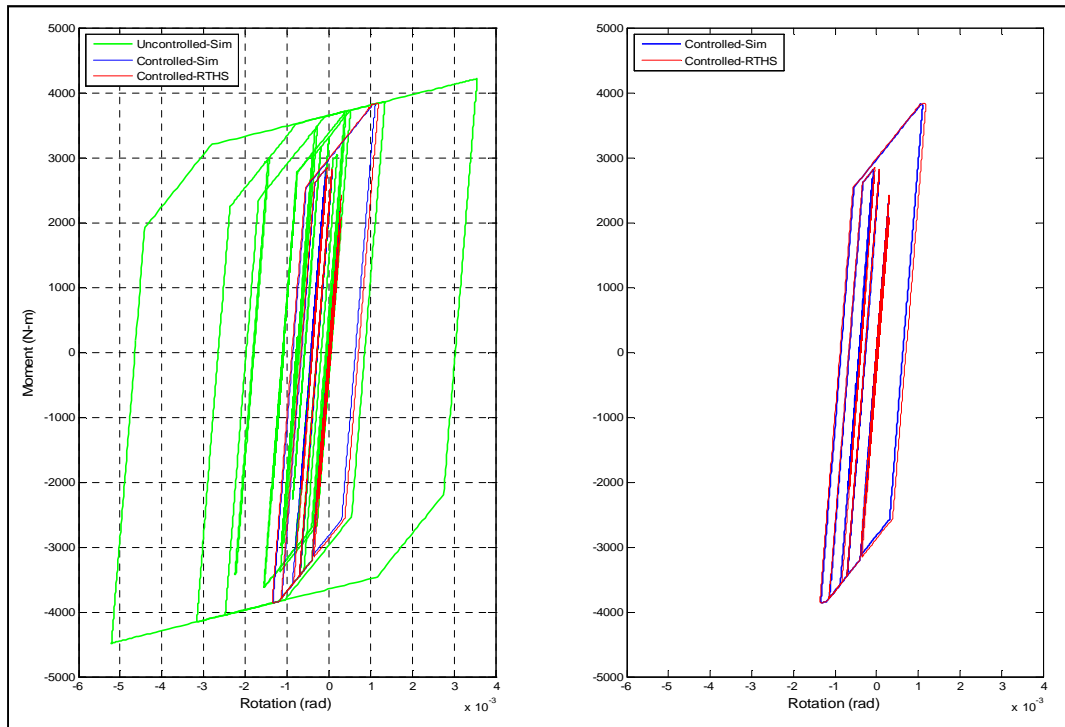


Figure 4.77: Hysteresis loops based on Test 15

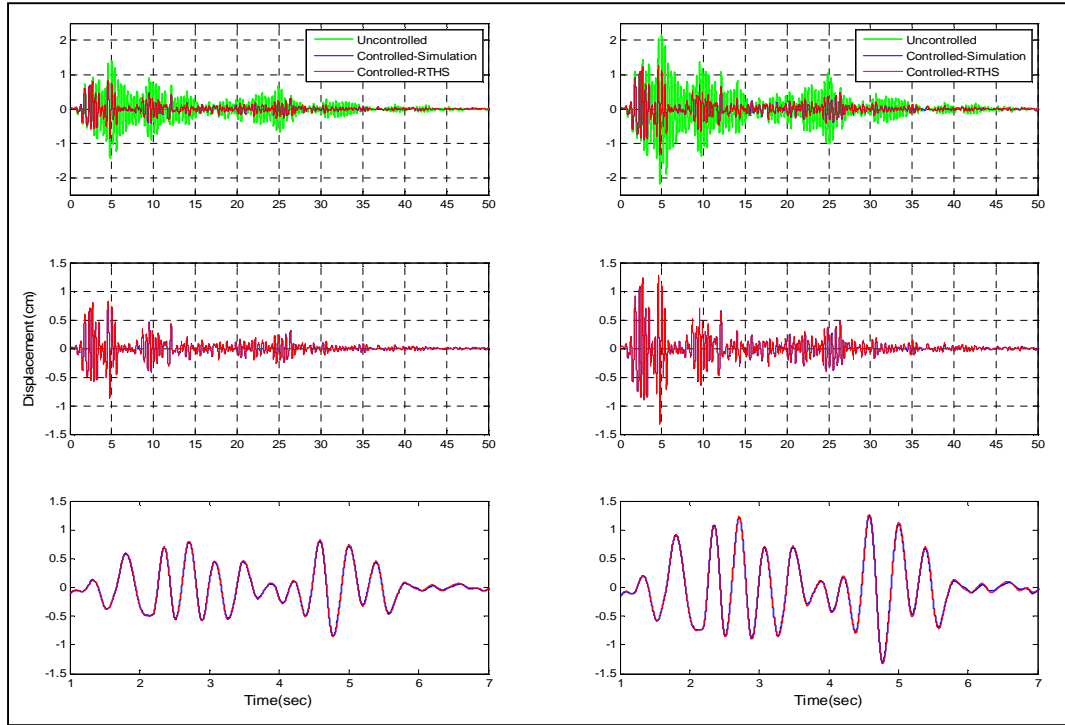


Figure 4.78: Displacement records based on Test 16

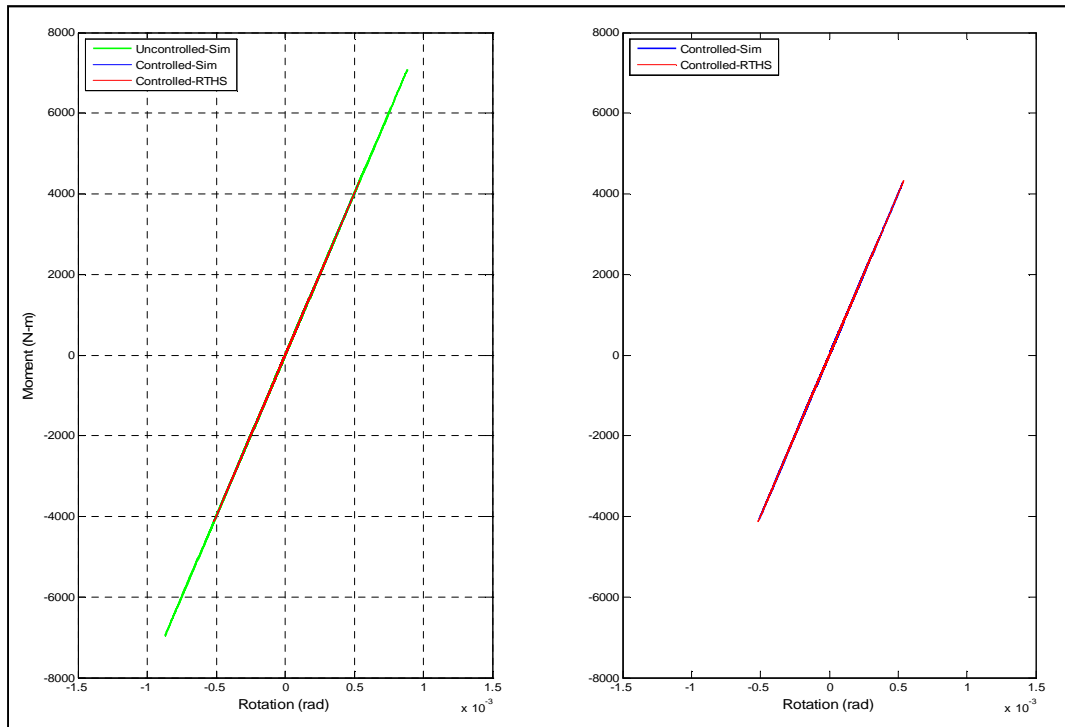


Figure 4.79: Hysteresis loops based on Test 16

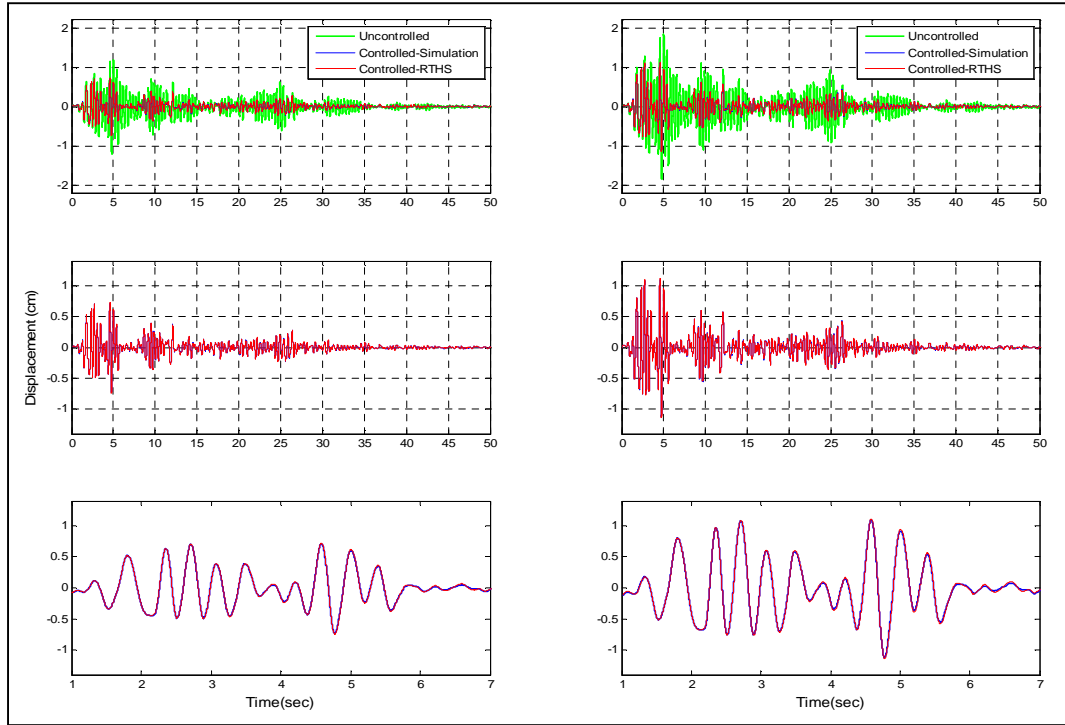


Figure 4.80: Displacement records based on Test 17

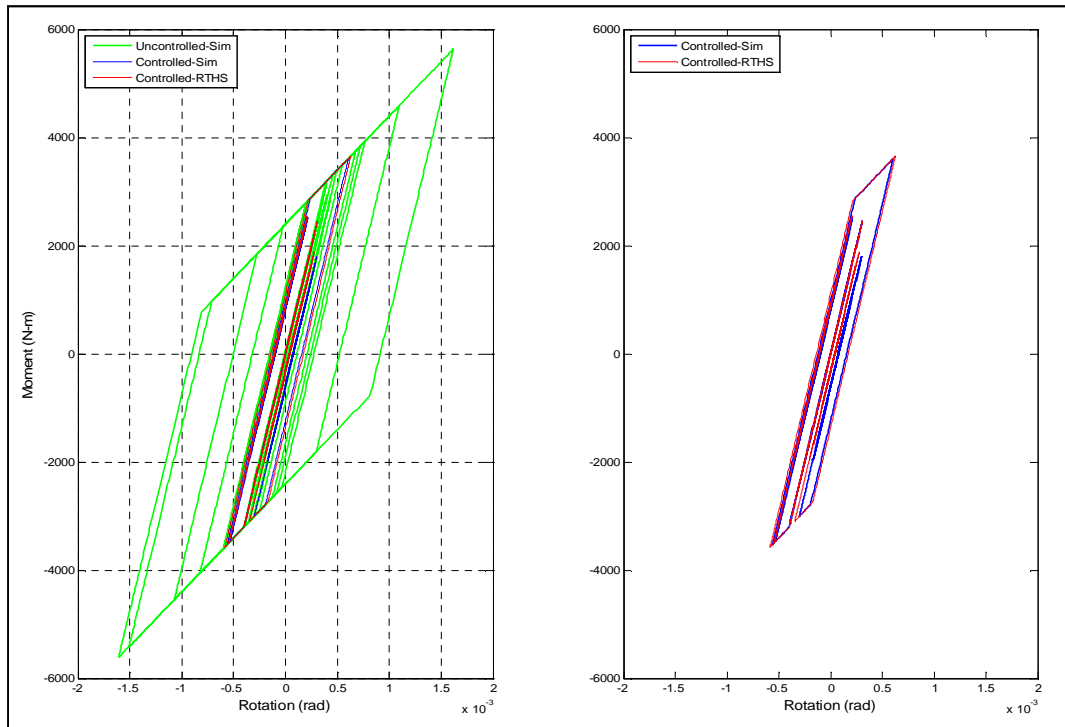


Figure 4.81: Hysteresis loops based on Test 17

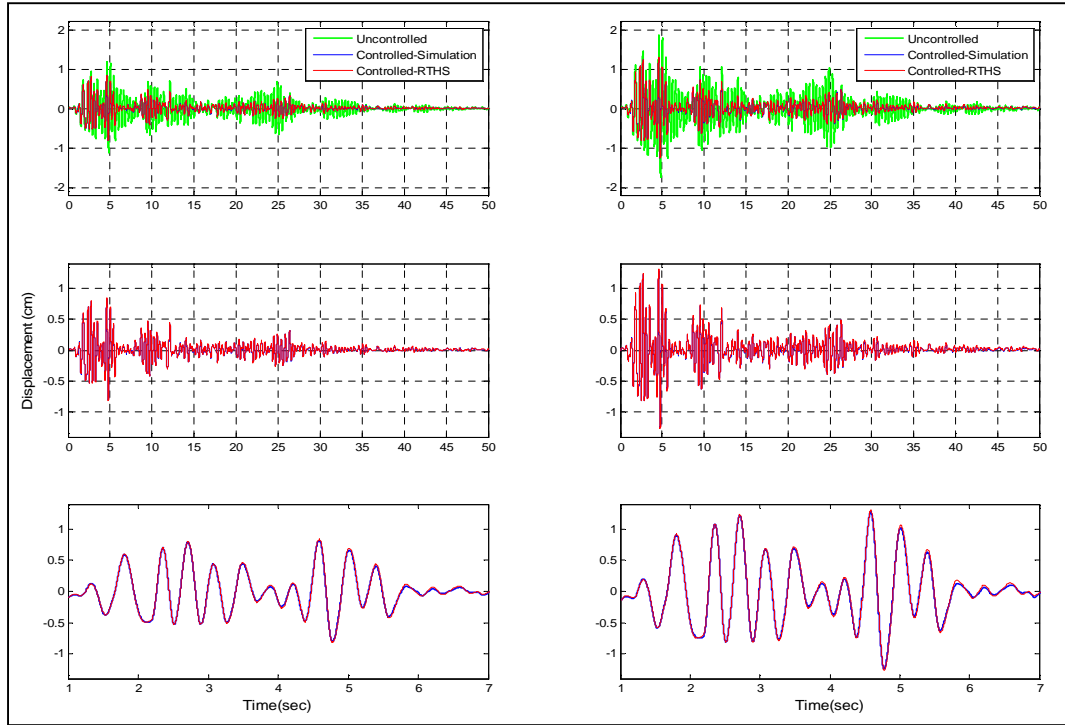


Figure 4.82: Displacement records based on Test 18

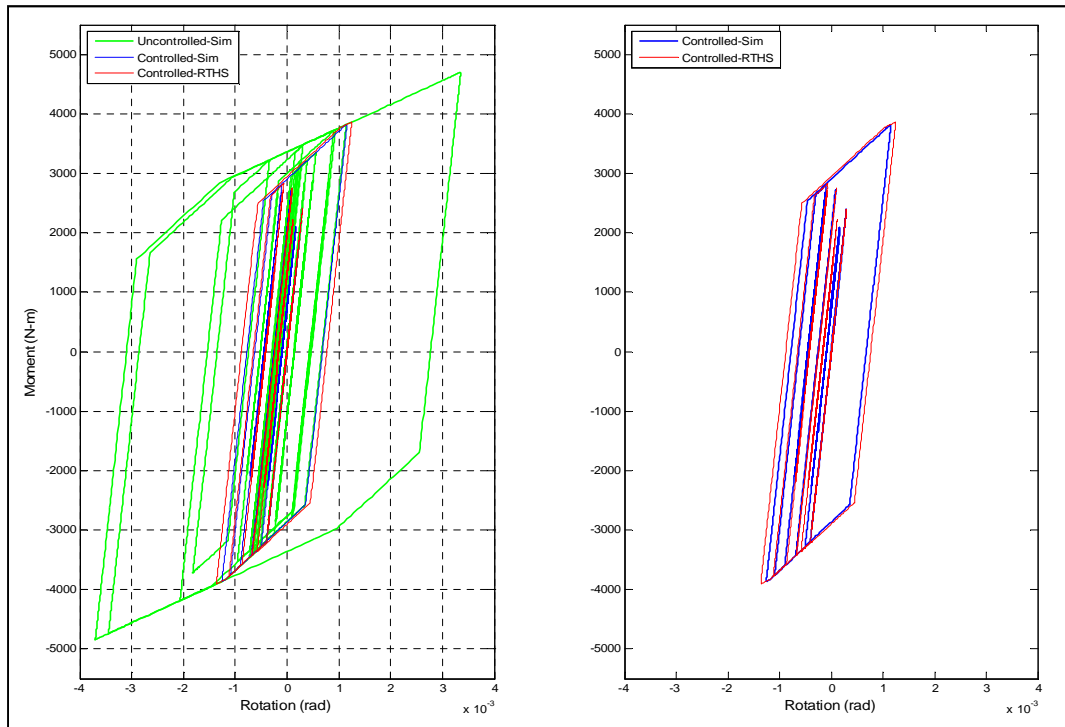


Figure 4.83: Hysteresis loops based on Test 18

CHAPTER 5. EXPERIMENTAL VALIDATION II: REAL-TIME HYBRID SIMULATION AT THE SSTL

The performance of the proposed RT-Frame2D computational platform is also investigated when subjected to real-time execution during a hybrid simulation of a frame structure of increased complexity and scale. The frame is equipped with a large-scale damper device. The experimental implementation is performed using a large-scale magneto-rheological damper specimen as the physical substructure. Additionally, the computational platform is evaluated using a different real-time kernel (dSPACE). The RT-Frame2D is used in RTHS for the evaluation of the corresponding computational counterpart i.e. the frame structure. The test setup selected for this experiment is located in the Smart Structures Technology Laboratory (SSTL) (<http://sstl.cee.illinois.edu>) at the University of Illinois in Urbana-Champaign. Successful studies of RTHS for frame structures equipped with a large-scale MR Dampers (Phillips et al., 2010) have been performed with this test setup. This chapter begins with a discussion of the experimental plan followed by a description of relevant components of the test setup. Finally, experimental results are presented.

5.1 Experimental plan

The RTHS implementation is intended to replicate the global nonlinear dynamic response of a frame structure equipped with a damper device when subjected to a ground motion. Only one RTHS scenario, RTHS - Phase 1, is evaluated in this implementation. RTHS Phase - 1 considers the mass and frame structure as computational substructures while the damper device is the experimental substructure.

A prototype full-scale frame structure designed by the Lehigh University research team as a part of the NEESR research project: *Performance-Based Design and Real-time, Large-scale Simulation to Enable Implementation of Advanced Damping Systems* is utilized as the computational substructure. A modified version of this frame structure was presented in Chapter 3 for evaluation of the real-time execution capabilities facilitated by RT-Frame2D. A large-scale MR damper with a 200 kN capacity is utilized as the experimental substructure. Mass is also considered computationally within the RTHS. The dominant modal content of the hybrid system does not exceed the allowed operational frequency range of the test setup. Additionally, the frequency content is comparable to those observed in realistic steel frame structures. These RTHS scenarios are performed for evaluating RT-Frame2D in terms of accuracy and stability, as well as the ability to execute the computations in real-time. A description of the experimental setup and corresponding experimental results are presented and discussed in the next sections.

5.2 RTHS platform at the Smart Structures Technology Laboratory

The features of the RTHS setup located in the SSTL and utilized for completion of the proposed experimental plan are presented in this section. The setup includes a dynamically-rated linear hydraulic actuator with a digital servo-controller for actuator control (Phillips and Spencer, 2011). The hydraulic actuator, manufactured by the Shore Western Corporation and equipped with an 80 gpm servo-valve, allows for a force capacity of 125 kips with a stroke of 6 in. Additionally, the actuator relies on both an AC LVDT for displacement measurement and feedback and a load cell of 100 kip capacity for force measurement. Hydraulic oil is provided through a hydraulic service manifold which can operate at 80 gpm. The actuator is mounted on a 3 in thick steel plate which is attached to the strong floor of the laboratory through threaded rods and shear keys to avoid translational movement during testing. A photograph of the hydraulic actuator is shown in Figure 5.1.

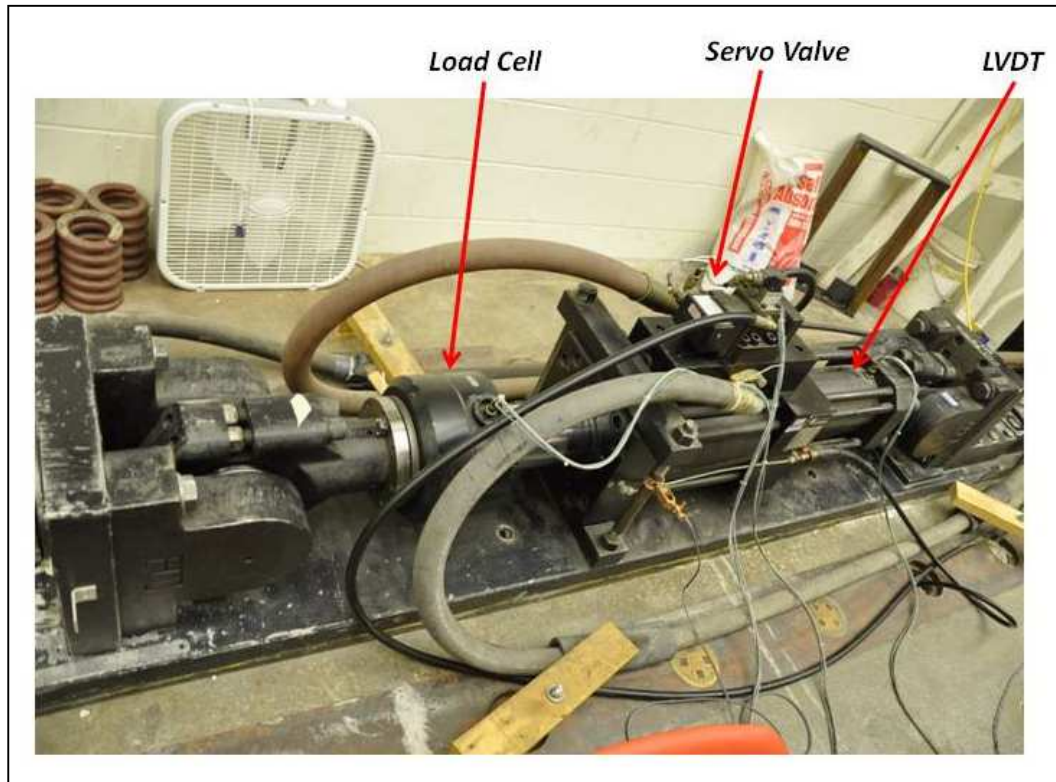


Figure 5.1: Hydraulic actuator at the SSTL

A Shore Western model 1104 digital servo-controller is used to control the actuator in a displacement feedback mode. *Simulink* is used to integrate all of the RTHS components, including the computational block, with the servo-hydraulic and MR damper controller algorithms. Additionally, analog and digital (DAQ) boards for data exchange between computational and experimental substructures during test are also included within the *Simulink* platform. Rather than the *Speedgoat/xPC* real-time kernel utilized in the previous experiments, here a dSPACE system is utilized for real-time execution. dSPACE system is a software/hardware solution for the execution, development and testing of rapid control prototyping and real-time execution of dynamical system applications. Therefore, the C-source code generated and compiled from the *Simulink* model (host PC) using the *MATLAB/Real-Time Workshop* is downloaded into a dSPACE model 1103 DSP board (target PC) for real-time execution.

5.3 Experimental set-up

This section introduces the features and mathematical modeling of the experimental substructure, i.e. a large-scale 200 kN force capacity MR damper. The design philosophy for the tracking control strategy that is adopted for compensating the hydraulic actuator dynamics during RTHS execution is also presented.

5.3.1 Large-scale magneto-rheological damper device

A brief description of the main components of the large-scale MR damper specimen utilized in this experiment is presented. Two different views of the MR damper are shown in Figure 5.2. The specimen, manufactured by Lord Corporation, has a length of 1.47m with an approximate weight of 2,734 kN and available stroke of ± 292 mm. The accumulator in the damper can accommodate a temperature change in the fluid of 27° C. The force capacity that can be achieved with this device is around 200 kN. Forces in the MR damper are reached by exposing the MR fluid to a current driven command signal through the electromagnet coil as explained in the precedent chapter. The coil for this device has an approximate resistance of 4.8 ohms with an associated inductance of 5 henrys (H) at 1 ampere (A) and 3 H at 2 A, as reported by Lord Corporation. The current command signal is applied to the MR damper using a pulse-width modulator system which consists of an Advanced Motion Controls PWM Servo-Amplifier model 20A8 powered by an unregulated power supply of 80 VDC. This system is utilized so that power efficiency and quick response time can be achieved while operating the MR damper device. The PWM Servo-Amplifier is operated by a 0 - 5 VDC signal while the input control signal can be switched at a rate up to 1 kHz. A view of the attachment setup in the SSTL between the hydraulic actuator and the MR damper specimen is depicted in Figure 5.3. A mathematic model for describing the highly nonlinear behavior developed by the MR damper device is introduced in the next section. Parameters are then identified in the following section.

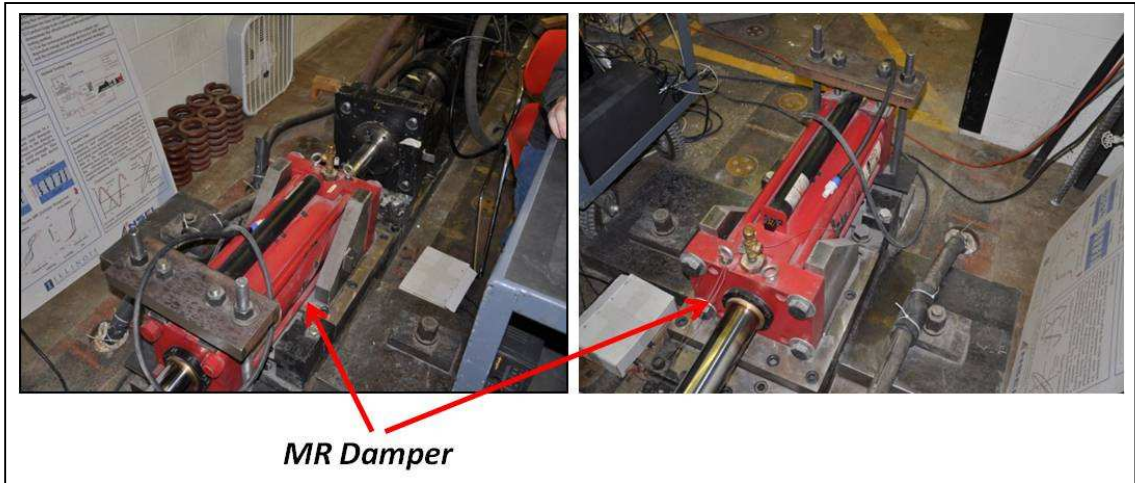


Figure 5.2: MR dampers view

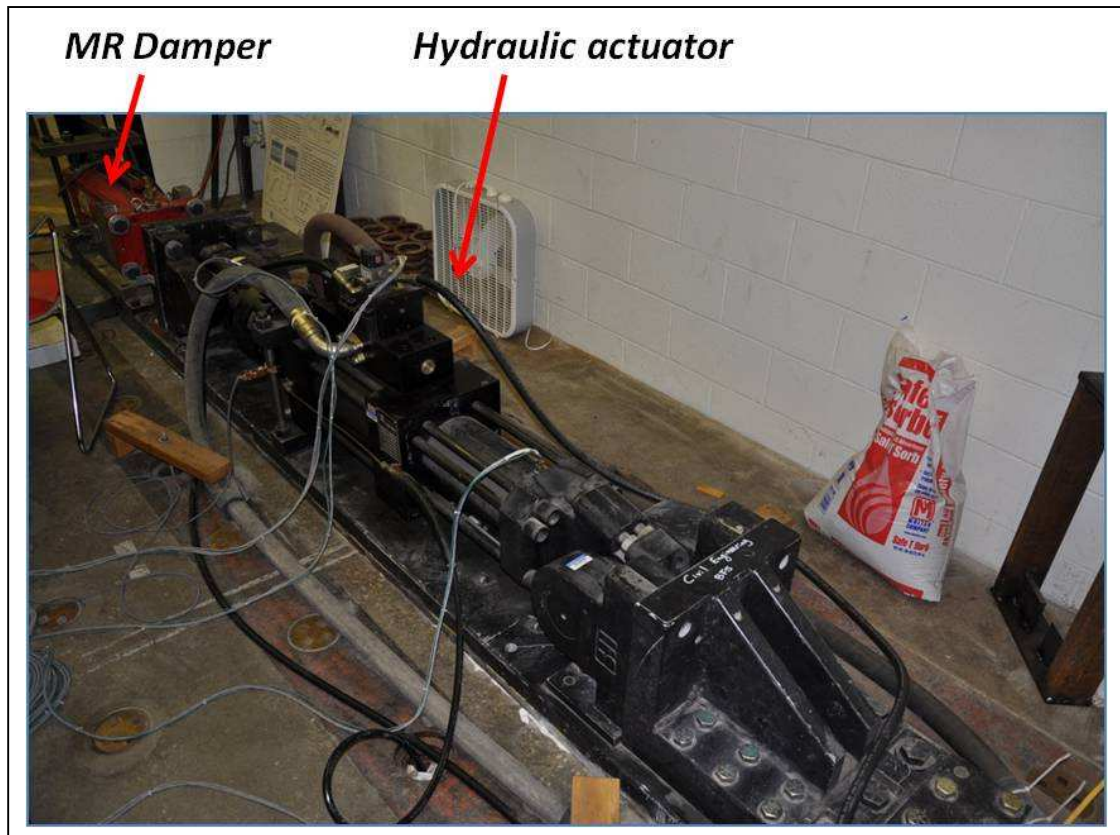


Figure 5.3: MR damper and actuator set-up

5.3.2 Hyperbolic tangent model

A simulation of the full RTHS scenario is performed for later comparison with the RTHS results. Thus, a mathematical model for describing the behavior of the large-scale MR damper device to be tested in the laboratory is required. The hyperbolic tangent model, originally proposed by Gavin (Gavin, 2001), is selected for this simulation. The hyperbolic tangent model describes the nonlinear behavior of the MR damper based on a simplified mechanical system composed by two spring-dashpot systems arranged in series and connected through an inertial mass element m_0 as shown in Figure 5.4. Additionally, a Coulomb friction element is included to add resistance to the relative motion between the inertial mass and the fixed based.

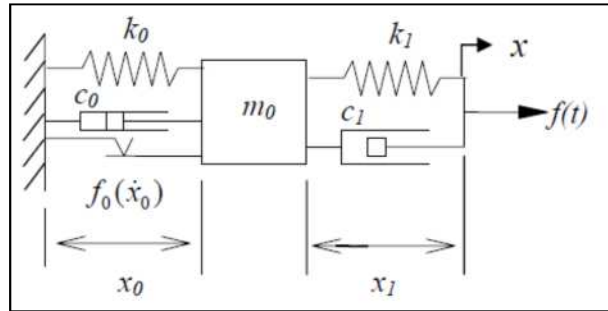


Figure 5.4: Hyperbolic tangent model (after Bass and Christenson, 2008)

Mass in this model represents the inertia of both the fluid and the moving piston. Parameters k_1, c_1 account for the pre-yield viscoelastic behavior of the device. Parameters k_0, c_0 describe the post-yield viscoelasticity phase. Additionally, the force and relative velocity are related in the Coulomb friction element as

$$f(\dot{x}_0) = f_0 \tanh\left(\frac{\dot{x}_0}{V_{ref}}\right) \quad (5.1)$$

Here \dot{x}_0 is the relative velocity between the mass and the fixed base. f_0 is the yield force and V_{ref} is the reference velocity. As observed in Figure 5.4, the total displacement and velocity developed by the damper piston can be expressed in terms of the relative displacement and velocity developed by the two dynamical systems, i.e. between the mass and fixed base and the piston and the mass, respectively. This behavior is idealized as

$$x = x_0 + x_1 \text{ and } \dot{x} = \dot{x}_0 + \dot{x}_1 .$$

Rearranging the previous expressions yields to a state-space form of the dynamical systems as

$$\begin{bmatrix} \dot{x}_0 \\ \ddot{x}_0 \end{bmatrix} = \begin{bmatrix} 0 & 1 \\ \frac{-k_0 - k_1}{m_0} & \frac{-c_0 - c_1}{m_0} \end{bmatrix} \begin{bmatrix} x_0 \\ \dot{x}_0 \end{bmatrix} + \begin{bmatrix} 0 & 0 \\ \frac{k_1}{m_0} & \frac{c_1}{m_0} \end{bmatrix} \begin{bmatrix} x \\ \dot{x} \end{bmatrix} + \begin{bmatrix} 0 \\ \frac{-1}{m_0} \end{bmatrix} f_0 \tanh\left(\frac{\dot{x}_0}{V_{ref}}\right) \quad (5.2)$$

and

$$\hat{f} = [-k_1 \quad -c_1] \begin{bmatrix} x_0 \\ \dot{x}_0 \end{bmatrix} + [k_1 \quad c_1] \begin{bmatrix} x \\ \dot{x} \end{bmatrix} \quad (5.3)$$

Here, \hat{f} is the MR damper nonlinear force exerted by the piston. Seven parameters can be distinguished from the previous equations for complete definition of the model. The parameters are listed as $k_0, c_0, k_1, c_1, m_0, f_0, V_{ref}$. Values for these parameters are identified based on a curve-fitting procedure using experimental data as explained in the next section.

5.3.3 MR Damper device characterization

Calibration of the proposed hyperbolic tangent model was performed at the University of Connecticut as an effort within the NEESR research project: *Performance-Based Design and Real-time, Large-scale Simulation to Enable Implementation of Advanced Damping Systems*. Parameters of the proposed hyperbolic tangent model were identified based on experimental data measured from the large-scale 200 kN capacity MR damper specimen used in this validation. The data was generated by subjecting the MR damper to a set of sinusoidal displacement inputs each having fixed amplitude and frequency. This was accomplished with the hydraulic actuator and repeated for different voltage values.

Table 5.1: Hyperbolic tangent model parameters

<i>Parameter as function of current “i”</i>	<i>Unit</i>
$k_0 = 0.0006227 + 0.00023018*i + 0.00013221*i^2 - 0.00009981*i^3 + 0.00001456*i^4$	<i>kN/mm</i>
$c_0 = 0.12641107 + 0.35800654*i - 0.29955199*i^2 + 0.09324886*i^3 - 0.00979318*i^4$	<i>kN/mm</i>
$k_1 = 55.0833414 + 110.61993240*i - 80.70250595*i^2 + 23.75858844*i^3 - 2.43069439*i^4$	<i>kN/mm</i>
$c_1 = 0.35673105 - 0.46060436*i + 0.26691922*i^2 - 0.06725950*i^3 + 0.00618122*i^4$	<i>kN-sec/mm</i>
$m_0 = 0.00485337 - 0.00705031*i + 0.00547653*i^2 - 0.00162172*i^3 + 0.00016424*i^4$	<i>kg</i>
$f_0 = 5.9964 + 91.5708*i + 2.7022*i^2 - 9.9421*i^3 + 1.4691*i^4$	<i>kN</i>
$V_{ref} = 0.75927313 + 13.11818851*i - 6.18812701*i^2 + 1.36241327*i^3 - 0.11574068*i^4$	<i>mm/sec</i>

Because of the functional dependency of the MR damper with respect to the magnetic field, parameters in the proposed mathematical model are defined as function of the applied voltage (or current). Here, fourth-order polynomials are considered for the definition of the MR damper parameters as function of current i . Polynomial coefficients are identified based on a multidimensional unconstrained nonlinear optimization procedure. The optimization is performed using an objective function defined as the RMS value of the error between the experimental and computed MR damper forces. The optimization problem was solved by the use of a Nelder-Mead direct search simplex

method available in *MATLAB* (Bass and Christenson, 2008). The resulting identified polynomial coefficients defining the model parameters are shown in Table 5.1.

5.3.4 Hydraulic actuator compensation scheme

The tracking control strategy for compensation of the hydraulic actuator dynamics in this experiment is briefly described in this section. As discussed in the prior chapter, adequate hydraulic actuator motion control is required to improve RTHS performance and guarantee stability during execution. A model-based control strategy, designed and implemented at the SSTL by Carrion (Carrion and Spencer, 2007; Carrion et al., 2009) is utilized in this experiment. This approach compensates for the actuator dynamics via a feedforward-feedback tracking command implementation. The feedforward portion compensates the plant dynamics using an inverse model of a frequency domain open-loop identified model of the plant. The plant includes the servo-controller for the hydraulic actuator, the hydraulic actuator itself and the MR damper specimen. The feedback portion compensates for the plant dynamics with simple proportional constant gain as in PID type control. A schematic view of the control framework is depicted in Figure 5.5.

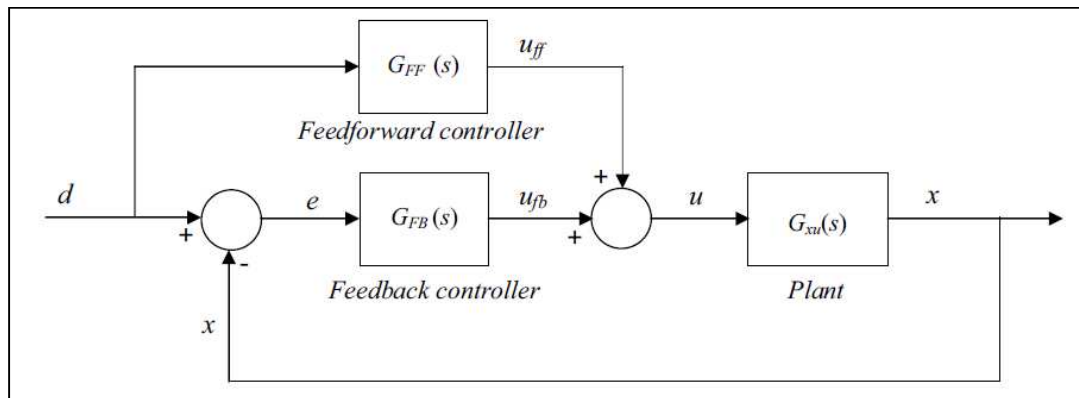


Figure 5.5: Block Diagram of Combined control strategy (after Carrion, 2009)

As implied by Figure 5.5, when the feedforward portion of the control implementation reduces completely the error between measured and desired displacements, then the feedback control does not act. Conversely, when the dynamics of the plant are not

completely compensated for, the feedback portion takes part to further reduce the error. Therefore, this combined implementation takes full advantage of both control strategies. This control strategy is utilized for acquiring the results discussed in the next section.

5.4 MR Damper evaluation at the SSTL (UIUC)

In the experimental implementation, the RTHS Phase-1 scenario is adopted. Here a 60% scale frame structure and associated mass are considered as the computational substructures. The large-scale MR damper is the experimental substructure.

Simulated responses of the RTHS will be used for the evaluation of the computational platform performance. The identified mathematical model of the MR damper based on the hyperbolic tangent model (see Section 5.3.3) is used in the simulation. The RT-Frame2D model is constructed based on the geometry and member section configuration as shown in Figure 5.6.

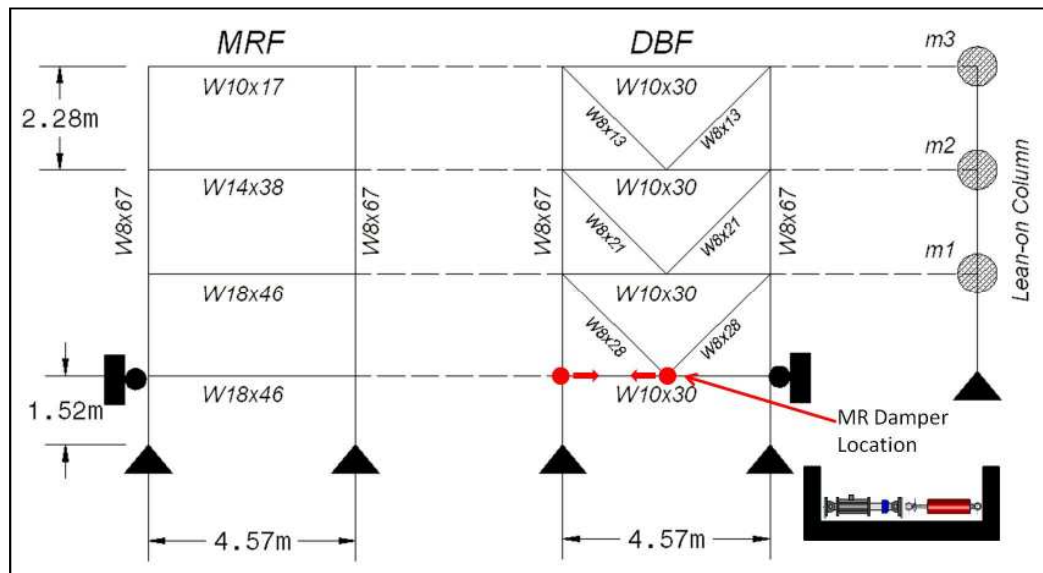


Figure 5.6: Prototype structure computational model

As observed, the frame structure includes a moment resisting frame (MRF) and damped braced frame (DBF) (designed to hold the MR damper devices), and a lean-on column to carry out the mass. As further reference, a photograph of the prototype frame structure showing the MRF (yellow) and DBF (orange) components is depicted in Figure 5.7. In addition to the self-weight distributed over the beam elements as distributed mass, concentrated mass is lumped at the lean-on column, as shown in Figure 5.6. Mass values of $1.00e5$ kg and $7.35e4$ kg are applied at the first/second and third floor, respectively. This mass distribution is used to assemble the global mass matrix. Damping global matrix is defined with a stiffness-proportional damping assumption, yielding a fundamental damping ratio of 2%. Column members are defined with the *linear elastic beam-column element*. Beam members are defined with the *nonlinear beam-column element* offered by the RT-Frame2D element library. Sections for the nonlinear beam elements are defined with a bilinear moment-curvature hysteresis model based on a kinematic hardening assumption and a post yielding ratio of 2.5%. Yielding moments and corresponding yielding curvatures are calculated based on the flexural section properties for each member.

Boundary conditions are imposed as shown in Figure 5.6. Rigid diaphragm constraints are imposed among translational DOF of three previous components to guarantee equal lateral displacement at each floor. As a result, the three first natural frequencies for the resulting computational model are calculated with values of 1.05 Hz, 3.47 Hz and 7.85 Hz, respectively. The unconditionally-explicit CR integration scheme is used to solve the incremental equation of motion.

Six RTHS scenarios are tested using the N-S component recorded at the Imperial Valley Irrigation District substation in El Centro, California, during the Imperial Valley, California earthquake of May 18, 1940. Earthquake intensities considered in each RTHS scenario are shown in Table 5.2.

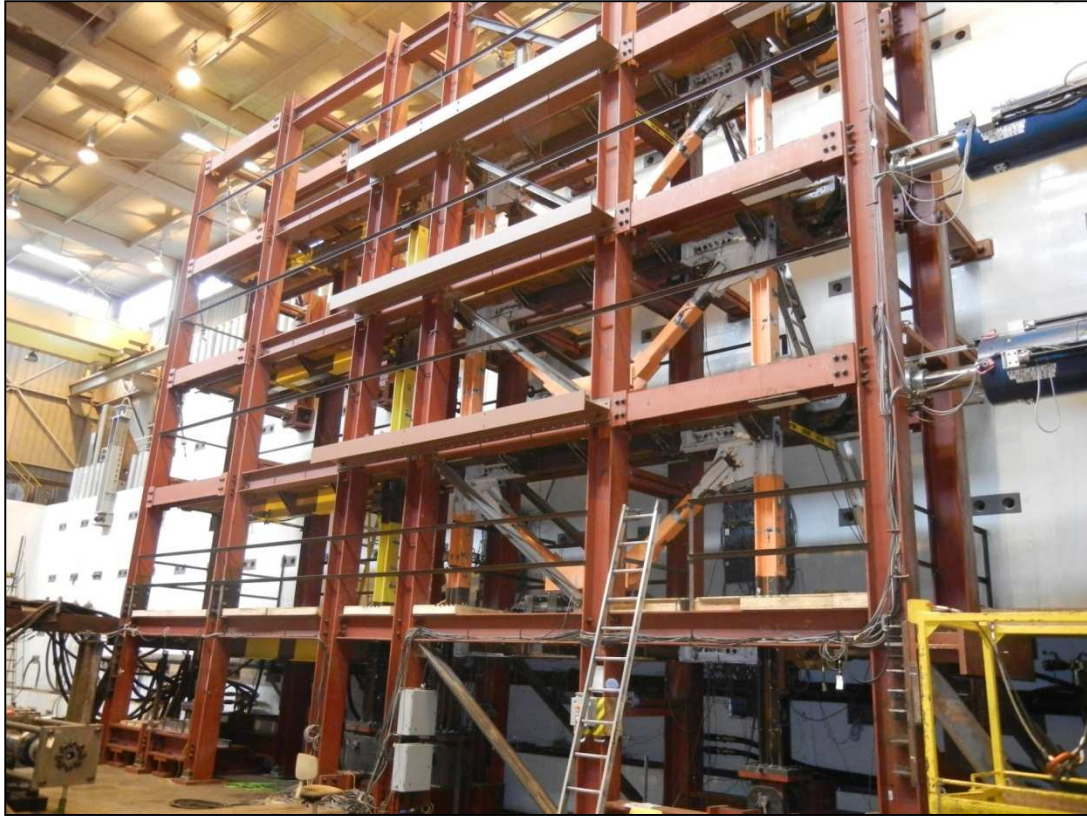


Figure 5.7: Prototype frame structure in the Lehigh University NEES Laboratory

Table 5.2: Testing scenarios

<i>Test</i>	<i>EQ Intensity</i>	<i>MR Damper Mode</i>
1	0.50	Semi-active
2	0.75	Semi-active
3	0.50	Passive Off
4	0.75	Passive Off
5	0.75	Passive On
6	1.00	Passive On

In agreement with the RTHS Phase-1 configuration, the large-scale MR damper specimen is utilized as the experimental substructure. The computational model of the frame structure developed for simulation is used as the computational counterpart within the RTHS. Therefore, a full-DOF RT-Frame2D computational block is used within the

Simulink implementation with two inputs. These inputs are defined as the force provided by the MR damper when displaced by the hydraulic actuator and the ground motion record. The MR damper is assumed to be located and attached to the frame structure at the position shown in Figure 5.6. Therefore, displacements computed at 1024 Hz and outputted from the attachment position are imposed on the MR damper specimen with the hydraulic actuator. The experimental restoring force from the MR damper is measured from the load cell located at the hydraulic actuator for feedback. The MR damper tested here is used in different operational modes. Three operation modes: a semi-active mode, a passive-off mode and a passive-on mode are tested for the MR damper. Table 5.2 also shows the operational modes that are adopted for the MR damper for the testing scenarios. The same hydraulic actuator control design is used for all tests scenarios because the same physical substructure, i.e. the large-scale MR damper is utilized.

Table 5.3: Error values

<i>Test</i>	<i>Story</i>	E_{RTHS}	$E_{Tracking}$
1	1	7.40	1.05
	2	7.27	-
	3	7.45	-
2	1	4.88	1.21
	2	4.65	-
	3	4.93	-
3	1	1.77	0.45
	2	1.71	-
	3	1.74	-
4	1	1.80	0.45
	2	1.65	-
	3	1.64	-
5	1	5.00	1.26
	2	4.74	-
	3	4.92	-
6	1	5.38	1.45
	2	5.08	-
	3	5.15	-

Time history records of the floor displacements in the controlled RTHS and the corresponding simulation outputs are plotted simultaneously in Figure 5.8 to Figure 5.25. The uncontrolled simulated response is also included for comparison. Only 70 sec of the response is included for clarity. Additional plots zooming in on the region from 1 to 20 sec are included. An excellent match is observed between both the RTHS and the simulated displacement responses, demonstrating the accuracy and stability of the computational platform and the hydraulic actuator control.

RTHS error values are listed in Table 5.3. These values are calculated using Equation (4.11) for each floor displacement output yielding to an approximate mean value of 4.3% and thus clearly demonstrating the accuracy the results. Error values for the actuator tracking control are also included for reference in Table 5.3 and also demonstrate the accuracy in the tracking control performance. Note that these error values are only considered for the first floor where the MR damper is assumed to be attached to the frame structure. Note that nonlinear computational restoring forces for a full-DOF model are calculated within the computational block. Thus, performance of nonlinear modeling capabilities under real-time execution is directly evaluated here. As explained in Implementation IV at Chapter 4, stability performance of the CR integration scheme is guaranteed for both linear and nonlinear behavior. These excellent results further validate the adequate selection of modeling capabilities for implementation within the RT-Frame2D platform. Moreover, note that in contrasts to Implementation IV, here the MR damper is operated based on different modes and still yielding excellent results. Because the MR damper is considered the only experimental substructure, errors in the computational restoring force measurements have less impact in the RTHS performance. Noise effect is no longer considered of relevant importance as in previous implementations.

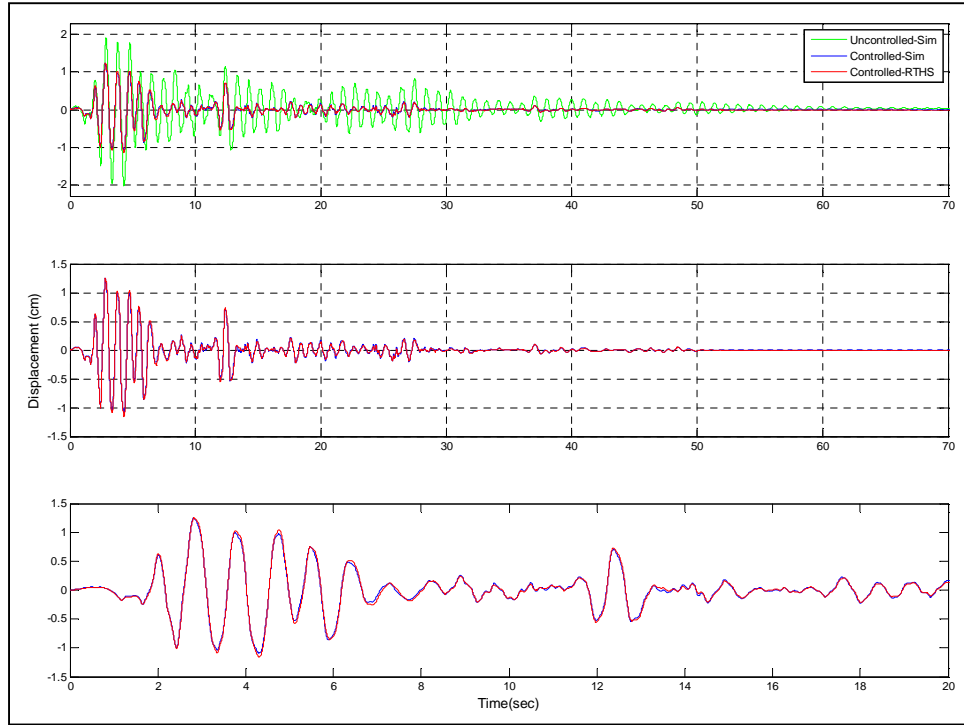


Figure 5.8: Test 1 – Displacement first floor

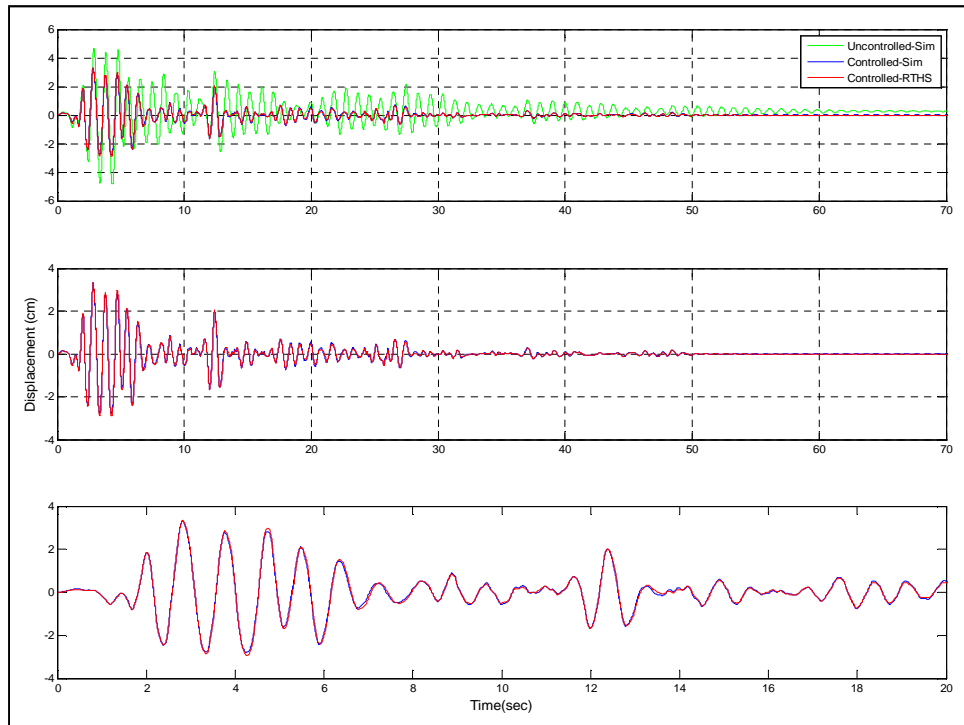


Figure 5.9: Test 1 – Displacement second floor

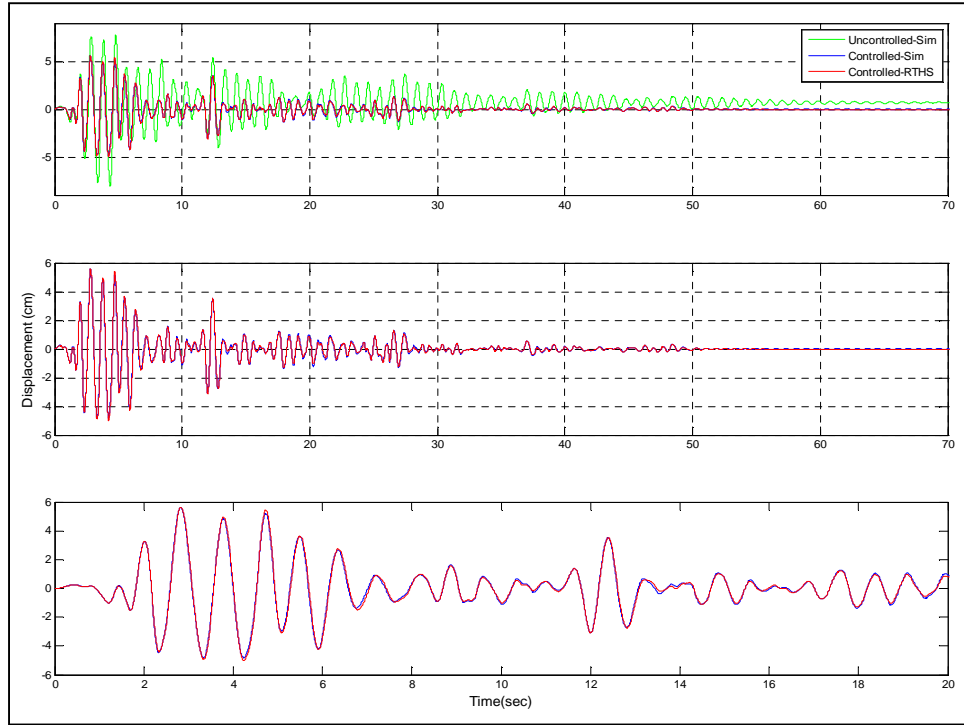


Figure 5.10: Test 1 – Displacement third floor

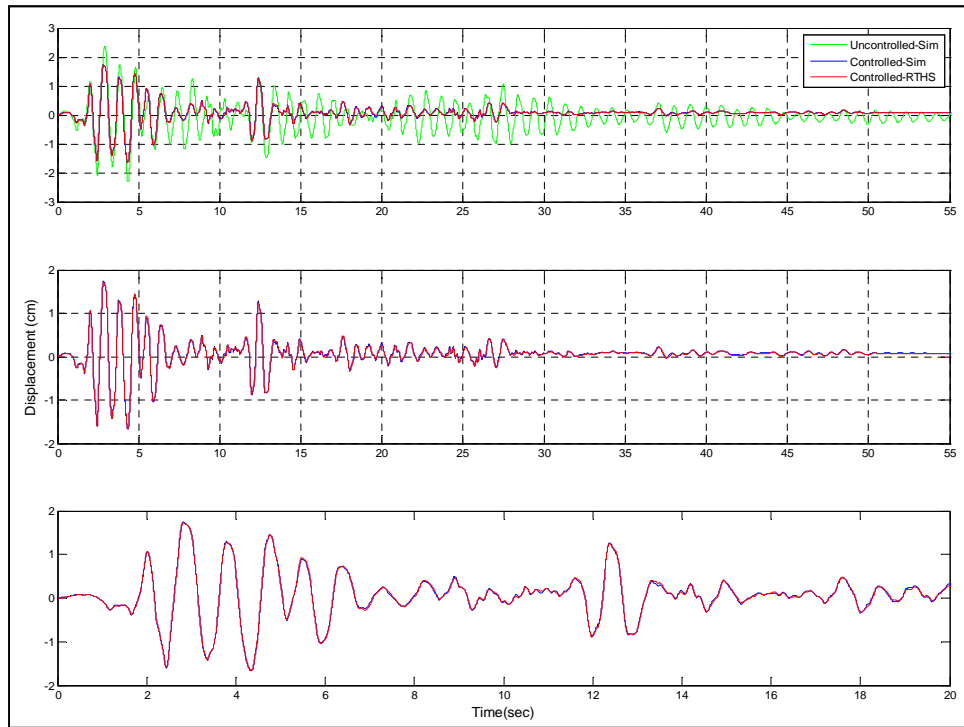


Figure 5.11: Test 2 – Displacement first floor

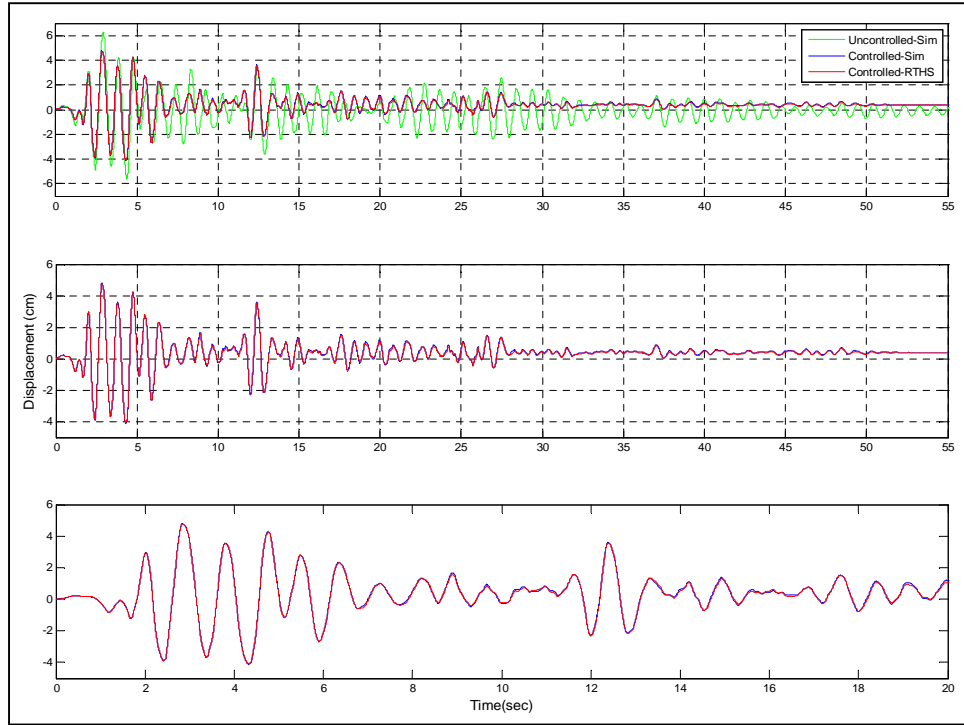


Figure 5.12: Test 2 - Displacement second floor

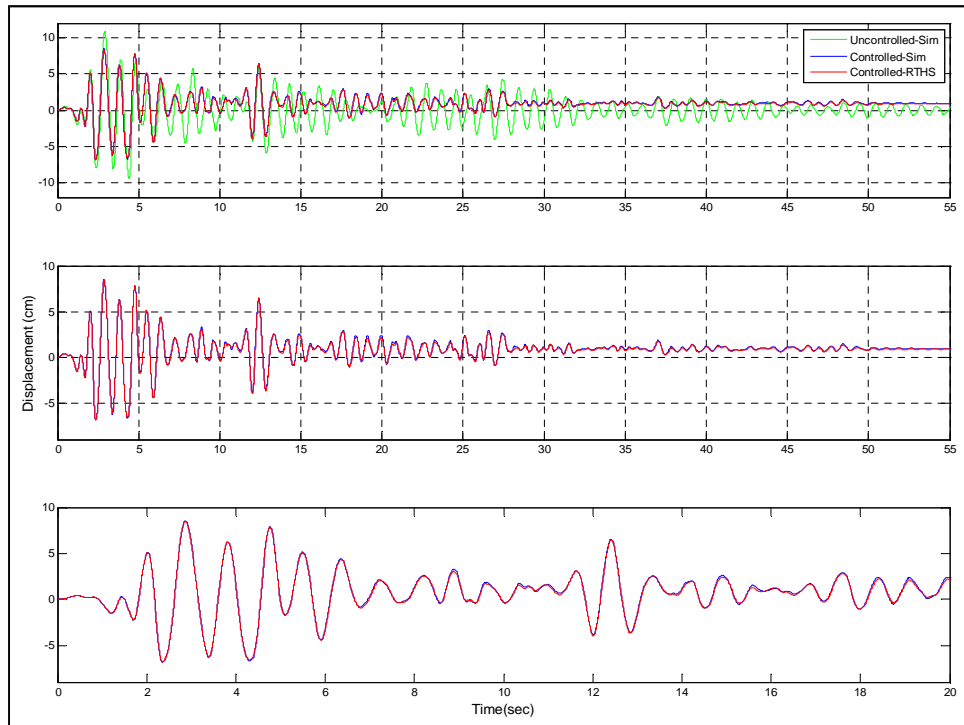


Figure 5.13: Test 2 - Displacement third floor

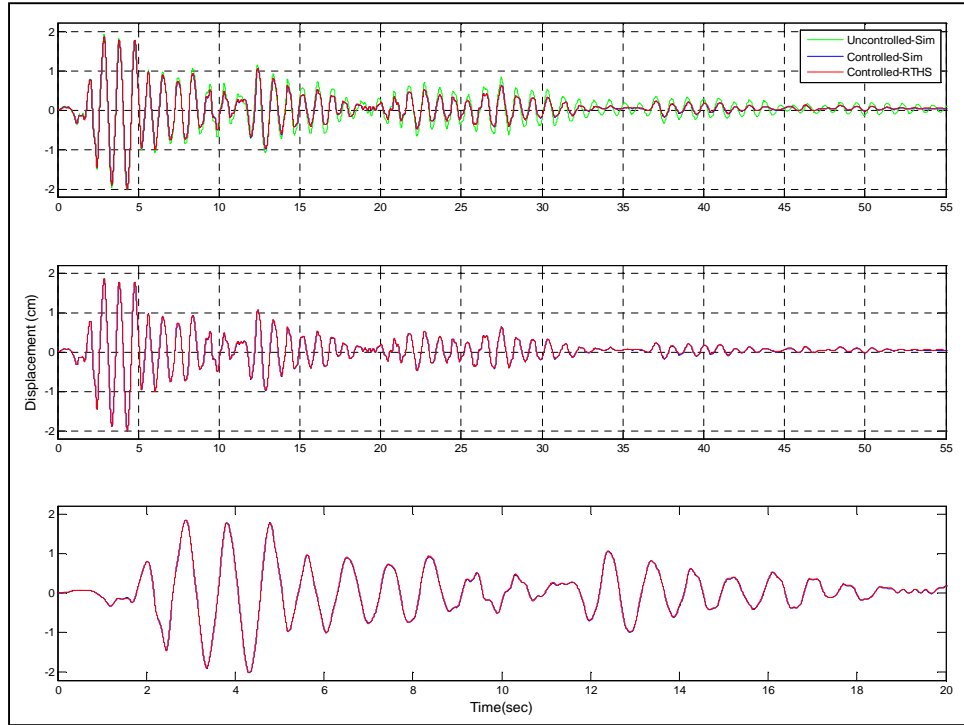


Figure 5.14: Test 3 - Displacement first floor

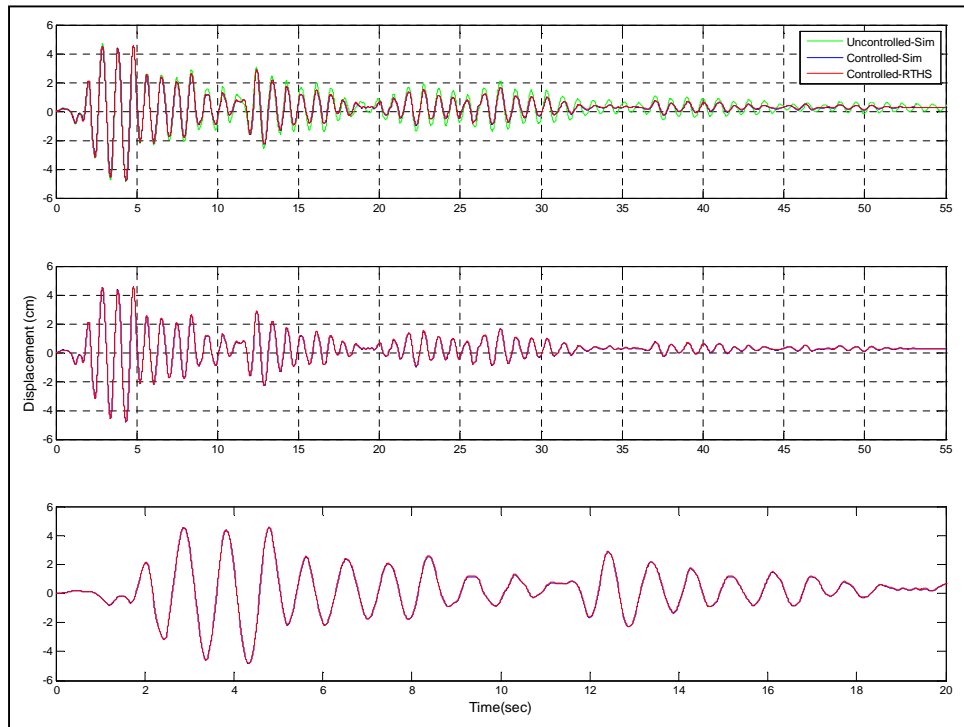


Figure 5.15: Test 3 - Displacement second floor

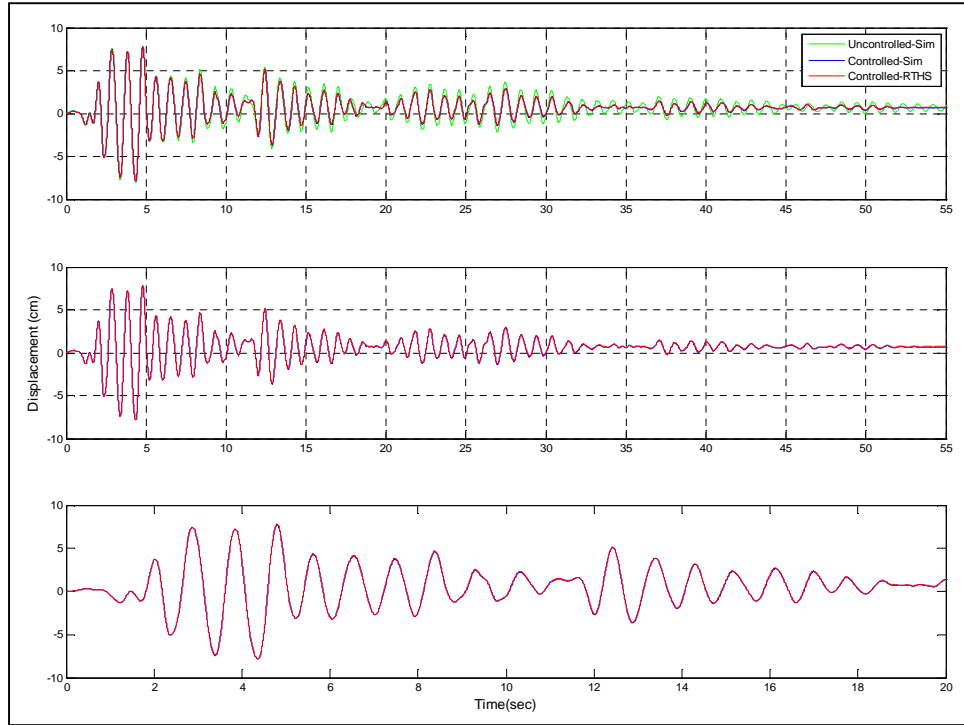


Figure 5.16: Test 3 - Displacement third floor

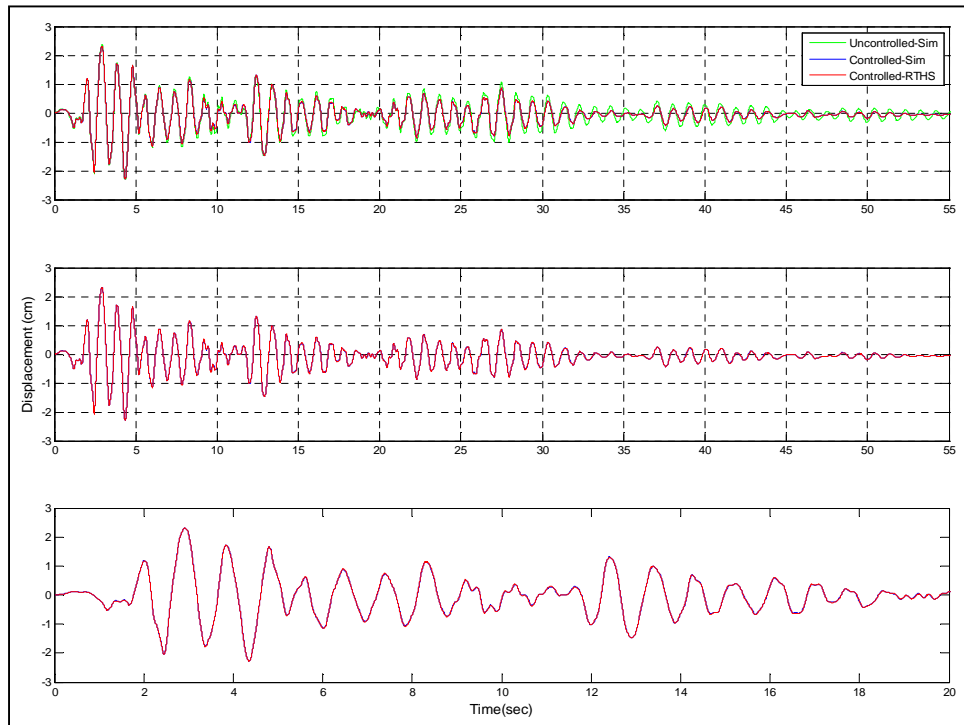


Figure 5.17: Test 4 - Displacement first floor

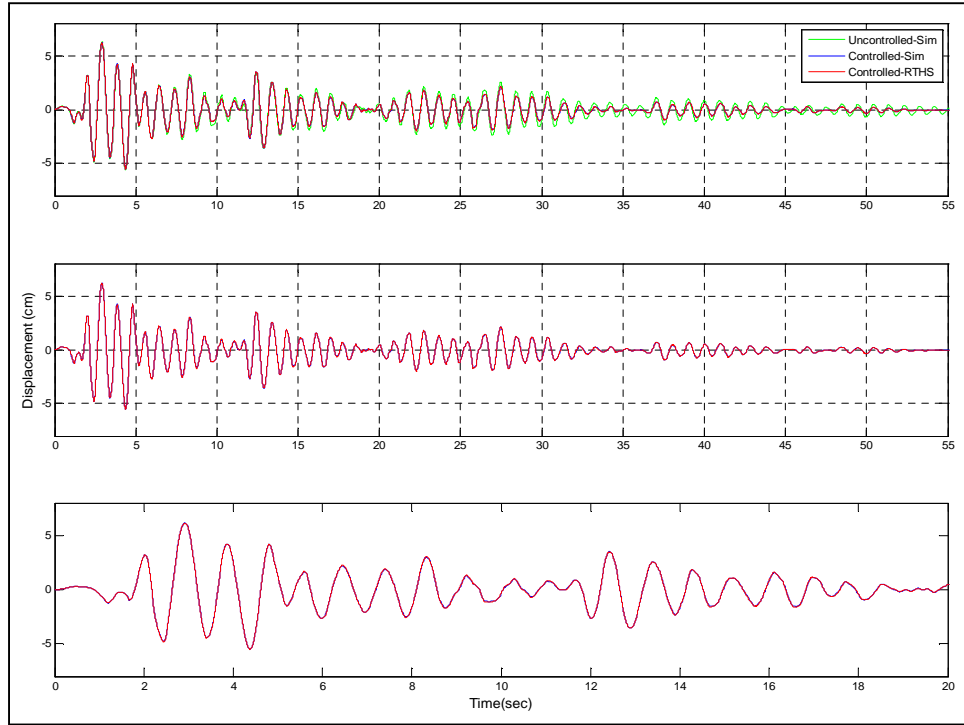


Figure 5.18: Test 4 - Displacement second floor

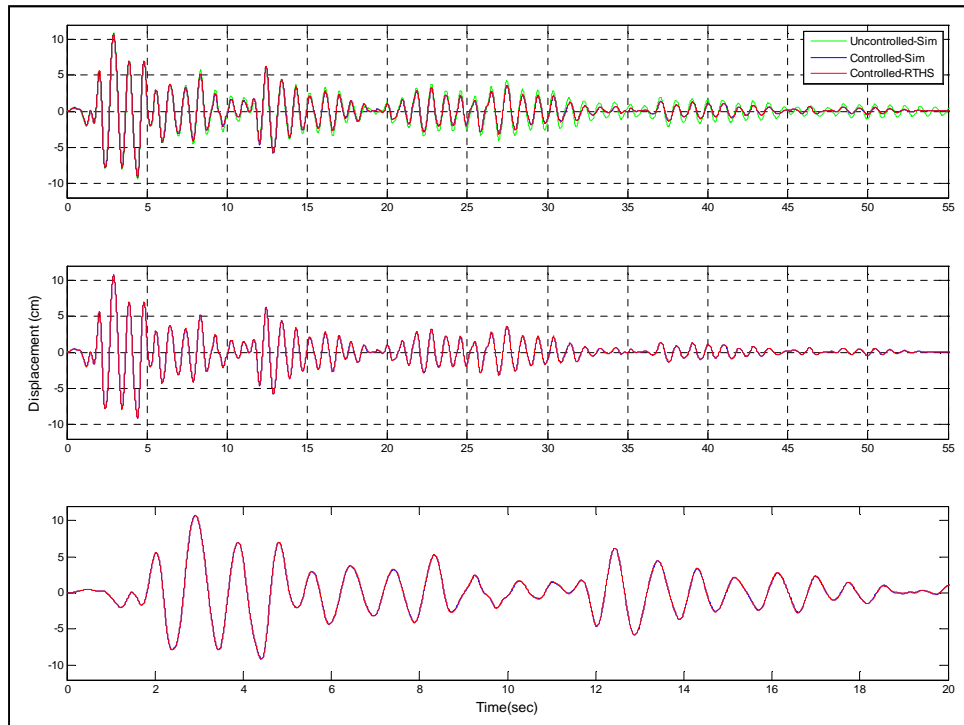


Figure 5.19: Test 4 - Displacement third floor

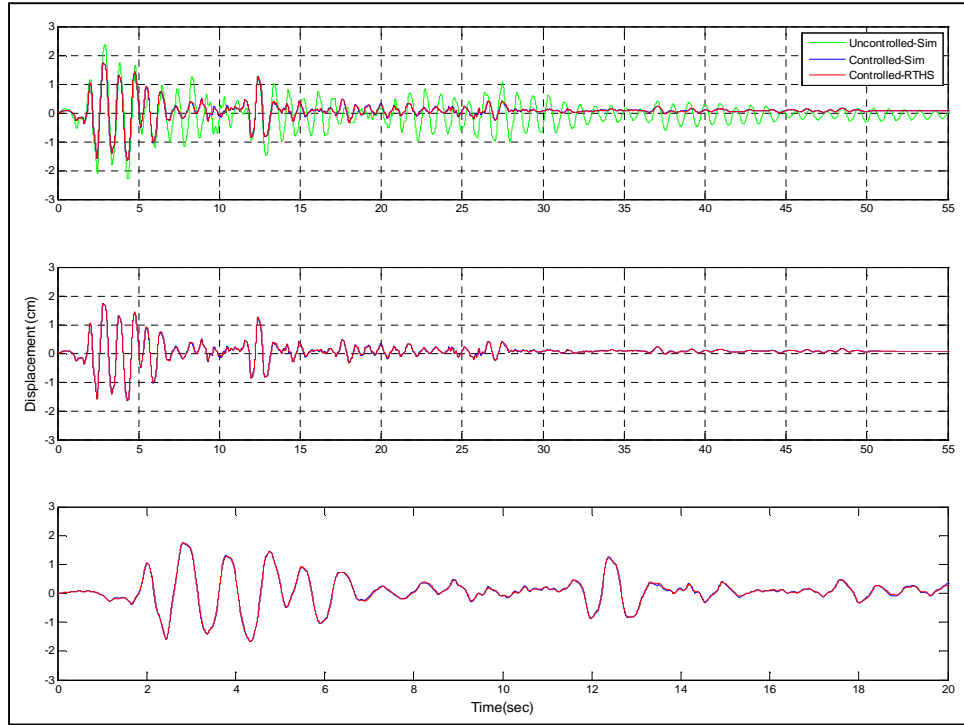


Figure 5.20: Test 5 - Displacement first floor

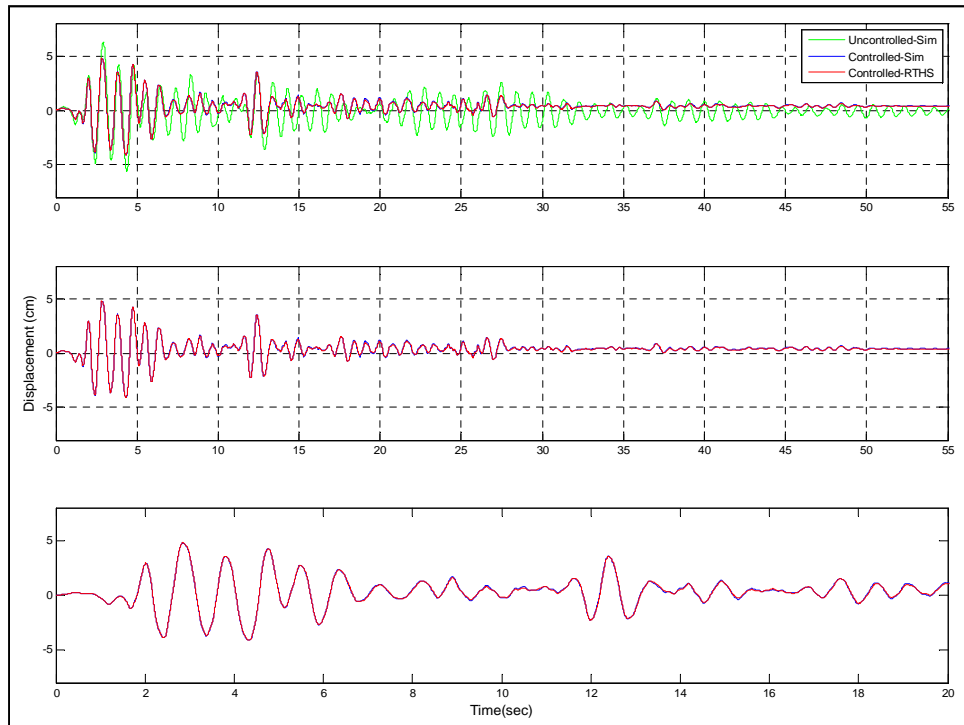


Figure 5.21: Test 5 - Displacement second floor

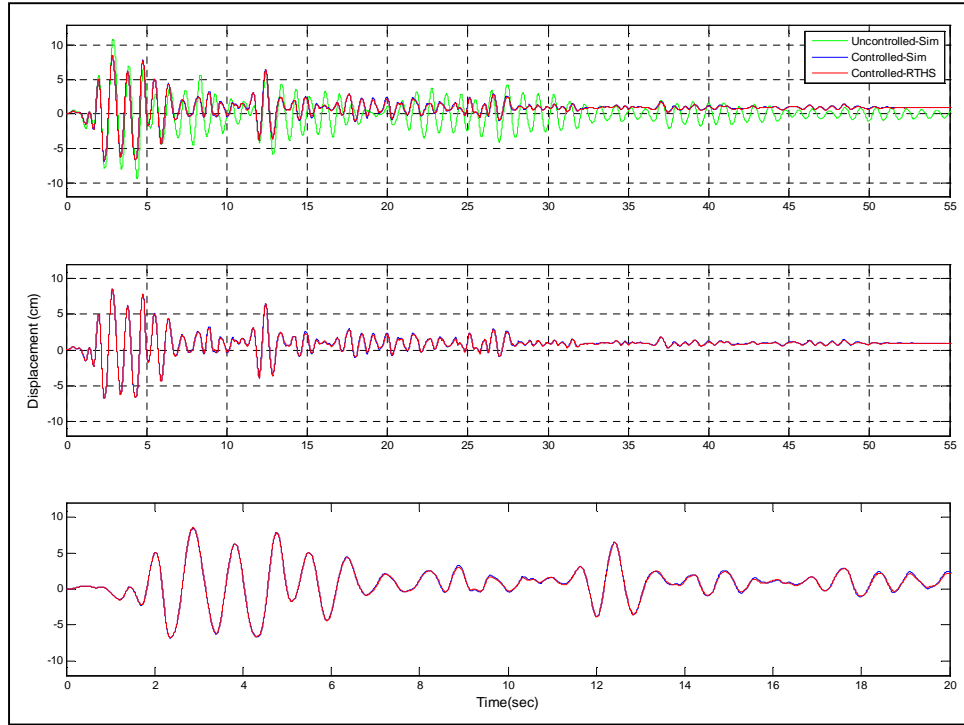


Figure 5.22: Test 5 - Displacement third floor

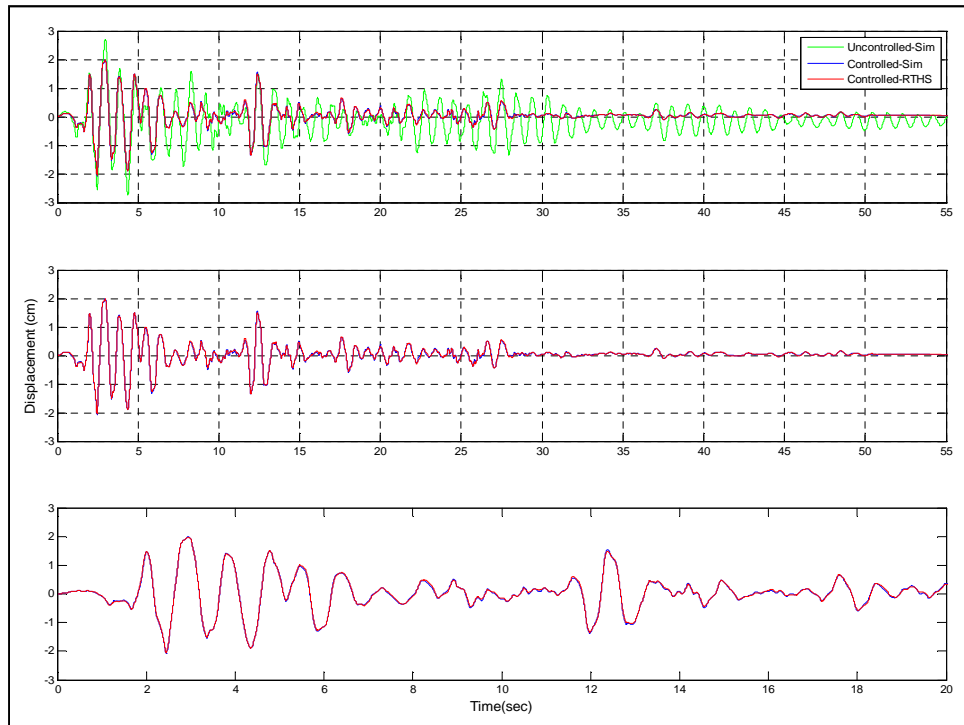


Figure 5.23: Test 6 - Displacement first floor

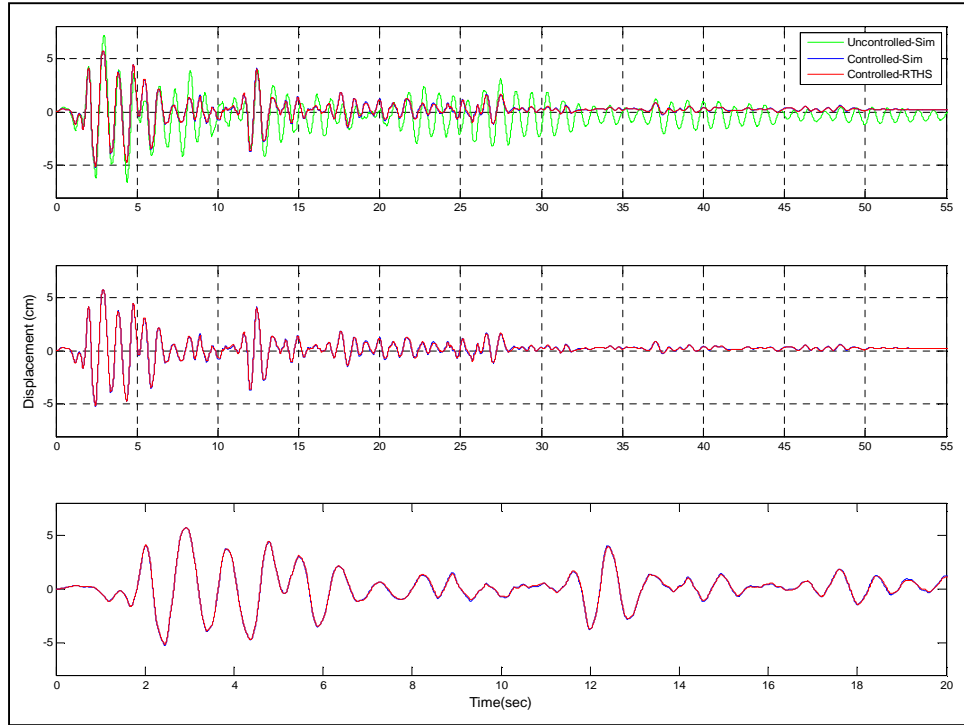


Figure 5.24: Test 6 - Displacement second floor

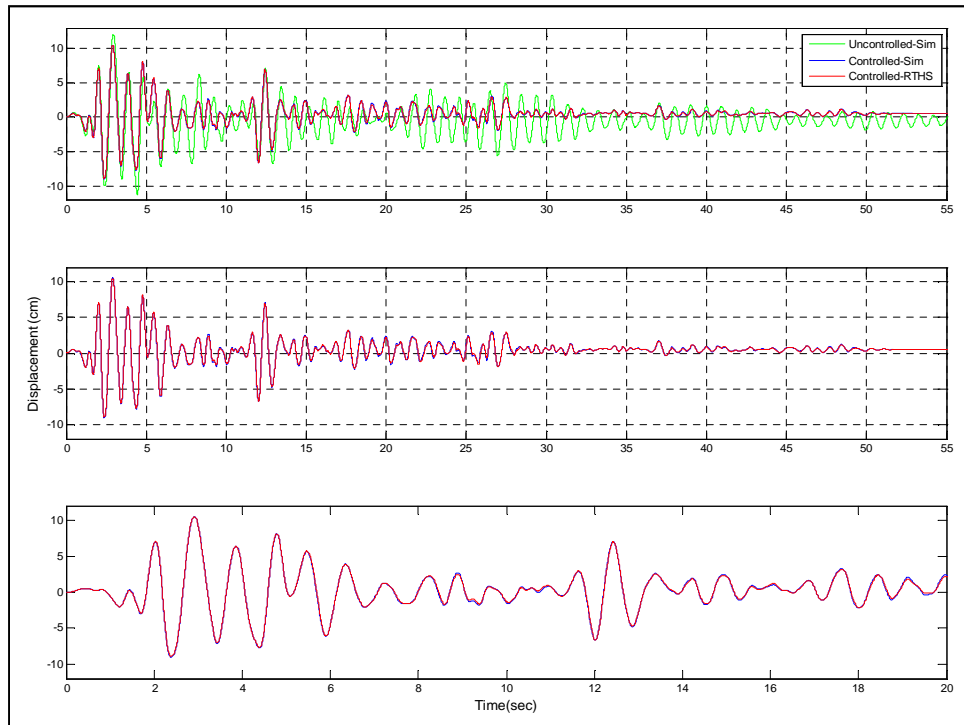


Figure 5.25: Test 6 - Displacement third floor

CHAPTER 6. CONCLUSIONS

The development, implementation and validation of an open-source computational platform, RT-Frame2D, for the real-time hybrid simulation of dynamically-excited steel frame structures have been presented in this study. This computational platform was proposed in response to the lack of and need for appropriate software with real-time and sufficient modeling capabilities for the hybrid simulation of steel frame structures. The present chapter summarizes the most relevant contributions and main observations during the development, implementation and validation of RT-Frame2D (RT-Frame2D and user manual are available at nees.org <http://nees.org/resources/realtimeframe2d>).

RT-Frame2D was developed and entirely implemented within the context of a *MATLAB/Simulink* environment using a *MATLAB/Embedded Subset Function* format. *MATLAB/Simulink* environment was selected to facilitate RT-Frame2D integration with remaining RTHS components so that a unified platform can be generated, compiled and executed within a real-time kernel platform. Several modeling features for the nonlinear dynamic analysis of steel frames were developed and coded within the RT-Frame2D framework using *MATLAB/Embedded functions*. The modeling features included in RT-Frame2D are:

- Linear elastic beam-column element including optional moment releases at element ends.
- Linear elastic beam-column element with flexible linear/nonlinear connections at element ends.
- Nonlinear beam-column element with concentrated or spread plasticity models to represent yielding evolution at element ends or within the element, respectively.

- Optional transverse shear effects for any of the previous beam-column element models.
- Bilinear and tri-linear kinematic hardening material models for modeling of the moment-curvature and moment-rotation interaction.
- Novel panel zone model with two different behaviors: a rigid body and a linear with three deformation modes including bidirectional tension/compression and shear distortion effect.
- Consideration of second order or P- Δ effects in building response by the use of the lean-on column concept and the geometric stiffness matrix approach.
- Two integration schemes for solving the equations of motion depending on the selected type of analysis: the implicit unconditionally-stable Newmark type scheme (only available in the first executable) and the explicit unconditionally-stable CR integration scheme (available for all remaining executables).

These modeling capabilities were accommodated under seven independent executable *RT_F2D_k.mdl* files to improve the real-time execution capacity. For instance, executable RT_F2D_1 considers the nonlinear beam-column element and the Newmark type integration scheme. Executables RT_F2D_2,5 consider the nonlinear beam-column element (RT_F2D_2) and beam-column element with nonlinear flexible connections (RT_F2D_5) in conjunction with the CR integration scheme. Executables RT_F2D_3,6 consider the rigid-body panel zone model in addition to the nonlinear beam-column element (RT_F2D_3) and beam-column element with nonlinear flexible connections (RT_F2D_6) in conjunction with the CR integration scheme. Executables RT_F2D_4,7 consider the linear deformable panel zone model in addition to the nonlinear beam-column element (RT_F2D_4) and beam-column element with nonlinear flexible connections (RT_F2D_7) in conjunction with the CR integration scheme. Bilinear and tri-linear hysteresis models and P- Δ effects were considered in all executables.

Numerical evaluation of RT-Frame2D to investigate its real-time execution performance and modeling capabilities for the nonlinear dynamic analysis of steel frame structures

was also performed. Real-time execution capabilities were investigated by recording and comparing TET values when subjecting the RT-Frame2D platform to the analysis of several frame computational models of increased complexity. Some key observations were obtained from this study:

- Main sources for increment in the recorded TET value through the different evaluation models were attributed to: the number of DOF, the extent of nonlinear response, the integration scheme and the CPU performance. However, storage capacity for definition of variables in the analysis and the amount of code that needs to be generated and compiled for execution was considered of more relevance based on the analysis of TET results.
- An approximately equal qualitatively real-time execution performance between executables RT_F2D_4,7 and among executables RT_F2D_2,3,5,6 was observed.
- Executables RT_F2D_2,3,5,6 showed improved real-time execution performance over executables RT_F2D_4,7, i.e. executables RT_F2D_2,3,5,6 have faster execution performance.
- The advantage of the explicit form in the CR integration scheme to avoid the need for stiffness matrix inversion while solving the equations of motion was also observed. This advantage was more evident when computational models with considerable number of DOF were evaluated.
- Average number of DOF with values of 201, 173 and 287 were approximated for executables RT_F2D_1, RT_F2D_4,7 and RT_F2D_2,3,5,6; respectively. Due to the consistency in the evaluation process, these values were considered as a fair reference regarding the maximum number of DOF that can be achieved by the proposed computational platform under real-time execution conditions (1024 Hz).

Evaluation of the nonlinear dynamic analysis capabilities offered by RT-Frame2D was also performed through comparison with the well-known open-source numerical platform *OpenSEES*. Five computational models including different modeling features in RT-Frame2D were considered for the study. *OpenSEES* models were developed with

modeling options considered equivalent to those in the RT-Frame2D platform. Some observations were also obtained from this evaluation:

- Excellent match in the global response was achieved for all the computational models.
- Excellent match was also achieved for hysteresis outputs between models with exact beam-column modeling schemes. However, certain discrepancy was observed for computational models in which no exact beam-column modeling scheme was used. Despite these minor hysteresis output differences, excellent agreement between global responses was still achieved, as mentioned before.
- The last observation was explained based on an overall average effect i.e. differences in the updating of one element state was compensated by the differences in the update of another.

The RTHS performance of the proposed computational platform was then investigated and experimentally validated. The computational platform was evaluated under several hybrid simulation scenarios of different complexity. An experimental validation consisting of four experimental implementations (I-IV) was performed first. Here, a MR damper and modular steel frame specimens were utilized as physical substructures and used depending on the RTHS scenario under evaluation. Several observations were concluded from these experimental results:

- RTHS of the one/two-story, two-bay configuration of the frame structure when subjected to ground motion was performed at Implementation I and II, respectively. The frame structure was considered as the physical substructure. A one and a two-DOF version of the computational platform were utilized here. Excellent agreement between RTHS and simulated displacement responses was achieved for each test scenario. The stability of the CR integration scheme was validated for both implementations. RTHS error was mainly attributed to the noise presence in the experimental measurements for both the actuator tracking

control and restoring force, in conjunction to the small amplitude of displacement records.

- RTHS of the two-story, one-bay configuration of the frame structure, equipped with a MR damper device and subjected to ground motion was performed at Implementation III. The frame structure and the MR damper were considered as physical substructures depending on the testing scenario, i.e. RTHS Phase-1 and Phase-2. A two-DOF version of the computational platform was utilized here. Excellent agreement between RTHS and simulated displacement responses was achieved for RTHS Phase-1. However, results for RTHS Phase-2 showed a certain degree of discrepancy. The stability of the CR integration scheme was also validated for both implementations. RTHS error was mainly attributed to the noise presence in the experimental measurements, in conjunction to the small amplitude of displacement records. However, incorrect alignment in the experimental set-up was attributed to have greater impact in results associated to RTHS Phase-2.
- Implementation IV focused in the RTHS evaluation of the two-story, one-bay configuration of the frame structure equipped with a MR damper device. The MR damper specimen was utilized as the physical substructure. Several RTHS scenarios were performed to evaluate different nonlinear modeling capabilities offered by the computational platform. Excellent agreement between RTHS and simulated displacement responses was achieved for each testing scenario. Moreover, comparison of hysteresis loops further confirmed the excellent results. Therefore, accuracy and stability in the computational restoring force calculation as well as stability of the CR integration scheme during the RTHS execution were verified and validated. Due to larger amplitude responses, noise ratio was considered of less relevance in the RTHS error.

The RTHS performance of the proposed computational platform was also validated with a second experimental evaluation. The following was observed:

- RTHS evaluation of a scaled prototype frame structure equipped with a large-scale MR damper and subjected to ground motion was performed. The large-scale MR damper specimen was utilized as the physical substructure. Several RTHS scenarios based on different earthquake intensities and operational modes of the damper were performed. Excellent agreement between RTHS and simulated displacement responses was achieved for each testing scenario. No instability in the CR integration scheme performance was observed. Moreover, accuracy and stability in the computational restoring force calculation during the RTHS execution was also verified based on the results.

LIST OF REFERENCES

- Allemang, R.J. & Brown, D.L. (1982). A correlation for modal vector analysis. *Proceedings of IMAC I: 1st International Modal Analysis Conference: 110-116.*
- American Institute of Steel Construction (AISC) 2005. Specification for Structural Steel Buildings, ANSI/AISC Standard 360/05, AISC, Chicago, Illinois, USA.
- Bass, B.J and Christenson, R.E. (2008). Hyperbolic Tangent Model of a 200 kN Magneto-Rheological Fluid Damper. *Submitted to ASCE Journal of Engineering Mechanics.*
- Blakeborough A., Williams M.S., Darby A.P., Williams D.M. (2001). The development of real-time sub-structure testing. *Phil. Trans. R. Soc. London.* A359, 1869-1891.
- Bonnet P.A., Lim C.N., Williams, M.s., Blakeborough, A., Neild, S.A., Stoten, D.P., and Taylor, C.A. (2007). Real-time hybrid experiments with Newmark integration, MCSmd outer-loop control and multi-tasking strategies. *Earthquake Engineering and Structural Dynamics.* 36(1): p.119-141.
- Bouc, R. (1967). Forced Vibration of Mechanical Systems with Hysteresis. *Proceedings of the 4th Conference on Non-linear Oscillations.* Prague
- Bursi, O.S. and Wagg, D. (2008). Modern Testing Techniques for Structural Systems. International Centre for Mechanical Sciences (CISM) - Courses and Lectures, Vol. 502.
- Carrion, J. and Spencer, B. (2007). Model-based Strategies for Real-time Hybrid Testing. *Newmark Structural Engineering Laboratory Report Series.* University of Illinois at Urbana-Champaign.
- Castaneda, N., Gao, X. and Dyke, S. (2012). A real-time hybrid testing platform for the evaluation of seismic mitigation in building structures. *Proceedings of the 2012 Structures Congress Conference.* Chicago.

- Castaneda, N., Gao, X. and Dyke, S. (2012). RT-Frame2D User's Manual.
- Chae, Y. (2011). Seismic Hazard Mitigation of Buildings Structures Using Magneto-Rheological Dampers. *Ph.D. Study*. Department of Civil and Environmental Engineering, Lehigh University.
- Chang, S. Y. (1999). An unconditionally stable explicit algorithm in time history analysis. *Report No. NCREE-99-001*. National Center for Research on Earthquake Engineering, National Taiwan University, Taipei, Taiwan.
- Chang, S. Y. (2002). Explicit pseudodynamic algorithm with unconditional stability. *Journal Engineering Mechanics*. 128(9), 935–947.
- Chen, W. F. and Kishi, N. (1989). Semi-rigid steel beam-to-column connections: Database and modeling. *Journal Structural Engineering – ASCE*. 115(1), pp. 105-119.
- Chen, C. (2007). Development and numerical simulation of a hybrid effective force testing method. *Ph.D. Study*. Lehigh University, Bethlehem, PA.
- Chen, C. and Ricles, J. M. (2008). Development of Direct Integration Algorithms for Structural Dynamics using Discrete Control Theory. *Journal of Engineering Mechanics*. 134, no. 8: 676-683.
- Chen, C. and Ricles, J. M. (2010). Tracking Error-based Servohydraulic Actuator Adaptive Compensation for Real-time Hybrid Simulation. *Journal of Structural Engineering*. 136, no. 4: 432-440.
- Chopra, A. K. (2001). Dynamics of structures: Theory and applications to earthquake engineering, 2nd Ed., Prentice-Hall, Upper Saddle River, N.J.
- Christenson, R. E., Lin Y. Z., Emmons, A. T., and Bass, B. (2008). Large-Scale Experimental Verification of Semiactive Control through Real-Time Hybrid Simulation. *ASCE Journal of Structural Engineering*. 134(4) p 522-535.
- Chung, Y. S., Meyer, C. and Shinozuka, M. (1988). SARCF User's Guide: Seismic Analysis of Reinforced Concrete Frames. *Technical Report NCEER-88-0044*. State University of New York at Buffalo.

- Clough, R.W. and Johnson, S. (1966). Effect of stiffness degradation on earthquake ductility requirements. *Proceedings of the Japan Earthquake Engineering Symposium*. Tokyo.
- Cook, R.D., Malkus, D.S. and Plesha, M.E. (1989). Concepts and Applications of Finite Element Analysis. Third Edition, John Wiley & Sons, Inc, ISBN 0-471-84788-7.
- Darby A.P., Blakeborough A., Williams M.S. (1999). Real-time substructure tests using hydraulic actuator. *Journal Engineering Mechanics*. 125, 1133-1139.
- Darby A.P., Blakeborough A., Williams M.S. (2000). Improved control algorithm for real-time substructure testing. *Earthquake Engineering Structural Dynamics*. 30, 431-448.
- Dyke, S.J. (1996). Acceleration feedback control strategies for active and semi-active control systems: Modeling, Algorithm development, and experimental verification. *Ph.D. Study*. Department of Civil Engineering and Geological sciences, University of Notre Dame.
- Dyke, S.J., Spencer, B.F., Jr., Sain, M.K., and Carlson, J.D. (1997). Phenomenological Model of a Magnetorheological Damper. *ASCE Journal of Engineering Mechanics*. 123(3): 230-238
- El-Tawil, S., Vidarsson E., Mikesell, T. and Kunnath, K. (1999). Inelastic behavior and design of steel panel zones. *Journal of Structural Engineering*. 125, 2, pages 183-193.
- El-Tawil, S., and Deierlein, G., (2001a). Nonlinear analyses of mixed steel-concrete moment frames. Part I: Beam-column element formulation. *Journal Structural Engineering*. 127(6), 647–655.
- El-Tawil, S., and Deierlein, G., (2001b). Nonlinear analyses of mixed steel-concrete moment frames. Part II: Implementation and verification. *Journal Structural Engineering*. 127(6), 656–665.
- Elwood, K. J. (2002). Shake table tests and analytical studies on the gravity load collapse of reinforced concrete frames. *Ph.D. Study*. Department of Civil and Environmental Engineering, University of California, Berkeley.
- ETABS. (1988). User's Manual. Computers and Structures Inc., Berkeley, CA.

- Franklin, G. F., Powell, J. D., and Naeini, A. E. (2002). Feedback control of dynamic system. 4th Ed., Prentice-Hall, Upper Saddle River, N.J.
- Friedman, A., Zhang, J., Phillips, B., Jiang, Z., Agrawal, A.K., Dyke, S., Ricles, J.M., Spencer, B.F., Sause, R., Christenson, R. (2010). Accommodating MR Damper Dynamics for Control of Large Scale Structural Systems. <https://nees.org/resources/674>
- Galambos, T. V. (1988). Guide to Stability Design Criteria for Metal Structures. 4th Ed., John Wiley & Sons, New York, NY, USA.
- Gao, X., Castaneda, N. and Dyke, S. J. Real-time Hybrid Simulation - from Dynamic System, Motion Control to Experimental Error. *Earthquake Engineering and Structural Dynamics* (Submitted).
- Gao, X. (2012). Development of a Robust Real-time Hybrid Simulation Framework: from System, Control to Experimental Error Verification. *Ph.D. Study*. School of Civil Engineering, Purdue University, West Lafayette.
- Gavin, H.P. (2001). Multi-Duct ER Dampers. *Journal of Intelligent Material Systems and Structures*. Vol. 12, No. 5, pp.353-366.
- Geschwindner, L. F. (1994). A practical approach to the 'leaning' column. *Engineering Journal*. 31(4), 141–149.
- George E. Brown, Jr. Network for Earthquake Engineering Simulation (NEES) <http://www.nees.org/>
- Giberson, M.F. (1967). The response of nonlinear multistory structures subjected to earthquake excitation. *Ph.D. Study*. Caltech. (<http://thesis.library.caltech.edu/3604>).
- Glover, K. and McFarlane, D. (1989). Robust Stabilization of Normalized Coprime Factor Plant Descriptions with H_∞ -bounded Uncertainty. *IEEE Transactions on Automatic Control*. 34, no. 8: 821-830.
- Gomez, S. R., Chung, Y. S., and Meyer, C. (1990). SARCF-II User's Guide: Seismic Analysis of Reinforced Concrete Frames. *Technical Report NCEER-90-0027*. State University of New York at Buffalo.
- GTSTRUDL User's Manual. Georgia Tech Research Corp., Atlanta, GA.

- Hajjar, J. F., and Gourley, B. C. (1997). A cyclic nonlinear model for concrete-filled tubes I: Formulation. *Journal Structural Engineering*. 123(6), 736–744.
- Hilber, H. M., Hughes, T. J. R., and Taylor, R. L. (1977). Improved numerical dissipation for time integration algorithms in structural mechanics. *Earthquake Engineering Structural Dynamics*. 5(3), 283–292.
- Hilmy, S. I., and Abel, J. F. (1985). A strain-hardening concentrated plasticity model for nonlinear dynamic analysis of steel buildings. *Proceedings, NUMETA85. Numerical Methods in Engineering, Theory and Applications*, 1, 303–314.
- Hjelmstad, K.D. and Haikal, G. (2006). Analysis of Steel Moment Frames with Deformable Panel Zones. *Steel Structures*. Pages 129-140
- Horiuchi, T., Nakagawa, M., Sugano, M. and Konno, T. (1996). Development of a Real-Time Hybrid Experimental System with Actuator Delay Compensation. *Proceedings 11th World Conf. on Earthquake Engineerin*. Paper No 660.
- Horiuchi, T., Inoue, M., Konno, T. and Namita, Y. (1999). Real-Time Hybrid Experimental System with Actuator Delay Compensation and its Application to a Piping System with Energy Absorber. *Earthquake Engineering and Structural Dynamics*. 28, no. 10: 1121-1141.
- Hudson, D.E. (1961). A new Vibration Exciter for Dynamic Test of Full-Scale Structures. California Institute of Technology Reports (<http://authors.library.caltech.edu/26489/>).
- Hudson, D.E. (1962). Synchronized Vibration Generators for Dynamic Tests of Full-Scale Structures. California Institute of Technology Reports (<http://authors.library.caltech.edu/26490/>).
- Ibarra, L, Medina, R., and Krawinkler, H. (2002). Collapse Assessment of Deteriorating SDOF Systems. *12th European Conference on Earthquake Engineering*. Paper Reference 665, London, UK, September 9-13.
- Iwan, W.D. (1961). The Dynamic Response of Bilinear Hysteretic Systems. California Institute of Technology Reports (<http://thesis.library.caltech.edu/3924/>).

- Jiang, Z., Christenson, R., Chae, Y., Ricles, J.M., Friedman, A., Dyke, S., Phillips, B., Spencer, B.F. (2010). Comparison of 200 KN MR Damper Models for use in Real-time Hybrid Simulation. <https://nees.org/resources/670>.
- Jiang, Z. and Christenson, R. (2011). A comparison of 200 kN magneto-rheological damper models for use in real-time hybrid simulation pretesting. *Journal of Smart Materials and Structures*. 20 065011.
- Jiang, Z. and Christenson, R. (2012). A fully dynamic magneto-rheological fluid damper model. *Smart Materials and Structures*. 21 (2012) 065002 (12pp)
- Juang, J.N. and Pappa, R.S. (1985). An eigensystem realization algorithm for modal parameter identification and model reduction. *Journal of Guidance Control and Dynamics*. 8:620-627
- Kanaan, A. E. and Powell, G.H. (1973). DRAIN-2D A General Purpose Compute Program for Dynamic Analysis of Inelastic Plane Structures. *Reports No. UCB/EERC/73/06 and 73/22*. University of California, Berkeley.
- Kang THK. (2004). Shake Table Tests and Analytical Studies of Reinforced Concrete Flat Plate Frames and Post-Tensioned Flat Plate Frames. *PhD Thesis*. Department of Civil and Environmental Engineering, University of California, Los Angeles.
- Karavasilis, T.L., Ricles, J.M., Marullo, T., Chen, C. (2009). HybridFEM: A program for nonlinear dynamic time history analysis and real-time hybrid simulation of structures. *ATLSS Engineering Research Center Report*. Lehigh University, Bethlehem, PA.
- Kent, D. C., and Park, R. (1971). Flexural members with confined concrete. *Journal Structural Division ASCE*, 97(7), 1969–1990.
- Kishi, N., and Chen, W. F. (1986). Database of steel beam-to-column connections. *Vol. 1 & 2, Structural Engineering Report No. CE-STR-86-26*. School of Civil Engineering, Purdue University, West Lafayette, IN.
- Kunnath, S. K., Reinhorn, A. M., and Lobo, R. F. (1992). IDARC Version 3.0: A Program for the Inelastic Damage Analysis of Reinforced Concrete Structures. *Report No. NCEER-92-002*. National Center for Earthquake Engineering Research, State University of New York at Buffalo.

- Kwon O.S., Nakata N, Elnashai A.S., and Spencer B.F. (2005). Technical Note: A framework for multi-site distributed simulation and application to complex structural systems. *Journal of Earthquake Engineering*. 9(5): p. 741-753.
- Leon, R.T. (1989). Interior joints with variable anchorage lengths. *Journal of Structural Engineering*. 115,9, pages 2261-2275.
- Lobo, R.F. (1994). Inelastic Dynamic Analysis of Reinforced Concrete Structures in Three Dimensions. *Ph.D. Study*. Department of Civil Engineering. New York State University at Buffalo.
- Magonette, G. (2001). Development and Application of Large-scale Continuous Pseudodynamic Testing Techniques. *Phil. Trans. Royal Society*, 359: 1771-1799.
- Mahafza, B.R. (1998). Introduction to Radar Analysis. *CRC Press*.
- Mahin SA and Shing PSB. (1985). Pseudodynamic method for seismic testing. *Journal of Structural Engineering-ASCE*, 111(7): p. 1482-1503.
- Mahin SA, Shing PSB, Thewalt CR, and Hanson RD. (1989). Pseudodynamic test method - current status and future directions. *Journal of Structural Engineering-ASCE*. 115(8): p. 2113-2128.
- Mckenna, F. and Fenves, G.L. (2002). The OpenSEES command language primer. <http://opensees.berkeley.edu>. Department of Civil and Environmental Engineering, University of California, Berkeley, CA.
- Mckenna, F., Fenves, G.L. and Scott, M.H. (2002). Open system for earth-quake engineering simulation. <http://opensees.berkeley.edu>. Pacific Earthquake Engineering Research Center, University of California, Berkeley, CA.
- Mercan, O. (2003). Evaluation of Real-Time Pseudodynamic Simulation Algorithms for Seismic Simulation of Structural Assemblages. *M.S. Thesis*. Lehigh University.
- Mercan, O. and Ricles, J.M. (2004). A New Real-Time Pseudodynamic (PSD) Simulation Algorithm. *6th International Congress on Advances in Civil Engineering*. Bogazici University, Istanbul, Turkey.
- Mostaghel, N. (1999). Analytical description of pinching, degrading hysteretic systems. *Journal of Engineering Mechanics*. 125,2, pages 216-224.

- Nakashima, M., Kato, H. and Takaoka, E. (1992). Development of Real-time Pseudodynamic Simulation. *Earthquake Engineering and Structural Dynamics*, Vol.21, pp. 79-92.
- Nakashima, M. and Masaoka, N. (1999). Real-Time On-Line Test for MDOF Systems. *Earthquake Engineering and Structural Dynamics*. Vol. 28, pp. 393-420
- Nakata, N. (2011). Error Analysis of Digitally-Controlled Servo Hydraulic Actuators for Structural Testing. *Journal of Earthquake Engineering*. 15(6). 901-923.
- Nakata, N. and Sehman, M. (2012). Substructure Shake Table test Method Using Controlled Masses: Formulation and Numerical Simulation. *Earthquake Engineering and Structural Dynamics*.
- Newmark, N.M. (1959). A method of computation for structural dynamics. *Journal of Engineering Mechanics Division, ASCE*. Vol. 85, pp.67–94.
- Ohtori, Y., Christenson, R.E., Spencer, B.F. and Dyke, S.J. (2004). Nonlinear Benchmark Control Problem for Seismically Excited Buildings. *ASCE Journal of Engineering Mechanics*. 130(4), pp.366-385,2004
- OpenSEES*: <http://opensees.berkeley.edu/index.php>
- Oughourlian, C. V., and Powell, G. H. (1982). ANSR-III: General Purpose Computer Program for Nonlinear Structural Analysis. *Report No. UCB/EERC-82/21*. Earthquake Engineering Research Center, University of California at Berkeley.
- Ozdemir, H. (1976). Nonlinear Transient Dynamic Analysis of Yielding Structures. *Ph.D. Study*. University of California, Berkeley.
- Park, Y. J., Reinhorn, A. M., and Kunnath, S. K. (1987). IDARC: Inelastic Damage Analysis of Reinforced Concrete Frame - Shear-Wall Structures. *Technical Report NCEER-87-0008*. State University of New York at Buffalo.
- Phillips B.M., Chae, Y., Jiang, Z., Spencer, B.F., Ricles, J.M., Christenson, R.E., Dyke, S.J. and Agrawal, A. (2010). Real-Time Hybrid Simulation Benchmark Structure with a Large-Scale MR Damper. *Proceedings of the Fifth World Conference on Structural Control and Monitoring*. Shinjuku, Tokyo.

- Phillips, B. M. and Spencer, B. F. (2011). Model-Based Servo-Hydraulic Control for Real-Time Hybrid Simulation. *Newmark Structural Engineering Laboratory Report Series*. University of Illinois at Urbana-Champaign.
- Phillips, B. M. and Spencer, B. F. (2012). Model-based multi-actuator control for real-time hybrid simulation. *Journal of Engineering Mechanics*. (accepted for publication).
- Phillips, B. M. (2012). Model-Based Feedforward-Feedback Control for Real-Time Hybrid Simulation of Large-Scale Structures. *Ph.D. Study*. Department of Civil Engineering, University of Illinois at Urbana-Champaign, Illinois, USA.
- Popovics, S. (1973). A numerical approach to the complete stress strain curve for concrete. *Cement and concrete research*. 3(5), 583-599.
- Reinhorn, A., Sivaselvan, M., Liang, Z. and Shao, X. (2004). Real-time Dynamic Hybrid Testing of Structural Systems. *13th World Conference on Earthquake Engineering*. Vancouver, B.C., Canada, 2004. 1644.
- RT-Frame2D: <http://nees.org/resources/realtimetype2d>
- RISA-2D User's Guide, RISA Technologies, Lake Forest, CA.
- Rutenberg, A. (1982). Simplified P-Delta Analysis for Asymmetric Structures. *ASCE Journal of the Structural Division*. Vol. 108, No. 9.
- SAC Steel project: <http://quiver.eerc.berkeley.edu:8080/>.
- SAP2000. (2008). Static and Dynamic Finite Element Analysis of Structures. Version 12.0.0. Computer and Structures, Inc., Berkeley, California.
- Saouma, V., Kang, D., Haussman, G. (2010). A Computational Finite-Element Program for Hybrid Simulation
- Schellenberg A and Mahin SA. (2006). Integration of hybrid simulation within the generalpurpose computational framework OpenSEES. *Proceedings, 8th National Conference on Earthquake Engineering*. San Francisco, CA.
- Schellenberg A, Mahin SA, and Fenves GL. (2007). A software framework for hybrid simulation of large structural systems. *Proceedings, ASCE Structures Congress*. Long Beach, CA.

- Scott, B. D., Park, R., and Priestley, M. J. N. (1982). Stress-strain behavior of concrete confined by overlapping hoops at low and high strain rates. *ACI Journal*. 79(1), 13–27.
- Scott, M.H. and G.L. Fenves. (2006). Plastic Hinge Integration Methods for Force-Based Beam-Column Elements. *Journal of Structural Engineering, ASCE*. 132(2):244-252.
- Shao, X., Reinhorn, A.M., Sivaselvan, M.V. (2011). Real time hybrid simulation using shake tables and dynamic actuators. *ASCE-Journal of Structural Engineering*. 137(7):748-760.
- Shao, X and Enyart, G. (2012). Development of a Versatile Hybrid Testing System for Seismic Experimentation. *Society of Experimental Mechanics*. doi:10.1111/j.1747-1567.2012.00837.x.
- Shi, S. (1997). Evaluation of Connection Fracture and Hysteresis Type on the Seismic Response of Steel Buildings. *Ph.D. Study*. Department of Civil Engineering, University of Illinois at Urbana-Champaign, Illinois, USA.
- Shing, P.B. and Mahin, S.A. (1983). Experimental error propagation in pseudodynamic testing. *Report UCB/EERC-83/12*. Earthquake Engineering Research Center, University of California, Berkeley, CA.
- Shing, P.B. and Mahin S.A. (1987). Cumulative experimental errors in pseudo-dynamic tests. *Earthquake Engineering and Structural Dynamics*. 15: 409-424.
- Shing, P.B., Vannan, M.T., and Carter, E. (1991). Implicit time integration for pseudodynamic tests. *Earthquake Engineering and Structural Dynamics*. 20(6): 551-576.
- Shing, P.B. and Vannan, M.T. (1991). Implicit time integration for pseudodynamic tests: convergence and energy dissipation. *Earthquake Engineering and Structural Dynamics*. 20(6): 809-819.
- Shing, P.B, Wei, Z., Jung, R., and Stauffer, E. (2004). NEES fast hybrid test system at the University of Colorado. *In Proceedings of the 13th World Conference in Earthquake Engineering*.

- Shiohara, H. (2001). New model for shear failure of RC interior beam-column connections. *Journal of Structural Engineering*. 127,2, pages 152-160.
- Sivaselvan, M. V. and Reinhorn, A. M. (2000). Hysteretic models for deteriorating inelastic structures. *Technical Report MCEER-99-0018*. Multidisciplinary Center for Earthquake Engineering Research, State University of New York at Buffalo, Buffalo, N.Y.
- Skolnik, M. (1990). Radar Handbook. *Second Edition, McGraw Hill Pub. Company*.
- Soong TT and Spencer, B.F. (2002). Supplemental energy dissipation: state-of-the-art and state-of-the-practice. *Engineering Structures*, 24: 243-259.
- Spacone, E., Filippou, F. C., and Taucer, F. F. (1996a). Fiber beam-column model for nonlinear analysis of R/C frames. Part I: Formulation. *Earthquake Engineering Struct. Dynamincs*. 25(7), 711–742.
- Spacone, E., Filippou, F. C., and Taucer, F. F. (1996b). Fiber beam column model for nonlinear analysis of R/C frams. Part II: Application. *Earthquake Engineering Structural Dynamics*. 25(7), 728-742.
- Spencer, B.F. (2003). The MOST Experiment, July 30, 2003. *NEESgrid Report*, December 17, 2003.
- Spencer B. F., Dyke S. J., Sain M. K. and Carlson J. D. (1997). Phenomenological model of a magnetorheological damper. *Journal of Engineering Mechanics Division ASCE*. 123 230–8
- STAAD-III Structural Analysis and Design Program User's Manual. Revision 16, Research Engineers, Inc., Marlton, N.J., 1992.
- Subbaraj, K. and Dokainish, M.A. (1989). A Survey of Direct Time-Integration Methods in Computational Structural Dynamics - II. Implicit Method. *Computers and Structures*. Vol.32, No.6, pp.1387–1401.
- Takanashi K, Udagawa K, Seki M, Okada T, and Tanaka H. (1975). Nonlinear earthquake response analysis of structures by a computer-actuator on-line system. *Bulletin of Earthquake Resistant Structure Research Center*. University of Tokyo.

- Takeda, T., Sozen, M.A., and Nielsen, N.N. (1970). Reinforced Concrete Response to Simulated Earthquakes. *Journal of the Structural Division, ASCE*. Vol. 96(12), 2557–2573.
- The MathWorks. (2009, 2010, 2011): <http://www.mathworks.com/>
- The RAM Structural System, RAM Frame, Version 6, RAM International, Carlsbad, CA, 1998.
- Thewalt CR and Mahin SA. (1987). Hybrid solution techniques for generalized pseudodynamic testing. *Report UCB/EERC-87/09*. University of California, Berkeley, CA.
- Thewalt CR and Roman M. (1994). Performance parameters for pseudodynamic tests. *Journal of Structural Engineering – ASCE*. 120(9): p. 2768-2781.
- Valles, R.E., Reinhorn, A.M., Kunnath, S.K., Li, C. and Madan, A. (1996). IDARC2D Version4.0: A Computer Program for the Inelastic Damage Analysis of the Buildings. *Technical Report NCEER-96-0010*. National Center for Earthquake Engineering Research, Buffalo, New York.
- Wen, Y.K. (1976). Method of Random Vibration of Hysteretic Systems. *Journal of Engineering Mechanics Division, ASCE*. Vol. 102, No. EM2, pp. 249–263.
- Wilson, E. L. (1968). A computer program for the dynamic stress analysis of underground structures. *SESM Report No. 68-1*. Division of Structural Engineering and Structural Mechanics, University of California, Berkeley, California.
- Wilson, E.L. and Habibullah, A. (1987). Static and Dynamic Analysis of Multi-story Buildings including P-Delta Effects. *Earthquake Spectra Journal, EERI*. Vol. 3, No.2, pp.289-298.
- Wu, B., Wang, Q., Shing, P. B. and Ou, J. (2007). Equivalent Force Control Method for Generalized Real-time Substructure Testing. *Earthquake Engineering and Structural Dynamics*. 36: 1127-1149.
- Yamaguchi, N. and Minowa, C. (1998). Dynamic performance of Wooden Bearing Walls By Shaking Table Test. *Proc. Fifth World Conference on Timber Engineering*. August 17-20, 1998, Montreux, Switzerland. V2, pp 26-334.

Zhang, X.Y., Sim, S.H., and Spencer, Jr., B.F. (2008). Finite Element Model Updating of a Truss Model using Incomplete Modal Data. *Proceedings World Forum on Smart Materials and Smart Structures Technology 2007*. Chongqing, China.